THE UNIVERSITY OF QUEENSLAND

AUSTRALIA

Development of High-Performance Bismuth Telluride-Based Thermoelectric Nanomaterials through Structure Manipulating and Band Engineering

Min Hong

Bachelor of Mechanical Engineering

A thesis submitted for the degree of Doctor of Philosophy at

The University of Queensland in 2016

School of Mechanical and Mining Engineering

Abstract

Thermoelectrics enable the direct conversion between heat and electricity, offering an alternative opportunity to address the environmental problems and the upcoming energy crisis. The prominent advantages of thermoelectric energy conversion, for instance, without moving part, zero emission, and long working life endow thermoelectric devices with promising prospect of wide applications. In this regard, massive efforts have been dedicated to enhancing the conversion efficiency, evaluated by the dimensionless figure-of-merit (ZT), which is proportional to the power factor ($S^2\sigma$) and inversely proportional to the thermal conductivity (κ).

Bi_2Te_3 and the family of similar compounds potentially satisfying the criteria of large $S^2\sigma$, and low κ are the dominant thermoelectric candidates for low temperature (200 K - 400 K) power-generation and refrigeration applications. Compared with bulk counterparts, nanostructuring provides extra possibilities to manipulate thermoelectric properties. Because of the quantum confinement effect, the band gap of nanomaterials can be enlarged by reducing the dimension, which secures a high $S^2\sigma$ at relatively high temperature due to the suppressed bipolar conduction. In addition, phonon scatterings for nanomaterials are significantly strengthened; therefore, an ultra-low κ is secured. For these reasons, we employed nanostructuring to enhance the thermoelectric performance of Bi_2Te_3 systems. Nevertheless, there are at least five issues impeding the substantive applications of the nanostructured Bi_2Te_3-based materials. (1) The conventional solvothermal method for synthesizing nanostructures is time-consuming, and the product yield is low. (2) Their ZT values deteriorate severely at temperature over 450 K, predominately due to the bipolar conduction. (3) For most of thermoelectric semiconductors, acoustic phonons dominate the charge carrier scattering, which yield the rapid decrease in carrier mobility. (4) It is necessary to clarify the underlying reason for the reversely coupling relationship between S and σ for further enhancing $S^2\sigma$. (5) How to further reduce κ on the basis that grain boundary phonon scattering has already been greatly strengthened through nanostructuring. In order to solve these issues, the research in this PhD project has been conducted in the following steps.

i. We developed a rapid microwave assisted solvothermal method to fabricate Bi_2Te_3-based nanomaterials with high product yield through effective growth controlling. From which, high quality Bi_2Se_3 nanosheets, Te/Bi_2Te_3 hierarchical nanostructures, and $Bi_xSb_{2-x}Te_3$ nanoplates, $Bi_2Te_{3-x}Se_x$ nanoplates were fabricated.

ii. Large-scale Bi_2Se_3 nanosheets with controllable thickness have been synthesized and their thermoelectric performance has been detailed investigated by experiments and fundamental nonparabolic Kane models. A significantly reduced thermal conductivity (only 0.41 W/mK), and enhanced power factor (4.71×10^{-4} W/mK^2 with a Seebeck coefficient of -155.32 μV/K and an electrical conductivity of 1.96×10^4 S/m) are observed in the pellet composed of single-layered Bi_2Se_3 nanosheets. Such an enhanced thermoelectric performance is ascribed to the broadened band gap and optimized Fermi level in ultrathin Bi_2Se_3 nanosheets.

iii. To further reduce the thermal conductivity, Te/Bi_2Te_3 hierarchical nanostructures assembled with well-aligned Bi_2Te_3 nanoplates are designed and fabricated by using Te nanotubes as templates. From the comparison of the thermoelectric performance and theoretical calculations with simple Bi_2Te_3 nanostructures, it has been found that Te/Bi_2Te_3 hierarchical nanostructures exhibits higher figure-of-merit due to the optimized reduced Fermi level and enhanced phonon scattering, as well as suppressed the bipolar conduction.

iv. High quality ternary $Bi_xSb_{2-x}Te_3$ nanoplates exhibited a peak ZT of 1.2, caused by the obtained high power-factor of 28.3×10^{-4} $Wm^{-1}K^{-2}$ and ultra-low thermal conductivity of 0.7 $Wm^{-1}K^{-1}$. Based on the single Kane band model with a newly introduced variable (λE_{def} — the dimensionless λ representing the square root of ratio between the initial effective mass and the free electron mass, and E_{def} representing the deformation potential) to serve as the decoupling factor, $Bi_xSb_{2-x}Te_3$ nanoplates with tunable compositions can decrease λE_{def} and simultaneously optimize the reduced Fermi level to ultimately enhance the power-factor. Moreover, detailed structural characterizations reveal dense grain boundaries and dislocations in our nanostructures. These two phonon scattering sources in conjunction with the inherently existed Bi-Sb lattice disorders lead to a strong wide-frequency phonon scattering, and consequently result in a significantly decreased thermal conductivity.

v. High-quality n-type $Bi_2Te_{3-x}Se_x$ nanoplates exhibited a high ZT of 1.23 at 480 K. By detailed electron microscopy investigations, coupled with theoretical analysis on phonon transports, we propose that the achieved κ reduction is attributed to the strong wide-frequency phonon scattering. The shifting of peak $S^2\sigma$ to high temperature is due to the weakened temperature dependent transport properties

governed by the synergistic carrier scattering and the suppressed bipolar effects by enlarging the band gap.

Overall, aiming at the issues of hindering the thermoelectric applications, we proposed some new concepts, which were realized in our massive experimental studies. To fundamentally understand the effects of the proposed concepts, we also employed simulation studies on electronic transport using Kane band model or parabolic band model, and on phonon transport using Callaway model with various phonon scattering mechanisms.

Declaration by author

This thesis is composed of my original work, and contains no material previously published or written by another person except where due reference has been made in the text. I have clearly stated the contribution by others to jointly-authored works that I have included in my thesis.

I have clearly stated the contribution of others to my thesis as a whole, including statistical assistance, survey design, data analysis, significant technical procedures, professional editorial advice, and any other original research work used or reported in my thesis. The content of my thesis is the result of work I have carried out since the commencement of my research higher degree candidature and does not include a substantial part of work that has been submitted to qualify for the award of any other degree or diploma in any university or other tertiary institution. I have clearly stated which parts of my thesis, if any, have been submitted to qualify for another award.

I acknowledge that an electronic copy of my thesis must be lodged with the University Library and, subject to the policy and procedures of The University of Queensland, the thesis be made available for research and study in accordance with the Copyright Act 1968 unless a period of embargo has been approved by the Dean of the Graduate School.

I acknowledge that copyright of all material contained in my thesis resides with the copyright holder(s) of that material. Where appropriate I have obtained copyright permission from the copyright holder to reproduce material in this thesis.

Publications during candidature

Journal papers

1. **Hong, M.**; Chen, Z.G.; Yang, L.; Han, G.; Zou, J. Enhanced Thermoelectric Performance of Ultrathin Bi_2Se_3 Nanosheets through Thickness Control. *Adv. Electron. Mater.* **2015**, 1, 1500025.
2. **Hong, M.**; Chen, Z.G.; Yang, L.; Zou, J. $Bi_xSb_{2-x}Te_3$ Nanoplates with Enhanced Thermoelectric Performance due to Sufficiently Decoupled Electronic Transport Properties and Strong Wide-Frequency Phonon Scatterings. *Nano Energy* **2016**, 20, 144-155.
3. **Hong M.**; Chen, Z.G.; Yang, L.; Zou, J. Enhancing Thermoelectric Performance of Hierarchical Te-Bi_2Te_3 Nanostructures through Rational Design. *Nanoscale* **2016**, 16, 8681-8686.
4. **Hong M.**; Chasapis, T.C.; Chen, Z.G.; Yang, L.; Kanatzidis, M.G.; Snyder, G.J.; Zou, J. *n*-Type $Bi_2Te_{3-x}Se_x$ Nanoplates with Enhanced Thermoelectric Efficiency Driven by Wide-Frequency Phonon Scatterings and Synergistic Carrier Scatterings. *ACS Nano* **2016**, 10, 4719-4727.
5. Chen, Z.G.; Zhang, C.; Zou, Y.; Zhang, E.; Yang, L.; **Hong, M.**; Xiu, F.; Zou, J. Scalable Growth of High Mobility Dirac Semimetal Cd_3As_2 Microbelts. *Nano Lett.* **2015**, 15, 5830-5834.
6. Han, G.; Chen, Z.G.; Yang, L.; **Hong, M.**; Drennan, J.; Zou, J. Rational Design of Bi_2Te_3 Polycrystalline Whiskers for Thermoelectric Applications. *ACS Appl. Mater. Interf.* **2015**, 7, 989-995.
7. Yang, L.; Chen, Z.G.; Han, G.; **Hong, M.**; Zou, Y.; Zou, J. High-performance thermoelectric Cu2Se nanoplates through nanostructure engineering. *Nano Energy* **2015**, 16, 367-374.
8. Yang, L.; Chen, Z.G.; **Hong, M.**; Han, G.; Zou, J. Enhanced Thermoelectric Performance of Nanostructured Bi2Te3 through Significant Phonon Scattering. *ACS Appl. Mater. Interf.* **2015**, 7, 23694-23699.
9. Yang, L.; Chen, Z.G.; Nie, T.; Han, G.; Zhang, Z.; **Hong, M.**; Wang, K. L.; Zou, J. Co-doped Sb_2Te_3 paramagnetic nanoplates. *J. Mater. Chem. C* **2016**, 4, 521-525.

Conference abstracts

1. **Hong M.**; Chen Z.G.; Zou J. Ultra-thin Nanostructured Bi_2Se_3 Synthesized by Microwave-Assisted Solvothermal Method. ***EAIT Postgraduate Conference*** (University of Queensland, 2013, oral presentation).
2. **Hong M.**; Chen Z.G.; Zou J. Ultra-thin nanostructured Bi_2Se_3 with enhanced thermoelectric performance synthesized by microwave-assisted solvothermal method. ***ICAMP8*** (Gold Coast, 2014, oral presentation).
3. **Hong M.**; Chen Z.G.; Zou J. *n*-Type $Bi_2Te_{3-x}Se_x$ Nanoplates with Enhanced Thermoelectric Efficiency. ***EAIT Postgraduate Conference*** (University of Queensland, 2015, oral presentation).
4. **Hong M.**; Chen Z.G.; Zou J. High Thermoelectric Performance of N-type $Bi_2Te_{2.7}Se_{0.3}$ Nanoplates. ***ICONN*** (Canberra, 2016, oral presentation).
5. **Hong M.**; Chen Z.G.; Zou J. $Bi_xSb_{2-x}Te_3$ Nanoplates with Enhanced Thermoelectric Performance due to Sufficiently Decoupled Electronic Transport Properties and Strong Wide-Frequency Phonon Scatterings. ***35th ICT/ACT Conference*** (Wuhan, China, 2016, oral presentation).

Publications included in this thesis

Hong, M.; Chen, Z.G.; Yang, L.; Han, G.; Zou, J. Enhanced Thermoelectric Performance of Ultrathin Bi_2Se_3 Nanosheets through Thickness Control. *Adv. Electron. Mater.* **2015**, 1, 1500025. – incorporated as Chapter 4.

Contributor	Statement of contribution
Min Hong	Designed the experiments (70%) Carried out characterization (80%) Carried out thermoelectric property measurement (70%) Carried out data analysis (60%) Prepared the paper (60%)
Zhi Gang Chen	Designed the experiments (20%) Carried out characterization (10%) Carried out thermoelectric property measurement (30%) Carried out data analysis (10%) Prepared the paper (10%)
Lei Yang	Carried out characterization (10%)
Guang Han	Carried out data analysis (10%)
Jin Zou	Designed the experiments (10%) Carried out data analysis (20%) Prepared the paper (30%)

Hong M.; Chen, Z.G.; Yang, L.; Zou, J. Enhancing Thermoelectric Performance of Hierarchical Te-Bi_2Te_3 Nanostructures through Rational Design. *Nanoscale* **2016**, 16, 8681-8686. – incorporated as Chapter 5.

Contributor	Statement of contribution
Min Hong	Designed the experiments (70%) Carried out characterization (80%) Carried out thermoelectric property measurement (70%) Carried out data analysis (60%) Prepared the paper (60%)
Zhi Gang Chen	Designed the experiments (20%) Carried out characterization (10%) Carried out thermoelectric property measurement (30%) Carried out data analysis (10%) Prepared the paper (10%)
Lei Yang	Carried out characterization (10%) Carried out data analysis (10%)
Jin Zou	Designed the experiments (10%) Carried out data analysis (20%) Prepared the paper (30%)

Hong, M.; Chen, Z.G.; Yang, L.; Zou, J. $Bi_xSb_{2-x}Te_3$ Nanoplates with Enhanced Thermoelectric Performance due to Sufficiently Decoupled Electronic Transport Properties and Strong Wide-Frequency Phonon Scatterings. *Nano Energy* **2016**, 20, 144-155. – incorporated as Chapter 6.

Contributor	Statement of contribution
Min Hong	Designed the experiments (70%) Carried out characterization (80%) Carried out thermoelectric property measurement (70%) Carried out data analysis (60%) Prepared the paper (60%)
Zhi Gang Chen	Designed the experiments (20%) Carried out characterization (10%) Carried out thermoelectric property measurement (30%) Carried out data analysis (10%) Prepared the paper (10%)
Lei Yang	Carried out characterization (10%) Carried out data analysis (10%)
Jin Zou	Designed the experiments (10%) Carried out data analysis (20%) Prepared the paper (30%)

Hong, M.; Chasapis, T.C.; Chen, Z.G.; Yang, L.; Kanatzidis, M.G.; Snyder, G.J.; Zou, J. *n*-Type $Bi_2Te_{3-x}Se_x$ Nanoplates with Enhanced Thermoelectric Efficiency Driven by Wide-Frequency Phonon Scatterings and Synergistic Carrier Scatterings. *ACS Nano* **2016***,* 10, 4719-4727. – incorporated as Chapter 7.

Contributor	Statement of contribution
Min Hong	Designed the experiments (70%) Carried out characterization (80%) Carried out thermoelectric property measurement (70%) Carried out data analysis (60%) Prepared the paper (50%)
Thomas C. Chasapis	Carried out infrared reflectance measurement (100%) Carried out data analysis (20%) Prepared the paper (10%)
Zhi Gang Chen	Designed the experiments (20%) Carried out characterization (10%) Carried out thermoelectric property measurement (30%) Carried out data analysis (10%) Prepared the paper (10%)
Lei Yang	Carried out characterization (10%)
Mercouri G. Kanatzidis	Prepared the paper (5%)
G. Jeffery Snyder	Prepared the paper (10%)
Jin Zou	Designed the experiments (10%) Carried out data analysis (10%) Prepared the paper (15%)

Contributions by others to the thesis

“No contributions by others.”

Statement of parts of the thesis submitted to qualify for the award of another degree

“None”

Acknowledgements

First of all, I would like to express my special appreciation to my principle supervisor Prof Jin Zou, who has been a tremendous mentor for me. My background was mechanical engineering. At the beginning of this PhD research on thermoelectric materials, I was totally lost. It is the support and guidance from Professor Jin Zou that enable me to conduct this PhD project smoothly and productively. As he said, he is always the back-bone for students, who work hard. Also, I would like to thank my vice supervisor, Dr Zhi-Gang Chen, for his time, discussion and encouragement. The equipment training, experimental skills, ideas, and journal paper writing skills are of critical importance for my PhD research.

Secondly, I want to thank the former and current group members, including Dr Yang Huang, Dr Yanan Guo, Dr Lina Cheng, Dr Hongyi (Justin) Xu, Dr Wen Sun, Dr Guang Han, Dr Kun Zheng, Dr Jing Lin, Dr Lihua Huang, Lei Yang, Zhiming Liao, Yichao Zou, Liqing Huang, Mun Soo, and Chen Zhou. They have made the research work to be more delighting, and the discussions and suggestions from them have been really helpful.

Meanwhile, I want to thank Prof G. Jeffrey Snyder, Prof Mercouri G. Kanatzidis, and Dr Thomas C. Chasapis from Northwestern University, US. The discussions on modelling studies helped me a lot to understand the thermoelectric properties through band engineering. I also really appreciate Dr Thomas C. Chasapis for his efforts and time in carrying out experiment for my research.

Additionally, I gratefully acknowledge the China Scholarship Council (CSC), the University of Queensland International Scholarship (UQI), and the University of Queensland Graduate School International Travel Award (GSITA) for their final support. The Australian Microscopy & Microanalysis Research Facility is acknowledged for providing characterization facilities.

Lastly, I thank my family: mother, father, and brother in China for their endless love and support. They have always been the motivation for me to keep going on. In addition, I want to thank my girlfriend, Guangli Li. Since we met at UQ, life becomes so beautiful.

Keywords

Bi_2Te_3-based thermoelectric materials, Nanostructural designing, Band engineering, Phonon scattering manipulating, Microwave-assisted solvothermal synthesis, Electronic microscopy characterization

Australian and New Zealand Standard Research Classifications (ANZSRC)

ANZSRC code: 090608, Renewable Power and Energy Systems Engineering (excl. Solar Cells), 40%

ANZSRC code: 091205, Functional Materials, 30%

ANZSRC code: 100712, Nanoscale Characterisation, 30%

Fields of Research (FoR) Classification

FoR code: 0912 Materials Engineering, 80%

FoR code: 1007, Nanotechnology, 20%

Table of Contents

List of Figures

Figure 2-11 (a) κ, and (b) κ- κ_e for $Bi_{0.5}Sb_{1.5}Te_3$ nanoplates,[93] $Bi_2Te_{2.7}Se_{0.3}$ nanoplates, Bi_2Se_3 ultrathin nanosheets,[102] Bi_2Te_3/Bi_2Se_3 nanoflowers,[95] and Bi_2Te_3 nanoplates,[100] compared with the ingot.[107]

Figure 2-12 (a) κ, (b) κ_l, (c) $S^2\sigma$, and (d) ZT for $Bi_{0.5}Sb_{1.5}Te_3$ ingot,[66] Te-MS,[66] Xie MS,[63] Zheng MS,[130] and Ivanova MS.[131]

Figure 2-13 Calculated (a) S, (b) σ, (c) $S^2\sigma$, (d) L, (e) κ_e, and (f) κ_e as a function of η at 300 K with the blue curve representing the total values, the purple curve representing the CB component, green curve representing the VB component.

Figure 2-14 (a) Determined η with n_H ranging from 10^{18} to 10^{21} cm^{-3} for evenly selected ten m_d^* values from 0.2 m_0 to 2 m_0 as indicated by the colorbar in the right-hand side. Correspondingly calculated (b) S, (c) μ_H, and (d) $S^2\sigma$ as a function of n_H for different m_d^* values. The bold green lines in (b) and (c) are calculated using SKB model with m_d^* = 2 m_0 for S and μ_H, respectively.

Figure 2-15 (a) Determined η with n_H ranging from 10^{18} to 10^{21} cm^{-3} for evenly selected ten E_g values from 0.1 to 0.5 eV as indicated by the colorbar in the right-hand side. Correspondingly calculated (b) S, (c) μ_H, and (d) $S^2\sigma$ as a function of n_H for different E_g values. The bold green lines in (b) and (c) are calculated using SKB model with E_g = 0.1 eV for S and μ_H, respectively.

Figure 2-16 (a) Determined η with n_H ranging from 10^{18} to 10^{21} cm^{-3} for evenly selected ten E_{def} values from 5 to 20 eV as indicated by the colorbar in the right-hand side. Correspondingly calculated (b) S, (c) μ_H, and (d) $S^2\sigma$ as a function of n_H for different E_{def} values. The bold green lines in (b) and (c) are calculated using SKB model with E_{def} = 8 eV for S and μ_H, respectively.

Figure 2-17 Calculated (a) κ_{bi}, and (b) S as a function of n_H at 300 K, 400 K and 500 K for evenly selected ten E_g values from 0.1 to 0.5 eV as indicated by the colorbar in the right-hand side.

Figure 2-18 (a) Calculated $S^2\sigma$ as functions of n_H and m_d^*, and (b) the corresponding contour map with the white curve indicating the m_d^* dependent n_H^{opt}.

Figure 2-19 (a) Calculated room-temperature κ_s considering various phonon scatterings. (b) Schematic diagram showing the scattering of wide-frequency phonons by various sources.

Figure 2-20 (a) Data points of $|S|$ versus n_H compared with the calculated n_H dependent $|S|$ curves, and (b) the reported data points of μ_H versus n_H compared with the calculated n_H dependent μ_H curves for n-type $Bi_2Te_{3-x}Se_x$ single crystals.[106] (c) Data points of S versus n_H compared with the calculated n_H dependent S curves, and (d) the reported data points of μ_H versus n_H compared with the calculated n_H dependent μ_H curves for p-type $Bi_xSbe_{3-x}Te_3$ single crystals.[116] (e) and (f) are the Data points of $S^2\sigma$ versus n_H compared with the calculated n_H dependent $S^2\sigma$ curves for n-type $Bi_2Te_{3-x}Se_x$ single crystals and p-type $Bi_xSbe_{3-x}Te_3$ single crystals, respectively.

Figure 2-21 The determined $Coe_{\sigma\perp c}/Coe_{\sigma\parallel c}$ as a function of the corresponding (a) n_H and (b) $\sigma_{\perp c}/\sigma_{\parallel c}$, respectively. The determined $\eta_{\perp c} - \eta_{\parallel c}$ as a function of the corresponding (c) n_H and (d) $S_{\perp c}/S_{\parallel c}$, respectively. The data points are for both n-type $Bi_2Te_{3-x}Se_x$[106] and p-type single $Bi_xSb_{3-x}Te_3$ crystals.[116]

Figure 2-22 The Se content dependent data points of (a) n_H, (b) determined η, (c) determined m_d^*, and (d) determined E_{def}. The n_H dependent data points of (e) μ_H, and (f) S compared with the theoretical curves of μ_H versus n_H, and S versus n_H calculated with the correspondingly determined E_{def}, and m_d^*. In all figures, the solid green data points are from $Bi_2Te_{3-x}Se_x$ ingots doped with I (wt 0.08%),[107] the hollow red data points are from $Bi_2Te_{3-x}Se_x$ processed by BM+HP+HD,[75] and the hollow blue data points are from $Bi_2Te_{3-x}Se_x$ single crystals.[106]

Figure 2-23 (a) Data points of n_H dependent $S^2\sigma$ compared with the theoretical curves of $S^2\sigma$ versus n_H calculated with correspondingly determined E_{def}, and m_d^*. (b) Determined data points of n_H dependent m_d^* with the grey curve indicating the m_d^* as a function of n_H^{opt}. (c) Data points of λE_{def} dependent $S^2\sigma$ compared with the theoretical curves of $S^2\sigma$ versus λE_{def} for compositions of Bi_2Te_3 (labelled with $1^{\#}$), $Bi_2Te_{2.4}Se_{0.6}$ (labelled with $2^{\#}$) and Bi_2Se_3 (labelled with $3^{\#}$) calculated with corresponding η^{opt}. (d) Determined data points of λE_{def} versus η. In all figures, the solid green data points are from $Bi_2Te_{3-x}Se_x$ ingots doped with I (wt 0.08%),[107] the hollow red data points are from $Bi_2Te_{3-x}Se_x$ processed by BM+HP+HD,[75] and the hollow blue data points are from $Bi_2Te_{3-x}Se_x$ single crystals.[106]

Figure 3-1 (a) the photo of MARS 6 microwave oven, and (b) the EasyPrep vessel selected for the thermoelectric material synthesis in this PhD project.

Figure 3-2 Diagram of microwave-assisted solvothermal synthesis process.

List of Tables

List of Abbreviations used in the thesis

XRD: X-ray diffraction

SEM: scanning electron microscopy

TEM: transmission electron microscopy

AFM: atomic force microscopy

EDS: energy dispersive X-ray spectrometry

SAED: selected area electron diffraction

FTIR: Fourier transform infrared spectroscopy

JCPDS: joint committee on powder diffraction standards

DOS: density of states

S: Seebeck coefficient

σ: electrical conductivity

$S^2\sigma$: power factor

ZT: Figure of Merit

ZT_{avg}: average Figure of Merit

κ: thermal conductivity

κ_e: electronic thermal conductivity

κ_l: lattice thermal conductivity

T: absolute temperature

T_C: cold side temperature

T_H: hot side temperature

n_H: Hall carrier concentration

μ_H: Hall carrier mobility

R_H: Hall coefficient

L: Lorenz number

A: Hall factor

η: reduced Fermi level

E_f: Fermi level

k_B: Boltzmann constant

$\hbar$: reduced Planck constant

N_v: band degeneracy

K: ratio of longitudinal ($m^*_{\parallel}$) and transverse ($m^*_{\perp}$) effective mass

C_l: combination of elastic constants

m^*_b: band effective mass

m^*_i: inertial effective mass

m^*_d: density of states effective mass

e: is free electron charge

m_0: free electron mass

E_{def}: deformation potential

CB: conduction band

VB: valance band

θ_D: Debye temperature

Γ: point defect scattering parameter

B_D: magnitude of Burger's vector

r :Poisson's ratio

γ: Grüneisen parameter

K: Bulk modulus

ϕ_{TE}: Carnot efficiency

ϕ_C: Carnot efficiency

Q_H: net heat flow rate

W: generated electric power

E_g: band gap

$E_{g,opt}$: optical band gap

ρ_m: mass density

v_s: sound velocity

MSS: microwave solvothermal

CP: cold pressing

SG: solution grow

SPS: spark plasma sintering

HP: hot pressing

LIE: lithium ionic exfoliation

BMA: ball milling alloy

MA: melting alloy

BS: Bridgman–Stockbarger

BM: ball milling

THM: travelling heater method

MS: melt spinning

Te-MS: Te rich melt spinning

ZM: zone melting

1

Introduction

1.1 Background

The development of human society strongly depends on energy. Currently, the majority of energy comes from fossil fuel trio of oil, coal, and natural gas, while only a small amount comes from carbon-free renewable power, such as geothermal, wind, solar power, and biofuels. The consumption of the non-renewable fossil fuel discharges toxic emission and greenhouse gas resulting in environmental pollution and global warming. Furthermore, the utilization efficiency of the conventional energy source is extremely low. As an example, in the internal-combustion engine, only 25% of the energy from the petrol burning is used to motivate the vehicle, while the vast majority is wasted in the way including exhaust gas emission, thermal dissipation and friction.[1] The rising demand of energy depletion, the elimination of greenhouse gas due to carbon-based energy sources and the enhancement in the utilization efficiency of energy resources have sparked significant research into alternative energy sources and energy harvesting technologies.[2] One of energy conversion technologies is thermoelectricity, in which heat is transferred directly into electricity using a class of materials known as thermoelectric materials.[3]

Because of the distinct advantages exhibited by thermoelectric devices: without moving parts, long steady-state operation period, zero emission, precise temperature control and capable of function in extreme environment,[4-6] the prospect of thermoelectric applications is promising, especially for power generation and refrigeration. For the power generation mode, energy is captured from waste, environmental, or mechanical sources, and is converted into an exploitable form, i.e. electricity by thermoelectric facilities. One example is to extract electricity from the hot exhaust stream of cars.[7-10] Another interesting case is to use thermoelectric materials to boost the efficiency of stoves, decrease smoke emission and reduce the amount of wood or coal. Thermoelectric materials are also able to generate power from the sun by using solar energy to create a temperature difference

across thermoelectric materials.[11-13] In terms of the aeronautics and space applications, thermoelectric power planet can take advantage of the solar energy to generate sufficient electricity for lunar crew to exploit the moon. Nuclear reactors and radioisotope thermoelectric generators can be used as spacecraft propulsion and for power supply.[14-17] For the refrigeration mode, micro thermoelectric cooling modules can be installed in the integrated circuit to tackle the heat-dissipation problem, and flexible thermoelectric materials can be equipped in the uniform of people working in the extreme environment to serve as the wearable climate control device.[18-21]

It is obvious that there is a large potential market for thermoelectric materials far beyond the few applications discussed here. However, currently thermoelectric devices are not in common use. This is partially because they have a low efficiency relative to mechanical cycles, and partly because there are engineering challenges related to using thermoelectric devices for general applications.[22] Selecting the right material systems and employing the appropriate synthesis methods are critical to fabricate thermoelectric device with high energy conversing efficiency. Bulk materials comprising heavy elements, like the binary and ternary V-VI based semiconductors,[23] lead-based chalcogenides,[24] and those materials with complicated crystal structures, such as clathrates[25] and skutterudites[26] are proved to show high thermoelectric performance. Fabricating materials with nanostructures and doping with suitable impurities are theoretically and practically confirmed to enhance the thermoelectric performance.[27-29]

1.2 Objective and Scope

As a state-of-the-art bulk thermoelectric material, Bi_2Te_3 family naturally has better performance compared with bulk counterparts. Integrating this advantage, the use of nanostructures can tune the *ZT* through new methods such as quantum confinement, dimensional restriction, and modulation doping. This research project concentrates on fabricating nanostructured Bi_2Te_3 by microwave assisted method, and measuring the thermoelectric properties. The main goal is to enhance the thermoelectric performance through nanostructuring, compositional tuning and band engineering. What's more, this project is aimed to exploit alternative eco-friendly as well as non-toxic solvents for the solvothermal synthesis process assisted by microwave radiation, which can improve the yields so as to make it possible to produce thermoelectric nanocomposites efficiently and cost-effectively.

Apart from nanostructured synthesis, the challenges on optimizing the ZT highlight the need to establish a comprehensive understanding of electron-hole-phonon transport. In order to obtain a better predetermination of thermoelectric performance, the models used in this research project include various factors such as electron and phonon mean free path, electron mobility, effect of quantum confinement, influences of superlattice interfaces on phonon scattering as well as electron transport etc.

1.3 Thesis outline

To understand the parameters affecting the thermoelectric performance and enhance the thermoelectric performance of Bi_2Te_3 families, we did modelling simulations and experimental studies. Based on these results, this thesis is organized as follows

Chapter 1 is the introduction part, including the necessity of developing thermoelectric materials, the promising prospect of practical applications, and the goal of this research project.

Chapter 2 is the literature review. Specifically, we presented the working principle, the figure of merit, and the working modes of thermoelectric materials. In addition, we summarized the development of Bi_2Te_3 systems as the dominating candidates for near room temperature thermoelectric applications. Finally, we presented the modeling studies for enhancing thermoelectric performance.

Chapter 3 is the methodology and approach. Here, we demonstrated the experimental details in this thesis, including the electronic microscopies, atomic force microscopy, and Raman spectroscopy for morphology characterization or crystal structure examination; as well as the techniques for performance evaluation or band structure exploration.

Chapter 4 presents the thermoelectric performance enhancement achieved in Bi_2Se_3 by reducing the thickness. This chapter is based on the publication of *Adv. Electron. Mater.* **2015**, 1.

Chapter 5 illustrates the enhanced performance of Te/Bi_2Te_3 by rationally designing the nanostructures. This chapter is based on the publication of *Nanoscale* **2016**, DOI: 10.1039/C6NR00719H.

Chapter 6 shows the performance promotion of $Bi_xSb_{2-x}Te_3$ nanoplates by broadening the frequency of phonon scattering and decoupling the thermoelectric properties. This chapter is based on the publication of *Nano Energy* **2016**, 20.

Chapter 7 depicts the increased performance of n-type $Bi_2Te_{3-x}Se_x$ nanoplates through modifying the carrier scattering mechanism and introducing dislocations to further enhance phonon scattering. This chapter is based on the manuscript submitted to ACS Nano (minor change).

Chapter 8 draws the conclusions of this thesis and point out the potential future directions.

2

Literature Review

In this literature review, we provide an overview of the fundamental theories on thermoelectric effects, and current research progress as well as new trends on Bi_2Te_3-based thermoelectric materials.

2.1 Principles of thermoelectric energy conversion

In 1821, Thomas Seebeck, a German physicist, discovered that when two wires of different metals were twisted together, and heated at one end, a small current would flow through the wires[30]. This heat-electricity conversion phenomenon has been named as Seebeck effect, and this is the working principles of thermoelectric materials as power generator, which can generate electric energy from waste heat[31]. The mechanism of thermoelectricity is revealed in Figure 2-1. At a constant temperature, the free charge carriers (electrons as an example) move randomly (Figure 2-1 (b)), while they will migrate from the cold side to the hot side after applying a temperature gradient (Figure 2-1 (b)). Eventually, an electric field is generated between the two ends to balance the thermal gradient effect on charger carrier movement (Figure 2-1 (c)). This electrochemical potential is known as the Seebeck voltage, and the amount of voltage generated per unit temperature gradient is called the Seebeck coefficient, which is generally denoted as *S*. Likewise, temperature difference can also be acquired from electricity, and this is the Peltier effect[32], the reverse of the Seebeck effect. On this basis, electric current in the circuit can be applied to cause temperature difference on the junction of thermoelectric compounds[33].

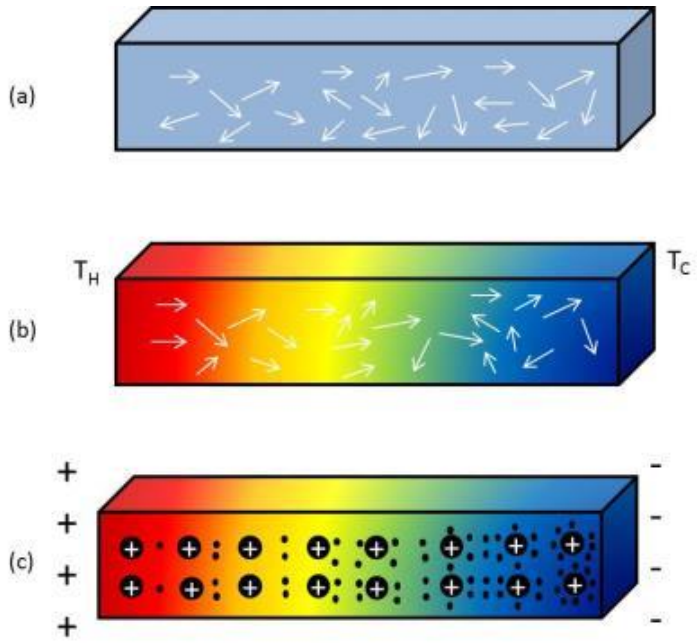

Figure 2-1 illustration of thermoelectricity: (a) Charge carriers (electrons as an example) move randomly at a constant temperature. (b) Due to a temperature difference, charge carriers diffuse from the hot side to the cold side. (c) Electric field is produced by electrons gathered at the cold side and the holes left at the hot side.

2.2 Figure of merit

Materials which are able to generate electrical power using the Seebeck effect or can refrigerate using the Peltier effect are known as thermoelectric materials. In order to be a good thermoelectric candidate, we need to examine the relavent performance. For both the power generation and refrigeration mode (refer to Figure 2-3), the energy is transferred by the directional movement of charger carriers; therefore thermoelectric materials should have high electrical conductivity. In addition, with a given temperature gradient, the generated voltage is expected to be as large as possible, suggesting a high Seebeck coefficient is critical. Finally, the temperature difference across the material should be maintained; thereby low thermal conductivity is highly demanded. Overall, the dimensionless figure of merit, *ZT* was defined to quantify the thermoelectric performance, and is given by[34]

$$ZT = \frac{S^2 \sigma T}{\kappa} \tag{2.1}$$

where, S, σ, κ and T are the Seebeck coefficient, electrical conductivity, thermal conductivity (including electronic component κ_e, lattice component κ_l, and bipolar component κ_{bi}), and the working temperature, respectively.[29] The term of $S^2\sigma$ in Equation (2.1) is defined as the power factor.

As can be seen, the criteria of thermoelectric materials are high $S^2\sigma$ and low κ. To achieve this, good thermoelectric candidates should satisfy:

- A decent band gap (E_g)

To suppress the bipolar conduction at high temperature, E_g should be large enough. However, a too large E_g is more likely to reduce σ. Therefore, Sofo & Mahan theoretically predicted that an optimum E_g is in the range of 6 k_BT to 10 k_BT with k_B representing the Boltzmann constant.[35]

- Semiconductors with large average atomic mass (A)

Goldsmid developed the ratio of electric mobility μ to the lattice thermal conductivity κ_l as a function of the average atomic weight (A) *i.e.* $\frac{\mu}{\kappa_l} \approx K\frac{\rho_m}{C_V v_s} \approx K'\frac{\rho_m A}{v_s}$ where ρ_m is the mass density, v_s is the sound velocity, C_V is the specific heat, K is a constant for all materials and K' is an another constant.[36] As can be see, μ/κ_l increases with increasing A. The reason for this is due to the strong phonon scattering caused by atoms with large mass. Heavy elements can considerably reduce the sound velocities, while carrier mobility will not be affected significantly; thus electrical conductivity and Seebeck coefficient will not be reduced when thermal conductivity is low.

- Alloys composed of various semiconductors

Alloying elements with different mass in the lattice can create point defects, which is supposed to reduce the phonon mean free pass;[37] therefore, lattice thermal conductivity will be lower. This kind of alloying is realized by replacing host atoms with an element from the same group in the periodic table. Nevertheless, the mobility of charger carriers will be unfortunately affected by the electronegativity difference between the host atoms and the substituting atoms. In spite of these adverse impacts, alloy point defect scattering can contribute to a net increase in the ZT by decreasing the thermal conductivity substantially. This kind of optimizing method can be found in $Si_{1-x}Ge_x$[38]and $Bi_{2-x}Sb_xTe_{3-y-z}Se_yS_z$[39].

- Materials with complicated crystal structure

The complicated crystal structure can lead to high electric conductivity due to the highly periodic characterization and can result in a significant decrease in thermal conductivity as well. The filled skutterudites[26,40,41] and clathrates[42-44] which belong to the family with complicated structures are widely used as thermoelectric application. In addition, Half-Heusler intermetallic alloys[45], β-Zn_4Sb_3 allyos[46-51], Zintl phase compounds[52], layered cobalt oxides[53] and chalcogenide compounds[54] the thermoelectric materials with complex structure to improve thermoelectric performance. These complicated structures are potential to be the "electron crystal and phonon glass" material, which exhibit high electronic conductivity as well as low thermal conductivity at the same time.

Good thermoelectric materials should have the above common characterizations. Because of the rapid development in physical understandings and the material preparation techniques in thermoelectric field, *ZT* has been improved significantly. Figure 2-2 plots the achieved state-of-the-art *ZT* values for materials working over a wide temperature range. For example, ZT of 1.8 for $Bi_{0.5}Sb_{1.5}Te_3$ working near room temperature, *ZT* of 2.6 for SnSe working in the mid-temperature range, and *ZT* of 1.2 for $Yb_{14}Mn_{1.05}Sb_{11}$ serving as high temperature applications have been made.

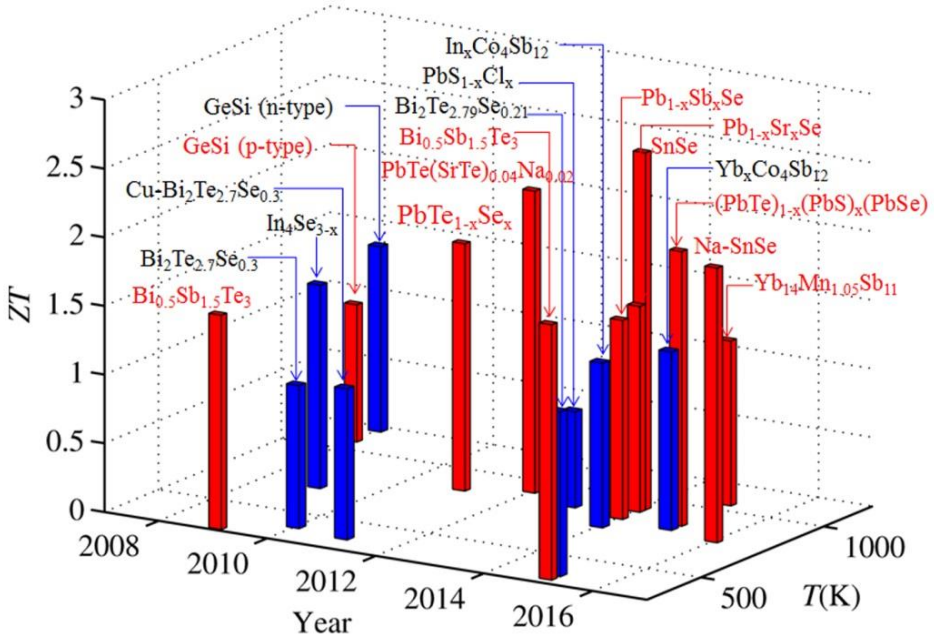

Figure 2-2 The achieved state-of-the-art *ZT* values for both n-type (blue bar) and p-type (red bar) thermoelectric materials in recent years. (n-type) GeSi,[55] Cu-$Bi_2Te_{2.7}Se_{0.3}$,[56] $Bi_2Te_{2.7}Se_{0.3}$,[57] In_4Se_{3-x},[58] $In_xCo_4Sb_{12}$,[59] $Yb_xCo_4Sb_{12}$,[60] $PbS_{1-x}Cl_x$,[61] $Bi_2Te_{2.79}Se_{0.21}$,[62] (p-type) GeSi, [55] $Bi_{0.5}Sb_{1.5}Te_3$,[63] $PbTe(SrTe)_{0.04}Na_{0.02}$,[64] $PbTe_{1-x}Se_x$,[65] $Bi_{0.5}Sb_{1.5}Te_3$,[66] $Pb_{1-x}Sb_xSe$,[67] $Pb_{1-x}Sr_xSe$,[68] SnSe,[69] $(PbTe)_{1-x}(PbS)_x(PbSe)$,[70] Na-SnSe,[71] $Yb_{14}Mn_{1.05}Sb_{11}$.[72]

2.3 Thermoelectric device and the efficiency

Categorized by free charge carriers, thermoelectric materials are classified into n-type (containing free electrons) and p-type (containing free holes) elements. For real applications, both types of thermoelectric elements should work together to form a thermoelectric couple, shown in Figure 2-3. The total *ZT* for this thermoelectric couple is given by[73]

$$ZT_{tot} = \frac{\left(S_P - S_N\right)^2 T}{\left[\sqrt{\kappa_P / \sigma_P} + \sqrt{\kappa_N / \sigma_N}\right]^2} \tag{2.2}$$

where, *ZT*, *κ* and *σ* for n-type and p-type elements are respectively marked by the subscripts of *N* and *P*.

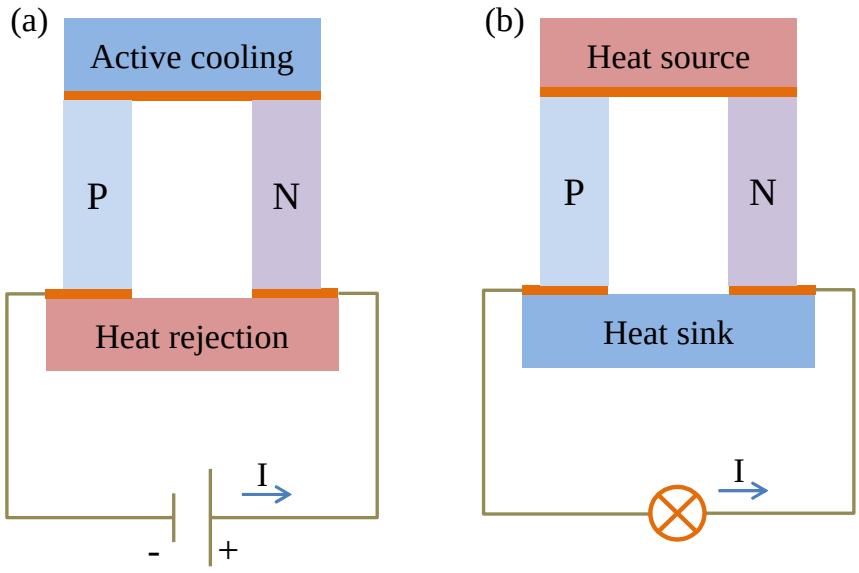

Figure 2-3 A generic diagram of the two thermoelectric working modes: (a) refrigeration and (b) power generation.

To improve the total output, thermoelectric devices contain many thermoelectric couples. The thermoelectric power generator illustrated in Figure 2-4 is a combination of numerous n-type and p-type thermoelectric elements, which are connected electrically in series and thermally in parallel.

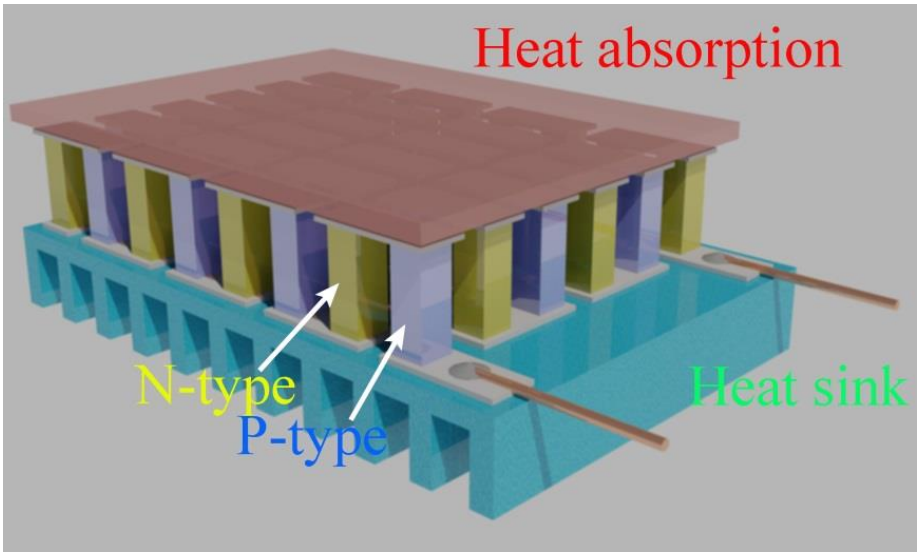

Figure 2-4. Schematic of a thermoelectric generator.

The efficiency (ϕ_{TE}) of this device as a function of ZT_{tot} is calculated by

$$\phi_{TE} = \frac{W}{Q_H} = \phi_C \left(\frac{\sqrt{1+ZT_{tot}} - 1}{\sqrt{1+ZT_{tot}} + T_C/T_H} \right) \tag{2.3}$$

and ϕ_C is Carnot efficiency, given by

$$\phi_C = \frac{T_H - T_C}{T_H} \tag{2.4}$$

In the above equations, Q_H is the net heat flow rate, W is the generated electric power, T_C is the the cold side temperature, and T_H is that of the hot side, respectively. As can be seen, ϕ_{TE} depends on ϕ_C and the ZT_{tot} of the thermoelectric couple. To enhance ϕ_{TE}, for one thing we want to ensure a large ZT. According to Equation (2.3), the dependence of thermoelectric efficiency on peak ZT for single-leg state-of-the-art thermoelectric materials is plot in Figure 2-5(a), in which the cold side temperature is set as 300 K, and the hot side temperature is the corresponding temperature for peak ZT. As can be seen, the efficiency of thermoelectric materials for room temperature (300 K – 500 K) power generation is lower than 5%, for mid-temperature applications, the peak efficiency could be ~25%, and for high temperature applications, the efficiency is 22%. In terms of the practical applications, the entire thermoelectric leg is under the temperature difference. Therefore, it is more precise to use the average ZT (ZT_{avg}) to calculate the efficiency, and ZT_{avg} is calculated by

$$ZT_{avg} = \frac{\int ZTdT}{T_h - T_c} \tag{2.5}$$

On this basis, Figure 2-5(b) plots the efficiency for ZT_{avg}. As can be seen, The maximum efficiency is ~18%, achieved in p-type K-doped $PbTe_{0.7}S_{0.3}$.[74] It looks like the energy transfer efficiency for the state-of-the-art thermoelectric materials is large enough to compete with the traditional heat engineering. However, there are still at least four issues hindering the wide application:

i. Good thermoelectric materials are highly doped semiconductors, and in some cases hierarchical nanoprecipitates are used to reduce κ. It is of significance to ensure the stability of these materials at high temperature. Moreover, the reproducibility and repeatability are also critical for scale-up fabrication.

ii. The final energy transfer efficiency of thermoelectric device depends on both n-type and p-type legs. Currently, *ZT* of n-type legs are lower than that for p-type ones. For example, the peak *ZT* for n-type $Bi_2Te_{3-x}Se_x$ is ~1.2,[75] while that for $Bi_xSb_{2-x}Te_3$ is ~1.8.[66]

iii. The cold side temperature should be ensured to be cold, because the increase in temperature of cold side lead to the decline of Carnot efficiency (refer to Equation (2.3)). Therefore, we need to carefully design the device for heat dissipation at the cold side.

iv. The bonding materials used to connect the thermoelectric legs to the basis boarders are supposed to be stable at high temperature and should not react with or diffuse into the thermoelectric legs. In addition, the *ZT* values of the bonding materials affect the overall thermoelectric performance of the device. Applying bonding materials with high *ZT* is also required.

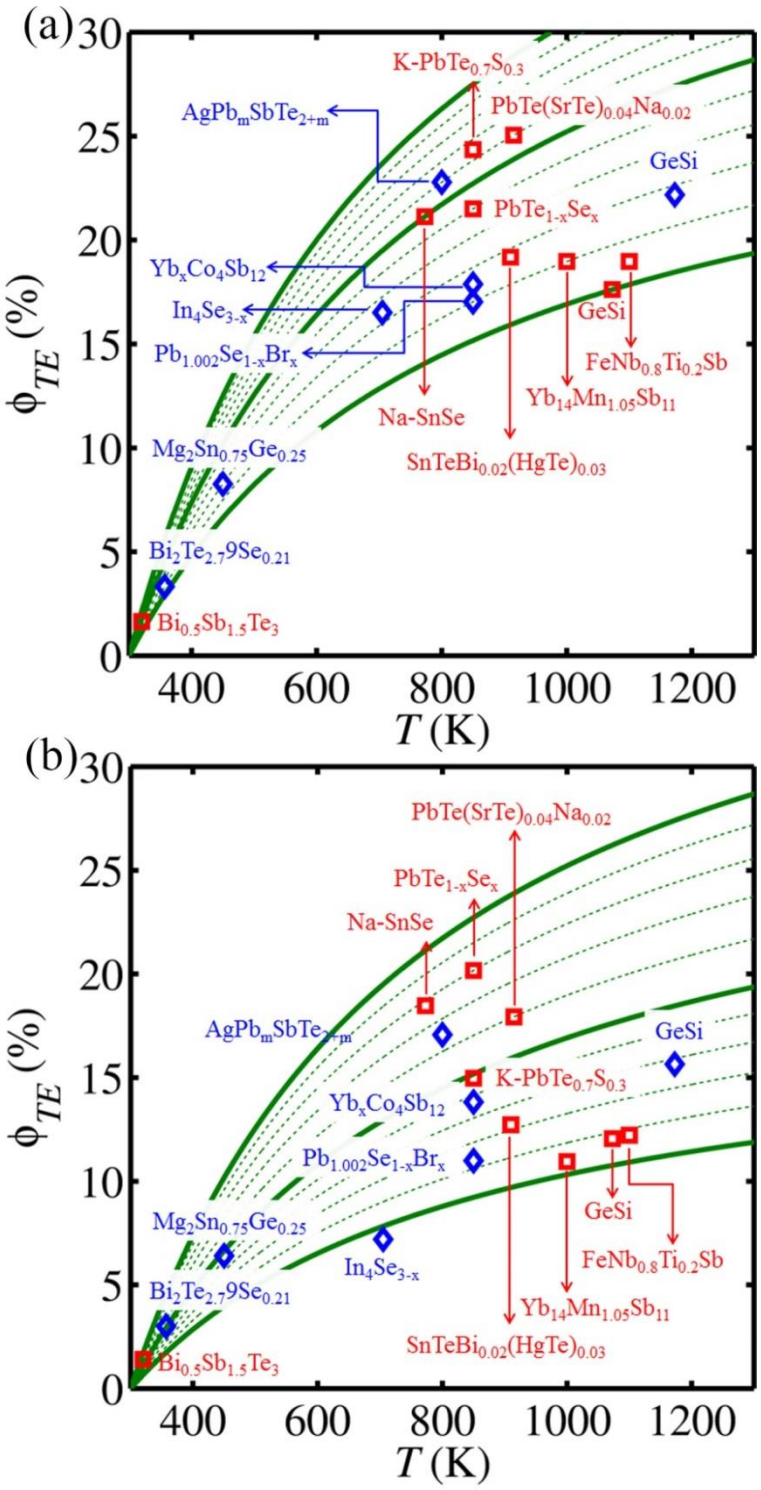

Figure 2-5 Thermoelectric efficiency of single-leg state-of-the-art n-type (blue diamond) and p-type (red square) thermoelectric materials for (a) peak *ZT* and (b) average *ZT* as a function of temperature difference T_h with anassumptionof T_c=300K. $Bi_{0.5}Sb_{1.5}Te_3$,[66] $Bi_2Te_{2.7}9Se_{0.21}$,[62] $Mg_2Sn_{0.75}Ge_{0.25}$,[76] $AgPb_mSbTe_{2+m}$,[77] In_4Se_{3-x},[58] $Pb_{1.002}Se_{1-x}Br_x$,[78] $Yb_xCo_4Sb_{12}$,[60] $SnTeBi_{0.02}(HgTe)_{0.03}$,[79] $Yb_{14}Mn_{1.05}Sb_{11}$,[72] $FeNb_{0.8}Ti_{0.2}Sb$,[80] n-type GeSi,[81] p-type GeSi,[55] K-$PbTe_{0.7}S_{0.3}$,[74] Na-SnSe,[71] $PbTe_{1-x}Se_x$,[65] $PbTe(SrTe)_{0.04}Na_{0.02}$.[64]

2.4 Bi_2Te_3-based thermoelectric materials

Pnictogen (Bi and Sb) and chalcogenides (Te and Se) materials have been preferably studied for room-temperature thermoelectric applications.[82] These materials share the same rhombohedral crystal structure of the space group $R\bar{3}m$ (see Figure 2-6). This category consists of five-atom layers arranged along the *c*-axis, known as quintuple layers. The coupling is strong between two atomic layers within one quintuple layer but much weaker, predominantly of the van der Waals type, between two quintuple layers. Lattice parameters and E_g of these layered materials are shown in Table 2-1.

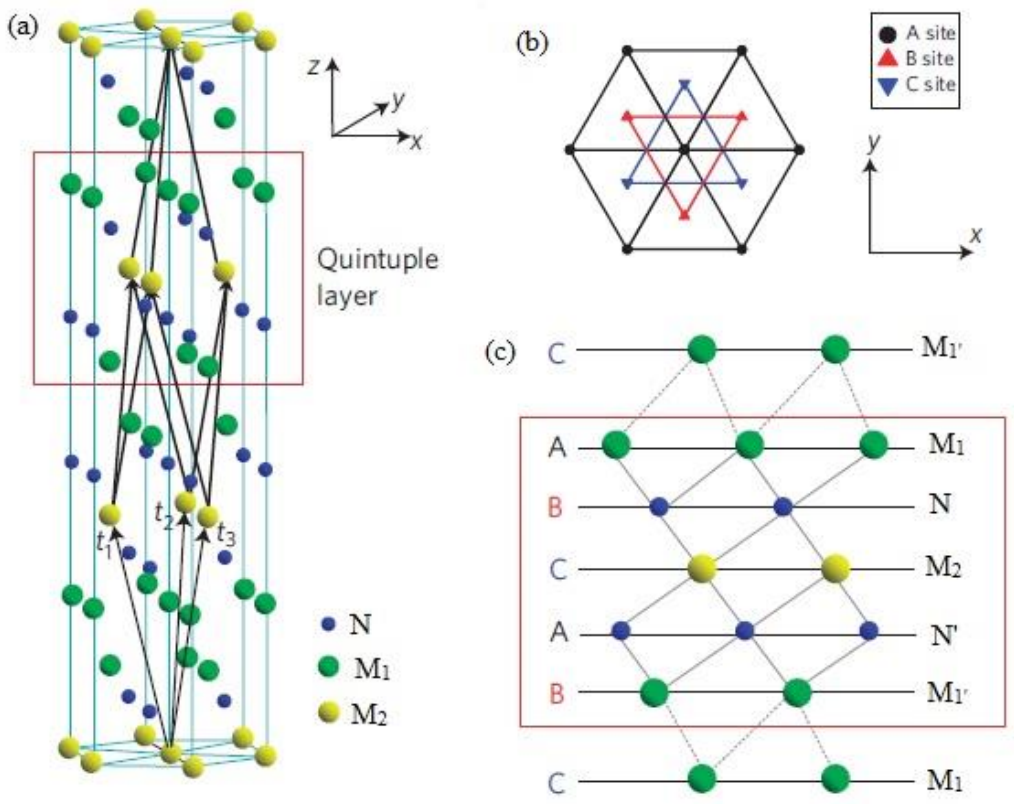

Figure 2-6 Crystal structure of N_2M_3 (N: Bi *or* Sb; M: Te *or* Se).[83]

Table 2-1 Physical properties of N_2M_3 (N: Bi, Sb; M: Te, Se).[84,85]

	Bi_2Te_3	Bi_2Se_3	Sb_2Te_3
Structure	Hexagonal	Hexagonal	Hexagonal
a (Å)	4.38	4.14	4.26
c (Å)	30.48	28.64	30.45
Unit layer (Å)	10.16	9.55	10.15
Band Gap (eV)	0.15	0.3	0.22

The electron band structures of Bi_2Te_3 are shown in Figure 2-7. According to pseudo potential band structure calculations, both the highest valence band and lowest conduction band have six valleys. Despite these two bands, the second conduction and valence band with energy separations of 30 meV and 20 meV, respectively.[86]

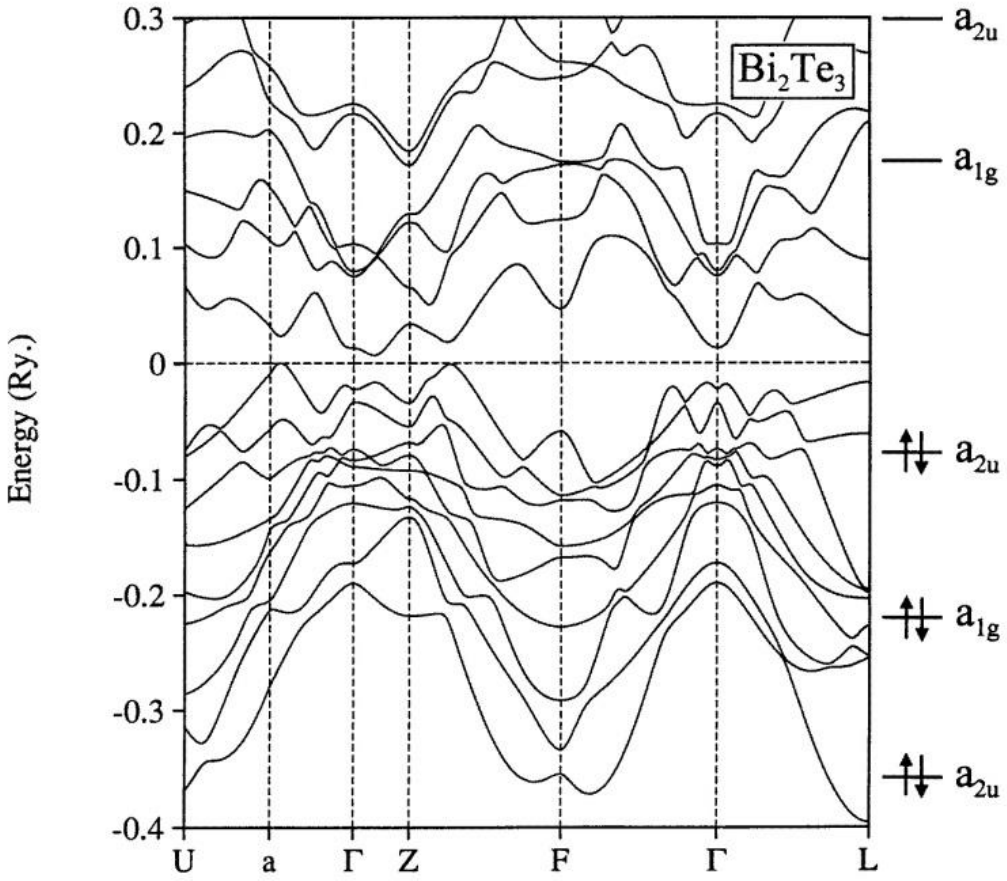

Figure 2-7 The electric band structure of Bi_2Te_3.[86]

Based on above discussions, Bi_2Te_3 families crystalize in layered structures and consist of heavy atoms, which can potentially ensure low κ. Moreover, the narrow band gaps can secure a high σ, and the large band degeneracy is also beneficial to produce a high $S^2\sigma$. Because of these advantages, great efforts have been dedicated to enhance the thermoelectric efficiencies of Bi_2Te_3 families. Table 2-2 summarizes the reported thermoelectric properties for both n-type Bi_2Te_3 and p-type Sb_2Te_3 based thermoelectric materials. As can be seen, the highest ZT of 1.2 has been achieved in n-type Bi_2Te_3,[62,75,87,88] and the highest ZT of 1.8 has been obtained in p-type Sb_2Te_3.[66,89] The big difference between the n-type and the p-type materials is mainly due to the much lower $S^2\sigma$ in Bi_2Te_3, although the obtained lowest κ of Bi_2Te_3 is even smaller than that of Sb_2Te_3.

Table 2-2 Thermoelectric properties of the Bi_2Te_3-based materials prepared by different methods.

Material	Type	$S^2\sigma$ (10^{-4} $Wm^{-1}K^{-2}$)	κ (κ_l) ($Wm^{-1}K^{-1}$)	ZT	T (K)	Preparation method*
Nanostructuring						
Bi_2Te_3[90]	n	11.9	0.46(0.25)	0.91	350	MSS+CP
$Bi_{0.5}Sb_{1.5}Te_3$[90]	P	14.9	0.45(0.25)	1.2	363	MSS+CP
$Bi_2Te_{2.7}Se_{0.3}$[91]	n	11	0.6	0.55	300	SG+SPS
$Bi_2Te_{2.7}Se_{0.3}$[92]	n	11	0.6	0.54	300	SG+SPS
$Bi_{0.5}Sb_{1.5}Te_3$[93]	p	28	0.7(0.4)	1.2	320	MSS+SPS
$Bi_{0.4}Sb_{1.7}Te_{3.0}$[94]	p	9	0.35(0.16)	0.9	413	SG+SPS
$(Bi_2Te_3)_{0.85}(Bi_2Se_3)_{0.15}$[95]	n	12	0.68(0.45)	0.71	480	SG+SPS
$(Bi_2Te_3)_{0.8}(Bi_2Se_3)_{0.2}$[96]	n	9	0.53(0.38)	0.71	450	SG+SPS
$Bi_{0.5}Sb_{1.5}Te_3$[97]	p	24	0.66(0.3)	1.13	360	MSS+SPS
Bi_2Te_3[98]	n	15.4	1.1	0.66	470	SG+HP
Bi_2Te_3-Te[99]	n	18.7	1.22(0.45)	0.6	390	SG+HP
Bi_2Te_3[100]	n	6.9	0.45(0.28)	0.62	400	SG+SPS
Bi_2Se_3[101]	n	4.4	0.42	0.35	400	LIE+HP
Bi_2Se_3[102]	n	4.7	0.41(0.3)	0.48	425	MSS+SPS
S doped Sb_2Te_3[103]	p	20.0	0.7(0.35)	0.95	423	MSS+CP
Bulk materials						
$Bi_{0.5}Sb_{1.5}Te_3$[82]	p	44	1	1.4	373	BM+HP
$Bi_{0.5}Sb_{1.5}Te_3$[104]	p	43	1	1.3	373	BMA+HP
$Bi_2Te_{2.7}Se_{0.3}$ [57]	n	26	1.08	1.04	400	BMA+HP
Bi_2Te_3[88]	n	33	1.1	1.2	425	BMA+HP
$Bi_{0.5}Sb_{1.5}Te_3$[105]	p	38	0.85(0.48)	1.4	300	MA+HP
$Bi_2Te_{2.7}9$ $Se_{0.21}$[62]	n	42	0.8(0.56)	1.2	357	HP
$Bi_2Te_{2.3}Se_{0.7}$[75]	n	28	1.1(0.4)	1.2	445	MA+BM+HP
$Bi_{0.3}Sb_{1.7}Te_3$[75]	p			1.3	380	MA+BM+HP
$Bi_2Te_{2.925}Se_{0.075}$[106]	n	47	1.65(1.27)	0.85 (*a*-*b*)	293	THM
$Bi_{0.52}Sb_{1.48}Te_3$[63]	p	35	0.65(0.25)	1.56	300	MS

$Bi_{0.5}Sb_{1.5}Te_3$[66]	p	39	0.6(0.31)	1.86	320	Te-MS+SPS
$Bi_{0.4}Sb_{1.6}Te_3$[89]	p	37	0.65(0.16)	1.8	316	MA+MS+HP
$Cu_{0.01}Bi_2Te_{2.7}Se_{0.3}$[56]	n	31.2	1.1	1.06	373	BM+HP
$Bi_2Te_{2.7}Se_{0.3}$[87]	n	53.8	1.87	1.18	410	BS
$Bi_2(Te_{1-x}Se_x)_3$-I(0.08%)[107]	n	55	1.5(0.9)	1.1	340	ZM
$Bi_2(Te_{0.5}Se_{0.5})_3$-I 0.1%[107]	n	25	1.42(0.45)	0.85	570	ZM

* The abbreviations used in the column of preparation method represent the following meanings: MSS = microwave solvothermal, CP = cold pressing, SG = solution grow, SPS = spark plasma sintering, HP = hot pressing, LIE = lithium ionic exfoliation, BMA = ball milling alloy, MA = melting alloy, BS = Bridgman–Stockbarger, BM = ball milling, THM = travelling heater method, MS = melt spinning, Te-MS = Te rich melt spinning, ZM = zone melting.

2.5 Chief characteristics of Bi_2Te_3-based alloys affecting their thermoelectric performance

2.5.1 Anti-site defects and vacancies

For Bi_2Te_3, the most common defects are vacancies at Te sites, and antisite defects of Bi in Te-sites.[108] The formation of vacancies is caused by the evaporation of consisting elements,[56] and the motivation of antisite defects is the differences of electronegativity and atomic size between Te and Bi[109]. The formation of Te vacancies (assuming *x* mol from 1 mol Bi_2Te_3) follows

$$Bi_2Te_3 \rightleftharpoons 2Bi_{Bi}^{\times} + (3-x)Te_{Te}^{\times} + xTe(g)\uparrow + xV_{Te}^{2+} + 2xe^{-} \quad (2.6)$$

On the basis of *x* mol V_{Te}^{2+} in 1 mol Bi_2Te_3, the generation of *y* mol antisite defects of Bi at Te site can be expressed as

$$Bi_2Te_3 \rightleftharpoons (2-z)Bi_{Bi}^{\times} + zBi_{Te}^{-} + (3-x)Te_{Te}^{\times} + xTe(g)\uparrow + (x-z)V_{Te}^{2+} + 2xe^{-} + 3zh^{+} \quad (2.7)$$

In the above equations, $Bi_{Bi}^{\times}$ and $Te_{Te}^{\times}$ are Bi and Te atoms at their original sites of the lattice, respectively, Te (g) is the evaporation of Te, V_{Te}^{2+} is the Te vacancies, and Bi_{Te}^{-} is the antisite defect of Bi at Te site. From Equations (2.6) and (2.7), we can see that V_{Te}^{2+} is

positively charged, and one V_{Te}^{2+} contributes two electrons, whereas Bi_{Te}^{-} is negatively charged, and one Bi_{Te}^{-} gives one hole. Most Bi_2Te_3 single crystals or ingots with coarse grains are intrinsically p-type, because Bi_{Te}^{-} is the dominating defects. For fine-grained polycrystalline samples and nanostructures, the dangling bonds at grain boundaries due to Te deficiencies can also be considered as fractional V_{Te}^{2+}, therefore more V_{Te}^{2+} is generated, suggesting fine-grained polycrystalline samples and nanostructures are generally n-type.

Likewise, in Bi_2Se_3, Sb_2Se_3 and Sb_2Te_3, there also exist positively charged anion vacancies of V_{Te}^{2+}, and V_{se}^{2+}, as well as negatively charged antisite defects of Bi_{Se}^{-}, Sb_{Se}^{-}, and Sb_{Te}^{-}. The formation of anion vacancies depends on the evaporation heat, and the formation of antisite defects rely on the differences of electronegativity and covalent radius between the consisting cation and anion atoms. Table 2-3 lists the parameters of evaporation heat, electronegativity and covalent radius of Te, Se, Bi, and Sb. As can be seen, V_{se}^{2+} is easier to happen than V_{Te}^{2+}, and the formation of antisite defects follows the sequence (easy to difficult) of Sb_{Te}^{-}, Bi_{Te}^{-}, Sb_{Se}^{-} and Bi_{Se}^{-}. That is why single crystal Sb_2Te_3 shows strong p-type, Bi_2Te_3 is weak p-type, and Bi_2Se_3 is strong n-type.

Table 2-3 Electronegativity and evaporation heat for Te, Se, Bi and Sb

	Te	Se	Bi	Sb
Evaporation heat (kJ/mol)[110]	52.55	37.70	104.8	77.14
Electronegativity[109]	2.1	2.55	2.02	2.05
Covalent radius (Å)[110]	127.6	78.96	208.98	121.75

The existence of defects can enhance the scattering of phonons with high frequency due to the mass fluctuation and strain. However, defects make it hard to tune the thermoelectric properties, and lead to the irreproducibility of the obtained high thermoelectric properties. The anion vacancies lead to the Fermi level residing deep in the conduction band, which worsens the power factor. For the nanostructures and ball milling samples, there are more anion vacancies due to the dangling bonds in the dense grain boundaries. Unfortunately, the amount of anion vacancies cannot be well controlled. Therefore, the ultimately obtained thermoelectric performance is perhaps irreproducible.[56]

2.5.2 Intensive bipolar conduction at relatively high temperature

Bipolar conduction is the excitation of minor charger carriers. In n-type thermoelectric semiconductors (as an example), electrons are thermally executed from the valance band to the conduction band, leaving behind holes as the minor charger carriers in the valance.[111] Since electrons and holes have opposite charges, the overall S is suppressed if both electrons and holes are present. For semiconductors, S increases with elevating temperature. The turn-over of S is caused by the bipolar conduction at high temperature. Because bipolar conduction is related to E_g, the Goldsmid-Sharp relation (i.e. $E_g = 2eS_{max}T$ with S_{max} and T representing the peak value of S and the corresponding temperature, respectively) was proposed to roughly estimate E_g according to the variation of S with temperature.[112] Recently, a more precise method taking into account the different weighted carrier mobility ratios between valance band and conduction was proposed to estimate E_g based on temperature dependent S.[113]

Despite the detrimental effect on S, the minor charger carriers also contribute to thermal conductivity, namely κ_{bi}. Although κ_{bi} is generally lower than κ_e and κ_l, the high-temperature ZT is sensitive to κ_{bi}. The estimation of κ_{bi} is outlined in Ref,[114] and we also intensively studied the estimation of κ_{bi} using this method.[102] Specifically, κ_e is firstly calculated based on the Wiedemann-Franz Law, and then κ - κ_e is the sum of κ_l and κ_{bi}. For phonon-phonon Umklapp scatterings, κ_l is proportional to T^{-1}. As a consequence, κ_l in intrinsic excitation region can be estimated by extrapolating the linear relationship in extrinsic region between κ_l and T^{-1}, when phonon-phonon scattering is the dominant scattering mechanism. Finally, κ - κ_e - κ_l can be indirect evaluation of κ_{bi}.[114] However, this derivation method of κ_{bi} is not applicable for polycrystalline samples, where grain boundary phonon scattering is significantly. Another method based on the two band model can be used to calculate κ_{bi},[115] which will be discussed later. Based on above discussions, the suppression of bipolar conduction can enhance the overall ZT from two aspects — shifting the peak of S to high temperature and reducing κ.

2.5.3 Strong anisotropic behavior

Bi_2Te_3 crystal has remarkable anisotropy that originates from the layered rhombohedral structure. The σ and κ in a-b plane (perpendicular to the c-axis) are approximately four and two times, respectively, larger than those along the c-axis in Bi_2Te_3. The S shows only

slight difference along the two directions. So, the *a-b* plane *ZT* can approximately double that along the *c*-axis, as shown in Table 2-4.[106] On the contrary, thermoelectric properties of Sb_2Te_3 single crystal exhibit weaker anisotropic behavior, and the *ZT* values along the two perpendicular directions are nearly identical.

The anisotropy behavior will detrimentally affect the $S^2\sigma$ in the polycrystalline samples. In most cases, we use nanostructuring or ball milling to reduce the grain size for obtaining a significantly reduced. However, this deteriorates $S^2\sigma$ to some extent, resulted from the random crystal orientation. The ultimate *ZT* cannot be significantly enhanced in Bi_2Te_3. Favorably, anisotropy for Sb_2Te_3 is much weaker. *ZT* in polycrystalline Sb_2Te_3 can be up to 1.8 because of the dramatically reduced κ and the preserved high $S^2\sigma$.

Table 2-4 Anisotropic behavior for single crystals of Bi_2Te_3 families.

	$\sigma_{\perp c}/\sigma_{\parallel c}$	$S_{\perp c}/S_{\parallel c}$	$(S^2\sigma)_{\perp c}/(S^2\sigma)_{\parallel c}$	$\kappa_{\perp c}/\kappa_{\parallel c}$	$ZT_{\perp c}/ZT_{\parallel c}$
$Bi_2Te_{2.6}Se_{0.4}$[106]	4.38	1.03	4.65	2.15	2.17
$Bi_{0.5}Sb_{1.5}Te_3$[116]	2.65	1.02	2.75	1.93	1.42

2.6 Strategies for enhancing thermoelectric performance of Bi_2Te_3 families

2.6.1 Point defect engineering

As mentioned previously, point defects unavoidably present in Bi_2Te_3 families, and significantly affect the thermoelectric properties. Firstly, the anion vacancies and anitisite defects serve as electron donors and acceptors, respectively; thus, the overall carrier type and carrier concentration depend on the competition of vacancies and anitiste defects. Secondly, point defects are supposed to induce the fluctuations of mass and strain in the lattice, which are likely to scatter charge carriers, leading to low carrier mobility. Finally, point defects can enhance the scattering of high-frequency phonons, resulting in low κ_l. In this regard, it is necessary to control the intrinsic vacancies and antisite defects by point defect engineering. Currently, the most effective methods are mainly to form the ternary phases (*i.e.* n-type $Bi_2Te_{3-x}Se_x$ and p-type $Bi_xSb_{2-x}Te_3$), and doping. In this part, we mainly focus on the effect of point defects on electronic transport. Note that the smaller evaporation energy leads to the easier formation of vacancies, and the smaller differences of electronegativity and atomic size motivates the formation of antisite defects.[117] From Table 2-3, the related parameters are different, which means the point defects strongly

depend on the composition of $Bi_2Te_{3-x}Se_x$ and $Bi_xSb_{2-x}Te_3$. Increasing Se content in $Bi_2Te_{3-x}Se_x$ increases anion vacancies but decreases antisite defects, and increasing Bi content in $Bi_xSb_{2-x}Te_3$ can suppress antisite defects but does not notably affect the anion vacancies.

We summarized the reported data for these ternary phases. Here, we mainly focus on the variations of n_H, μ_H, σ, and S with Se or Bi contents in the ternary phases due to point defect engineering. Next, we will theoretically study the overall thermoelectric performance in the ternary phases. Figure 2-8 summarized Se content dependent n_H, μ_H, σ, and S at 300 K for n-type $Bi_2Te_{3-x}Se_x$ single crystal,[118] single crystal $Bi_2Te_{3-x}Se_x$ doped with Ag (0.1%),[118] BM+HP+HD processed $Bi_2Te_{3-x}Se_x$ sample,[75] and ingot $Bi_2Te_{3-x}Se_x$ doped with I (0.08 wt%).[107] From Figure 2-8a, with increasing Se content in $Bi_2Te_{3-x}Se_x$, Hall carrier concentration (n_H) for the single crystals and the ingot gently increases, whereas n_H for the samples prepared by ball milling, hot pressing plus hot deformation (BM+HP+HD) initially decreases and then increases. The increases in n_H for the single crystals, the ingot, and the BM+HP+HD processed samples with high Se content are ascribed to the increase in anion vacancies dominating over that in antisite defects, and the decrease in n_H for the BM+HP+HD processed samples with low Se content is caused by the antisite defects exhibiting stronger effect on carrier concentration over vacancies. From Figure 2-8b, Hall carrier mobility (μ_H) for single crystals and ingot show intensive fluctuations, while that for BM+HP+HD processed samples stabilize to a plateau, which means the effects of point defects on μ_H also depends on the sample preparation methods. Because of the variation of electronic transport caused by point defects, σ, and S are modified, shown in Figure 2-8c and d. The effect of Bi content in p-type $Bi_xSb_{2-x}Te_3$ on electronic transport properties was shown in Figure 2-9.

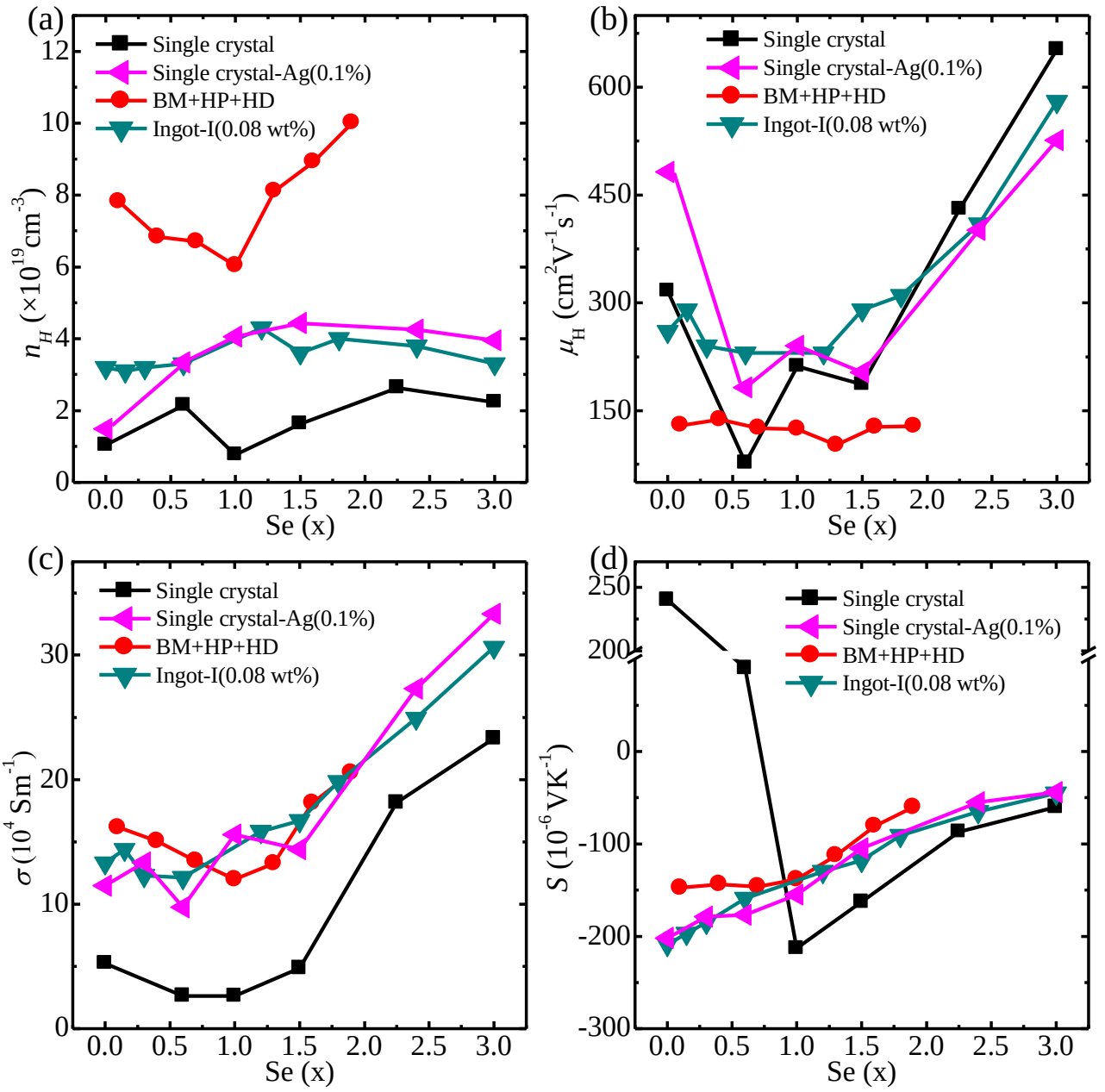

Figure 2-8 N-type $Bi_2Te_{3-x}Se_x$ with (a) n_H, (b) μ_H (c) σ, and (d) S at 300 K as a function of Se content for single crystal,[118] single crystal doped with Ag (0.1%),[118] BM+HP+HD processed sample,[75] and ingot doped with I (0.08 wt%).[107]

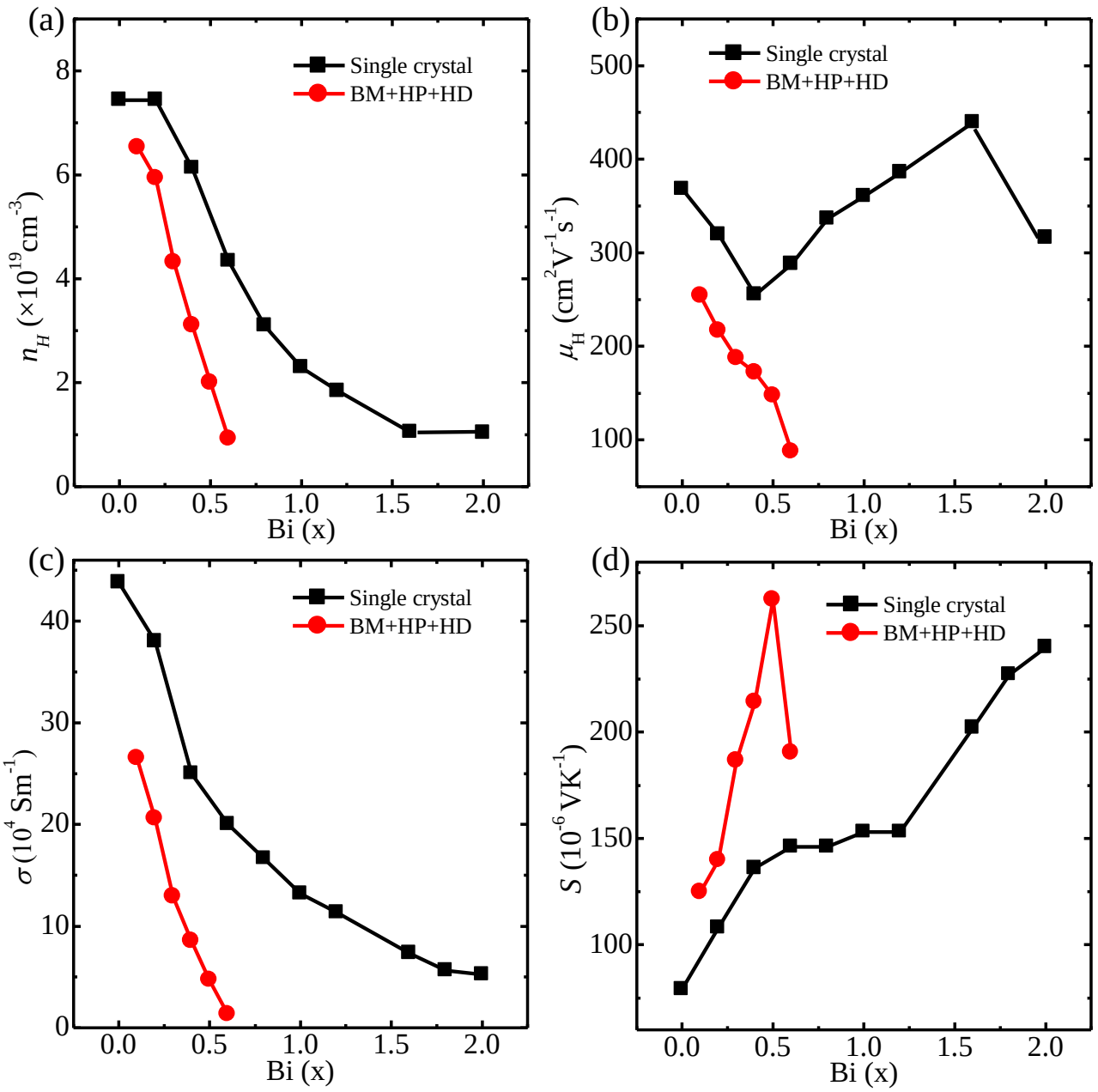

Figure 2-9 P-type $Bi_xSb_{2-x}Te_3$ with (a) n_H, (b) μ_H (c) σ, and (d) S at 300 K as a function of Bi content for single crystal,[116] and BM+HP+HD processed sample.[75]

In addition, doping can also modify the point defects. S-doped Sb_2Te_3 can suppress the antisite defects so as to reduce the carrier concentration and diminish the effect of impurity scattering on holes to enhance the carrier mobility.[103] Cu-doped $Bi_2Te_{2.7}Se_{0.3}$ can suppress the vacancies to enhance the carrier mobility.[56] We also noted that hot deformation can also reduce the donor effect of anion vacancies to reduce the carrier concentration for the sintered n-type polycrystalline samples. Zhao *et al.* reported that n_H for SPS sintered Bi_2Te_3 was reduced to only 1.5×10^{19} cm^{-3} by hot deformation at 733 K, compared with the

n_H of 5.9×10^{19} cm^{-3} in the unprocessed counterpart. As a consequence, S increased from -116 to -141 μV/K. The similar phenomenon was also reported elsewhere.[62,75]

2.6.2 Crystalline alignment by hot deformation

To reduce κ, polycrystalline materials with dense grain boundaries are potentially to exhibit enhanced ZT. Nevertheless, in the case of Bi_2Te_3, the strong anisotropic behavior would cripple $S^2\sigma$ in polycrystalline materials. Enhancing texture (i.e. crystal orientation) in the polycrystalline samples is most likely to enhance the overall ZT. Figure 2-10 summarizes the cutting-edge thermoelectric performance of both n-type $Bi_2Te_{3-x}Se_x$ and p-type $Bi_xSb_{2-x}Te_3$ benefiting from the hot deformation to enhance the texture of the sintered samples. As can be seen, for n-type ones, σ is enhanced significantly after the hot deformation; specifically, its value in the hot-deformed $Bi_2Te_{2.3}Se_{0.7}$ nearly doubles that for the sample without hot deformation. Nevertheless, the enhancement of S caused by hot deformation is not notable. Therefore, $S^2\sigma$ for the n-type $Bi_2Te_{3-x}Se_x$ is elevated dramatically after hot deformation, which leads to enhanced ZT. In the case of p-type $Bi_xSb_{2-x}Te_3$, hot deformation does not affect $S^2\sigma$ notably, but can reduce κ to some extent. For this reason, ZT of p-type candidates is also enhanced. On this basis, hot deformation enhances ZT for n-type $Bi_2Te_{3-x}Se_x$ and p-type $Bi_xSb_{2-x}Te_3$ from different aspects. Specifically, the enhancement in ZT for n-type $Bi_2Te_{3-x}Se_x$ is mainly due to the enhanced $S^2\sigma$, and the enlarged ZT for p-type analogues is caused by the reduced κ.

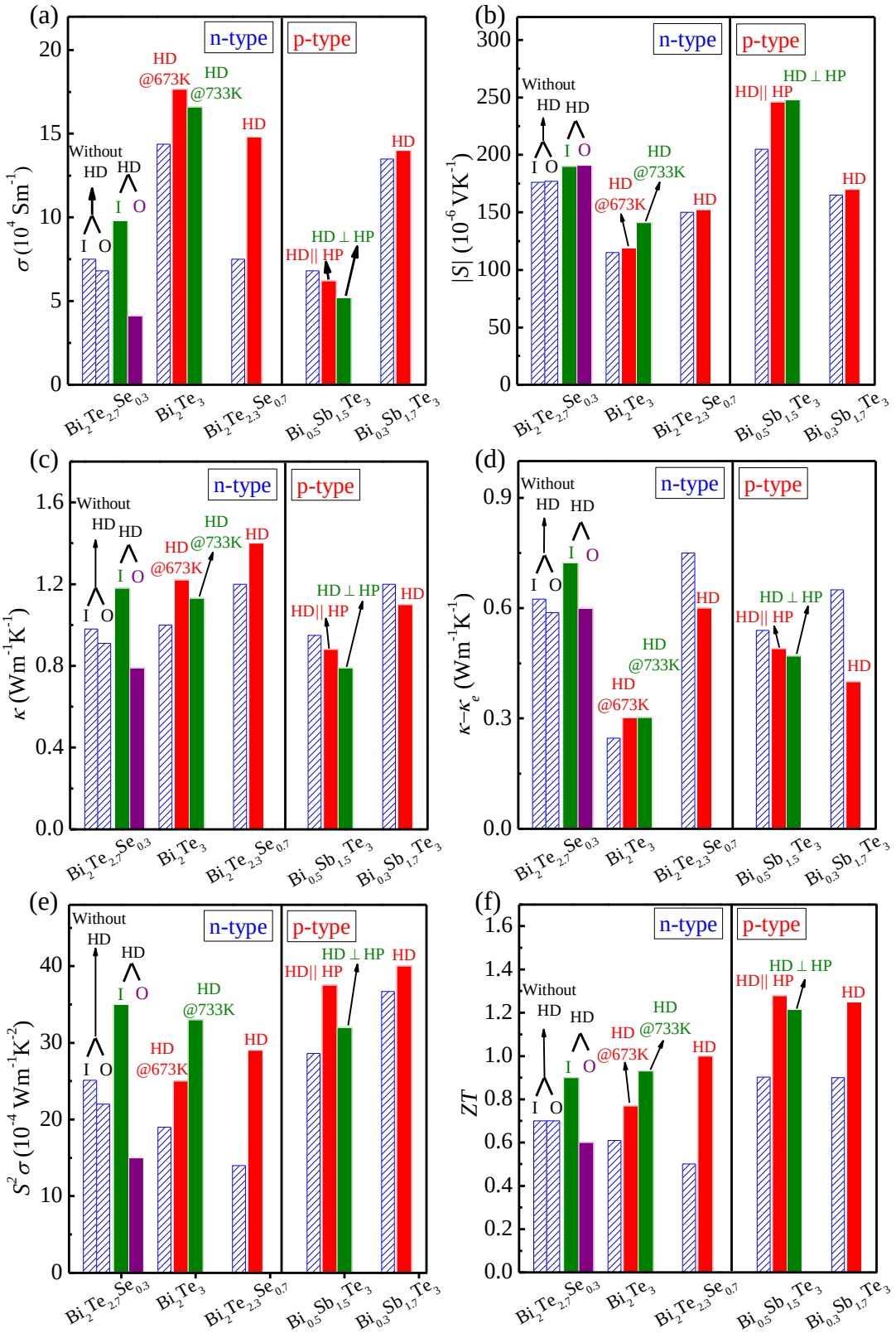

Figure 2-10 The effects of hot deformation on reported (a) σ, (b) S, (c) κ, (d) κ_l (e) $S^2\sigma$, and (f) ZT for n-type $Bi_2Te_{2.7}Se_{0.3}$,[57] Bi_2Te_3,[88] $Bi_2Te_{2.3}Se_{0.7}$,[75] and p-type $Bi_{0.5}Sb_{1.5}Te_3$,[105] $Bi_{0.3}Sb_{1.7}Te_3$.[75]

2.6.3 Enhancing phonon scattering

Enhancing phonon scattering to reduce κ is also effectively to enhance the final ZT. Despite the point defect scattering and hot deformation discussed above, we will cover additional strategies for reducing κ.

2.6.3.1 Nanostructuring

A variety of one-dimensional, two-dimensional and three-dimensional nanostructures of Bi_2Te_3 have been synthesized by solution grow method, including one-dimensional nanowires Bi_2Te_3,[119,120] T-shaped Bi_2Te_3-Te heteronanojunctions,[121] Te/Bi_2Te_3 nanostring-cluster hierarchical nanostructures,[122-124] two dimensional hexagonal nanoplates,[92,122,125] Bi_2Se_3 ultrathin nanosheets,[101,102,126] Bi_2Te_3/Bi_2Se_3 multishell nanoplates, three-dimensional nanoflowers.[95,127] In the synthesis of nanostructures, surfactants are generally used to control the morphology. However, the residuals of surfactants are detrimental to the final thermoelectric performance. Therefore, it is necessary to remove the surfactants or employ the synthesis without surfactants.

Because of the enhanced phonon scatterings in the nanostructures, thermal conductivities are reduced. Figure 2-11 shows the temperature dependent κ, and κ- κ_e for $Bi_{0.5}Sb_{1.5}Te_3$ nanoplates,[93] $Bi_2Te_{2.7}Se_{0.3}$ nanoplates, Bi_2Se_3 ultrathin nanosheets,[102] Bi_2Te_3/Bi_2Se_3 nanoflowers,[95] and Bi_2Te_3 nanoplates,[100] compared with the ingot.[107] As can be seen, κ of nanostructures can be lower than the half of ingots.

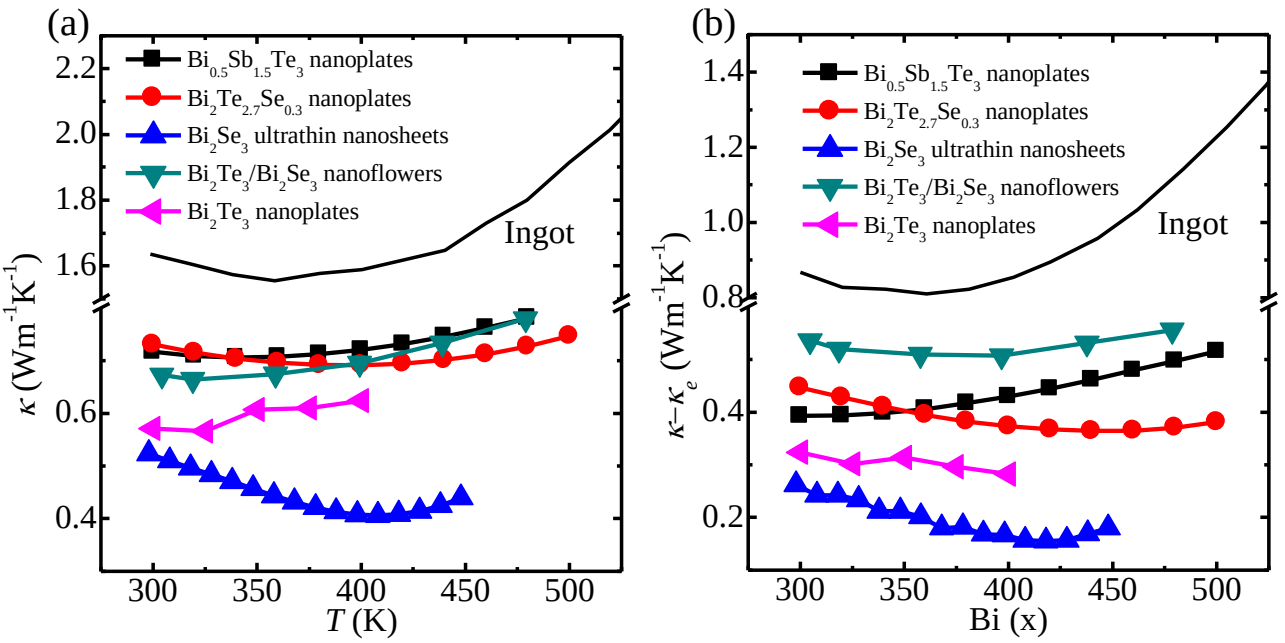

Figure 2-11 (a) κ, and (b) κ- κ_e for $Bi_{0.5}Sb_{1.5}Te_3$ nanoplates,[93] $Bi_2Te_{2.7}Se_{0.3}$ nanoplates, Bi_2Se_3 ultrathin nanosheets,[102] Bi_2Te_3/Bi_2Se_3 nanoflowers,[95] and Bi_2Te_3 nanoplates,[100] compared with the ingot.[107]

2.6.3.2 Ball milling

Ball milling can reduce the grain size so as to enhance the grain boundary scattering on phonons. Ball milling generally includes two methods: grounding the ingot with final product composition to obtain fine powders, and forming pure phases by mechanical allying. Both techniques of ball milling have been successfully used to enhance *ZT* for Bi_2Te_3 families.

Poudel B. *et al.* prepared the $Bi_{0.5}Sb_{1.5}Te_3$ polycrystalline sample with reduced grain size using the ball milling to ground the ingot. Because of the remarkably decreased κ, *ZT* was increased to 1.5 compared with that of 1.1 for the ingots.[82]

2.6.3.3 Melt spin

MS can also significantly reduce κ. Figure 2-12 summarizes the thermoelectric performance of p-type $Bi_{0.5}Sb_{1.5}Te_3$ prepared by MS. As can be seen, MS can reduce κ by 34% off compared with the corresponding ingot, and lattice component (κ- κ_e) could be even lower. Recently, Kim *et al.* newly developed Te rich MS method to prepare $Bi_{0.5}Sb_{1.5}Te_3$ with dense dislocations between grain boundaries. Due to the enhanced scattering on mid-frequency phonons, κ- κ_e and κ were further reduced.[66] Unavoidably, MS

also reduces $S^2\sigma$ slightly. Totally, ZT values for MS processed p-type $Bi_{0.5}Sb_{1.5}Te_3$ were enhanced.

In the case of n-type ones, MS cannot significantly reduce κ. Ivanova *et al.* employed MS to prepare n-type n-type $Bi_2Te_{2.7}Se_{0.3}$ solid solution, but κ was not significantly reduced, which resulted in a ZT similar to ingot.[129] Maybe, MS is not effective to reduce κ for n-type ones.

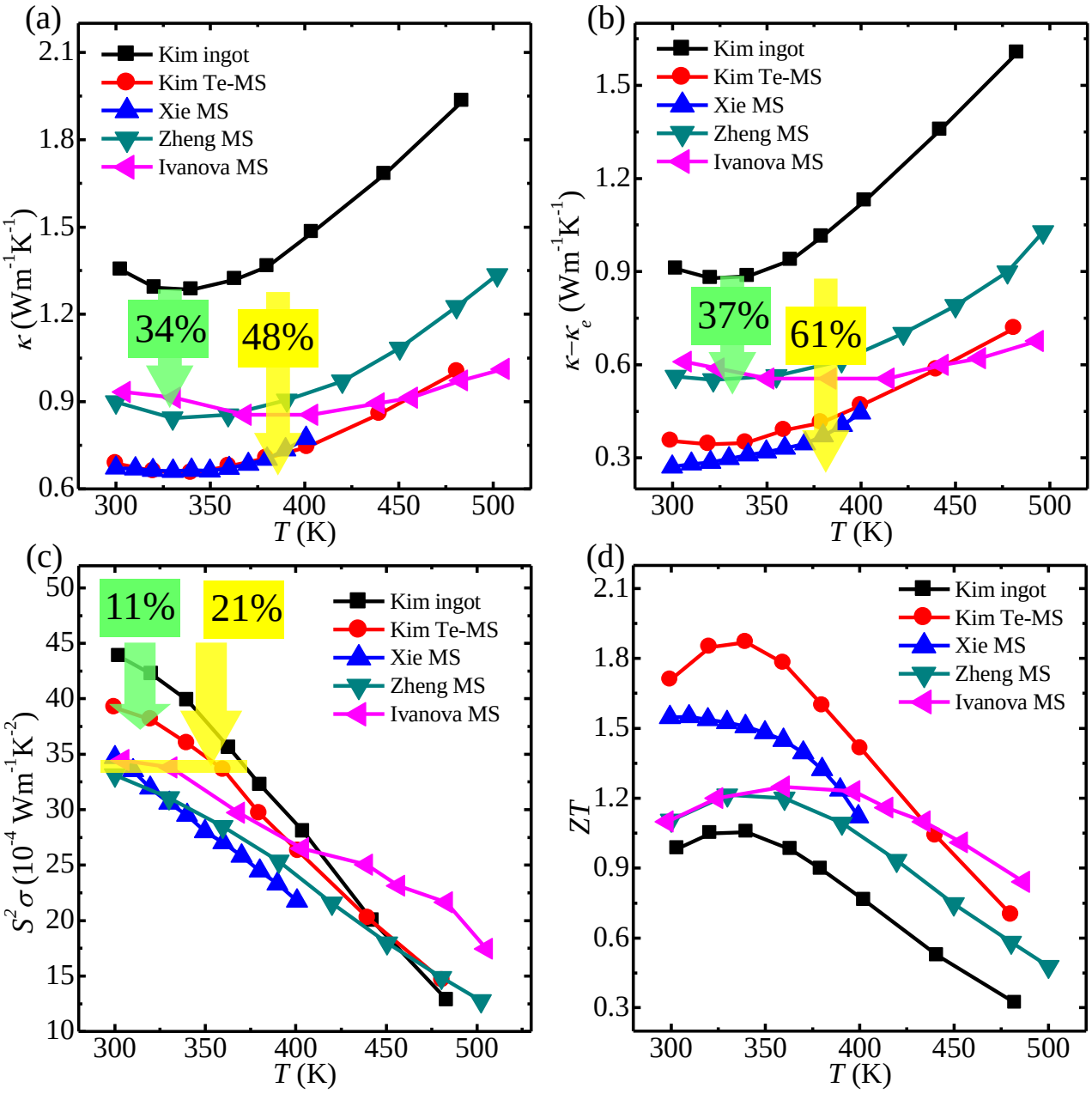

Figure 2-12 (a) κ, (b) κ_l, (c) $S^2\sigma$, and (d) ZT for $Bi_{0.5}Sb_{1.5}Te_3$ ingot,[66] Te-MS,[66] Xie MS,[63] Zheng MS,[130] and Ivanova MS.[131]

2.6.4 Other strategies

There are still many other strategies for enhancing *ZT* in the Bi_2Te_3 families, which includes Sn-doped Bi_2Te_3 due to resonant energy doping,[132] Bi_2Te_3/Bi_2Se_3 mixed phases with extra energy potentials to filter low charger carriers.[95] Here, we should highlight the success in enhancing the high temperature performance due to the reduced bipolar effect through enlarging band gap, and the enlarged band gap in Bi_2Te_3 families were achieved by reducing the thickness of nanosheets,[102] and forming ternaries.[117]

Because thermoelectric properties are correlated with each other, we must employed multi strategies to enhance thermoelectric performance. Thermoelectric properties are related to the electronic band structure, charger carrier scattering and phonon scattering. For a specific case with enhanced *ZT*, it is always due to the combination of multi strategies to achieve a compromise between these parameters so as to realize a net increase in *ZT*.

2.7 Modeling studies for the transport properties of Bi_2Te_3 based materials.

Thermoelectric properties are determined by the electronic band structure, charger carrier scatterings, and phonon scatterings. Electronic band structure mainly involves the effective mass, and E_g. For most good thermoelectric materials, acoustic phonons dominate the charger carrier scattering. Then, we focus on the magnitude of carrier mobility. Enhancing phonon scatterings is necessary to ensure a low κ.

2.7.1 Electronic transport properties

Electronic transport properties cover carrier concentration (n), carrier mobility (μ), S, σ, κ_e and κ_{bi}. Here, we firstly study the coupling relation between them, and then numerically examine the parameters, which affect them. Kane band model is employed, and the electronic transport properties are given by[133]

Seebeck coefficient

$$S = \frac{k_B}{e}\left[\frac{F_{1,-2}^{1}(\eta,\beta)}{F_{1,-2}^{0}(\eta,\beta)} - \eta\right] \tag{2.8}$$

Hall carrier concentration

$$n_H = \frac{N_v \left(2m_b^* k_B T\right)^{\frac{3}{2}}}{3\pi^2 \hbar^3} \frac{F_{3/2,0}^0(\eta,\beta)}{A} \tag{2.9}$$

Hall carrier mobility

$$\mu_H = A \frac{2\pi\hbar^4 e C_l}{m_I^* \left(2m_b^* k_B T\right)^{3/2} E_{def}^2} \frac{3F_{1,-2}^0(\eta,\beta)}{F_{3/2,0}^0(\eta,\beta)} \tag{2.10}$$

Hall factor

$$A = \frac{3K(K+2)}{(2K+1)^2} \frac{F_{1/2,-4}^0 F_{3/2,0}^0}{\left(F_{1,-2}^0\right)^2} \tag{2.11}$$

Lorenz number

$$L = \left(\frac{k_B}{e}\right)^2 \left[\frac{F_{1,-2}^2(\eta,\beta)}{F_{1,-2}^0(\eta,\beta)} - \left(\frac{F_{1,-2}^1(\eta,\beta)}{F_{1,-2}^0(\eta,\beta)}\right)^2\right] \tag{2.12}$$

Electrical conductivity

$$\sigma = n_H e \mu_H = \frac{3e^2 N_v \hbar C_l}{\pi m_I^* E_{def}^2} F_{1,-2}^0(\eta,\beta) \tag{2.13}$$

Electronic thermal conductivity is based on the Wiedemann–Franz law, namely

$$\kappa_e = L\sigma T \tag{2.14}$$

Generalized Fermi integration

$$F_{m,k}^n(\eta,\beta) = \int_0^\infty \left[-\frac{\partial f(\eta)}{\partial \varepsilon}\right] \varepsilon^n \left(\varepsilon + \beta\varepsilon^2\right)^m \left[\left(1+2\beta\varepsilon\right)^2 + 2\right]^{\frac{k}{2}} d\varepsilon \tag{2.15}$$

where η is the reduced Fermi level (for electrons, $\eta_e = \frac{E_f - E_c}{k_B T}$ with E_c denoting the conduction band edge; for holes, $\eta_h = \frac{E_v - E_f}{k_B T} = \frac{E_c - E_g - E_f}{k_B T} = -1/\beta - \eta_e$ with E_v denoting the valance band edge), β is reciprocal of reduced band gap (*i.e.* $\beta = \frac{k_B T}{E_g}$), k_B is the Boltzmann constant, $\hbar$ is the reduced Planck constant, N_v is the band degeneracy, K is the

ratio of longitudinal ($m_{\parallel}^{*}$) and transverse ($m_{\perp}^{*}$) effective mass, C_l is the combination of elastic constants, m_b^{*} is the band effective mass, m_I^{*} is the inertial effective mass, e is free electron charge, m_0 is the free electron mass, and E_{def} is the deformation potential, respectively. The relations of m_b^{*}, m_I^{*}, and density of state (DOS) effective mass are expressed as

$$m_b^{*} = N^{-\frac{2}{3}} m_d^{*} \tag{2.16}$$

and

$$m_I^{*} = N^{-\frac{2}{3}} m_d^{*} \frac{3K^{\frac{2}{3}}}{2K+1} \tag{2.17}$$

Because Bi_2Te_3-based materials are semiconductors with narrow band gaps, we should take into account both valance band (VB) and conduction band (CB) to calculate the total thermoelectric properties, which can be expressed as

Total Seebeck coefficient

$$S_{tot} = \frac{S_{CB}\sigma_{CB} + S_{VB}\sigma_{VB}}{\sigma_{CB} + \sigma_{VB}} \tag{2.18}$$

Total electrical conductivity

$$\sigma_{tot} = \sigma_{CB} + \sigma_{VB} \tag{2.19}$$

Total Hall coefficient

$$R_{Htot} = \frac{R_{HCB}\sigma_{CB}^2 + R_{HVB}\sigma_{VB}^2}{\left(\sigma_{CB} + \sigma_{VB}\right)^2} \tag{2.20}$$

Bipolar thermal conductivity

$$\kappa_{bi} = \frac{\sigma_{CB}\sigma_{VB}}{\sigma_{CB} + \sigma_{VB}} \left(S_{CB} - S_{VB}\right)^2 T \tag{2.21}$$

Total value of L

$$L_{tot} = \frac{L_{CB}\sigma_{CB} + L_{VB}\sigma_{VB}}{\sigma_{CB} + \sigma_{VB}} \tag{2.22}$$

In the above equations, the components contributed by CB and VB are presented by the corresponding subscripts. It should be mentioned that S and R_H are positive for p-type but negative for n-type in those equations.

Based on above equations, we calculated the electronic transport properties as a function of η. Figure 2-13a shows the calculated σ as a function of η at 300 K with the inset illustrating the variation of η in the band structure. From the inset, CB and VB are symmetrical relative to η of ~-3. As a consequence, σ for n-type (left side of -3) and p-type (right side of -3) is identical, and the total σ (blue curve) is respectively superimposed with the CB component (red curve) for n-type and VB component (green curve) for p-type. Furthermore, in the whole studied η range, σ increases with enlarging $|\eta|$ for either n-type or p-type. The observed characteristics of symmetry (i.e. the calculated curve as a function of η is symmetrical relative to the middle of band gap region.) and superimposition (i.e. the total value is respectively superimposed with the CB/VB component for n/p-type situation.) also appear in other calculated thermoelectric properties. Figure 2-13b shows the calculated S as a function of η at 300 K. The characteristics of symmetry and superimposition are also observed in $|S|$. In the intrinsic region of $-5.8 < \eta < 0$, the total S different from each component from either CB or VB reveals n/p- type transition, namely the bipolar conduction, and its peak values for n/p- type depend on the onset of bipolar conduction. Moreover, $|S|$ decreases with increasing $|\eta|$ for either n-type or p-type. Based on the calculated S and σ, the plots of $S^2\sigma$ as a function of η at 300 K are obtained, as shown in Figure 2-13c. Likewise, $S^2\sigma$ also shows symmetrical and superimposing characteristics. Because of the bipolar conduction, the positions of total $S^2\sigma$ peaks are slightly different from the CB/VB components. We named the η corresponding to the peak of $S^2\sigma$ as the optimized η (η^{opt}). As can be seen, η^{opt} for p-type is ~0.15, and for n-type is ~-5.9.

Figure 2-13d shows the plots of L as a function of η at 300 K. We can observe the superimposing and symmetrical features, and L increases with increasing $|\eta|$. Moreover, our calculated L for highly degenerated situation is ~2.4×10^{-8} V^2K^{-2}, which is in accordance with the reported values. Based on the calculated σ and L, we calculated the variations of κ_e, shown in Figure 2-13e, from which κ_e increases with increasing $|\eta|$. Figure 2-13f shows the calculated κ_{bi}. As can be seen, κ_{bi} is prominent in the band gap region, and it reaches the maximum value at the middle of band gap region. Moreover, κ_{bi} decreases with increasing $|\eta|$.

Based on above discussions, we can see that S and σ are inversely related with η, which determines the peak of $S^2\sigma$. Moreover, bipolar conduction has further limited the maximum values of S for n/p-type materials, therefore, the possible maximum values for $S^2\sigma$ is even smaller by considering both CB and VB. The charge carriers can not only transport electrical energy but also thermal energy in the form of κ_e and κ_{bi}.

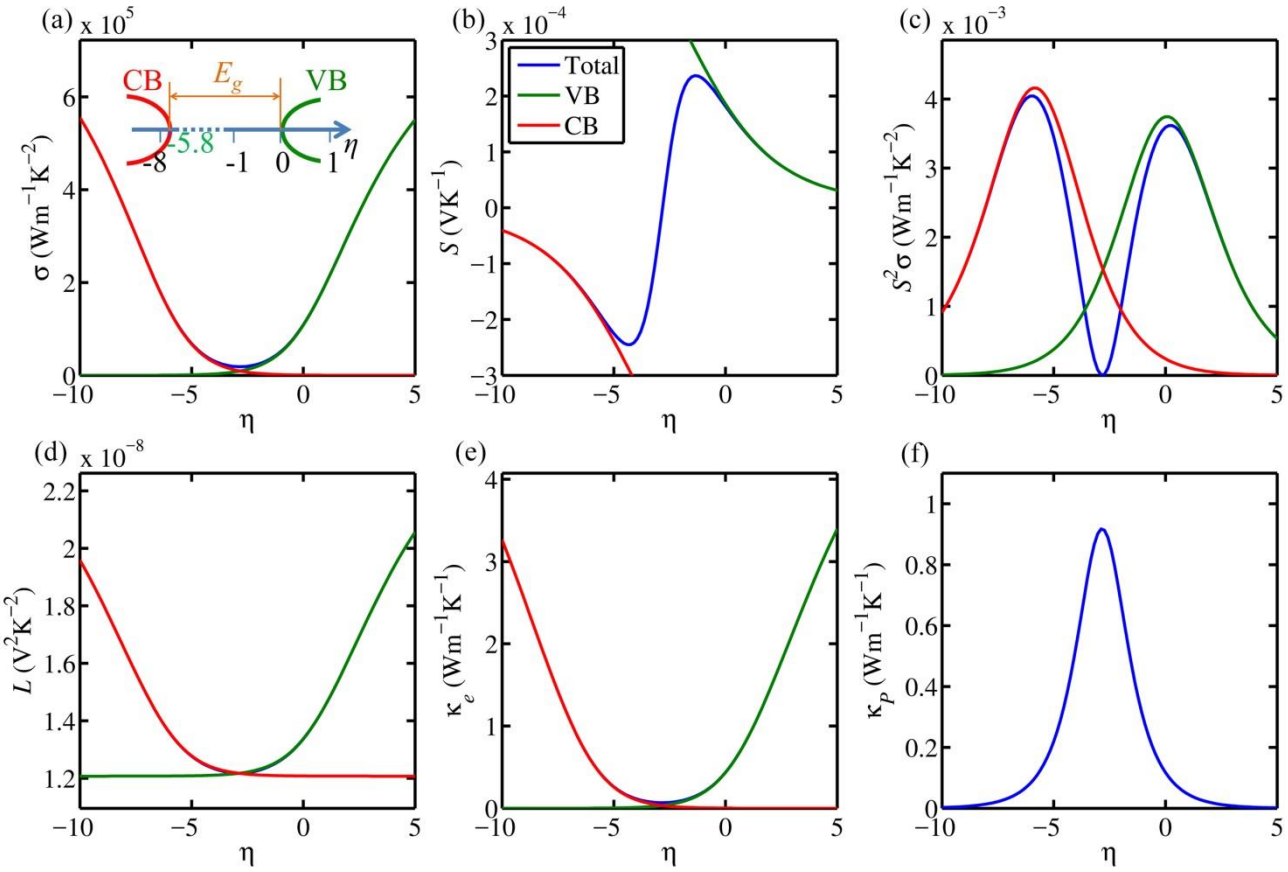

Figure 2-13 Calculated (a) S, (b) σ, (c) $S^2\sigma$, (d) L, (e) κ_e, and (f) κ_e as a function of η at 300 K with the blue curve representing the total values, the purple curve representing the CB component, green curve representing the VB component.

Based on the Kane band model, we can see S is only related to η and β (= k_BT/E_g). Apart from η and β, n_H, and μ_H are determined by m_d^*, m_l^*, and E_{def}. Therefore, σ, κ_e, and κ_{bi} are also related to these parameters. Through band engineering, we can tune these parameters to enhance the electronic transport. Here, we quantitatively predict the effects of m_d^*, E_{def} and E_g on the electronic transport properties. Note that from the Kane model equations, all thermoelectric properties are directly as a function of η. Here, we want to examine the variations of these thermoelectric properties with n_H. Therefore, we need to

firstly determine the η based on n_H, and this calculations is based on the neutrality condition, namely,

$$n_{HCB} - n_{HVB} = n_H \tag{2.23}$$

where n_{HCB} and n_{HVB} are the Hall carrier concentration from CB and VB, respectively.

Figure 2-14a shows the determined η with n_H ranging from 10^{18} to 10^{21} cm^{-3} for evenly selected ten m_d^* values from 0.2 m_0 to 2 m_0 as indicated by the colorbar in the right-hand side. As can be seen, with increasing n_H, η monotonically increases, and with increasing m_d^*, η decreases for a given n_H, which results in the Fermi level corresponding to high n_H still resides in the band gap region for large m_d^*. Thus, larger m_d^* would unfavorably leads to strong bipolar conduction. Based on the determined η, Figure 2-14b-d show the effects of m_d^* on n_H dependent S, μ_H, and $S^2\sigma$, respectively. With increasing n_H, S and μ_H increases and then decreases, which is different from the monotonic decreasing trends of both S and μ_H with increasing n_H calculated by the single Kane model (refer to the bold green lines labelled with SKB calculated for m_d^* = 2 m_0 in Figure 2-14b and c). The observed differences suggest that, at low n_H region (band gap region), both S and μ_H calculated by the two bands model are lower than those from single band model, and the reason is ascribed to the bipolar conduction. Moreover, with increasing m_d^*, S increases, while μ_H decreases, and μ_H is more sensitive to the variation of m_d^*. As a consequence, $S^2\sigma$ decreases with increasing m_d^*, as shown in Figure 2-14d. In addition, optimal n_H (n_H^{opt}) corresponding to the peak $S^2\sigma$ shift to higher values with increasing m_d^*.

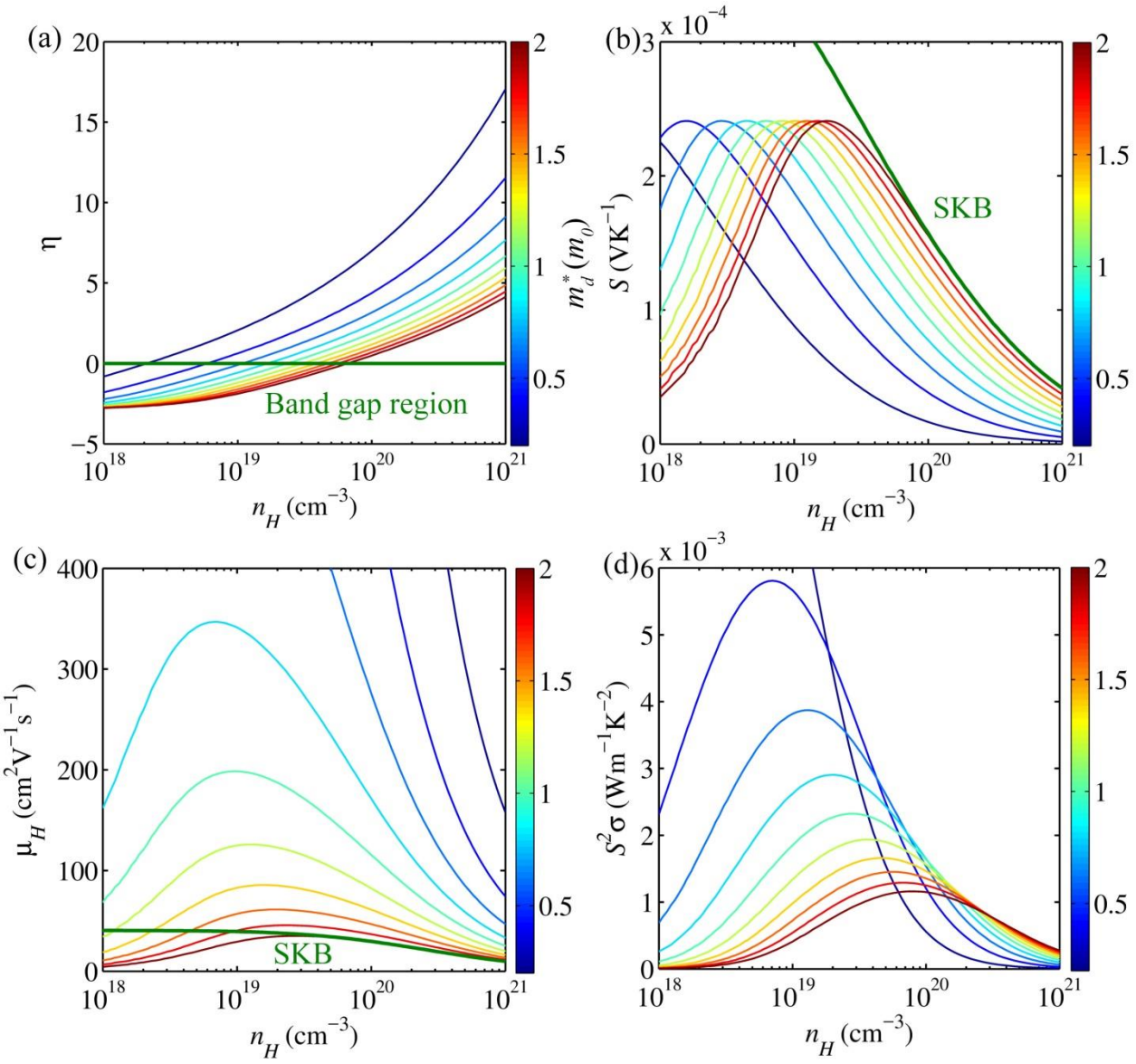

Figure 2-14 (a) Determined η with n_H ranging from 10^{18} to 10^{21} cm^{-3} for evenly selected ten m_d^* values from 0.2 m_0 to 2 m_0 as indicated by the colorbar in the right-hand side. Correspondingly calculated (b) S, (c) μ_H, and (d) $S^2\sigma$ as a function of n_H for different m_d^* values. The bold green lines in (b) and (c) are calculated using SKB model with m_d^* = 2 m_0 for S and μ_H, respectively.

Figure 2-15 shows the effects of E_g on thermoelectric properties. Firstly, we calculated η with n_H ranging from 10^{18} to 10^{21} cm^{-3} for evenly selected ten E_g values from 0.1 to 0.5 eV as indicated by the colorbar in the right-hand side, and results are exhibited in Figure 2-15a. As can be seen, η tends to increases with increasing E_g for a given n_H. On this basis, Figure 2-15b presents the plots of S as a function of n_H for different E_g values. Larger E_g produces larger S peak, and shifts the peak of S to low n_H, which verifies the

effectiveness of E_g on suppressing bipolar conduction. The suppressed bipolar conduction due to large E_g is also demonstrated in μ_H (see Figure 2-15c). Figure 2-15d shows the variations of $S^2\sigma$ with E_g, from which enlarging E_g can greatly enhance peak $S^2\sigma$ but does not change the n_H^{opt} significantly.

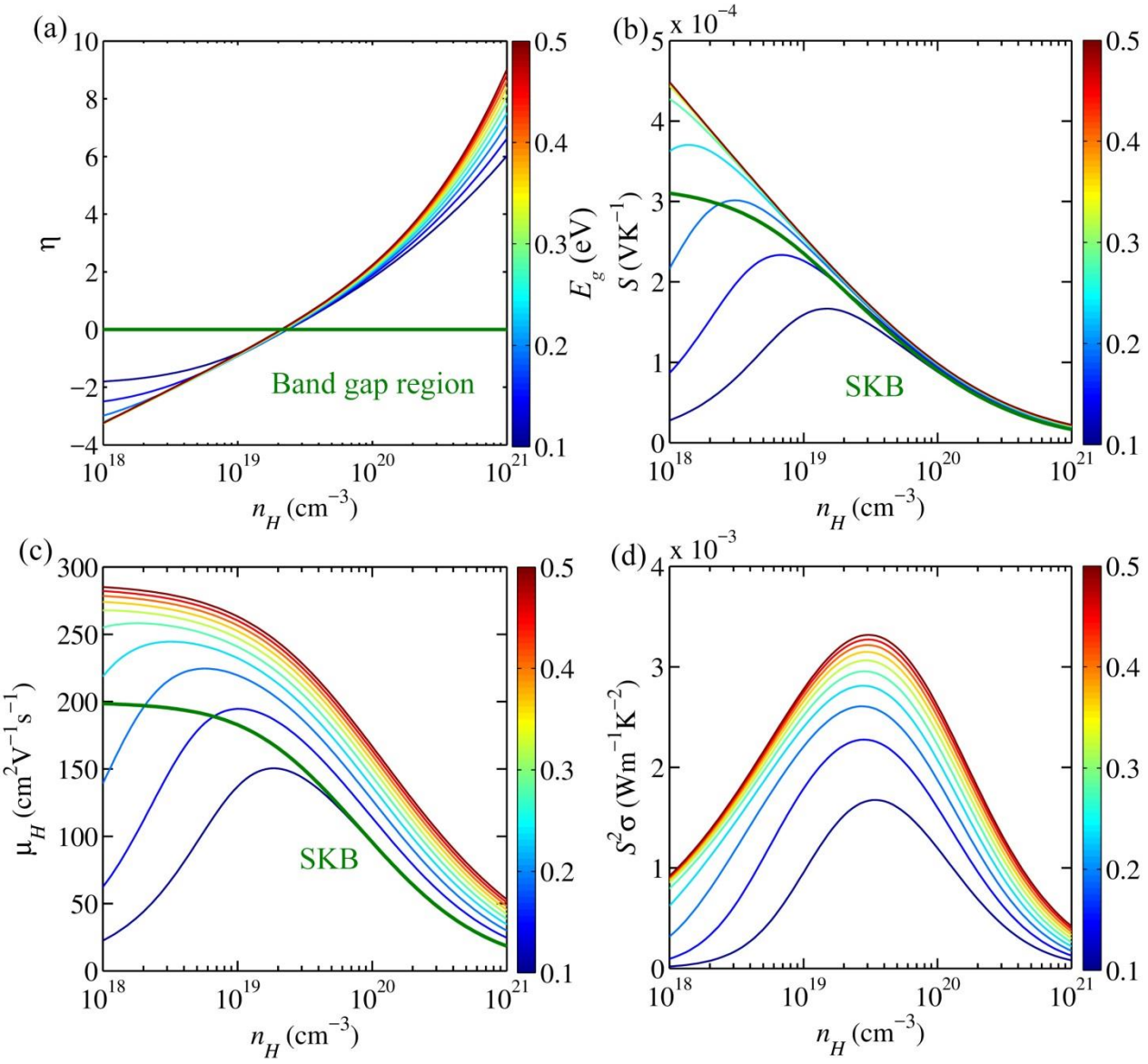

Figure 2-15 (a) Determined η with n_H ranging from 10^{18} to 10^{21} cm^{-3} for evenly selected ten E_g values from 0.1 to 0.5 eV as indicated by the colorbar in the right-hand side. Correspondingly calculated (b) S, (c) μ_H, and (d) $S^2\sigma$ as a function of n_H for different E_g values. The bold green lines in (b) and (c) are calculated using SKB model with E_g = 0.1 eV for S and μ_H, respectively.

Lastly, we study the E_{def}. Because E_{def} characterizes the strength of phonon scattering on free charger carriers, we anticipate that E_{def} would not affect η and bipolar conduction.

This has been confirmed by the determined η and the correspondingly calculated S, as shown in Figure 2-16a and b, respectively. However, E_{def} can greatly affect μ_H (refer to Figure 2-16c). As a consequently, large E_{def} lead to high $S^2\sigma$, which can be seen from Figure 2-16d.

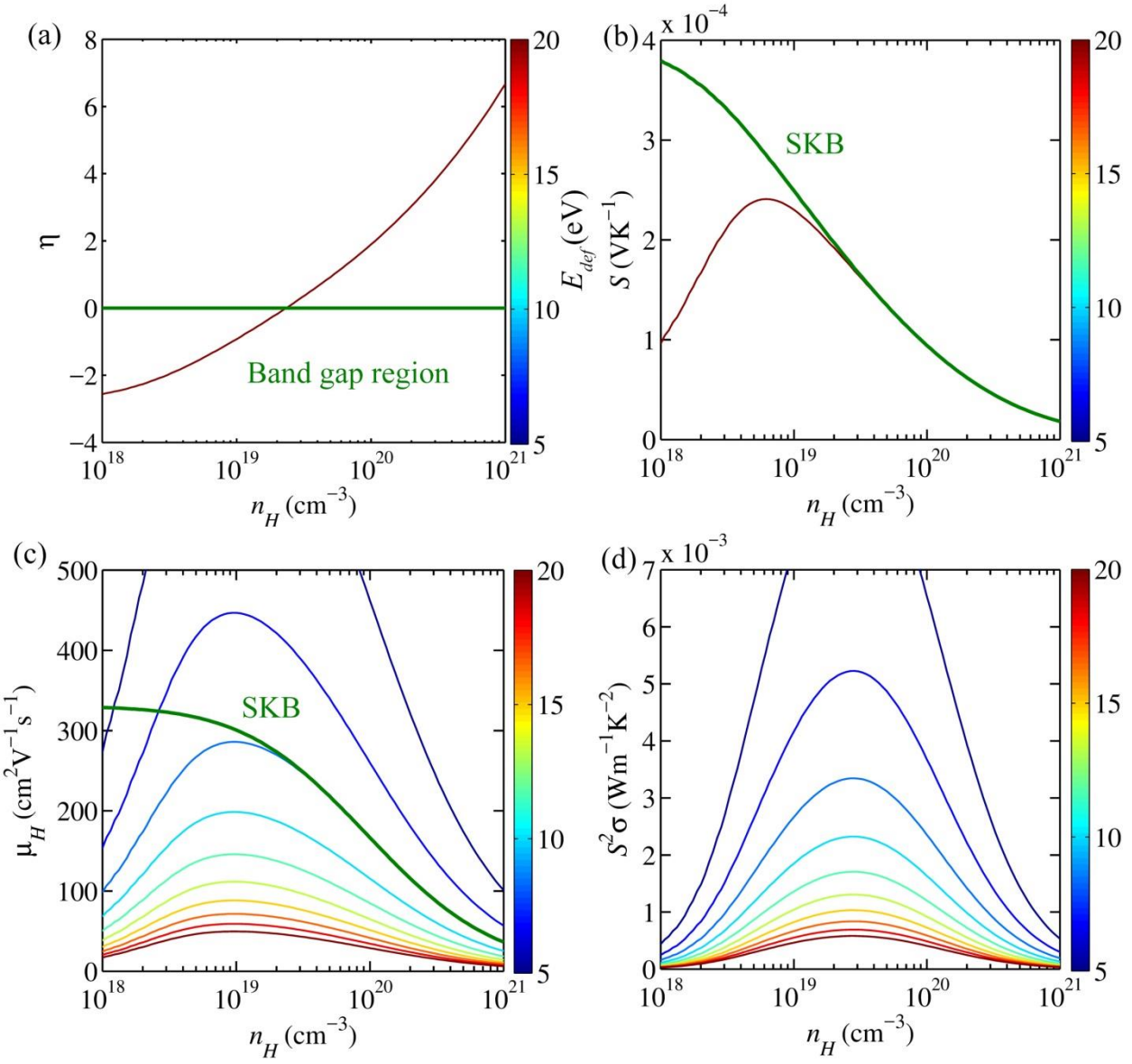

Figure 2-16 (a) Determined η with n_H ranging from 10^{18} to 10^{21} cm^{-3} for evenly selected ten E_{def} values from 5 to 20 eV as indicated by the colorbar in the right-hand side. Correspondingly calculated (b) S, (c) μ_H, and (d) $S^2\sigma$ as a function of n_H for different E_{def} values. The bold green lines in (b) and (c) are calculated using SKB model with E_{def} = 8 eV for S and μ_H, respectively.

It is well-documented that bipolar conduction is detrimental to the thermoelectric performance by contributing κ_{bi} and reducing S. Here, we want to emphasis the

importance in suppressing bipolar conduction by enlarging E_g. Figure 2-17a and b shows the calculated κ_{bi} and S as a function of n_H for evenly selected ten E_g values from 0.1 to 0.5 eV as indicated by the colorbar in the right-hand side. Because bipolar conduction is more notable at high temperature, the calculation covers the results at 300 K, 400 K, and 500 K. As can be seen, at high temperature, κ_{bi} is large but S is small, and enlarging E_g can greatly reduces κ_{bi} and increases S.

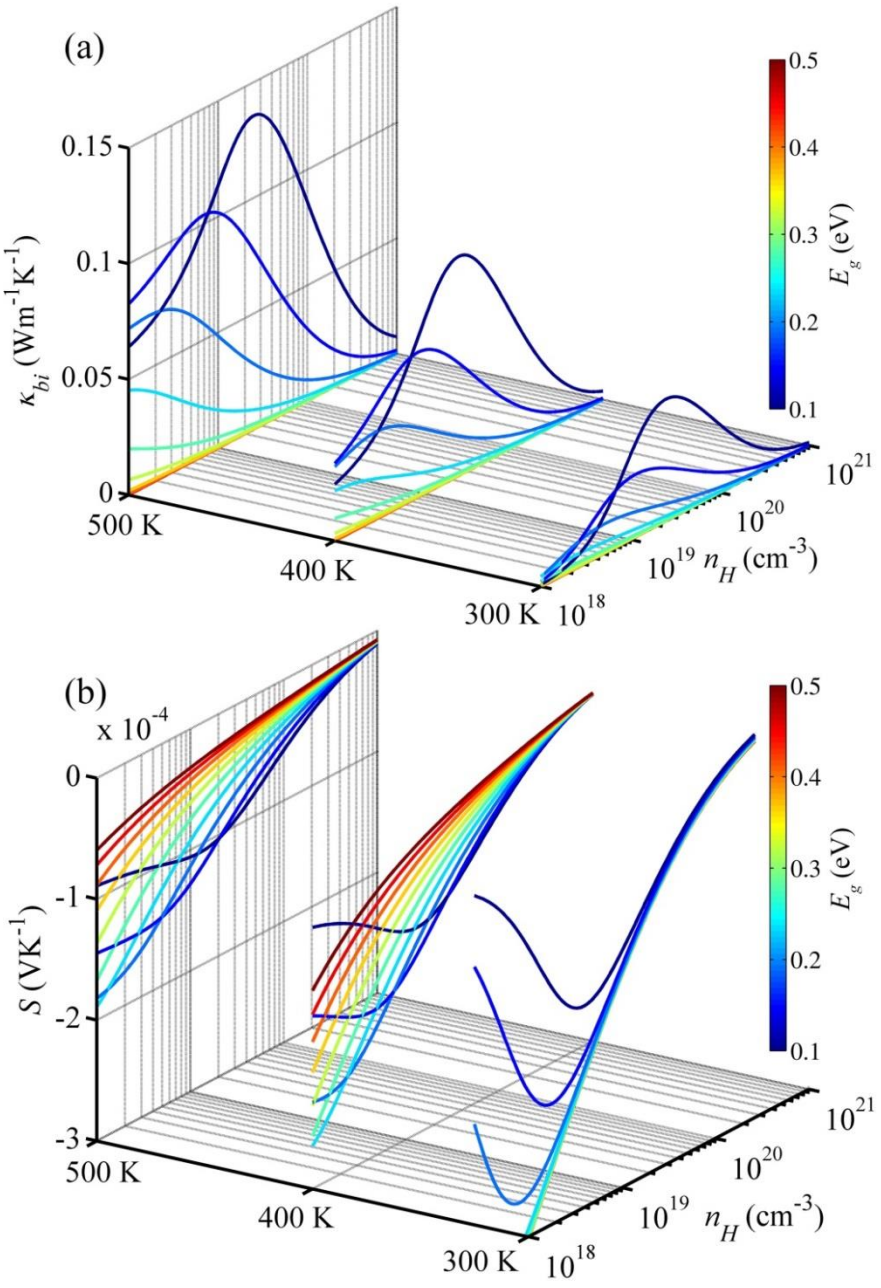

Figure 2-17 Calculated (a) κ_{bi}, and (b) S as a function of n_H at 300 K, 400 K and 500 K for evenly selected ten E_g values from 0.1 to 0.5 eV as indicated by the colorbar in the right-hand side.

Based on above discussions, we can see that m_d^*, E_g, and E_{def} can significantly affect the $S^2\sigma$, but only m_d^* is able to change the n_H^{opt}. To determine n_H^{opt}, we calculated the $S^2\sigma$ as functions of n_H and m_d^*, shown in Figure 2-18a. Based on this, the n_H^{opt} values corresponding to different m_d^* are shown in Figure 2-18b. To enhance thermoelectric performance, we want to ensure the real n_H approaching n_H^{opt}. The white curve in Figure 2-18b indicates the critical n_H^{opt} for Bi_2Te_3 families with different m_d^*.

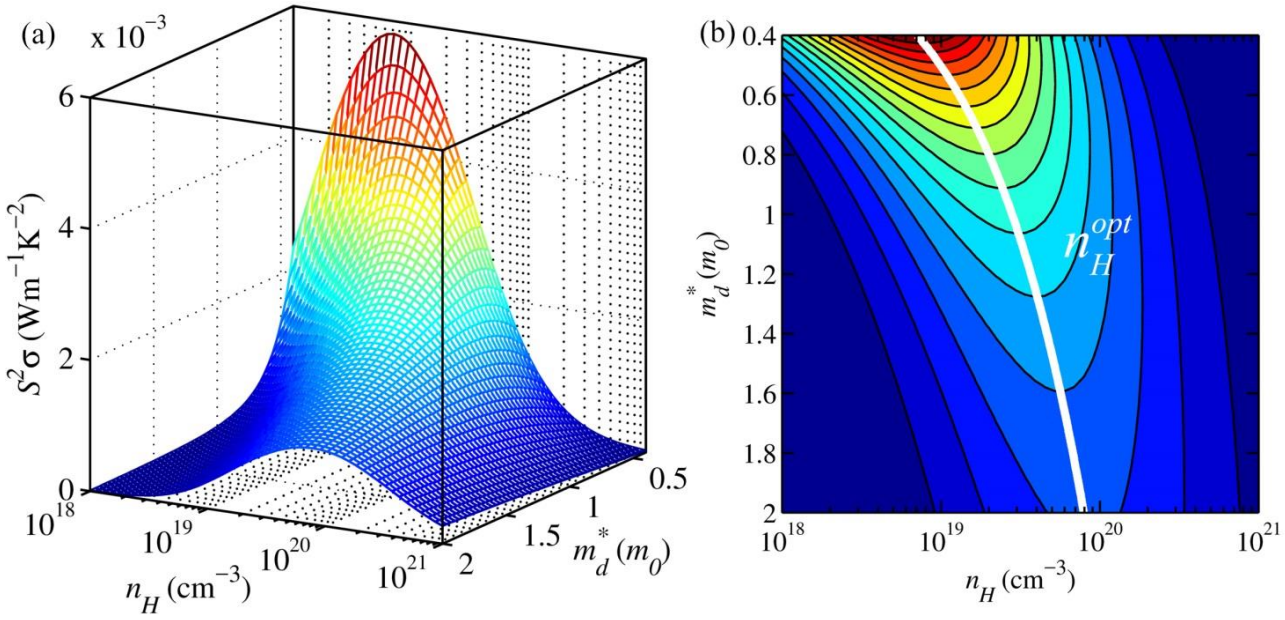

Figure 2-18 (a) Calculated $S^2\sigma$ as functions of n_H and m_d^*, and (b) the corresponding contour map with the white curve indicating the m_d^* dependent n_H^{opt}.

2.7.2 Phonon transport properties

According to the Debye-Callaway model,[134,135] κ_l can be calculated by

$$\kappa_l = \frac{k_B}{2\pi^2 \upsilon}\left(\frac{k_B T}{\hbar}\right)^3 \int_0^{\frac{\theta_D}{T}} \tau_{tot} \frac{z^4 \exp(z)}{\left[\exp(z)-1\right]^2} dz \tag{2.24}$$

The integrand item in conjunction with the coefficient of Equation (2.24) is the spectral lattice thermal conductivity (κ_s),[136] namely

$$\kappa_s = \frac{k_B}{2\pi^2 \upsilon}\left(\frac{k_B T}{\hbar}\right)^3 \tau_{tot} \frac{z^4 \exp(z)}{\left[\exp(z)-1\right]^2} \tag{2.25}$$

In the above equations, $z = \frac{\hbar\omega}{k_B T}$ (with ω denoting the phonon frequency) is the reduced phonon frequency, $\hbar$ is the reduced Plank constant, θ_D is the Debye temperature, $\upsilon = \left[\frac{1}{3}\left(\frac{1}{\upsilon_L^3} + \frac{2}{\upsilon_T^3}\right)\right]^{-1/3}$ (with υ_L and υ_T respectively denoting the longitudinal and transverse sound velocities) is the sound velocity, and τ_{tot} is the total relaxation time. The phonon scattering mechanisms generally include phonon-phonon Umklapp (U), electron-phonon (E), point defects (PD), and grain boundaries (B).[136,137] The relevant phonon relaxation times can be found in our previous study.[93] The total phonon relaxation time is calculated based on the Matthiessen rule.[66]

Figure 2-19a shows the phonon frequency (ω) dependent κ_s, determined respectively by models considering different scattering mechanisms at 300 K, including U+E, U+E+B, U+E+B+PD, U+E+B+PD+D. As can be seen, compared with the U+E model (considering scatterings from the Umklapp processes and electrons only), the introduction of grain boundaries in the U+E+B model gives lower κ_s, and the low-frequency Area (I) in Figure 2-19a represents the reduction in κ_l caused by grain boundaries. Similarly, the high-frequency Area (II) and the mid-frequency Area (III) in Figure 2-19a represent the further reductions in κ_l resulted from point defects and dislocations, respectively. Based on this, we conclude that grain boundaries, dislocations and point defects are effective to scatter low-, medium- and high-frequency phonons, respectively, as illustrated in **Figure 6**b. Overall, it is necessary to introduce multi-scale phonon scattering sources to achieve the wide-frequency phonon scattering, so that κ_l can be reduced significantly.

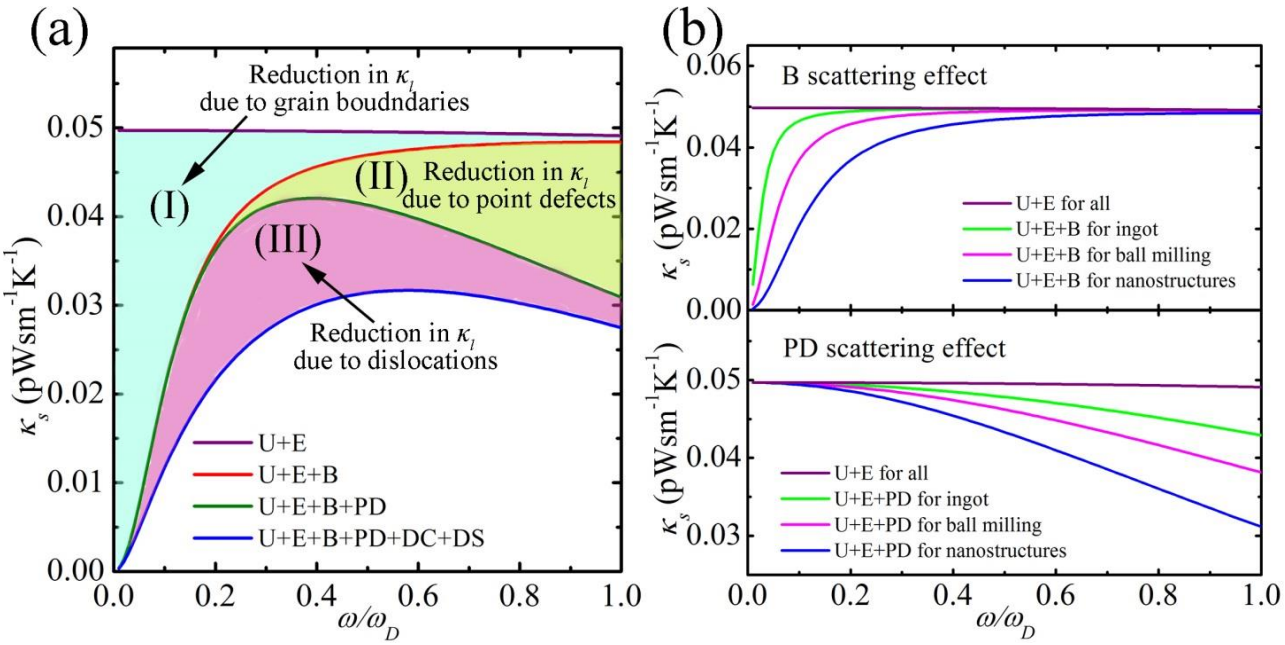

Figure 2-19 (a) Calculated room-temperature κ_s considering various phonon scatterings. (b) Schematic diagram showing the scattering of wide-frequency phonons by various sources.

2.8 Quantitatively Understanding the reported thermoelectric properties

Based on above modelling studies, we will combine the results with the reported thermoelectric properties for Bi_2Te_3-based materials to understand the underlying reasons and provide extra hints for further enhancing their performance.

2.8.1 Underlying reasons for the anisotropy behavior

Because of the strong anisotropic behavior, it is challenging to enhance *ZT* for n-type Bi_2Te_3. Here, based on the reported data for single crystals of both n-type and p-type Bi_2Te_3-based materials, we reveal the underlying reasons. Figure 2-20a and b show the data points of *S* and μ_H versus n_H for n-type $Bi_2Te_{3-x}Se_x$ single crystals,[106] respectively, and the corresponding curves are theoretical plots calculated with the determined m_d^* for *S*-n_H and E_{def} for μ_H -n_H. Note that the bold lines correspond to the average values, which are given in the figures. Figure 2-20c and d show the similar results for p-type $Bi_xSbe_{3-x}Te_3$ single crystals.[116] From Figure 2-20a and c, the data points of *S*-n_H for both n-type and p-type ones generally locate near the corresponding bold lines, which suggests that the difference of m_d^* along the *ab*-plane and along the *c* axis is small. From Figure 2-20b and

d, we can see that the data points of μ_H -n_H along the two perpendicular directions locate near different calculated bold lines. Therefore, the E_{def} values are significant different along the two directions.

Based on the calculated S-n_H and μ_H-n_H curves, we obtain the $S^2\sigma$-n_H curves. Figure 2-20e and f show the data points of $S^2\sigma$ versus n_H and the corresponding theoretical curves for n-type and p-type ones, respectively. As can be seen, the $S^2\sigma$ along the *ab*-plane is larger than that along the *c*-axis, and such anisotropy is stronger for n-type materials.

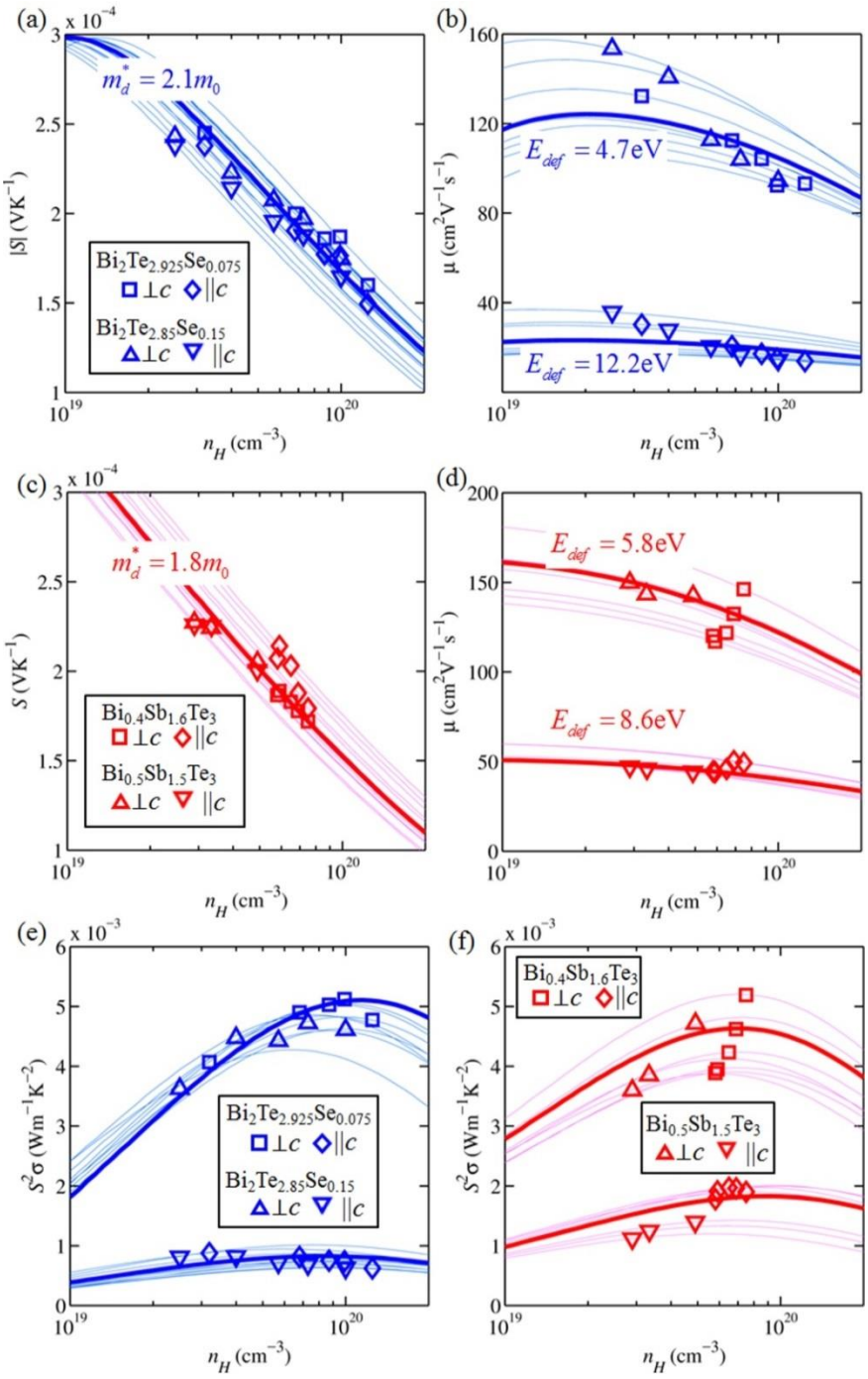

Figure 2-20 (a) Data points of |*S*| versus n_H compared with the calculated n_H dependent |*S*| curves, and (b) the reported data points of μ_H versus n_H compared with the calculated n_H dependent μ_H curves for n-type $Bi_2Te_{3-x}Se_x$ single crystals.[106] (c) Data points of *S* versus n_H compared with the calculated n_H dependent *S* curves, and (d) the reported data points of μ_H versus n_H compared with the calculated n_H dependent μ_H curves for p-type $Bi_xSbe_{3-x}Te_3$ single crystals.[116] (e) and (f) are the Data points of $S^2\sigma$ versus n_H compared with the calculated n_H dependent $S^2\sigma$ curves for n-type $Bi_2Te_{3-x}Se_x$ single crystals and p-type $Bi_xSbe_{3-x}Te_3$ single crystals, respectively.

The anisotropy of Bi_2Te_3 is mainly due to the different σ along *ab*-plane and *c*-axis. According to Equation (2.13), σ is determined by η, β, and $\frac{3e^2 N_v \hbar C_l}{\pi m_I^* E_{def}^2}$. The last term is related to the material's physical parameters, and defined it as Coe_σ. Based on the calculations discussed above, we determined the ratio of $Coe_{\sigma\perp c}/Coe_{\sigma\| c}$. Figure 2-21a shows the determined data points of $Coe_{\sigma\perp c}/Coe_{\sigma\| c}$ versus n_H for both n-type and p-type single crystals. The increasing trend of $Coe_{\sigma\perp c}/Coe_{\sigma\| c}$ versus n_H for n-type suggests that with increasing n_H the anisotropy between $\sigma \perp c$ and $\sigma \| c$ for n-type become larger. However, for p-type case, with increasing n_H $Coe_{\sigma\perp c}/Coe_{\sigma\| c}$ fluctuates, indicating that the anisotropy between $\sigma \perp c$ and $\sigma \| c$ for p-type is not affected be n_H. Figure 2-21b presents the data points of $Coe_{\sigma\perp c}/Coe_{\sigma\| c}$ versus $\sigma\perp c/\sigma\| c$, and the linear relation reveals that $\sigma\perp c/\sigma\| c$ for both n-type and p-type is mainly due to $Coe_{\sigma\perp c}/Coe_{\sigma\| c}$, which represents intrinsic characters of the materials. So, Fermi level and even band gap are not responsible for the anisotropy.

In addition, we studied the anisotropy of *S*. According to Equation (2.8), *S* is mainly related to η and β. For the single crystal with a given composition, band gap is nearly constant.[138] Therefore, we determined $\eta_{\sigma\perp c} - \eta_{\sigma\| c}$. Figure 2-21c shows the data points of $\eta_{\sigma\perp c} - \eta_{\sigma\| c}$ versus n_H. As can be seen, $\eta_{\sigma\perp c} - \eta_{\sigma\| c}$ for all n-type compositions and p-type $Bi_{0.5}Sb_{1.5}Te_3$ is nearly zero, indicating anisotropy of *S* in these materials is negligible. But, $\eta_{\sigma\perp c} - \eta_{\sigma\| c}$ for p-type $Bi_{0.4}Sb_{1.6}Te_3$ is around 0.3, which means $S_{\sigma\perp c}$ is slightly smaller than $S_{\sigma\| c}$ in this case. Figure 2-21d shows the the data points of $\eta_{\sigma\perp c} - \eta_{\sigma\| c}$ versus $S_{\sigma\perp c}/S_{\sigma\| c}$, from which the linear relation also suggests that the anisotropy of S is only related to η.

To sum up, we conclude that the anisotropy of σ is mainly related to Coe_σ, which is determined by the material intrinsic feature, and anisotropy of *S* is caused by η. The strong

anisotropy of n-type Bi_2Te_3 single crystals can be ascribed to the large difference of Coe_{σ} along the *ab*-plane and *c*-axis.

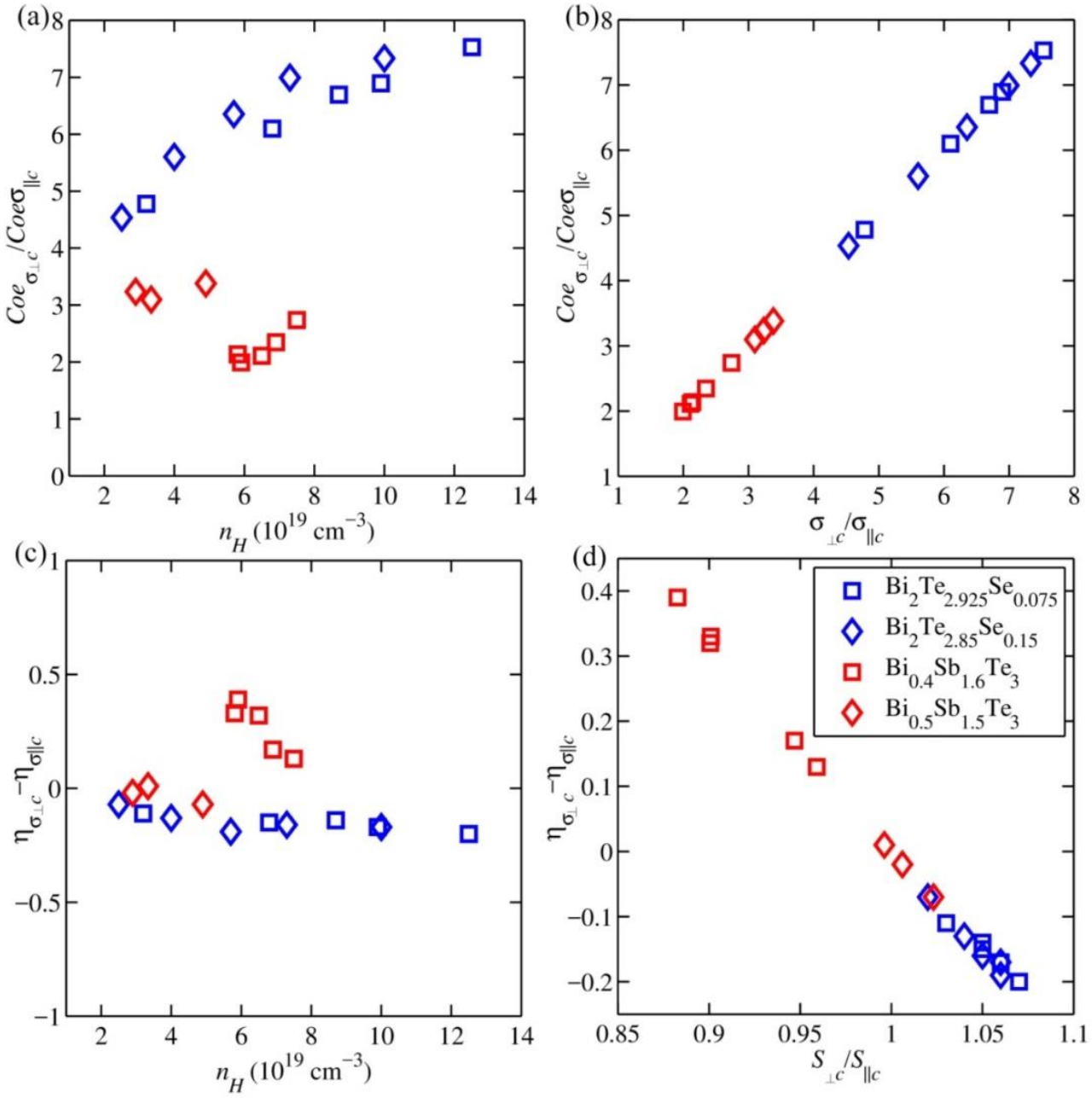

Figure 2-21 The determined $Coe_{\sigma\perp c}/Coe_{\sigma\|c}$ as a function of the corresponding (a) n_H and (b) $\sigma_{\perp c}/\sigma_{\|c}$, respectively. The determined $\eta_{\perp c} - \eta_{\|c}$ as a function of the corresponding (c) n_H and (d) $S_{\perp c}/S_{\|c}$, respectively. The data points are for both n-type $Bi_2Te_{3-x}Se_x$[106] and p-type single $Bi_xSb_{3-x}Te_3$ crystals.[116]

2.8.2 Understanding the enhanced for ternary phases

Here, we studied the fundamental reasons for the achieved enhancement in $S^2\sigma$ for the reported n-type $Bi_2Te_{3-x}Se_x$ phases. Figure 2-22a is the reported Se content dependent data points of n_H for $Bi_2Te_{3-x}Se_x$ ingots doped with I (wt 0.08%) (solid green data points),[107] $Bi_2Te_{3-x}Se_x$ processed by BM+HP+HD (hollow red data points),[75] and $Bi_2Te_{3-x}Se_x$ single crystals (hollow blue data points).[106] Considering the reported n_H, S, and μ_H data, we determined η, m_d^*, and E_{def} for all compositions using the Kane band model with CB and VB, shown in Figure 2-22b, c and d, respectively. On this basis, we calculated the theoretical curves of μ_H and S as a function of n_H for each data point with the correspondingly determined m_d^*, and E_{def}, exhibited in Figure 2-22e and f, respectively, in which the corresponding data points were also presented. The compassions of data points with the theoretical curves suggest that our determinations for m_d^* and E_{def} are sufficiently precise because the data points locate on the relevant curves, and the values of m_d^* and E_{def} strongly depends on the compositions and the material fabrication methods.

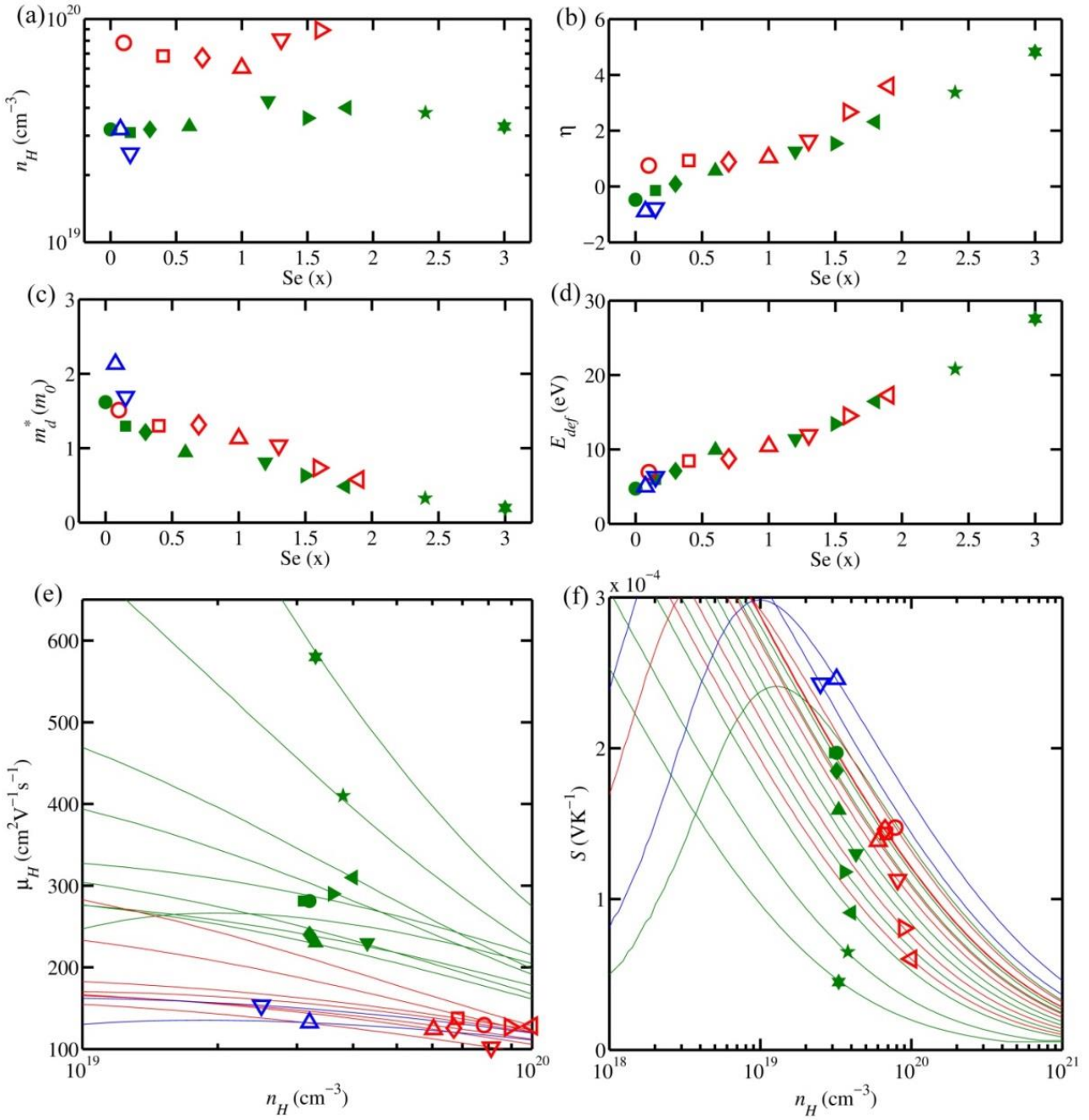

Figure 2-22 The Se content dependent data points of (a) n_H, (b) determined η, (c) determined m_d^*, and (d) determined E_{def}. The n_H dependent data points of (e) μ_H, and (f) S compared with the theoretical curves of μ_H versus n_H, and S versus n_H calculated with the correspondingly determined E_{def}, and m_d^*. In all figures, the solid green data points are from $Bi_2Te_{3-x}Se_x$ ingots doped with I (wt 0.08%),[107] the hollow red data points are from $Bi_2Te_{3-x}Se_x$ processed by BM+HP+HD,[75] and the hollow blue data points are from $Bi_2Te_{3-x}Se_x$ single crystals.[106]

The combination of theoretical curves of μ_H versus n_H and S versus n_H enables to calculate the theoretical curves of $S^2\sigma$ versus n_H, shown in Figure 2-23a, in which the

corresponding data points are also plotted. Moreover, according our previous discussions, the n_H^{opt} mainly depends on m_d^*. To examine the relations of $S^2\sigma$ peak with n_H, Figure 2-23b demonstrates the data points of determined m_d^* and n_H for all studied materials, compared with the previously determined curve of m_d^* versus n_H^{opt}. As can be seen, the data points locate closer to the grey curve in Figure 2-23b, it is more likely for the data points in Figure 2-23a approach to the peaks of corresponding theoretical curves of $S^2\sigma$ versus n_H. However, the different $S^2\sigma$ values for the different data points cannot be fully explained by m_d^*. For instance, the green hexagon star with m_d^* of ~0.2m_0 shows $S^2\sigma$ of ~7×10^{-4} Wm^{-1}K^{-2}, which is much smaller than $S^2\sigma$ of ~6×10^{-3} Wm^{-1}K^{-2} for the round disk with m_d^* of ~1.7m_0. Here, we cannot ascribe the enhanced $S^2\sigma$ to the decreased m_d^*.

Therefore, we should develop new concepts to understand the enhancement in $S^2\sigma$. As reported in our previous study,[93] we defined the λE_{def} (with $\lambda = \sqrt{m_I^*/m_0}$), serving as the decoupling factor for S and σ, and we concluded that reducing λE_{def} is the key to enhance $S^2\sigma$, provided that η has been sufficiently optimized. Figure 2-23c shows the data points of determined λE_{def} dependent $S^2\sigma$, compared with the theoretical curves of $S^2\sigma$ versus λE_{def} in the range of 2 – 6 eV. Note that theoretical curves of $S^2\sigma$ versus λE_{def} were calculated according to the η^{opt}, and η^{opt} is affected by the E_g; therefore, for each composition with different E_g, there is a unique theoretical curve of $S^2\sigma$ versus λE_{def}. Considering the small difference of these theoretical curves for various composition, in Figure 2-23c we only plotted the representative ones for Bi_2Te_3 ingot, $Bi_2Te_{2.4}Se_{0.6}$ ingot and Bi_2Se_3 ingot. Figure 2-23d presents the data points of λE_{def} against η, compared with the η^{opt} values, indicated by the vertical lines. As can be seen, small λE_{def} indeed results in large $S^2\sigma$, and the small different between determined η and the corresponding η^{opt} in Figure 2-23d allows the data point in Figure 2-23c to approach the corresponding theoretical curve.

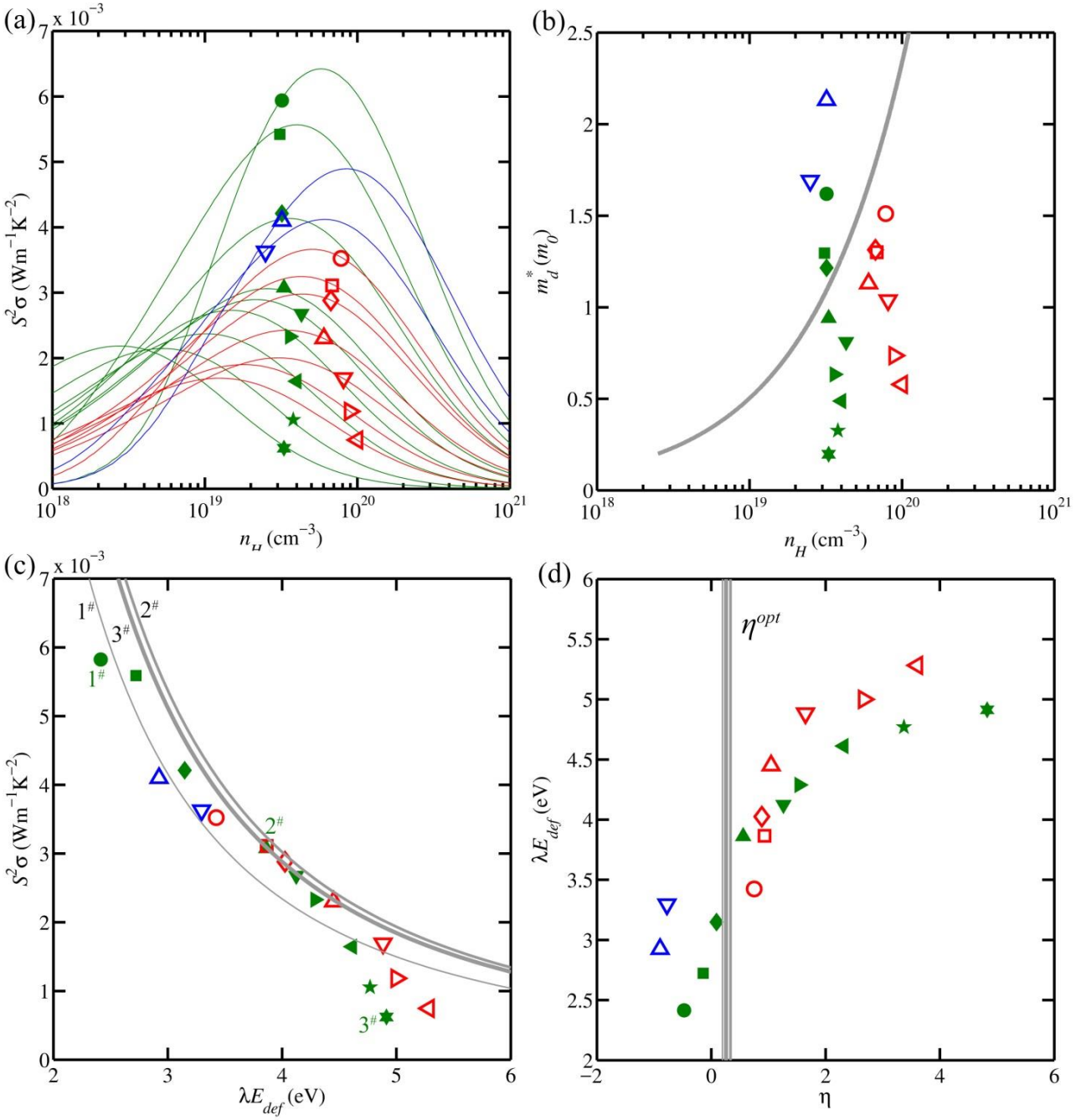

Figure 2-23 (a) Data points of n_H dependent $S^2\sigma$ compared with the theoretical curves of $S^2\sigma$ versus n_H calculated with correspondingly determined E_{def}, and m_d^*. (b) Determined data points of n_H dependent m_d^* with the grey curve indicating the m_d^* as a function of n_H^{opt}. (c) Data points of λE_{def} dependent $S^2\sigma$ compared with the theoretical curves of $S^2\sigma$ versus λE_{def} for compositions of Bi_2Te_3 (labelled with $1^{\#}$), $Bi_2Te_{2.4}Se_{0.6}$ (labelled with $2^{\#}$) and Bi_2Se_3 (labelled with $3^{\#}$) calculated with corresponding η^{opt}. (d) Determined data points of λE_{def} versus η. In all figures, the solid green data points are from $Bi_2Te_{3-x}Se_x$ ingots doped

with I (wt 0.08%),[107] the hollow red data points are from $Bi_2Te_{3-x}Se_x$ processed by BM+HP+HD,[75] and the hollow blue data points are from $Bi_2Te_{3-x}Se_x$ single crystals.[106]

2.9 Unsolved issues and opportunities

Bi_2Te_3 as a thermoelectric material working at room temperature has been a hot topic since 1950. Although *ZT* value of Bi_2Te_3 has been approved remarkably by band engineering and nanostructuring, there are still some problems, which should be tackled to further optimize thermoelectric properties.

(1) Inefficient fabrication of nanostructured Bi_2Te_3

Nanostructured Bi_2Te_3 has been successfully produced by physical methods as well as chemical methods. The major disadvantage of physical fabrication is difficult to control the grain size and morphology; therefore, quantum well confinement relying on the size of low-dimensional materials cannot fully take effect to improve electron transport properties. In the case of chemical methods, solvothermal synthesis has been widely applied to prepare Bi_2Te_3. Although the morphology of products can be controlled, long manufacturing duration and low product yield limit this method to produce commercial thermoelectric device. There is no controllable, low-cost, high quality, and high quantity synthesis process for nanostructured Bi_2Te_3 fabrication.

(2) Difficult to achieve thermoelectric materials with higher electrical conductivity and lower thermal conductivity systems simultaneously

As a good thermoelectric material, it should exhibit higher electrical conductivity as well as lower thermal conductivity simultaneously. However, charger carriers can also transport heat, which leads to an increase in electronic thermal conductivity. It is difficult to fabricate a low-dimensional material with higher electrical conductivity and lower thermal conductivity systems simultaneously. There is a compromise between these thermoelectric properties. An optimal carrier concentration is needed to achieve a net increase in *ZT* value.

(3) Insufficient detailed investigations on the growth mechanisms of nanostructured systems

Although low-dimensional materials, such as nanodots, nanosheets and nanowires have been successfully synthesized, the growth mechanism for these nanostructures with

various geometries is not clearly understood. Low-dimensional materials have different electrical DOS (2D: step shape; 1D: hill shape and 0D: Delta function shape); thus the relation between thermoelectric properties is different from that for bulk materials. Then it is possible to achieve a significant enhancement in *ZT* value. Nanostructures with diverse morphology would be important to further increase *ZT*. The growth mechanism for the currently owned structures will help us to develop new nanostructures.

(4) Scarcity in investigation on band engineering methodology to form n-type or p-type semiconductor nanomaterials

When both electrons and holes simultaneously contribute to electrical conduction, the Seebeck coefficient becomes very small due to the reduction in the asymmetry of differential conductivity. P-type and n-type thermoelectric materials will work together to form a thermoelectric couple in application. The thermoelectric device should be made from one kind of material which shows p-type and n-type. Although tuning doping level can change the type of semiconductor, the uniqueness of charge carriers needs precise control of doping level, which need further investigated.

Based on the issues in the development of nanostructured Bi_2Te_3 thermoelectric materials with enhanced *ZT* values, this research project will aim at the following contents.

(1) Exploiting microwave-assisted solvothermal method to synthesize Bi_2Te_3 with controllable nanostructures

We adopt the solvothermal method heated by microwave radiation to synthesize nanostructured Bi_2Te_3 -based thermoelectric family. The duration of this process is just over 15 minutes and the product yield has been increased as well. This is the outstanding advantage of the microwave-assisted solvothermal method, and it is possible to produce low-cost commercialized thermoelectric device. We attempt to optimize the morphology of Bi_2Te_3 sample by modifying reaction conditions. Besides, we will develop a green synthesis strategy without surfactant for the thermoelectric samples preparation.

(2) Extending the synthesis strategy to fabricate ternary thermoelectric materials

Due to similar layered crystal structures of Bi_2Te_3, Bi_2Se_3 and Sb_2Te_3, Se and Sb replacement can modify the crystalline structure and electronic DOS in Bi_2Te_3. Therefore, we extend the microwave-assisted method to produce ternary thermoelectric materials including $Bi_2Te_{3-x}Se_x$ and $Bi_{2-x}Sb_xTe_3$. Likewise, the grain size and the dimensional

distribution of these ternary products will be optimized via changing the reaction conditions and precursor.

(3) Doping of Bi_2Te_3 based nanostructures

After acquiring the Bi_2Te_3 based nanostructured thermoelectric materials including binary and ternary candidates, doping these layered structures will be carried out to enhance their thermoelectric properties. In order to further tune the electronic DOS and energy band gap, elements such as Pb Ag, Cu and Fe will be primarily selected.

2.10 References

(1) Nolas, G. S.; Poon, J.; Kanatzidis, M. Recent Developments in Bulk Thermoelectric Materials. *Mrs. Bull.* **2006**, 31, 199-205.

(2) Radousky, H. B.; Liang, H. Energy Harvesting: an Integrated View of Materials, Devices and Applications. *Nanotechnology* **2012**, 23.

(3) Bell, L. E. Cooling, Heating, Generating Power, and Recovering Waste Heat with Thermoelectric Systems. *Science* **2008**, 321, 1457-1461.

(4) Riffat, S. B.; Ma, X. L. Thermoelectrics: a Review of Present and Potential Applications. *Appl. Therm. Eng.* **2003**, 23, 913-935.

(5) Tritt, T. M.; Subramanian, M. A. Thermoelectric Materials, Phenomena, and Applications: a Bird's Eye View. *Mrs. Bull.* **2006**, 31, 188-194.

(6) Prasad, N. S.; Trivedi, S. B.; Palosz, W.; Rosemeier, R.; Rosemeier, C.; Kutcher, S.; Mayers, D.; Taylor, P. J.; Maddux, J.; Singh, J. Development of PbTe Material for Advanced Thermoelectric Power Generation. In *Energy Harvesting and Storage: Materials, Devices, and Applications Iii*, Dhar, N. K.; Wijewarnasuriya, P. S.; Dutta, A., Eds. 2012; Vol. 8377.

(7) Vining, C. B. An Inconvenient Truth about Thermoelectrics. *Nat. Mater.* **2009**, 8, 83-85.

(8) Ibrahim, E. A.; Szybist, J. P.; Parks, J. E. Enhancement of Automotive Exhaust Heat Recovery by Thermoelectric Devices. *P. I. Mech. Eng. D-j. Automob. Eng.* **2010**, 224, 1097-1111.

(9) Li, M.; Xu, S.; Chen, Q.; Zheng, L. Thermoelectric-Generator-Based DC-DC Conversion Networks for Automotive Applications. *J. Electron. Mater.* **2011**, 40, 1136-1143.

(10) Schierle-Arndt, K.; Hermes, W. An Opportunity for the Utilization of Waste Heat Thermoelectrics. *Chem. Unserer. Zeit.* **2013**, 47, 92-101.

(11) Bray, J. W.; Arik, M.; Weaver, S. E. Heating/Cooling System Includes Thermoelectric Device Comprising Two Thermoelements Disposed Between Two Substrates, in Which at Least One of Thermoelements Includes Thermally Insulating and Electrically Conducting Tunneling Element. US2008017237-A1.

(12) Hu, L. F.; Wu, L. M.; Liao, M. Y.; Fang, X. S. High-Performance $NiCo_2O_4$ Nanofilm Photodetectors Fabricated by An Interfacile Self-Assembly Strategy. *Adv. Mater.* **2011**, 23, 1988-1992.

(13) Chen, G. Theoretical Efficiency of Solar Thermoelectric Energy Generators. *J. Appl. Phys.* **2011**, 109.

(14) Friedensen, V. P. Space Nuclear Power: Technology, Policy, and Risk Considerations in Human Missions to Mars. *Acta Astronaut.* **1998**, 42, 395-409.

(15) Yang, J. H.; Caillat, T. Thermoelectric materials for space and automotive power generation. *Mrs Bulletin* **2006**, 31, 224-229.

(16) O'Brien, R. C.; Ambrosi, R. M.; Bannister, N. P.; Howe, S. D.; Atkinson, H. V. Safe Radioisotope Thermoelectric Generators and Heat Sources for Space Applications. *J. Nucl. Mater.* **2008**, 377, 506-521.

(17) Kraemer, D.; Poudel, B.; Feng, H.; Caylor, J. C.; Yu, B.; Yan, X.; Ma, Y.; Wang, X.; Wang, D.; Muto, A.; McEnaney, K.; Chiesa, M.; Ren, Z.; Chen, G. High-Performance Flat-Panel Solar Thermoelectric Generators with High Thermal Concentration. *Nat. Mater.* **2011**, 10, 532-538.

(18) Wei, J.; Xiong, L.; Wang, H. The Study of Thermoelectric Power Generation in the Cooling of Fin and Vibration Heat Pipe. In *2012 International Conference on Future Electrical Power and Energy System, Pt B*, Xiong, J., Ed. 2012; Vol. 17, pp 1570-1577.

(19) Tong, X. C. Thermoelectric Cooling through Thermoelectric Materials. In *Advanced Materials for Thermal Management of Electronic Packaging*, 2011; Vol. 30, pp 477-525.

(20) da Silva, L. W.; Kaviany, M.; DeHennis, A.; Dyck, J. S.; Ieee. *Micro Thermoelectric Cooler Fabrication: Growth and Characterization of Patterned Sb_2Te_3 and Bi_2Te_3 Films*. **2003**; p 665-668.

(21) Chowdhury, I.; Prasher, R.; Lofgreen, K.; Chrysler, G.; Narasimhan, S.; Mahajan, R.; Koester, D.; Alley, R.; Venkatasubramanian, R. on-Chip Cooling by Superlattice-Based Thin-Film Thermoelectrics. *Nat. Nano.* **2009**, 4, 235-238.

(22) DiSalvo, F. J. Thermoelectric Cooling and Power Generation. *Science* **1999**, 285, 703-706.

(23) Boulouz, A.; Chakraborty, S.; Giani, A.; Delannoy, F. P.; Boyer, A.; Schumann, J. Transport Properties of V-VI Semiconducting Thermoelectric BiSbTe Alloy Thin Films and Their Application to Micromodule Peltier Devices. *J. Appl. Phys.* **2001**, 89, 5009-5014.

(24) Ovsyannikov, S. V.; Shchennikov, V. V.; Ponosov, Y. S.; Gudina, S. V.; Guk, V. G.; Skipetrov, E. P.; Mogilenskikh, V. E. Application of the High-Pressure Thermoelectric Technique for Characterization of Semiconductor Microsamples: PbX-Based Compounds. *J. Phys. D. Appl. Phys.* **2004**, 37, 1151-1157.

(25) Nenghabi, E. N.; Myles, C. W. First-Principles Calculations of the Vibrational and Thermal Properties of the Type-I Clathrates $Ba_8Ga_{16}SixGe_{30-x}$ and $Sr_8Ga_{16}Si_xGe_{30-x}$. *Phys. Rev. B* **2008**, 78.

(26) Sales, B. C.; Mandrus, D.; Williams, R. K. Filled Skutterudite Antimonides: a New Class of Thermoelectric Materials. *Science* **1996**, 272, 1325-1328.

(27) Hicks, L.; Dresselhaus, M. Effect of Quantum-Well Structures on the Thermoelectric Figure of Merit. *Phys. Rev. B* **1993**, 47, 12727-12731.

(28) Chen, G.; Dresselhaus, M. S.; Dresselhaus, G.; Fleurial, J. P.; Caillat, T. Recent Developments in Thermoelectric Materials. *Int. Mater. Rev.* **2003**, 48, 45-66.

(29) Chen, Z.-G.; Han, G.; Yang, L.; Cheng, L.; Zou, J. Nanostructured Thermoelectric Materials: Current Research and Future Challenge. *Prog. Nat. Sci.* **2012**, 22, 535-549.

(30) Steele, W. H. A New Thermoelectric Phenon. *Science (New York, N.Y.)* **1893**, 22, 256-256.

(31) Geballe, T. H.; Hull, G. W. Seebeck Effect in Germanium. *Phys. Rev.* **1954**, 94, 1134-1140.

(32) Yamanashi, M. A New Approach to Optimum Design in Thermoelectric Cooling Systems. *J. Appl. Phys.* **1996**, 80, 5494-5502.

(33) Huang, B. J.; Chin, C. J.; Duang, C. L. A Design Method of Thermoelectric Cooler. *Int. J. Refrig.* **2000**, 23, 208-218.

(34) Hicks, L.; Dresselhaus, M. Thermoelectric Figure of Merit of a One-Dimensional Conductor. *Phys. Rev. B* **1993**, 47, 16631-16634.

(35) Sofo, J. O.; Mahan, G. D. Optimum Band Gap of a Thermoelectric Material. *Phys. Rev. B* **1994**, 49, 4565-4570.

(36) Goldsmid, H. J. On the Thermal and Electrical Conductivity of Semiconductor. *P. Roy. Soc. Lond. B* **1954**, 67, 360-363.

(37) Levin, A. J.; Black, M. R.; Dresselhaus, M. S. Indirect L to T Point Optical Transition in Bismuth Nanowires. *Phys. Rev. B* **2009**, 79.

(38) Dismukes, J. P.; Ekstrom, L.; Steigmeier, E. F.; Kudman, I.; Beers, D. S. Thermal and Electrical Properties of Heavily Doped Ge-Si Alloys up to 1300°K. *J. Appl. Phys.* **1964**, 35, 2899.

(39) Luk'yanova, L. N.; Kutasov, V. A.; Konstantinov, P. P. Multicomponent n-$(Bi,Sb)_2(Te,Se,S)_3$ Solid Solutions with Different Atomic Substitutions in the Bi and Te Sublattices. *Phys. Solid State* **2008**, 50, 2237-2244.

(40) Sales, B. C.; Mandrus, D.; Chakoumakos, B. C.; Keppens, V.; Thompson, J. R. Filled Skutterudite Antimonides: Electron Crystals and Phonon Glasses. *Phys. Rev. B* **1997**, 56, 15081-15089.

(41) Nolas, G. S.; Morelli, D. T.; Tritt, T. M. Skutterudites: a Phonon-Glass-Electron Crystal Approach to Advanced Thermoelectric Energy Conversion Applications. *Annu. Rev. Mater. Sci.* **1999**, 29, 89-116.

(42) Sales, B. C.; Chakoumakos, B. C.; Mandrus, D.; Sharp, J. W. Atomic displacement parameters and the lattice thermal conductivity of clathrate-like thermoelectric compounds. *Journal of Solid State Chemistry* **1999**, 146, 528-532.

(43) Paschen, S.; Tran, V. H.; Baenitz, M.; Carrillo-Cabrera, W.; Grin, Y.; Steglich, F. Clathrate Ba_6Ge_{25}: Thermodynamic, magnetic, and transport properties. *Physical Review B* **2002**, 65.

(44) Chakoumakos, B. C.; Sales, B. C.; Mandrus, D. G.; Nolas, G. S. Structural Disorder and Thermal Conductivity of the Semiconducting Clathrate $Sr_8Ga_{16}Ge_{30}$. *J. Alloy. Compd.* **2000**, 296, 80-86.

(45) Uher, C.; Yang, J.; Hu, S.; Morelli, D. T.; Meisner, G. P. Transport Properties of Pure and Doped MNiSn (M=Zr, Hf). *Phys. Rev. B* **1999**, 59, 8615-8621.

(46) Cui, J. L.; Mao, L. D.; Chen, D. Y.; Qian, X.; Liu, X. L.; Yang, W. Effects of a Cu-Contained Compound on the Microstructures and Thermoelectric Properties of Zn-Sb Based Alloys. *Current Applied Physics* **2009**, 9, 713-716.

(47) Zhang, L. T.; Tsutsui, M.; Ito, K.; Yamaguchi, M. Effects of ZnSb and Zn Inclusions on the Thermoelectric Properties of beta-Zn_4Sb_3. *J. Alloy. Compd.* **2003**, 358, 252-256.

(48) Pedersen, B. L.; Birkedal, H.; Iversen, B. B.; Nygren, M.; Frederiksen, P. T. Influence of Sample Compaction on the Thermoelectric Performance of Zn_4Sb_3. *Appl. Phys. Lett.* **2006**, 89, 242108.

(49) Mozharivskyj, Y.; Pecharsky, A. O.; Bud'ko, S.; Miller, G. J. Promising Thermoelectric Material: Zn_4Sb_3 or $Zn_{6-\square}Sb_5$. Its Composition, Structure, Stability, and Polymorphs. Structure and Stability of $Zn_{1-\square}$ Sb. *Chem. Mater.* **2004**, 16, 1580-1589.

(50) Ur, S. C.; Nash, P.; Kim, H. Thennoelectric Properties of Zn_4Sb_3 Processed by Sinter-Forging. *Mater. Lett.* **2004**, 58, 2937-2941.

(51) Stiewe, C.; Dasgupta, T.; Boettcher, L.; Pedersen, B.; Mueller, E.; Iversen, B. Thermoelectric Characterization of Zone-Melted and Quenched Zn_4Sb_3. *J. Electron. Mater.* **2010**, 39, 1975-1980.

(52) Toberer, E. S.; May, A. F.; Snyder, G. J. Zintl Chemistry for Designing High Efficiency Thermoelectric Materials†‡. *Chem. Mater.* **2010**, 22, 624-634.

(53) Nagira, T.; Ito, M.; Katsuyama, S.; Majma, K.; Nagai, H.; China Industrial Association Of Power Sources; China, I.; Association Of Power, S. *Effect of Na-site Partial Substitutions on the Thermoelectric Properties of Layered Oxide* $Na_xCo_2O_4$. **2001**; p 164-167.

(54) Rowe, D. M. *CRC handbook of thermoelectrics*. CRC Press: New York, **1995**.

(55) Joshi, G.; Lee, H.; Lan, Y.; Wang, X.; Zhu, G.; Wang, D.; Gould, R. W.; Cuff, D. C.; Tang, M. Y.; Dresselhaus, M. S.; Chen, G.; Ren, Z. Enhanced Thermoelectric Figure-of-

Merit in Nanostructured *p*-Type Silicon Germanium Bulk Alloys. *Nano Lett.* **2008**, 8, 4670-4674.

(56) Liu, W.-S.; Zhang, Q.; Lan, Y.; Chen, S.; Yan, X.; Zhang, Q.; Wang, H.; Wang, D.; Chen, G.; Ren, Z. Thermoelectric Property Studies on Cu-Doped *n*-Type $Cu_xBi_2Te_{2.7}Se_{0.3}$ Nanocomposites. *Adv. Energy Mater.* **2011**, 1, 577-587.

(57) Yan, X.; Poudel, B.; Ma, Y.; Liu, W. S.; Joshi, G.; Wang, H.; Lan, Y.; Wang, D.; Chen, G.; Ren, Z. F. Experimental Studies on Anisotropic Thermoelectric Properties and Structures of *n*-Type $Bi_2Te_{2.7}Se_{0.3}$. *Nano Lett.* **2010**, 10, 3373-3378.

(58) Rhyee, J.-S.; Lee, K. H.; Lee, S. M.; Cho, E.; Kim, S. I.; Lee, E.; Kwon, Y. S.; Shim, J. H.; Kotliar, G. Peierls Distortion as a Route to High Thermoelectric Performance in $In_4Se_{3-\square}$ Crystals. *Nature* **2009**, 459, 965-968.

(59) Tang, Y.; Qiu, Y.; Xi, L.; Shi, X.; Zhang, W.; Chen, L.; Tseng, S.-M.; Chen, S.-w.; Snyder, G. J. Phase Diagram of In-Co-Sb System and Thermoelectric Properties of In-Containing Skutterudites. *Energy Environ. Sci.* **2014**, 7, 812-819.

(60) Tang, Y.; Gibbs, Z. M.; Agapito, L. A.; Li, G.; Kim, H.-S.; Nardelli, M. B.; Curtarolo, S.; Snyder, G. J. Convergence of Multi-Valley Bands as the Electronic Origin of High Thermoelectric Performance in $CoSb_3$ Skutterudites. *Nat Mater* **2015**, 14, 1223-1228.

(61) Wang, H.; Schechtel, E.; Pei, Y.; Snyder, G. J. High Thermoelectric Efficiency of n-type PbS. *Adv. Energy Mater.* **2013**, 3, 488-495.

(62) Hu, L.; Wu, H.; Zhu, T.; Fu, C.; He, J.; Ying, P.; Zhao, X. Tuning Multiscale Microstructures to Enhance Thermoelectric Performance of *n*-Type Bismuth-Telluride-Based Solid Solutions. *Adv. Energy Mater.* **2015**, 5, 1500411.

(63) Xie, W.; Tang, X.; Yan, Y.; Zhang, Q.; Tritt, T. M. Unique Nanostructures and Enhanced Thermoelectric Performance of Melt-Spun BiSbTe Alloys. *Appl. Phys. Lett.* **2009**, 94, 102111.

(64) Biswas, K.; He, J.; Blum, I. D.; Wu, C. I.; Hogan, T. P.; Seidman, D. N.; Dravid, V. P.; Kanatzidis, M. G. High-performance Bulk Thermoelectrics with All-Scale Hierarchical Architectures. *Nature* **2012**, 489, 414-418.

(65) Pei, Y.; Shi, X.; LaLonde, A.; Wang, H.; Chen, L.; Snyder, G. J. Convergence of Electronic Bands for High Performance Bulk Thermoelectrics. *Nature* **2011**, 473, 66-69.

(66) Kim, S. I.; Lee, K. H.; Mun, H. A.; Kim, H. S.; Hwang, S. W.; Roh, J. W.; Yang, D. J.; Shin, W. H.; Li, X. S.; Lee, Y. H.; Snyder, G. J.; Kim, S. W. Dense Dislocation Arrays Embedded in Grain Boundaries for High-Performance Bulk Thermoelectrics. *Science* **2015**, 348, 109-114.

(67) Lee, Y.; Lo, S.-H.; Chen, C.; Sun, H.; Chung, D.-Y.; Chasapis, T. C.; Uher, C.; Dravid, V. P.; Kanatzidis, M. G. Contrasting Role of Antimony and Bismuth Dopants on the Thermoelectric Performance of Lead Selenide. *Nat Commun* **2014**, 5.

(68) Wang, H.; Gibbs, Z. M.; Takagiwa, Y.; Snyder, G. J. Tuning Pands of PbSe for Better Thermoelectric Efficiency. *Energy Environ. Sci.* **2014**, 7, 804-811.

(69) Zhao, L.; Lo, S. H.; Zhang, Y.; Sun, H.; Tan, G.; Uher, C.; Wolverton, C.; Dravid, V. P.; Kanatzidis, M. G. Ultralow Thermal Conductivity and High Thermoelectric Figure of Merit in SnSe Crystals. *Nature* **2014**, 508, 373-377.

(70) Yamini, S. A.; Mitchell, D. R. G.; Gibbs, Z. M.; Santos, R.; Patterson, V.; Li, S.; Pei, Y. Z.; Dou, S. X.; Jeffrey Snyder, G. Heterogeneous Distribution of Sodium for High Thermoelectric Performance of p-type Multiphase Lead-Chalcogenides. *Adv. Energy Mater.* **2015**, n/a-n/a.

(71) Zhao, L.-D.; Tan, G.; Hao, S.; He, J.; Pei, Y.; Chi, H.; Wang, H.; Gong, S.; Xu, H.; Dravid, V. P.; Uher, C.; Snyder, G. J.; Wolverton, C.; Kanatzidis, M. G. Ultrahigh Power Factor and Thermoelectric Performance in Hole-doped Single-Crystal SnSe. *Science* **2016**, 351, 141-144.

(72) Grebenkemper, J. H.; Hu, Y.; Barrett, D.; Gogna, P.; Huang, C.-K.; Bux, S. K.; Kauzlarich, S. M. High Temperature Thermoelectric Properties of $Yb_{14}MnSb_{11}$ Prepared from Reaction of MnSb with the Elements. *Chem. Mater.* **2015**, 27, 5791-5798.

(73) Lan, Y.; Minnich, A. J.; Chen, G.; Ren, Z. Enhancement of Thermoelectric Figure-of-Merit by a Bulk Nanostructuring Approach. *Adv. Funct. Mater.* **2010**, 20, 357-376.

(74) Wu, H. J.; Zhao, L. D.; Zheng, F. S.; Wu, D.; Pei, Y. L.; Tong, X.; Kanatzidis, M. G.; He, J. Q. Broad Temperature Plateau for Thermoelectric Figure of Merit ZT>2 in Phase-Separated $PbTe_{0.7}S_{0.3}$. *Nat Commun* **2014**, 5.

(75) Hu, L.; Zhu, T.; Liu, X.; Zhao, X. Point Defect Engineering of High-Performance Bismuth-Telluride-Based Thermoelectric Materials. *Adv. Funct. Mater.* **2014**, 24, 5211–5218.

(76) Liu, W.; Kim, H. S.; Chen, S.; Jie, Q.; Lv, B.; Yao, M.; Ren, Z.; Opeil, C. P.; Wilson, S.; Chu, C.-W.; Ren, Z. n-type Tthermoelectric Mmaterial $Mg_2Sn_{0.75}Ge_{0.25}$ for Hhigh Ppower Ggeneration. *Proceedings of the National Academy of Sciences* **2015**, 112, 3269-3274.

(77) Hsu, K. F.; Loo, S.; Guo, F.; Chen, W.; Dyck, J. S.; Uher, C.; Hogan, T.; Polychroniadis, E. K.; Kanatzidis, M. G. Cubic $AgPbmSbTe_{2+m}$: Bulk Thermoelectric Materials with High Figure of Merit. *Science* **2004**, 303, 818-821.

(78) Wang, H.; Pei, Y.; LaLonde, A. D.; Snyder, G. J. Weak Electron-Phonon Coupling Contributing to High Thermoelectric Performance in n-Type PbSe. *Proc. Natl. Acad. Sci. USA* **2012**, 109, 9705-9709.

(79) Tan, G.; Shi, F.; Doak, J. W.; Sun, H.; Zhao, L.-D.; Wang, P.; Uher, C.; Wolverton, C.; Dravid, V. P.; Kanatzidis, M. G. Extraordinary Role of Hg in Enhancing the Thermoelectric Performance of p-type SnTe. *Energy Environ. Sci.* **2015**, 8, 267-277.

(80) Fu, C.; Zhu, T.; Liu, Y.; Xie, H.; Zhao, X. Band Engineering of High Performance p-Type FeNbSb Based Half-Heusler Thermoelectric Materials for Figure of Merit ZT > 1. *Energy Environ. Sci.* **2015**, 8, 216-220.

(81) Wang, X. W.; Lee, H.; Lan, Y. C.; Zhu, G. H.; Joshi, G.; Wang, D. Z.; Yang, J.; Muto, A. J.; Tang, M. Y.; Klatsky, J.; Song, S.; Dresselhaus, M. S.; Chen, G.; Ren, Z. F. Enhanced Thermoelectric Figure of Merit in Nanostructured n-Type Silicon Germanium Bulk Alloy. *Appl. Phys. Lett.* **2008**, 93, 193121.

(82) Poudel, B.; Hao, Q.; Ma, Y.; Lan, Y.; Minnich, A.; Yu, B.; Yan, X.; Wang, D.; Muto, A.; Vashaee, D.; Chen, X.; Liu, J.; Dresselhaus, M. S.; Chen, G.; Ren, Z. High-thermoelectric Performance of Nanostructured Bismuth Antimony Telluride Bulk Alloys. *Science* **2008**, 320, 634-638.

(83) Zhang, H.; Liu, C.; Qi, X.; Dai, X.; Fang, Z.; Zhang, S. Topological Insulators in Bi_2Se_3, Bi_2Te_3 and Sb_2Te_3 with a Single Dirac Cone on the Surface. *Nat. Phys.* **2009**, 5, 438-442.

(84) Yavorsky, B. Y.; Hinsche, N. F.; Mertig, I.; Zahn, P. Electronic structure and transport anisotropy of Bi_2Te_3 and Sb_2Te_3. *Physical Review B* **2011**, 84.

(85) Richter, W.; Kohler, H.; Becker, C. R. A Raman and Far-Infrared Investigation of Phonons in Rhombohedral V2-VI3 Compounds Bi_2Te_3, Bi_2Se_3, Sb_2Te_3 and $Bi_2(Te_{1-x}Se_x)_3$ ($0<x<1$), $(Bi_{1-y}Sb_y)_2Te_3$ ($0<y<1$). *Phys. Status. Solidi. B* **1977**, 84, 619-628.

(86) Mishra, S. K.; Satpathy, S.; Jepsen, O. Electronic Structure and Thermoelectric Properties of Bismuth Telluride and Bismuth Selenide. *J. Phys-condens. Mat.* **1997**, 9, 461-470.

(87) Prokofieva, L. V.; Pshenay-Severin, D. A.; Konstantinov, P. P.; Shabaldin, A. A. Optimum Composition of a $Bi_2Te_{3-x}Se_x$ Alloy for the *n*-Type Leg of a Thermoelectric Generator. *Semiconductors* **2009**, 43, 973-976.

(88) Zhao, L. D.; Zhang, B. P.; Li, J. F.; Zhang, H. L.; Liu, W. S. Enhanced Thermoelectric and Mechanical Properties in Textured *n*-Type Bi_2Te_3 Prepared by Spark Plasma Sintering. *Solid State Sci.* **2008**, 10, 651-658.

(89) Fan, S.; Zhao, J.; Guo, J.; Yan, Q.; Ma, J.; Hng, H. H. p-Type $Bi_{0.4}Sb_{1.6}Te_3$ Nanocomposites with Enhanced Figure of Merit. *Appl. Phys. Lett.* **2010**, 96, 182104.

(90) Mehta, R. J.; Zhang, Y.; Karthik, C.; Singh, B.; Siegel, R. W.; Borca-Tasciuc, T.; Ramanath, G. A New Class of Doped Nanobulk High Figure-of-Merit Thermoelectrics by Scalable Bottom-up Assembly. *Nat. Mater.* **2012**, 11, 233-240.

(91) Soni, A.; Shen, Y.; Yin, M.; Zhao, Y.; Yu, L.; Hu, X.; Dong, Z.; Khor, K. A.; Dresselhaus, M. S.; Xiong, Q. Interface Driven Energy Filtering of Thermoelectric Power in Spark Plasma Sintered $Bi_2Te_{2.7}Se_{0.3}$ Nanoplatelet Composites. *Nano Lett.* **2012**, 12, 4305-4310.

(92) Soni, A.; Zhao, Y. Y.; Yu, L. G.; Aik, M. K. K.; Dresselhaus, M. S.; Xiong, Q. H. Enhanced Thermoelectric Properties of Solution Grown $Bi_2Te_{3-x}Se_x$ Nanoplatelet Composites. *Nano Lett.* **2012**, 12, 1203-1209.

(93) Hong, M.; Chen, Z. G.; Yang, L.; Zou, J. $Bi_xSb_{2-x}Te_3$ Aanoplates with Enhanced Thermoelectric Performance due to Sufficiently Decoupled Electronic Transport Properties and Strong Wide-Frequency Phonon Scatterings. *Nano Energy* **2016**, 20, 144-155.

(94) Scheele, M.; Oeschler, N.; Veremchuk, I.; Reinsberg, K.-G.; Kreuziger, A.-M.; Kornowski, A.; Broekaert, J.; Klinke, C.; Weller, H. ZT Enhancement in Solution-Grown $Sb_{(2-x)}$BixTe3 Nanoplatelets. *ACS Nano* **2010**, 4, 4283-4291.

(95) Min, Y.; Roh, J. W.; Yang, H.; Park, M.; Kim, S. I.; Hwang, S.; Lee, S. M.; Lee, K. H.; Jeong, U. Surfactant-Free Scalable Synthesis of Bi_2Te_3 and Bi_2Se_3 Nanoflakes and Enhanced Thermoelectric Properties of Their Nanocomposites. *Adv. Mater.* **2013**, 25, 1425-9.

(96) Min, Y.; Park, G.; Kim, B.; Giri, A.; Zeng, J.; Roh, J. W.; Kim, S. I.; Lee, K. H.; Jeong, U. Synthesis of Multishell Nanoplates by Consecutive Epitaxial Growth of Bi_2Se_3 and Bi_2Te_3 Nanoplates and Enhanced Thermoelectric Properties. *ACS Nano* **2015**.

(97) Suh, D.; Lee, S.; Mun, H.; Park, S.-H.; Lee, K. H.; Wng Kim, S.; Choi, J.-Y.; Baik, S. Enhanced Thermoelectric Performance of $Bi_{0.5}Sb_{1.5}Te_3$-Expanded Graphene Composites by Simultaneous Modulation of Electronic and Thermal Carrier Transport. *Nano Energy* **2015**, 13, 67-76.

(98) Zhang, Y.; Day, T.; Snedaker, M. L.; Wang, H.; Krämer, S.; Birkel, C. S.; Ji, X.; Liu, D.; Snyder, G. J.; Stucky, G. D. A Mesoporous Anisotropic n-Type Bi_2Te_3 Monolith with Low Thermal Conductivity as an Efficient Thermoelectric Material. *Adv. Mater.* **2012**, 24, 5065-5070.

(99) Zhang, Y.; Wang, H.; Kräemer, S.; Shi, Y.; Zhang, F.; Snedaker, M.; Ding, K.; Moskovits, M.; Snyder, G. J.; Stucky, G. D. Surfactant-Free Synthesis of Bi_2Te_3−Te Micro−Nano Heterostructure with Enhanced Thermoelectric Figure of Merit. *ACS Nano* **2011**, 5, 3158-3165.

(100) Son, J. S.; Choi, M. K.; Han, M.-K.; Park, K.; Kim, J.-Y.; Lim, S. J.; Oh, M.; Kuk, Y.; Park, C.; Kim, S.-J.; Hyeon, T. *n*-Type Nanostructured Thermoelectric Materials Prepared from Chemically Synthesized Ultrathin Bi_2Te_3 Nanoplates. *Nano Lett.* **2012**, 12, 640-647.

(101) Sun, Y.; Cheng, H.; Gao, S.; Liu, Q.; Sun, Z.; Xiao, C.; Wu, C.; Wei, S.; Xie, Y. Atomically Thick Bismuth Selenide Freestanding Single Layers Achieving Enhanced Thermoelectric Energy Harvesting. *J. Am. Chem. Soc.* **2012**, 134, 20294-20297.

(102) Hong, M.; Chen, Z.-G.; Yang, L.; Han, G.; Zou, J. Enhanced Thermoelectric Performance of Ultrathin Bi_2Se_3 Nanosheets through Thickness Control. *Adv. Electron. Mater.* **2015**, 1, 1500025.

(103) Mehta, R. J.; Zhang, Y.; Zhu, H.; Parker, D. S.; Belley, M.; Singh, D. J.; Ramprasad, R.; Borca-Tasciuc, T.; Ramanath, G. Seebeck and Figure of Merit Enhancement in

Nanostructured Antimony Telluride by Antisite Defect Suppression through Sulfur Doping. *Nano Lett.* **2012**, 12, 4523-4529.

(104) Ma, Y.; Hao, Q.; Poudel, B.; Lan, Y. C.; Yu, B.; Wang, D. Z.; Chen, G.; Ren, Z. F. Enhanced Thermoelectric Figure-of-Merit in p-Type Nanostructured Bismuth Antimony Tellurium Alloys Made from Elemental Chunks. *Nano Lett.* **2008**, 8, 2580-2584.

(105) Shen, J.-J.; Zhu, T.-J.; Zhao, X.-B.; Zhang, S.-N.; Yang, S.-H.; Yin, Z.-Z. Recrystallization Induced in situ Nanostructures in Bulk Bismuth Antimony Tellurides: a Simple Top Down Route and Iproved Thermoelectric Properties. *Energy Environ. Sci.* **2010**, 3, 1519-1523.

(106) Carle, M.; Pierrat, P.; Lahalle-Gravier, C.; Scherrer, S.; Scherrer, H. Transport Properties of *n*-Type $Bi_2(Te_{1-x}Se_x)_3$ Single Crystal Solid Solutions (x = 0.05). *J. Phys. Chem. Solids* **1995**, 56, 201-209.

(107) Wang, S.; Tan, G.; Xie, W.; Zheng, G.; Li, H.; Yang, J.; Tang, X. Enhanced Thermoelectric Properties of $Bi_2(Te_{1-x}Se_x)_3$-Based Compounds as *n*-Type Legs for Low-Temperature Power Generation. *J. Mater. Chem.* **2012**, 22, 20943-20951.

(108) Starý, Z.; Horák, J.; Stordeur, M.; Stölzer, M. Antisite Defects in $Sb_{2-x}Bi_xTe_3$ Mixed Crystals. *J. Phys. Chem. Solids* **1988**, 49, 29-34.

(109) Glen, A. S. New Materials and Performance Limits for Thermoelectric Cooling. In *CRC Handbook of Thermoelectrics*, CRC Press: 1995.

(110) Dean, J. A.; Lange, N. A. *Lange's Handbook of Chemistry*. McGraw-Hill: New York, **1999**; Vol. 15th.

(111) Minnich, A. J.; Dresselhaus, M. S.; Ren, Z. F.; Chen, G. Bulk Nanostructured Thermoelectric Materials: Current Research and Future Prospects. *Energy Environ. Sci.* **2009**, 2, 466-479.

(112) Goldsmid, H. J.; Sharp, J. W. Estimation of the Thermal Band Gap of a Semiconductor from Seebeck Measurements. *J. Electron. Mater.* 28, 869-872.

(113) Gibbs, Z. M.; Kim, H.-S.; Wang, H.; Snyder, G. J. Band Gap Estimation from Temperature Dependent Seebeck Measurement—Deviations from the $2e|S|_{max}T_{max}$ Relation. *Appl. Phys. Lett.* **2015**, 106, 022112.

(114) Liu, W.-S.; Zhang, B.-P.; Li, J.-F.; Zhang, H.-L.; Zhao, L.-D. Enhanced Thermoelectric Properties in $CoSb_{3-x}Te_x$ Alloys Prepared by Mechanical Alloying and Spark Plasma Sintering. *J. Appl. Phys.* **2007**, 102, 103717.

(115) Wang, H.; Bahk, J.-H.; Kang, C.; Hwang, J.; Kim, K.; Kim, J.; Burke, P.; Bowers, J. E.; Gossard, A. C.; Shakouri, A.; Kim, W. Right Sizes of Nano- and Microstructures for High-Performance and Rigid Bulk Thermoelectrics. *Proc. Natl. Acad. Sci. USA* **2014**, 111, 10949-10954.

(116) Caillat, T.; Carle, M.; Pierrat, P.; Scherrer, H.; Scherrer, S. Thermoelectric Properties of $(Bi_xSb_{1-x})_2Te_3$ Single Crystal Solid Solutions Grown by the T.H.M. Method. *J. Phys. Chem. Solids* **1992**, 53, 1121-1129.

(117) Hu, L. P.; Zhu, T. J.; Wang, Y. G.; Xie, H. H.; Xu, Z. J.; Zhao, X. B. Shifting up the Optimum Figure of Merit of *p*-Type Bismuth Telluride-Based Thermoelectric Materials for Power Generation by Suppressing Intrinsic Conduction. *NPG Asia Mater.* **2014**, 6, e88.

(118) Birkholz, U. Untersuchung der Intermetallischen Verbindung Bi_2Te_3 Sowie der Festen Lösungen $Bi_{2-x}Sb_xTe_3$ und $Bi_2Te_{3-x}Se_x$ Hinsichtlich Ihrer Eignung als Material für Halbleiter-Thermoelemente. In *Zeitschrift für Naturforschung A*, 1958; Vol. 13, p 780.

(119) Zhang, G.; Kirk, B.; Jauregui, L. A.; Yang, H.; Xu, X.; Chen, Y. P.; Wu, Y. Rational Synthesis of Ultrathin *n*-Type Bi_2Te_3 Nanowires with Enhanced Thermoelectric Properties. *Nano Lett.* **2012**, 12, 56-60.

(120) Xiu, F.; He, L.; Wang, Y.; Cheng, L.; Chang, L.-T.; Lang, M.; Huang, G.; Kou, X.; Zhou, Y.; Jiang, X.; Chen, Z.; Zou, J.; Shailos, A.; Wang, K. L. Manipulating Surface States in Topological Insulator Nanoribbons. *Nat. Nano.* **2011**, 6, 216-221.

(121) Cheng, L.; Chen, Z.-G.; Yang, L.; Han, G.; Xu, H.-Y.; Snyder, G. J.; Lu, G.-Q.; Zou, J. T-Shaped Bi_2Te_3-Te Heteronanojunctions: Epitaxial Growth, Structural Modeling, and Thermoelectric Properties. *J. Phys. Chem. C* **2013**, 117, 12458-12464.

(122) Hong, M.; Chen, Z. G.; Yang, L.; Zou, J. Enhancing Thermoelectric Performance of Bi2Te3-based Nanostructures through Rational Structure Design. *Nanoscale* **2016**.

(123) Mi, J. L.; Lock, N.; Sun, T.; Christensen, M.; Sondergaard, M.; Hald, P.; Hng, H. H.; Ma, J.; Iversen, B. B. Biomolecule-Assisted Hydrothermal Synthesis and Self-Assembly of Bi_2Te_3 Nanostring-Cluster Hierarchical Structure. *ACS Nano* **2010**, 4, 2523-2530.

(124) Lu, W. G.; Ding, Y.; Chen, Y. X.; Wang, Z. L.; Fang, J. Y. Bismuth Telluride Hexagonal Nanoplatelets and Their Two-Step Epitaxial Growth. *J. Am. Chem. Soc.* **2005**, 127, 10112-10116.

(125) Zhang, Y.; Hu, L. P.; Zhu, T. J.; Xie, J.; Zhao, X. B. High Yield Bi_2Te_3 Single Crystal Nanosheets with Uniform Morphology via a Solvothermal Synthesis. *Cryst. Growth Des.* **2013**, 13, 645-651.

(126) Min, Y.; Moon, G. D.; Kim, B. S.; Lim, B.; Kim, J.-S.; Kang, C. Y.; Jeong, U. Quick, Controlled Synthesis of Ultrathin Bi_2Se_3 Nanodiscs and Nanosheets. *J. Am. Chem. Soc.* **2012**, 134, 2872-2875.

(127) Fu, J.; Song, S.; Zhang, X.; Cao, F.; Zhou, L.; Li, X.; Zhang, H. Bi_2Te_3 Nanoplates and Nanoflowers: Synthesized by Hydrothermal Process and Their Enhanced Thermoelectric Properties. *CrystEngComm* **2012**, 14, 2159-2165.

(128) Son, J. H.; Oh, M. W.; Kim, B. S.; Park, S. D.; Min, B. K.; Kim, M. H.; Lee, H. W. Effect of Ball Milling Time on the Thermoelectric Properties of p-Type $(Bi,Sb)_2Te_3$. *J. Alloy. Compd.* **2013**, 566, 168-174.

(129) Ivanova, L. D.; Petrova, L. I.; Granatkina, Y. V.; Kichik, S. A.; Marakushev, I. S.; Mel'nikov, A. A. Melt-Spun Materials based on an n-Type $Bi_2Te_{2.7}Se_{0.3}$ Solid Solution. *Inorg. Mater+.* **2015**, 51, 741-745.

(130) Zheng, Y.; Zhang, Q.; Su, X.; Xie, H.; Shu, S.; Chen, T.; Tan, G.; Yan, Y.; Tang, X.; Uher, C.; Snyder, G. J. Mechanically Robust BiSbTe Alloys with Superior Thermoelectric Performance: A Case Study of Stable Hierarchical Nanostructured Thermoelectric Materials. *Adv. Energy Mater.* **2015**, 5, n/a-n/a.

(131) Ivanova, L. D.; Petrova, L. I.; Granatkina, Y. V.; Leontyev, V. G.; Ivanov, A. S.; Varlamov, S. A.; Prilepo, Y. P.; Sychev, A. M.; Chuiko, A. G.; Bashkov, I. V. Thermoelectric and Mechanical Properties of the $Bi_{0.5}Sb_{1.5}Te_3$ Solid Solution Prepared by Melt Spinning. *Inorg. Mater+.* **2013**, 49, 120-126.

(132) Jaworski, C. M.; Kulbachinskii, V.; Heremans, J. P. Resonant Level Formed by Tin in Bi_2Te_3 the Enhancement of Room-Temperature Thermoelectric Power. *Phys. Rev. B* **2009**, 80, 233201.

(133) Ravich, Y. I.; Efimova, B. A.; Smirnov, I. A. *Semiconducting Lead Chalcogenides*. Plenum Press: **1970**.

(134) Callaway, J.; von Baeyer, H. Effect of Point Imperfections on Lattice Thermal Conductivity. *Phys. Rev.* **1960**, 120, 1149-1154.

(135) Bessas, D.; Sergueev, I.; Wille, H. C.; Perßon, J.; Ebling, D.; Hermann, R. P. Lattice Dynamics in Bi_2Te_3 and Sb_2Te_3: Te and Sb Density of Phonon States. *Phys. Rev. B* **2012**, 86, 224301.

(136) Zhu, T. J.; Fu, C. G.; Xie, H. H.; Liu, Y. T.; Feng, B.; Xie, J.; Zhao, X. B. Lattice Thermal Conductivity and Spectral Phonon Scattering in FeVSb-Based Half-Heusler Compounds. *EPL* **2013**, 104, 46003.

(137) Xie, H.; Wang, H.; Pei, Y.; Fu, C.; Liu, X.; Snyder, G. J.; Zhao, X.; Zhu, T. Beneficial Contribution of Alloy Disorder to Electron and Phonon Transport in Half-Heusler Thermoelectric Materials. *Adv. Funct. Mater.* **2013**, 23, 5123-5130.

(138) Greenaway, D. L.; Harbeke, G. Band Structure of Bismuth Telluride, Bismuth Selenide and Their Respective Alloys. *J. Phys. Chem. Solids* **1965**, 26, 1585-1604.

3

Methodology and Approach

In this chapter, we introduced the microwave-assisted method for the fabrication of Bi_2Te_3-based thermoelectric materials. In addition, characterization of products is of significance, X-ray Diffraction and electron microscopy (including scanning electron microscopy and transmission electron microscopy) are represented as well. Finally, the measurement of thermoelectric properties is presented in detail.

3.1 Synthesis of nanostructured thermoelectric materials by microwave-assisted solvothermal method

The solvothermal synthesis is extensively used to fabricate a wide range of nanoscale and nanostructured materials. In this process, precursor materials with the end-product stoichiometry are mixed in an organic solvent with reduction and template reagents. After being stirred completely, the mixture is added into a sealed autoclave, which is heated at temperature normally between 100°C to 250°C for a period of time. Finally, cooled to room temperature, the products are washed, centrifuged and dried. One of the outstanding features of this method is that the morphology and size of products can be controlled. However, the conventional solvothermal method is time-consuming. To shorten the material preparation, we employed a microwave assisted solvothermal method, which only needs a few minutes to finish the synthesis due to the localized superheating mechanism of microwave irradiation.

In this PhD project, the MARS 6 microwave oven (Figure 3-1 (a)) supplied by CEM is used to carry out the synthesis process, and the EasyPrep (Figure 3-1 (b)) including one reference vessel and 11 normal vessels is selected for this synthesis process. This microwave synthesis unit with as large as 1800W power is equipped with magnetic stirring, which means reagents are stirred as the reaction is processing. Besides, there are temperature sensor and pressure sensor. The reaction can be conducted safely and the

temperature and pressure data can be saved for the experimental result analysis. The synthesis process can be programed in this device, including the temperature rising time, the reaction holding time as well as the temperature and pressure used in the synthesis process.

Figure 3-1 (a) the photo of MARS 6 microwave oven, and (b) the EasyPrep vessel selected for the thermoelectric material synthesis in this PhD project.

The detailed route of the sample synthesis is shown in Figure 3-2. Precursors and possible surfactant are weighed by the balance, and added into ethylene glycol as the solvent with a certain volume. Then, the solvent is stirred to form a clear solution. The solution is transferred into the vessels, which are afterwards loaded into the Mars 6 microwave systems. The reaction parameters are programed previously, including ramping time, holding time, reaction temperature and threshold pressure for security. After the reaction, the cooling down process is launched automatically. Then, the products need to be washed by ethanol and distilled water for at least six times. After being dried at 60℃ for at least 12 hours, the black powder is collected.

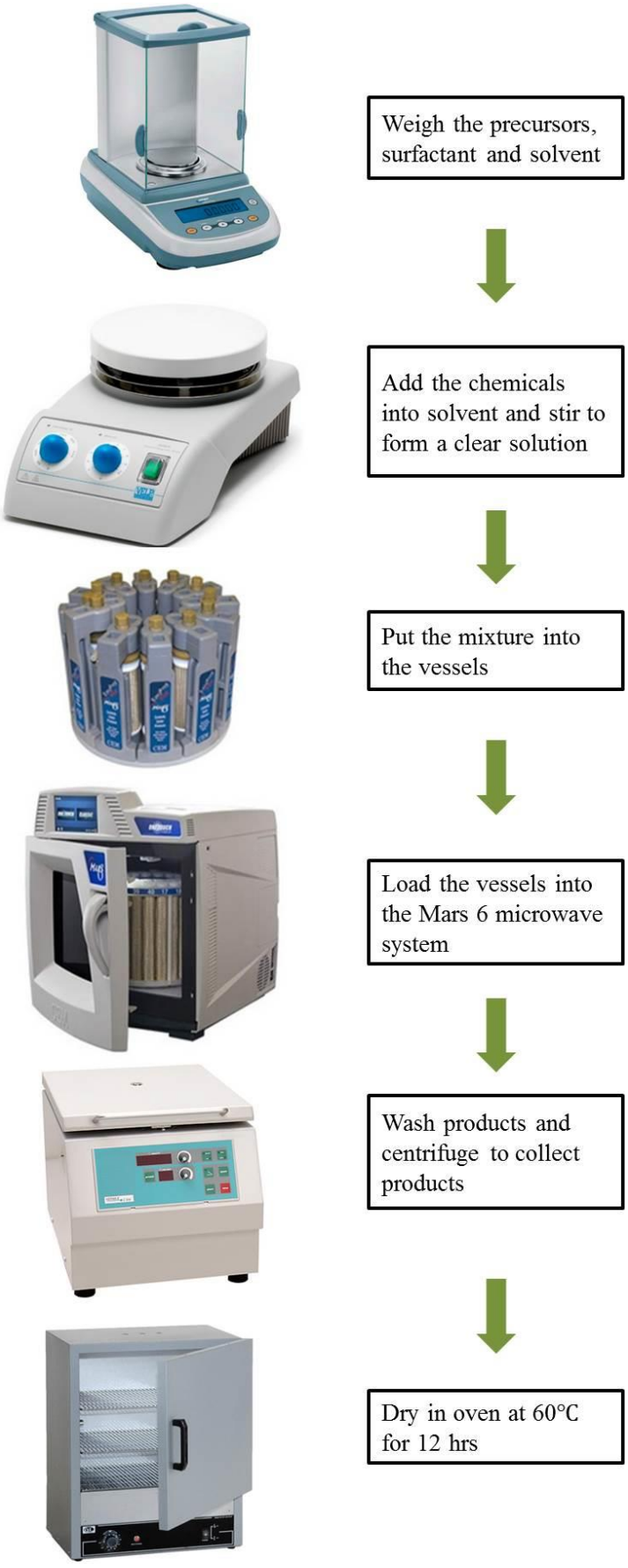

Figure 3-2 Diagram of microwave-assisted solvothermal synthesis process.

3.2 Characterization of Materials

The electron microscopes, including scanning electron microscope (SEM) and transmission electron microscope (TEM) are used to image the morphology and geometry of the as-synthesized nanomaterials. X-ray diffraction (XRD) pattern is used to analyze the phase purity and crystal structure. In addition, atomic force microscopy (AFM) is used to determine the thickness thin nanosheets, and Raman spectroscopy is applied to examine the crystal structure modification. The working principles of these techniques are introduced in this section.

3.2.1 Electron-specimen interactions

It is well-known that the resolution of any microscope δ ($\approx \lambda/2$) is fundamentally limited by the wavelength λ of the illumination used. The resolution of optical microscope is around 200 nm, while that of electrons is 0.1~0.2 nm. Although the defects of the electro-magnetic lens limit the actual resolution, this is sufficient to image atoms because the distance between neighboring atoms is about that range. Therefore, electron beam rather than light is selected to illuminate a specimen and create a highly magnified image.

Due to the wave-particle duality of fast moving electrons, the electrons can both transfer momentum and interfere constructively and destructively during their interaction with specimen. The interaction between the electrons and specimen becomes very important for understanding samples. The electron beam and the specimen interact in both elastic and inelastic modes, which are distinctive by whether the kinetic energy of the incident electrons is preserved or not. In elastic scattering, the kinetic energy of the incident electrons is preserved, only their direction of propagation is changed, while inelastic scattering is a process in which the kinetic energy of incident electrons is changed.

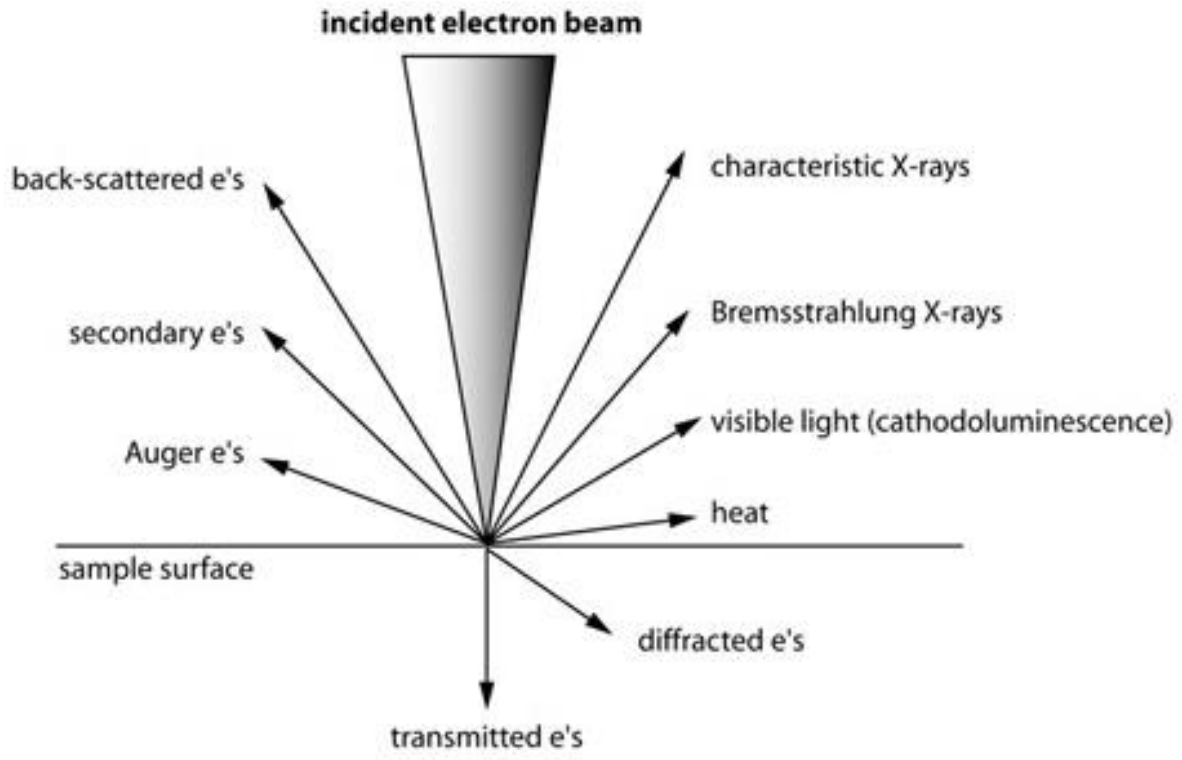

Figure 3-3 Schematic illustration of interaction between electron beam and specimen.[139]

There are a number of generated signals when electron beam hits a sample. Specifically, some electrons are bounced back out of the sample (backscattered electrons), others knock into atoms and replace electrons, that come out of the sample (secondary electrons (SEs)). In addition, X-rays, Auger electron emission, elastic scattered transmitted electrons and inelastic scattered transmitted electrons can be the result of electron-sample interactions as well (Figure 3-3). The detailed introductions of these generated signals and their applications in electronic microscopy are given as below:

Secondary electrons (SE) – are one of the major signals in SEM. After the high energy electrons interact with out-shell electrons in the specimen, the electrons from the specimen atoms are ejected to form the SEs. The energy of SEs is relatively low, generally less than 50 eV. SE signal comes from the surface region; therefore, it provides the surface information of samples.

Back-scatted electrons (BSE) –Being interacted with the nucleus of the atoms in the specimen, these electrons will travel around these nucleuses and get rejected back out of the specimen. BSEs are elastic scattered electrons with relatively high energies close to the incident beam energy, generally >50 eV. It is also one of the major signals of SEM.

The BSE will increase if the testing sample has large average atomic number. Thus, this signal reveals the composition of the examined sample.

Characteristic X-rays – Some of the incident electrons in the beam will knock out inner shell electrons circling around the nucleus in the specimen, which creates holes in the inner shell. As electrons are preferred to stay in low energy state, electrons in the outer shell will decay into the hole. Simultaneously, an X-ray wave will be emitted with the same energy as the energy difference between two electron shells (Figure 3-4). As shell energies for different elements are different, the emitted X-ray wave conveys compositional information of the specimen. X-ray analysis is used in both SEM and TEM.

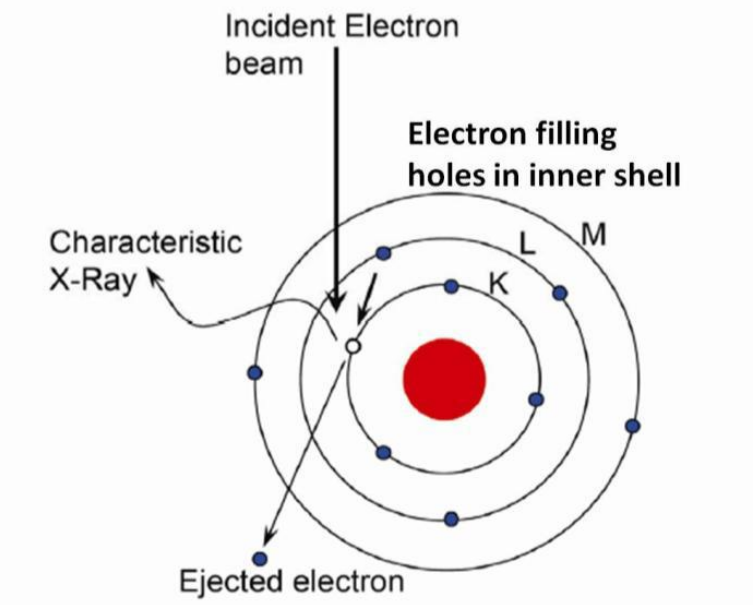

Figure 3-4 Schematic illustration of the characteristic X-ray generation.[140]

Auger electron emission – The weakly bound outer-shell electrons are emitted due to the interaction with electron beam. Outer shell electrons give the bonding information about the specimen, which makes auger electron emission very useful in the studies of surface.

Elastic scattered transmitted electrons – Typically in TEM, most of the incident electrons will penetrate through the specimen. Some of these electrons only change direction, but not kinetic energy after the penetration. In TEM, elastic scattered electrons will produce density contrast (incoherent elastic scattering) or diffraction (coherent elastic scattering).

Inelastic scattered transmitted electrons – Inelastic scattered transmitted electrons are the ones that penetrated the thin specimen and their kinetic energies or/and direction are changed. By analyzing the energy loss of these electrons, we are able to reveal the compositional characteristics of the specimen. They allow us to perform elemental analysis, such as the electron energy loss spectroscopy (EELS) in TEM.

3.2.2 Scanning Electron Microscope

Taking advantage of the interaction between electron beam and specimen, SEM is used to image the sample surface[141]. Specifically, when the high–energy beam of electrons scan the testing sample, the electrons interact with the sample atoms to produce signals containing information about the surface topography, chemical composition, as well as crystallographic, magnetic and electrical-characteristics of the examined samples[142]. Compared with traditional optical microscope, SEM is more competent to do microstructure analysis, because SEM resolution is as high as 10nm nearly equal to the distance between two closed atoms; SEM has much larger field depth to obtain three dimensional (3D) appearance of the specimen; the last but not least, SEM is able to conduct microanalysis.

After interacting with the electron beam, various signals in SEM including SE, BSE and characteristic X-ray will be generated near the sample surface, and a teardrop shaped interaction volume will be produced (Figure 3-5 (a)). The size of the interaction volume generally approximating 2 μm in width by 2 μm in depth is determined by the energy of scanning electrons as well the average atomic number density of the testing sample (Figure 3-5 (b)).

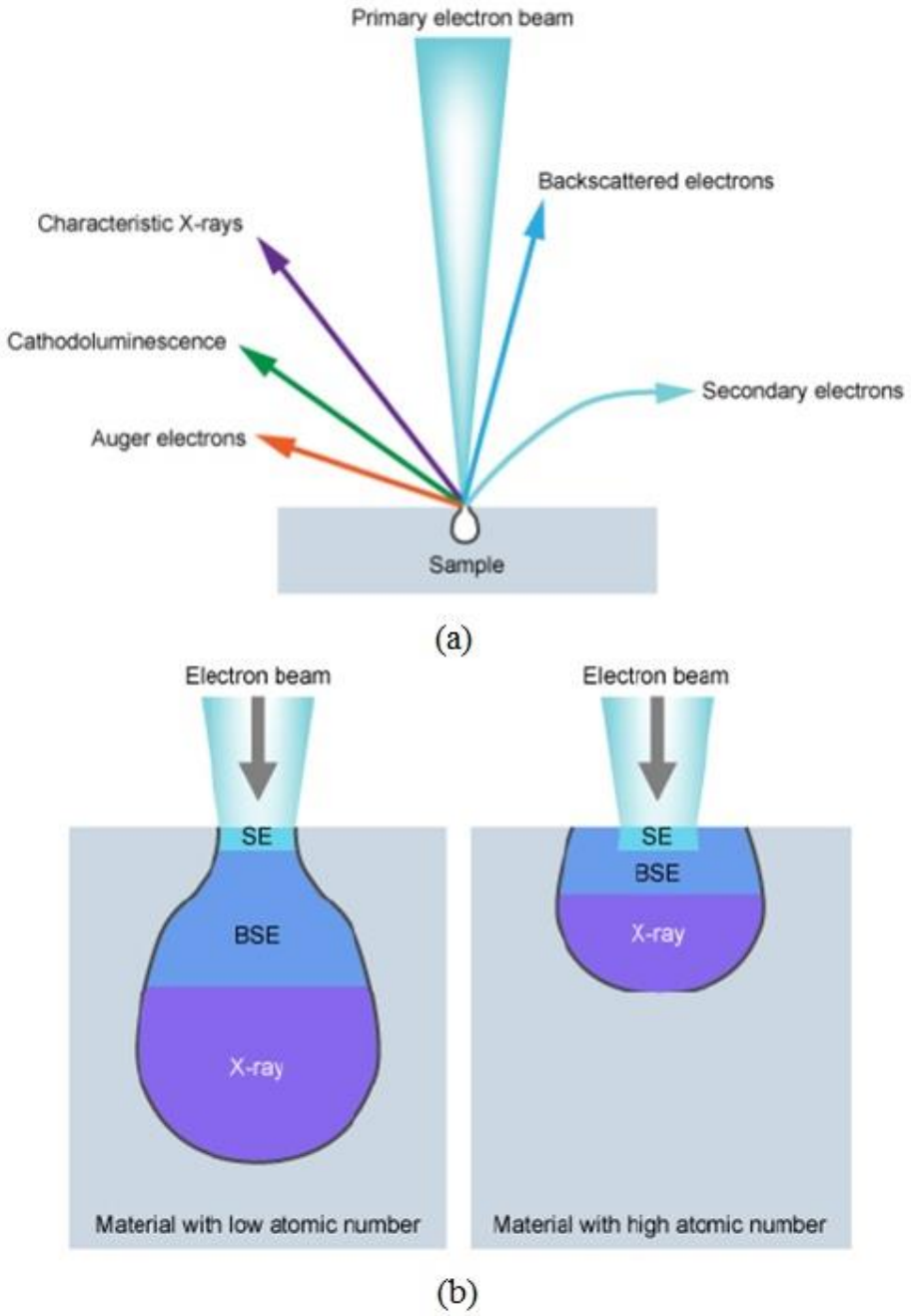

Figure 3-5 Schematic diagram of electron beam-sample interaction in SEM. (a) Five possible signals generated by electron beam strike, and (b) interaction volume produced in the interaction process.[143]

Figure 3-6 shows the working principle of SEM. At the top of SEM is the source of the ultrafine electron beam, electron gun, which includes three parts, the filament, Wehnelt cap and the anode. Thermoelectrons produced by the filament are accelerated through the application of a voltage between the filament and the anode, thus creating an electron beam that streams down the microscope column. Magnetic lens system is equipped in the column including condenser lens, objective lens and scanning coils. The condenser lens

controls the intensity of the electron beam reaching the specimen; the objective lens brings the electron beam into focus (de-magnifies) on the specimen; and the scanning coils deflect the electron beam horizontally and vertically over the specimen surface. Then the collimated and focused electron beam with high energy scans the sample surface to produce signals with sample surface information, such as secondary electrons, back-scattering electrons and characteristic X-rays. These signals can be received by corresponding detectors. The images obtained by SE detector and BSE detector reveal the information on the surface roughness and composition of the scanning sample. The characteristic X-rays collected by energy dispersive X-ray spectrometer can be used to identify the elements in samples, quantify their concentrations and even map their distribution as well.

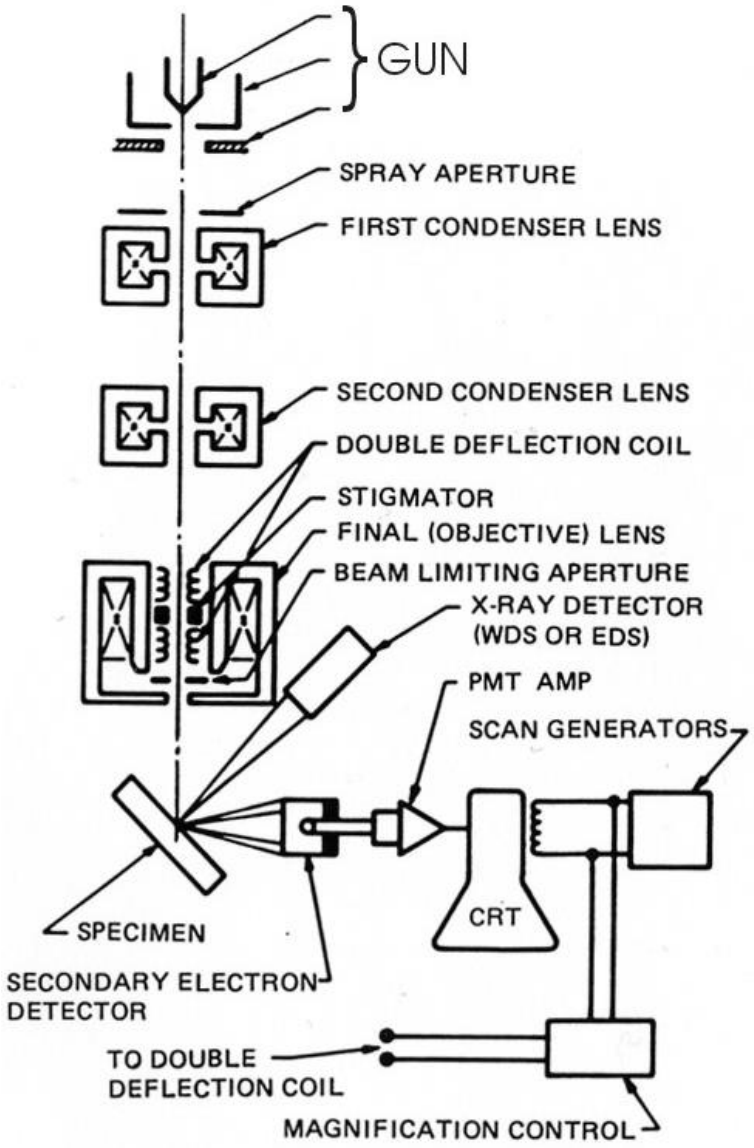

Figure 3-6 Schematic illustration of fundamental principles of SEM.[144]

Accelerate voltage, spot size, aperture and working distance are the key operational parameters which impacts the results of SEM analysis. Accelerating voltage is the voltage difference between the filament and the anode which accelerates the electron beam towards the anode. High accelerate voltage leads to smooth images with high resolution, while low accelerate voltage provides more surface information. Although larger spot size contributes to smooth image, smaller spot size is preferable because this can result in images with high resolution, greater depth of field and less electron beam damage. Aperture size plays the same role as spot size; therefore, relatively smooth images with high resolution conveying the detailed surface information can be obtained by adjusting these two parameters. Closer working distance can improve the resolution but reduce the depth of field. These parameters selected to analyze our as-prepared nanostructured thermoelectric materials for different SEMs located in the Centre for Microscopy and Microanalysis (CMM), University of Queensland are listed in Table 3-1.

Table 3-1 Operational parameters of SEMs for sample analysis

	Operational Parameters			
	kV	S	Ap	WD
JEOL 6610	5-15 kV	3-10	2	10mm
JEOL 7001	5-15 kV	6-8	Fixed	10mm
JEOL 7800	1-15 kV	6-8	Fixed	2-10mm

3.2.3 Transmission Electron Microscope

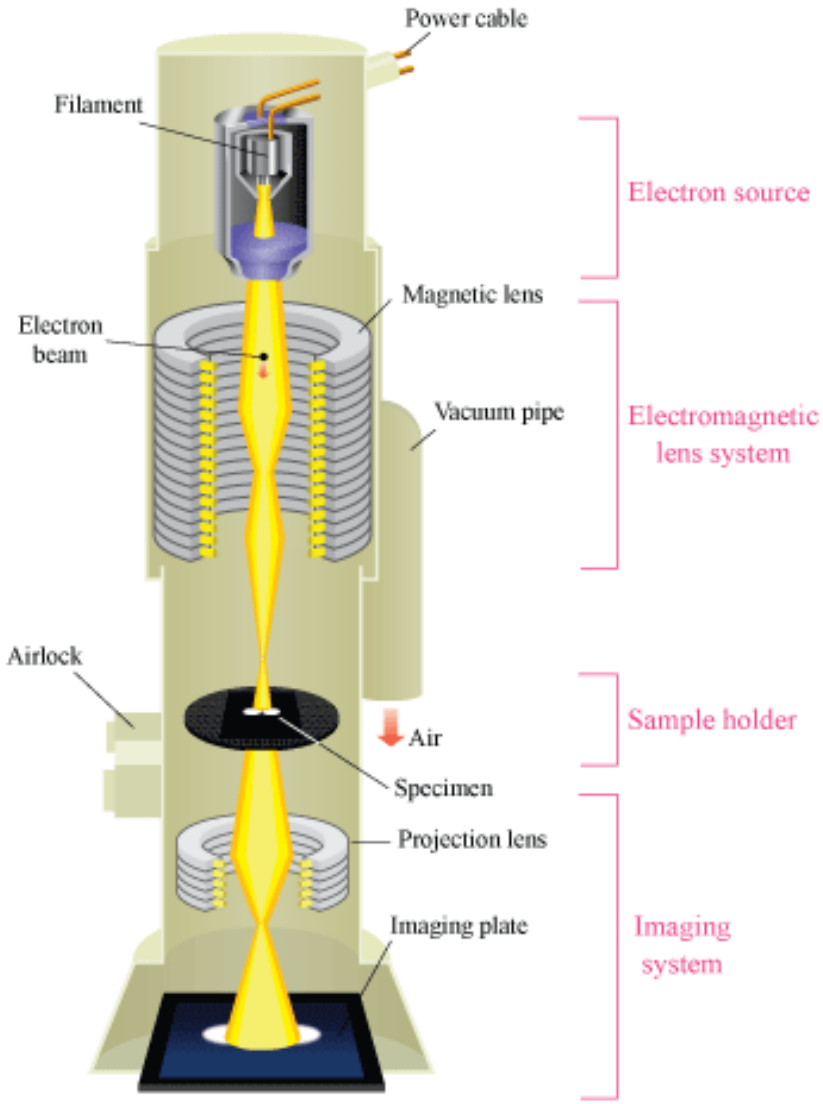

Figure 3-7 Schematic outline of a transmission electron microscopy[145]

A TEM contains four parts: electron source, electromagnetic lens system, sample holder, and imaging system (Figure 3-7). Electron beam accelerated to nearly the speed of light by an applied voltage up to 300kV is emitted from the electron source, and then the beam is tightly focused using electromagnetic lens and metal apertures. This system only allows electrons within a small energy range to pass through, so the electrons in the electron beam will have a well-defined energy. After that, electron beam will penetrates through an ultra-thin sample, which is loaded in the sample holder. Lastly, in the imaging system, the transmitted electrons will project onto the screen to form images about the topological and compositional information of the testing sample, and digital camera is equipped to capture these images. An amplified image will be produced in the image plane of the objective lens,

while diffraction pattern will be formed in the back focal plane. By changing objective plane of the intermediate lens, two basic viewing modes in TEM can be obtained, as shown in Figure 3-8.

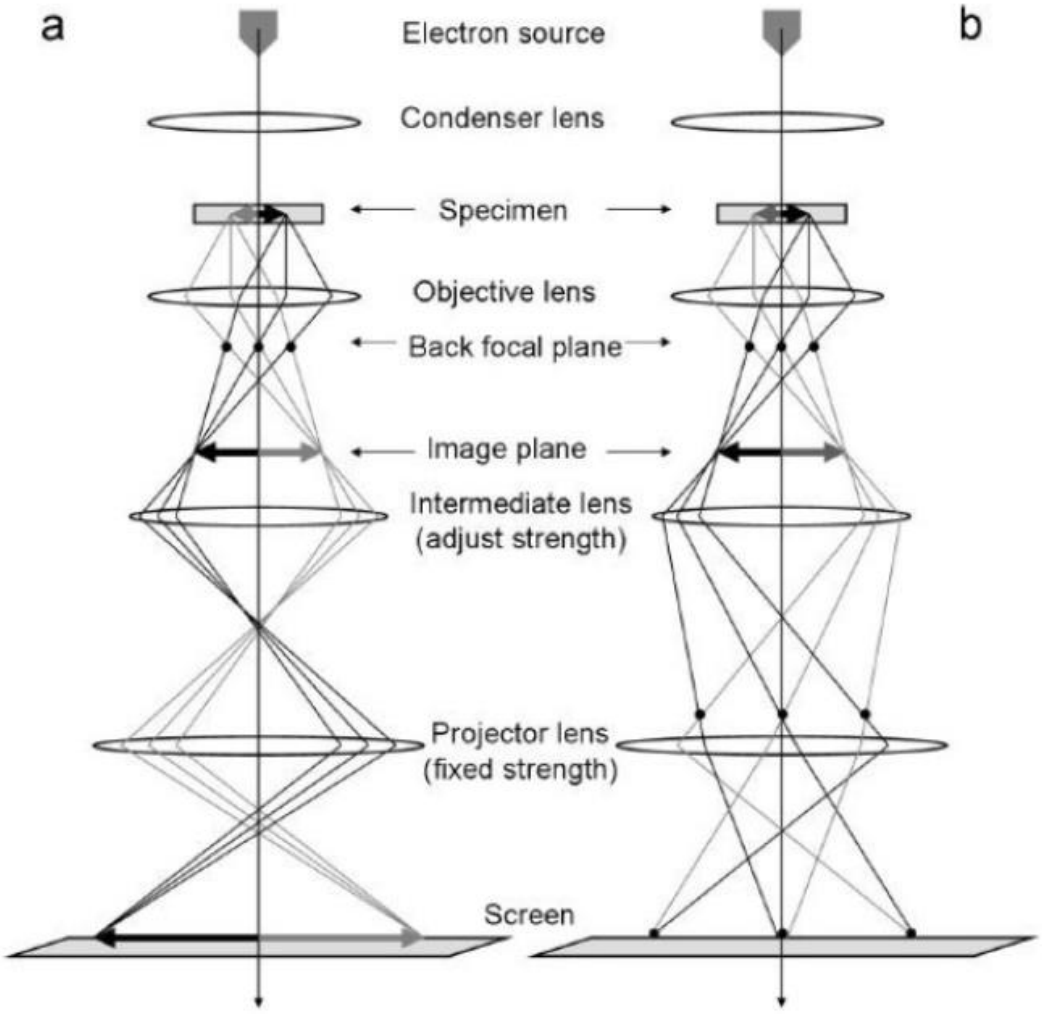

Figure 3-8 Schematic illustration of the diffraction (a) and imaging (b) mode of a TEM[146].

TEM has several working modes, which are listed below:

Diffraction Mode - When the specimen is crystalline, electrons will be diffracted by atomic planes of the crystal. The electrons that penetrated the specimen are focused by the objective lens. Electrons that have been diffracted to the same angle are focused at the same position in the back-focal plane of the objective lens, which gives the electron diffraction (ED) pattern. To make the ED patterns visible, the intermediate lens of the TEM is weakened, making the back focal plane of the objective lens coincide with the object plane of the intermediate lens. The diffraction pattern can then be viewed on the screen or recorded by a CCD camera. A selective area aperture can be inserted on the image plane

to perform an ED of a confined area on the specimen. This technique is called selective area electron diffraction (SAED).

Imaging Mode-After the electrons penetrate the specimen, they are focused by the objective lens. At the image plane, the image of the specimen is reconstructed. After passing the intermediate lens and projector lens, the enlarged image of the specimen is projected onto the fluorescent viewing screen at the bottom of the column. The images can be recorded by an electron sensitive CCD camera. In addition, the objective aperture can be inserted to increase the diffraction contrast in a TEM image.

Despite those basic viewing modes, there are still other advanced TEM techniques:

High Resolution TEM (HRTEM)- Both transmitted and scattered beams are used to create an HRTEM image of the specimen at the atomic level. The condition to acquire HRTEM image is that the direction of the incident electron plane wave is parallel to the low-index zone axis of a crystal. Besides, the TEM must have low spherical aberration and highly stable electron beam, the specimen also has to be thin enough (generally <50nm).

Scanning Transmitted Electron Microscopy (STEM) - STEM works like an SEM in some way, providing high angle annular dark field (HAADF) image. A small electron probe scans through the specimen and generates a number of different transmitted electron signals. These signals are collected by different detectors to form different images, such as a bright/dark field (B/DF) STEM image, high angle annular dark field (HAADF) image. The probe size and the spherical aberration of the TEM affect the resolution of the STEM image. Since the STEM images are formed by inelastic scattered electrons, no strain contrast is involved in the imaging process.

Energy Dispersive X-ray spectroscopy (EDXS, also known as EDS)- Similar to SEM, EDS analysis can also be performed in a TEM but with much higher resolution.

Electron Energy Loss Spectroscopy (EELS)- After the electron beam penetrates through the specimen, the inelastically scattered ones can form the EELS spectrum, which contains compositional information of the specimen. As EELS does not involve electrons jumping down to lower energy shells, materials with only one or two electron shell/s can also be analysed using EELS. This is the major advantage of EELS over EDS analysis.

Energy Filtered Transmission Electron Microscopy (EFTEM)- By using the EELS spectrum collected from the specimen, one can choose a certain element and obtain an

elemental map of the specimen. This is achieved by acquiring images using electrons with pre-defined energy losses. It works in a similar fashion as the EDS mapping in SEM.

Electron Tomography (ET)- By taking a series of images of the specimen through a range of tilting angles, a 3D image of the specimen can be reconstructed using specific software. This technique gives the scientists the opportunities to study the 3D structures of much more sophisticated materials.

3.2.4 X-ray Diffraction

W.C. Röntgen discovered the X-rays in 1895, and based on the elastic scattering of X-rays from crystalline specimen X-ray Diffraction (XRD) techniques were developed to characterize materials. XRD techniques include single-crystal X-ray diffraction (SCD) and powder X-ray diffraction (PXRD). SCD technique is the sound method to determine the identity and structure of new or already known compounds, thus it is a critical tool in chemical research, from mineralogy to pharmaceutical products, from catalysis to macromolecules. SCD is complicated, time consuming, and requires a high degree of homogeneity to the selected crystal. To overcome such hurdles, PXRD was proposed to study the crystal structure, crystalline size, and orientation distribution in polycrystalline or powdered crystalline materials.

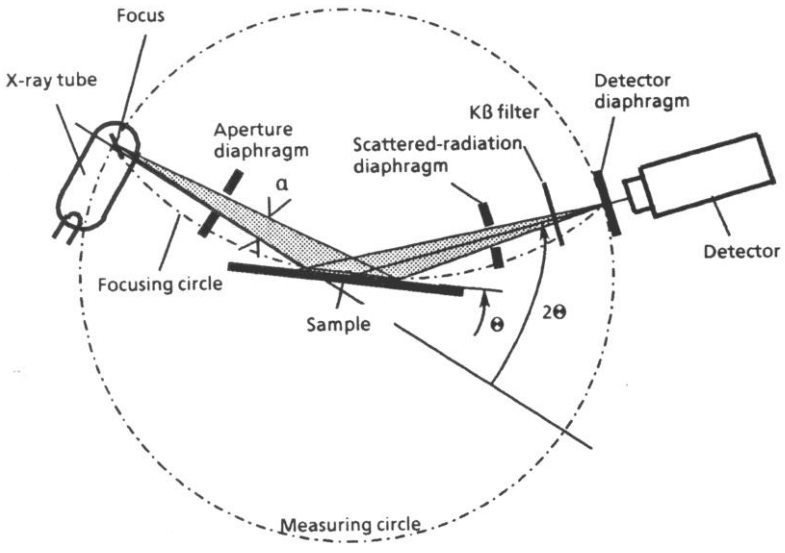

Figure 3-9 Schematic diagram of diffractometer system.[147]

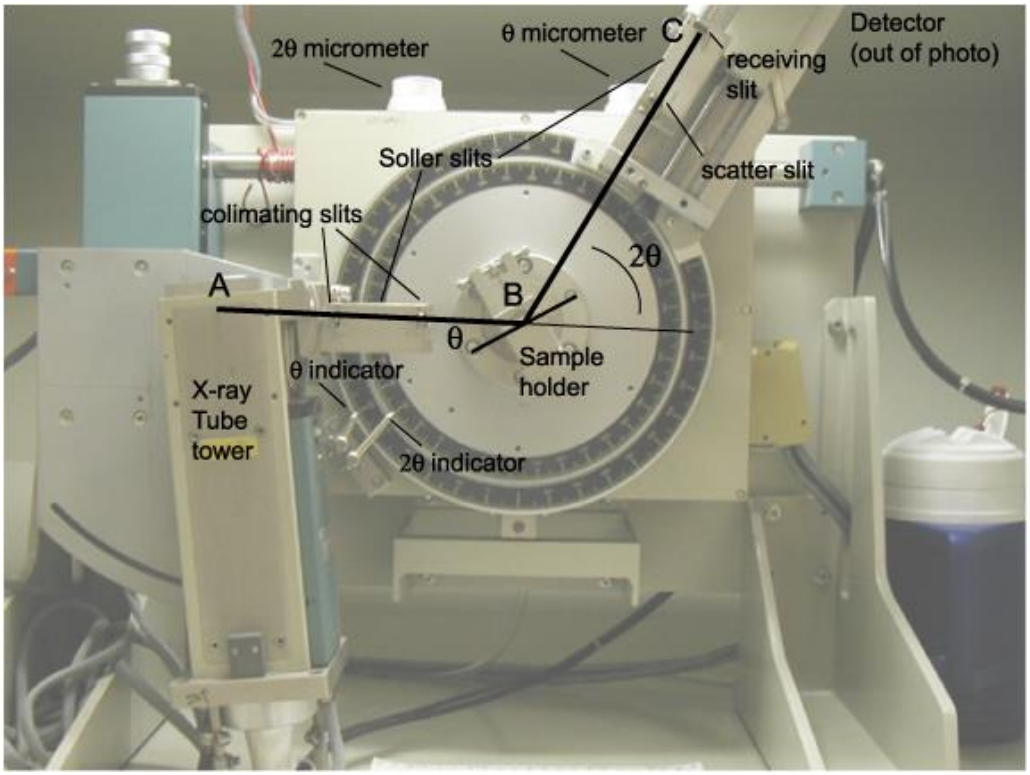

Figure 3-10 A photo of a X-ray diffractometer system.[148]

The working principle of XRD device is illustrated in Figure 3-9. X-ray diffractmeter, which is used to conduct XRD analysis is generally composed of three primary components: an X-ray tube to generate the X-ray source, a sample holder to hole the analyzing samples, and an X-ray detector. What is presented in Figure 3-10 is the real XRD analysis device. In a cathode ray tube, electrons are firstly emitted by a heated filament, and are then accelerated toward a target by applying an electric field. Afterwards, the high-velocity electrons are used to bombard the X-ray generating material. Characteristic X-rays can be produced to provide the X-ray sources providing that electrons with sufficient energy to dislodge inner shell electrons from the X-ray generating materials. Copper, for example, is commonly used as X-ray generating material, with the wavelength of the Cu K_α radiation λ=1.5418Å. These X-rays are collimated and directed onto the testing sample. As the sample and detector are rotated, the intensity of the reflected X-rays is recorded. When the geometry of the incident X-rays impinging the sample satisfies the Bragg equation, constructive interference occurs in a form of a peak at the position of 2θ. In the X-ray diffractometer, the sample rotates in the path of the X-ray beam at an angle θ, while the X-ray detector is mounted on an arm which rotates at an angle of 2θ to collect the diffracted X-rays. The instrument used to maintain the angle and

rotate the sample is termed a goniometer. For typical powder diffraction patterns, data is collected at 2θ from around 5° to 70°.

In this project, powder diffraction is applied for analysis of the crystalline phases of synthesized products. After being obtained, diffraction data is compared against a database maintained by the International Centre for Diffraction Data to identify the phase composition of the products.

3.3 Spark plasma sintering

We employed the SPS to compress the as-synthesized nanopowders for thermoelectric performance evaluation. Compared with other compressing techniques, SPS can compress the powder into pellet with relative density over 90% with relatively lower temperature and shorter processing time. Most importantly, grain growth is effectivley restrained dueing SPS sintering; therefore, we can obtain sintered products with dense grain boundaries and small grain size.[149] SPS process is a pressure assisted pulsed current sintering process utilizing ON-OFF DC pulse energizing. The repeated application of an ON-OFF DC pulse voltage and current between powder materials, the spark discharge point and the Joule heating point (local high temperature-state) are transferred and dispersed to the overall specimen.[150]

As shown in Figure 3-11, SPS system consists of a sintering machine with vertical single-axis pressurization and built-in water-cooled special energizing mechanism, a water-cooled vacuum chamber, atmosphere controls, vacuum exhaust unit, special sintering DC pulse generator and a SPS controller. The powder materials are stacked between the die and punch on the sintering stage in the chamber and held between the electrodes. Under pressure and pulse energized, the temperature instantly rises to 1000~2500℃ above the ambient temperature, resulting in the production of a high quality sintered compact in only a few minutes.

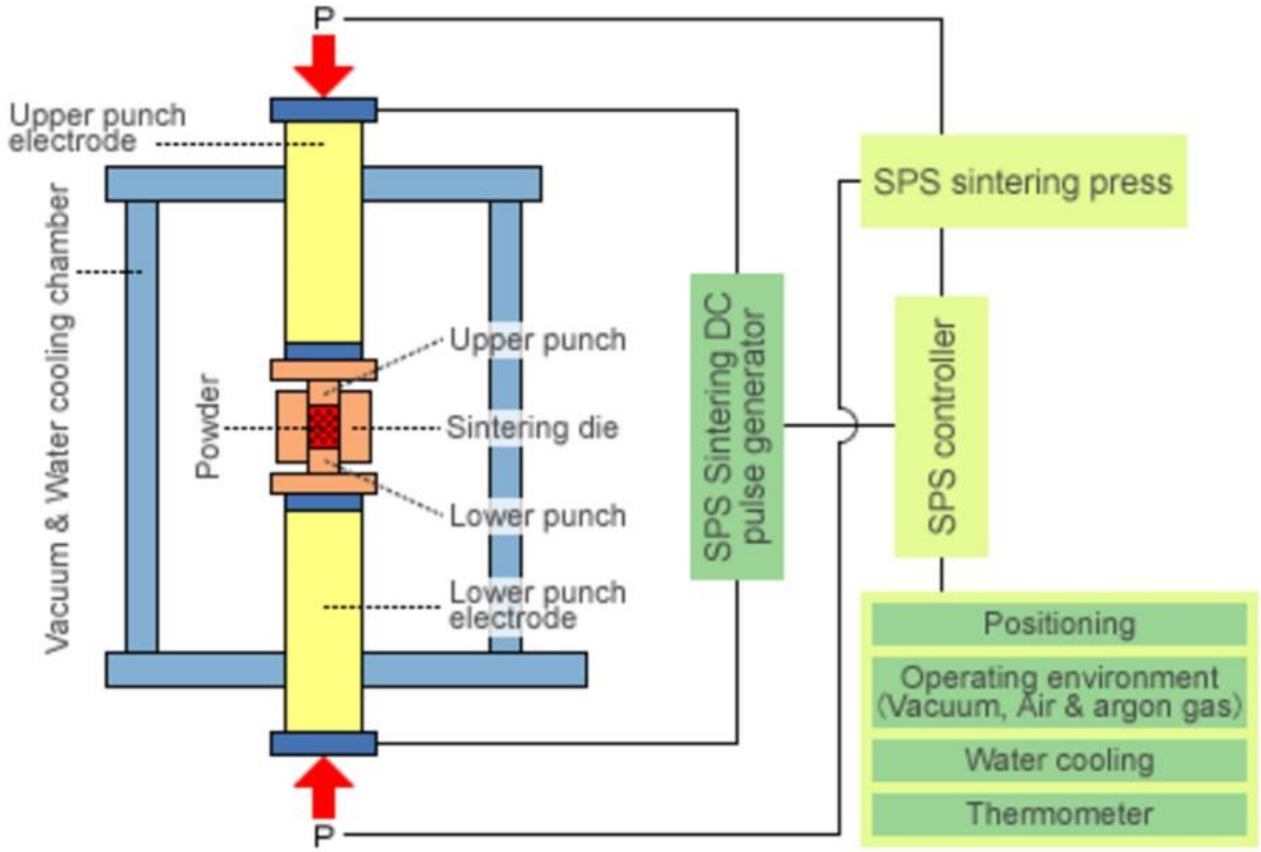

Figure 3-11 SPS system configuration (http://sps.fdc.co.jp/whats/whats3.html).

In this thesis, our as-prepared nanostructures of Bi_2Te_3 families were put into the high-strength graphite die with diameter of 12.5 mm and heigh of 35 mm. The amount of nanopowder was determined based on the size of finally obtained pellets and the density. After loading the graphite die into the chamber, it should be ensured that a thermo couple was fully insert into the hole on the wall of die. Then, the pump is turned on. To achive high vacuum, we used Ar gas to wash the chamber. After three circulation of pumping and inouting Ar gas, we obtained vacuum as high as ~5 $\times 10^{-5}$ Pa. Then, we add presser, and start the sintering. The temperature rising was programmable. The as-syntehsized nanopowders were sintered under 40 MPa and at 250 ˚C for 5 min in vacuum. After the sintering, the density could be over 90% based on the Archimedes method.

3.4 Thermoelectric performance evaluation

Based on the sintered pellets, we employed the ZEM-3, ULVAC to simultaneously measure the *S* and σ, and the laser flash method (LFA 457, NETZSCH) to measure the

thermal diffusivity (D). The working principles and the detailed measurement conditions in this PhD project are presented below.

3.4.1 The working principle of ZEM-3

ZEM-3 can simultaneously measure the electrical conductivity and Seebeck coefficient for the sample, which is required to be rectangular cylinder or circular cylinder. Figure 3-12 (a) illustrates the four probe method for resistivity measurement. Specifically, the sample is loaded between the two electrode blocks, and the side wall of the testing sample is contacted with the parallel probe A and probe B. To ensure the Ohmic contact between the sample and the two side parallel probes, V-I curve is measured before launching the measurement. Afterwards, to measure the resistance (R), a constant current is applied to the sample through the two electrode blocks, and then the voltage between the two parallel probes is measured by the digital multi meter. Finally, R of the sample is obtained. Then, the electrical conductivity is calculated by $\sigma = L/(Rs)$ with L representing the distance of the two side parallel probes, and s representing cross section area of the testing sample. Figure 3-12 (b) demonstrates the measurement of S. In the bottom electrode blocks, there is a heater for generating temperature difference. The two side parallel probes are thermocouples, which measure the temperature values at the two contact points on the samples, which means the temperature difference ΔT is obtained. Meanwhile, the correspondingly generated voltage V between the two contact points is obtained from the multi meter. Finally, S is calculated by $S = V/\Delta T$.

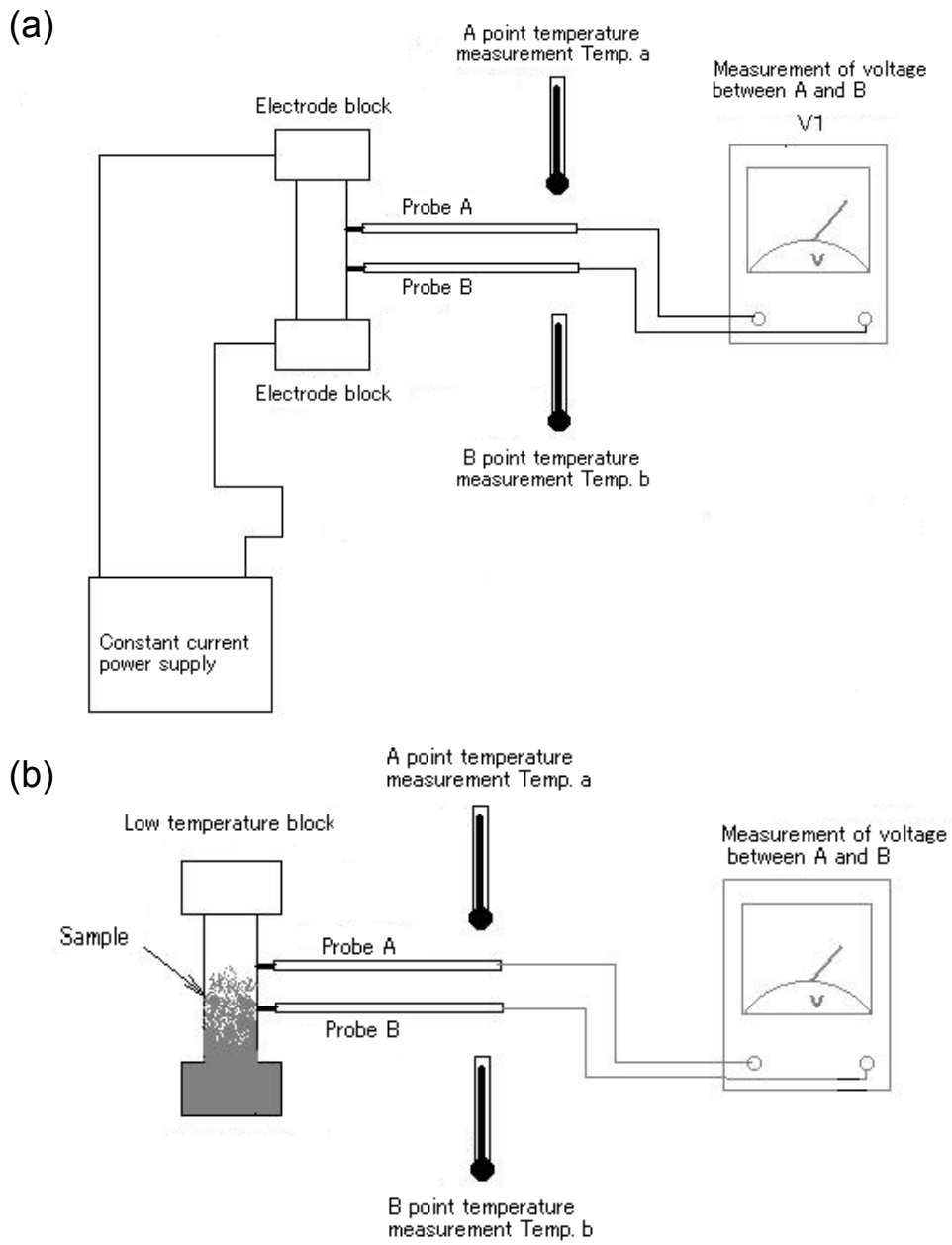

Figure 3-12 Schematic illustrating the working principle of ZEM-3: (a) resistivity measurement, and (b) Seebeck coefficient measurement (Reproduced form the ZEM-3 operation manual).

Figure 3-13 is the photograph of ZEM-3, which includes the heating furnace, temperature controller, power supply, digital multi-meter, etc. The heating furnace consisting of the infrared lamp heating system provides the surrounding high temperature for the testing sample. The electrode up/down dial enables to adjust the electrodes for loading samples with different length, and the probe movement knob is used to move the side probes to contact with the sample. Moreover, there are temperature controlling

systems for the heating furnace and the heating unit in the bottom electrode block, respectively. To measure the resistivity (electrical conductivity), a constant current should be applied to the sample, which is achieved by the constant. The multi meter is also equipped to measure the voltage.

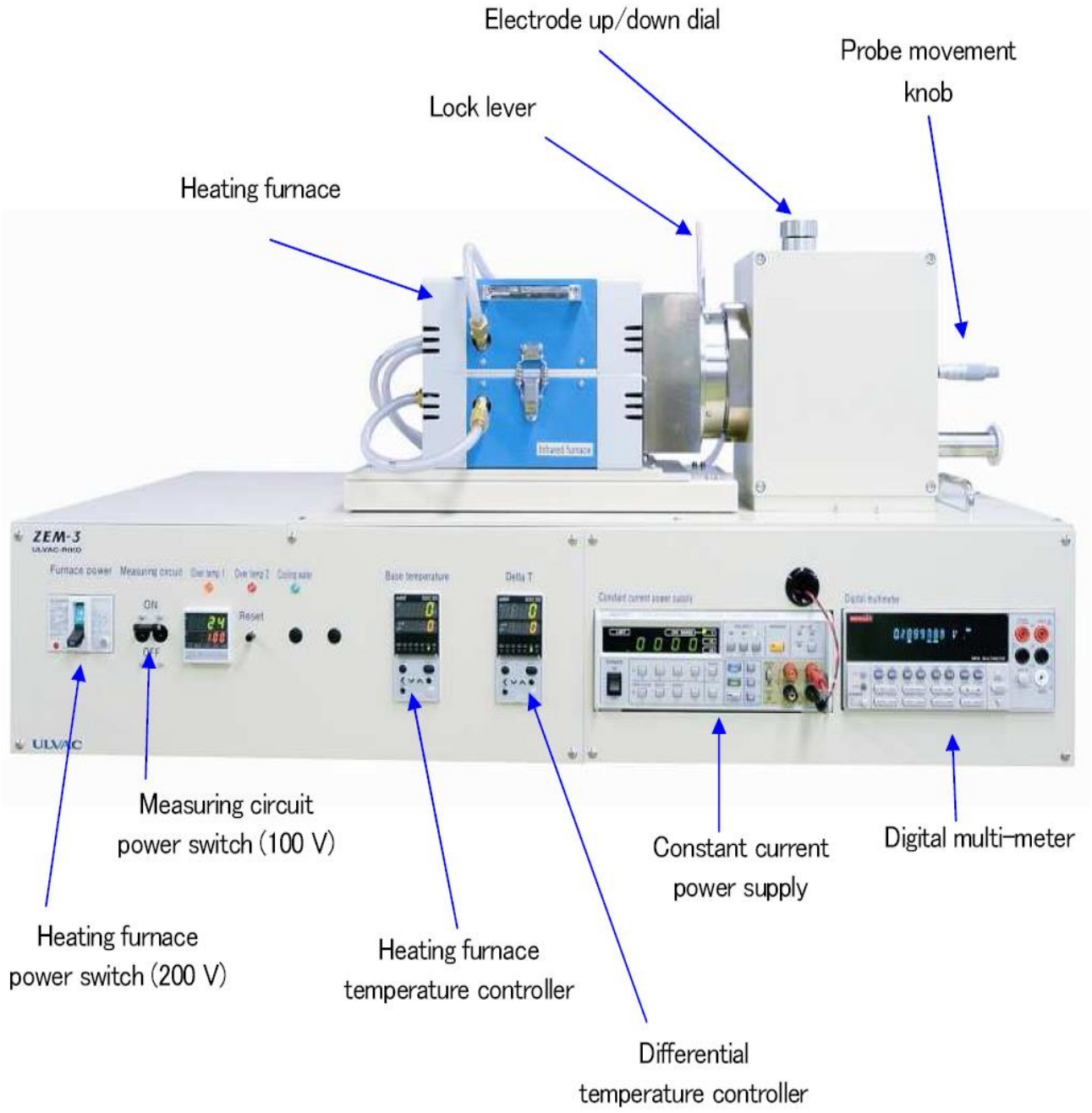

Figure 3-13 Overall view of the ZEM-3, ULVAC (Reproduced from ZEM-3 operation manual).

3.4.2 The working principle of laser flash

Laser flash method was developed by Parker et al. in 1961[151] and is the most used technique nowadays in determining thermal conductivity at high temperatures. Figure 3-14 (a) illustrates the working mechanism of laser flash method for measuring the thermal diffusivity. At a setting temperature controlled by the furnace, the laser beam from the laser generator is applied on the bottom surface of testing sample, so that the temperature of the bottom surface increases. Following that, the heat transfers from the hot side (bottom surface) of the sample to its cold side (top surface). The infrared detector above the sample continuously detects the temperature rising process of the center are of the top surface. As a consequence, we can obtain the curve of detected signal versus time, as shown in Figure 3-14 (b). The spot size of the laser beam is required to be as small as possible; therefore, the heat transfer through the bottom to the top of the testing sample is theoretically along one dimension without radial heat transfer. Through determining the half heating time marked in Figure 3-14 (b), we can obtain the thermal diffusivity of the testing with thickness of *l* at the setting temperature by[152]

$$D = 0.1388\frac{l^2}{t_{1/2}} \tag{3.1}$$

In real applications, it is impossible to avoid the heat loss on the surface and heat transfer along the radial direction, and the finite pulse wide of the laser is hardly to ensure the spot size of laser on the sample is finitely small. Thus, the directly obtained data needs to be corrected based on the certain algorithm, which can be done by choosing a proper correction model for each sample before measurement.

Then, thermal conductivity κ is calculated with

$$\kappa = DC_p d \tag{3.2}$$

where d is the density of the testing and C_p is the heat capacity, respectively. d is determined at room temperature by Archimedes method, and is regarded to be temperature independent. C_p can be measured by the commercial facility; however it turns out to be challenging to precisely measure its value. Therefore, in this research project, we used the empirical formulas, for instance $C_{P_{ST}} = 120.3 + 28.0\times10^{-3}T$ $JK^{-1}mol^{-1}$ for Sb_2Te_3,[153] $C_{P_{BT}} = 108.06 + 5.53\times10^{-2}T$ $JK^{-1}mol^{-1}$ for Bi_2Te_3,[154] and C_{pBS} = $118.61+1.92\times10^{-2}T$ $JK^{-1}mol^{-1}$ for Bi_2Se_3,[154] respectively.

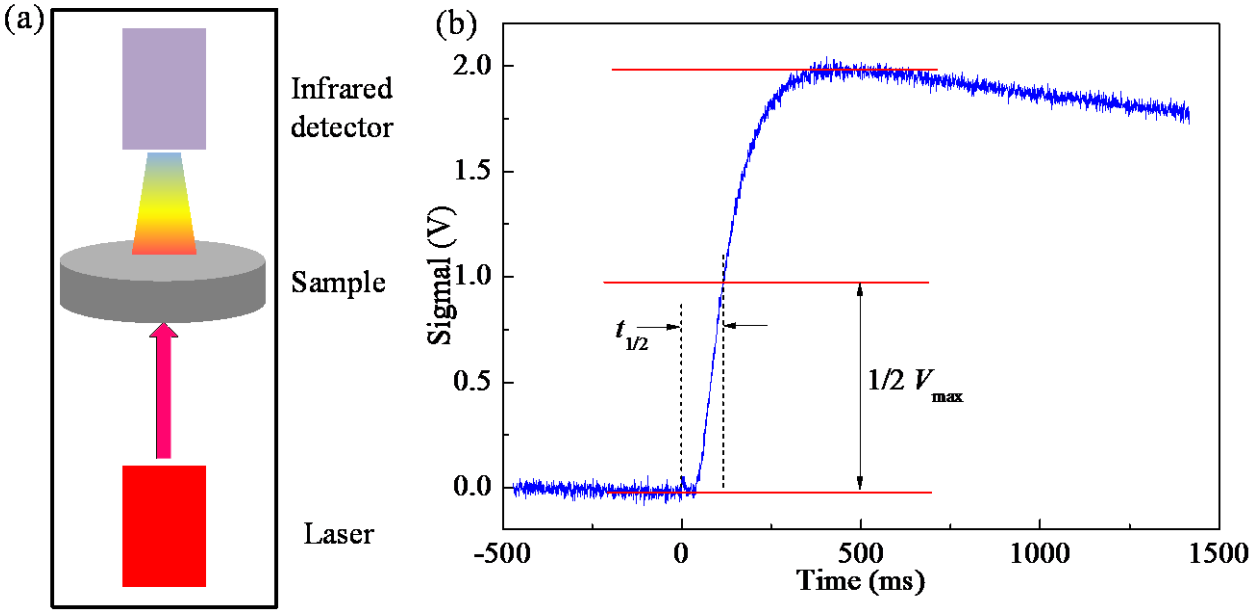

Figure 3-14 (a) Schematic illustrating the working principle of Laser flash. (b) Output signal from the infrared detector.

Figure 3-15 shows the commercial LFA 450 systems. In the bottom, there is a laser generator. The horizontal laser beam is reflected by the mirror to be vertical, and finally reach on the sample. The SiC sample carrier has two windows, the one underneath the sample being bigger. The sample is required to be circular (diameter of 12 mm) or square shape (length of 10 mm). Thickness depends on the thermal diffusivity. Normally, D > 50 mm^2/s, thickness should be in the range of 2 to 4 mm, 1< D < 50 mm^2/s, thickness should be in the range of 1 to 2 mm, and D < 1 mm^2/s, thickness should be less than 1 mm. The sample should be coated with graphite (thickness of ~ 0.2 mm) to ensure good light absorption. Above the sample, there is InSb infrared detector with the dewar on the top to load liquid N_2 for cooling the detector. To conduct high temperature measurement, there is a small heating furnace, which can be lift up by the hoist to load sample. The measurement temperature is detected by the thermal couple beside the sample.

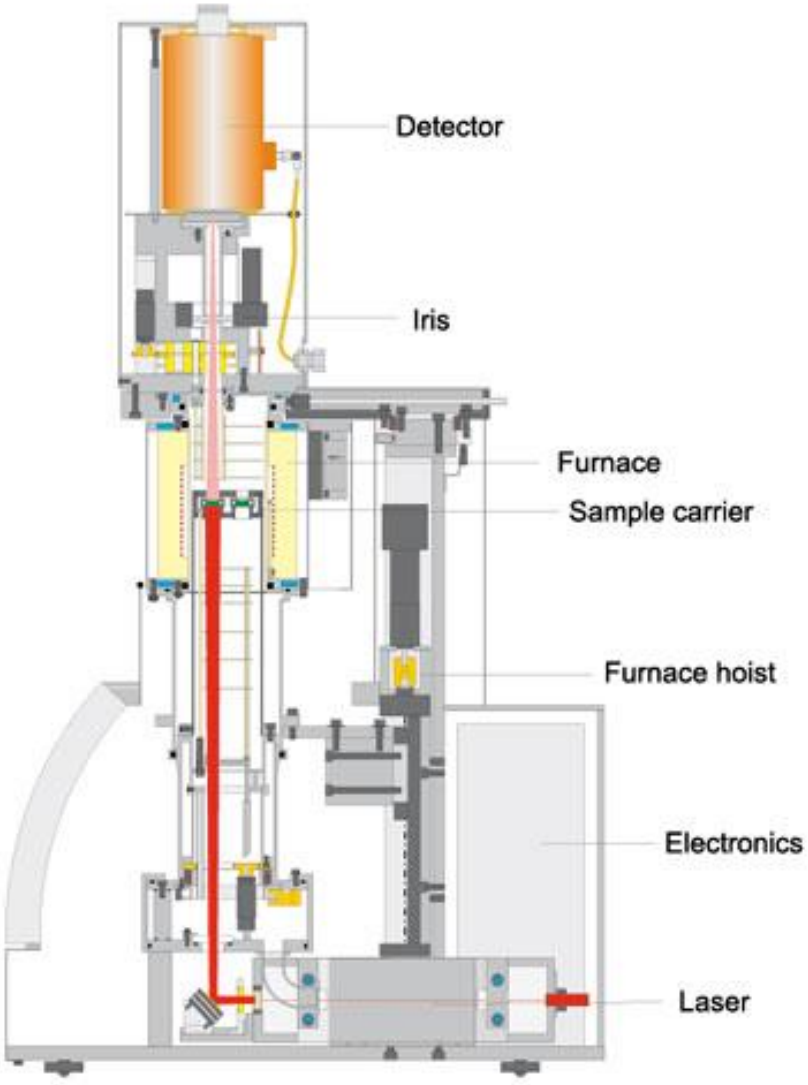

Figure 3-15 The LFA 457 system for high temperature thermal conductivity measurement (https://www.netzsch-thermal-analysis.com/us/products-solutions/thermal-diffusivity-conductivity/lfa-457-microflash/).

3.5 Van der Pawl Hall measurement

The carrier density and carrier mobility were measured using Van der Pauw method.[155] Figure 3-16 shows the contact arrangement for Van der Pauw method. Generally, the testing sample is in the circular shape or square shape. To ensure the Ohmic contact, the contant resistance for each contact is measured. This value depends on the specific material system, varing from 1 to 2 for heavily doped samples to high tens for undoped samples. Good Van der Pawl Hall measurement requires: (1) the sample must have a flat shape of uniform thickness; (2) the sample must not have any isolated holes; (3) the

sample must be homogeneous and laterially isotropic; (4) all four contacts must be located at the edges of the sample; and (5) The area of contact of any individual contact should be at least an order of magnitude smaller than the area of the entire sample.[156] Prior to measure the Hall coefficient, we obtain the resistivity. A constant current passes through 1,2, and a voltage can be measured at 3,4. According to the Ohm's law, the sheet resistance $R_{12,34}$ is obtained. Similarly, another sheet resistance $R_{34,12}$ is obtained as well. The resistivity (ρ) can be calculated using the Van der Pauw formula, namely[155]

$$e^{-\frac{\pi R_{12,34} l}{\rho}} + e^{-\frac{\pi R_{34,12} l}{\rho}} = 1 \tag{3.3}$$

where, l is the thickness of the testing sample.

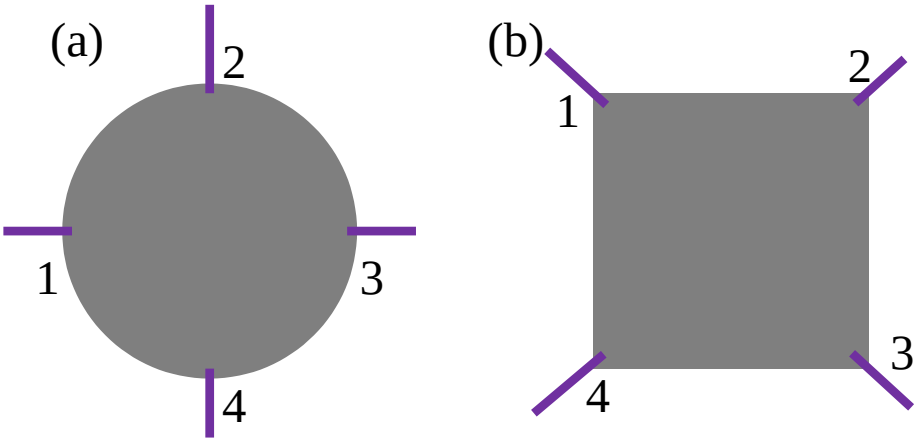

Figure 3-16 Contact arrangements of Van der Pauw method for (a) circular sample and (b) square sample.

To measure the Hall coefficient (R_H), a magnatic filed (B) is applied vertically to the surface of testing sample. A constant current flows through contacts 1,3, and then measure the voltage V_{24}. Then, after reversing the direction of magnative filed, measrue the voltage V'_{24} again. Similarly, applying the constant current flows though contacts 2,4, and the voltage V_{13} and (V'_{13} under opposite magnative filed direction) is measured. Finally, the Hall coefficient is calculated by[157]

$$R_{H1} = \frac{V_{24} \cdot B - V'_{24} \cdot (-B)}{2BI_{13}} \tag{3.4}$$

$$R_{H2} = \frac{V_{13} \cdot B - V'_{13} \cdot (-B)}{2BI_{24}} \tag{3.5}$$

$$R_H = \frac{R_{H1} + R_{H2}}{2} \tag{3.6}$$

The Hall carrier density (n_H) and Hall carrier mobility (μ_H) can be calculated by

$$n_H = \frac{1}{eR_H} \tag{3.7}$$

$$\mu_H = \frac{R_H}{\rho} \tag{3.8}$$

where, e is the electron charger.

In this research project, the Hall measurement was done in Prof Jeff Snyder's lab, Northwestern University, US. The magnititude of applied magnative filed is up to ±2 T. The temperature is in the range of 300 K to 500 K with the chamber under high vacuum to aviod oxidation.

3.6 Optical property measurement

We used the optical properties to explore the band structure information and the carrier scattering types. In this project, we employed Diffuse Reflectance Infrared Fourier Transform Spectroscopy (DRIFTS) to measure the optical properties. DRIFTS measurement requires a small amount of fine-grounded powder sample (200 mg or less). Because of the Fourier transform analysis, light at all frequencies can be measured simultaneously, greatly reducing sampling time. In this project, room temperature optical diffuse reflectance measurements were conducted in the mid-IR range 0 – 0.7 eV (400 – 6000 cm^{-1}) using a Nicolet 6700 FT-IR spectrometer. A silver mirror was used as background. The absorption spectra (α/s) are obtained by the Kubelka – Munk function relating the diffuse reflectance (R) with the absorption coefficient (α) and the scattering coefficient (s) through[158]

$$(\alpha / s) = \frac{(1-R)^2}{2R} \tag{3.9}$$

By fitting the optical absorption edge, we can obtain the optical band gap values. The method of extraction of the optical band gap depends on the type of transition observed. In direct transition, we used the $(\alpha/s)^2 \propto \hbar\omega$ with $\hbar\omega$ representing the phonon energy to fit the absorption, whereas in indirect transition, the fitting formular is in the form of $(\alpha/s)^{1/2} \propto \hbar\omega$.

By fitting the free carrier absorption tail, we can determine the free carrier scattering type(s). The details of optical band gap dirivation and carrier scattering type determination are discused in Chapter 7.

3.7 Other experimental techniques

In this thesis, we employed atomic force microscopy (AFM) to determine the thickness of Bi_2Se_3 nanosheets, Raman spectroscopy to examine the crystal structure modification, and Fourier transform infrared spectroscopy (FTIR) to explore the residuals of organic surfactant in the final products. Their working principles are introduced as follows

- ***atomic force microscopy* (*AFM*)**

AFM is a very-high-resolution type of scanning probe microscopy, with demonstrated resolution on the order of fractions of a nanometer, more than 1000 times better than the optical diffraction limit. The main component of AFM is the cantilever with a sharp tip (probe) at its end. When the tip is scanning the specimen surface, there is deformation happened to the cantilever due to the Van der Waals force between the tip and the atoms of the specimen surface. Based on the feedback of deformation, the imaging system can exhibit the topographic information of the examined specimen. In this thesis, we used AFM to test the thickness of Bi_2Se_3 nanosheets under tapping mode. The as-prepared nanopowders were fully dispersed in the ethanol by sonication, and then dripped onto the mica sheet.

- ***Raman spectroscopy***

Raman spectroscopy provides information about molecular vibrations that can be used for sample identification and quantitation. The technique involves shining a monochromatic light source (i.e. laser) on a sample and detecting the scattered light. The majority of the scattered light is of the same frequency as the excitation source; this is known as Rayleigh or elastic scattering. A very small amount of the scattered light (ca. 10-5% of the incident light intensity) is shifted in energy from the laser frequency due to interactions between the incident electromagnetic waves and the vibrational energy levels of the molecules in the sample. Plotting the intensity of this "shifted" light versus frequency results in a Raman spectrum of the sample. Generally, Raman spectra are plotted with respect to the laser frequency such that the Rayleigh band lies at 0 cm-1. In thesis, we employed Raman spectroscopy to explore the crystal structure modifications of Bi_2Se_3 nanosheets due to

thickness reduction, and $Bi_xSb_{2-x}Te_3$ as well as $Bi_2Te_{3-x}Se_x$ nanoplates because of alloying effect.

- ***Fourier transform infrared spectroscopy* (*FTIR*)**

In infrared spectroscopy, IR radiation is passed through a sample. Some of the infrared radiation is absorbed by the sample and some of it is passed through (transmitted). The resulting spectrum represents the molecular absorption and transmission, creating a molecular fingerprint of the sample. Like a fingerprint no two unique molecular structures produce the same infrared spectrum. This makes infrared spectroscopy useful for several types of analysis, including identification of unknown materials, determination the quality and the amount of constitutions in a mixture. In this thesis, we used FTIR to determine the residuals of PVP on the obtained final Bi_2Se_3 nanosheets, and analyzed the effect of removal of PVP by baking.

3.8 References

(1) http://serc.carleton.edu/research_education/geochemsheets/electroninteractions.html.

(2) Reimer, L. *Scanning electron microscopy: physics of image formation and microanalysis 3rd edition*. Springer: Berlin Heidelberg, **2010**.

(3) Egerton, R. F. *Physical principles of electron microscopy : an introduction to TEM, SEM, and AEM*. Springer: USA, **2005**.

(4) Reimer, L. *Scanning electron microscopy : physics of image formation and microanalysis 2nd edition*. Springer: Heidelberg, **1998**; Vol. Second edition.

(5) Mehta, R. Interactions, imaging and spectra in SEM. In *Scanning electron microscopy*, Kazmiruk, V., Ed. InTech: Rijeka, Croatia, 2012.

(6) Mehta, R. J.; Karthik, C.; Singh, B.; Teki, R.; Borca-Tasciuc, T.; Ramanath, G. Seebeck Tuning in Chalcogenide Nanoplate Assemblies by Nanoscale Heterostructuring. *ACS Nano* **2010**, 4, 5055-5060.

(7) Fan, X. A.; Yang, J. Y.; Xie, Z.; Li, K.; Zhu, W.; Duan, X. K.; Xiao, C. J.; Zhang, Q. Q. Bi_2Te_3 hexagonal nanoplates and thermoelectric properties of n-type Bi_2Te_3 nanocomposites. *J. Phys. D. Appl. Phys.* **2007**, 40, 5975-5979.

(8) Williams, D. B.; Carter, C. B. *Trasmission electron microscopy: a textbook for materials science*. Springer: Huntsville, **2009**.

(9) Yao, Q.; Zhu, Y.; Chen, L. Preparation of bismuth telluride nanometer tube using microwave liquid phase heating process comprises preparing reactant solution, placing solution into microwave reactor, and cooling off the obtained product. CN101254903-A; CN101254903-B.

(10) http://geology.uprm.edu/facilities/Class%20Forms/xrd.pdf.

(11) Zhang, Z.-H.; Liu, Z.-F.; Lu, J.-F.; Shen, X.-B.; Wang, F.-C.; Wang, Y.-D. The sintering mechanism in spark plasma sintering – Proof of the occurrence of spark discharge. *Scripta Mater.* **2014**, 81, 56-59.

(12) Diouf, S.; Molinari, A. Densification mechanisms in spark plasma sintering: Effect of particle size and pressure. *Powder Technol.* **2012**, 221, 220-227.

(13) Parker, W. J.; Jenkins, R. J.; Butler, C. P.; Abbott, G. L. Flash Method of Determining Thermal Diffusivity, Heat Capacity, and Thermal Conductivity. *J. Appl. Phys.* **1961**, 32, 1679-1684.

(14) Corbin, S. F.; Turriff, D. M. Thermal Diffusivity by The Laser Flash Technique. In *Characterization of Materials*, John Wiley & Sons, Inc.: 2002.

(15) Pashinkin, A. S.; Malkova, A. S.; Mikhailova, M. S. The Heat Capacity of Solid Antimony Telluride Sb_2Te_3. *Russ. J. Phys. Chem.* **2008**, 82, 878-879.

(16) Mills, K. C. *Thermodynamic Data for Inorganic Sulphides, Selenides and Tellurides*. Butterworths: London, **1974**.

(17) Borup, K. A.; Toberer, E. S.; Zoltan, L. D.; Nakatsukasa, G.; Errico, M.; Fleurial, J.-P.; Iversen, B. B.; Snyder, G. J. Measurement of the Electrical Resistivity and Hall Coefficient at High Temperatures. *Rev. Sci. Instrum.* **2012**, 83, 123902.

(18) Webster, J. G. *The Measurement, Instrumentation, and Sensors: Handbook*. CRC Press: **1999**.

(19) Borup, K. A.; de Boor, J.; Wang, H.; Drymiotis, F.; Gascoin, F.; Shi, X.; Chen, L.; Fedorov, M. I.; Muller, E.; Iversen, B. B.; Snyder, G. J. Measuring thermoelectric transport properties of materials. *Energy Environ. Sci.* **2015**, 8, 423-435.

(20) Philips-Invernizzi, B.; Dupont, D.; Caze´, C. Bibliographical Review for Reflectance of Diffusing Media. *Opt. Eng.* **2001**, 40, 1082-1092.

4

Enhanced Thermoelectric Performance of Ultrathin Bi_2Se_3 Nanosheets through Thickness Control

4.1 Introduction

Bipolar conduction is responsible for the reduction of *S* at high temperature, and consequently restrains the maximum value of $S^2\sigma$. The fundamental reason for bipolar conduction is the activation of minor charger carriers at high temperature, and opening band gap is effective to supress bipolar conduction. It is well known that band gap of nanostructures can be enlarged by reducing the size of nanostructures. In this study, we successfully fabricated large-scale Bi_2Se_3 nanosheets with controllable thickness by a microwave-assisted solvothermal method. High-quality Bi_2Se_3 nanosheets with average thickness of 1 nm, 4 nm, 7 nm, and 13 nm have been fabricated. Their thermoelectric performance has been detailed investigated by experiments and fundamental nonparabolic Kane model studies. A significantly reduced thermal conductivity (only 0.41 W/mK), and enhanced power factor (4.71×10^{-4} W/mK^2 with a Seebeck coefficient of -155.32 μV/K and an electrical conductivity of 1.96×10^4 S/m) are observed in the pellet composed of single-layered Bi_2Se_3 nanosheets. Such an enhanced thermoelectric performance is ascribed to the broadened band gap and optimized Fermi level in ultrathin Bi_2Se_3 nanosheets.

4.2 Journal Publication

The results in Chapter 4 are included as it appears in *Adv. Electron. Mater.* **2015**, 1.

http://onlinelibrary.wiley.com/wol1/doi/10.1002/aelm.201500025/abstract

Enhanced Thermoelectric Performance of Ultrathin Bi_2Se_3 Nanosheets through Thickness Control

Min Hong, Zhi-Gang Chen, Lei Yang, Guang Han, and Jin Zou**

M. Hong, Dr Z.-G. Chen, Mr L. Yang, Dr G. Han, Prof. J. Zou.

Materials Engineering, The University of Queensland, Brisbane, QLD 4072, Australia
E-mail: j.zou@uq.edu.au,z.chen1@uq.edu.au

Prof. J Zou

Centre for Microscopy and Microanalysis, The University of Queensland, Brisbane, QLD 4072, Australia

Keywords: Bi_2Se_3 nanosheets, thickness controls, thermoelectric, Kane band models, band structures

Abstract

Large-scale Bi_2Se_3 nanosheets with controllable thickness have been synthesized by a microwave assisted solvothermal method. Through detailed structural characterizations, high-quality Bi_2Se_3 nanosheets with average thickness of 1 nm, 4 nm, 7 nm, and 13 nm have been fabricated. Their thermoelectric performance has been detailed investigated by experiments and fundamental nonparabolic Kane models. A significantly reduced thermal conductivity (only 0.41 W/mK), and enhanced power factor (4.71×10^{-4} W/mK^2 with a Seebeck coefficient of -155.32 μV/K and an electrical conductivity of 1.96×10^4 S/m) are observed in the pellet composed of single-layered Bi_2Se_3 nanosheets. Such an enhanced

thermoelectric performance is ascribed to the broadened band gap and optimized Fermi level in ultrathin Bi_2Se_3 nanosheets.

1. Introduction

Thermoelectric (TE) materials are capable of converting heat into electricity, offering an alternative opportunity to settle the energy crisis and environmental problems caused by the excessive consumption of traditional fossil fuels.[1-3] Energy conversion efficiency of a TE material is gauged by the dimensionless figure of merit, $ZT=S^2\sigma T/\kappa$, where S, σ, κ and T are the Seebeck coefficient, electrical conductivity, thermal conductivity, and the absolute temperature, respectively.[4] Normally, κ includes the contributions from the electronic κ_e and lattice κ_l components, as well as the component from the ambipolar contribution (κ_{amb}).[5] So far, significant progress has been achieved in increasing ZT within low dimensional materials,[6-9] although most of these attempts were targeted on suppressing κ by enlarging phonon scattering with nanograins rather than improving the power factor ($S^2\sigma$).[9-11] Therefore, increasing $S^2\sigma$ for nanostructures with intrinsically low κ is likely to further enhance ZT.

As a representative material for TE refrigeration at the room temperature range, Bi_2Se_3 with a band gap of 0.3 eV has been widely studied.[12-15] In general, Bi_2Se_3 exhibits a very low ZT, mainly ascribed to the intrinsically small $S^2\sigma$.[16] Therefore, improving their TE performance is necessary and can be achieved by improving $S^2\sigma$. One effective method to enhance $S^2\sigma$ is through the broadening of the band gap (E_g) although the corresponding σ may be decreased.[17-18] In previous studies, the band gap for Bi_2Se_3 nanosheets (NSs) can be gradually enlarged to > 0.5 eV when their thickness is reduced to 1 nm.[19]

To achieve the thickness reduction for Bi_2Se_3 NSs, the Se-Bi-Se-Bi-Se layers (known as quintuple layers, QLs, with approximately 1 nm in thickness,[20] shown in Scheme 1a) of Bi_2Se_3 crystals should be disassembled.[15,21] Various methods, such as peeling by atomic force microscope (AFM) tips,[22] lithium ionic exfoliation,[23] sonication exfoliation,[24] or molecular beam epitaxial growth,[25-27] have been successfully employed to prepare ultrathin Bi_2Se_3 NSs. However, most of these techniques are expensive and low-yield, which significantly hinders the commercialization of ultrathin Bi_2Se_3 NSs in TE applications.[28]

In this study, we demonstrate a one-step microwave-heated solvothermal method to fabricate ultrathin Bi_2Se_3 NSs with a high yield within a very short period of time (several

minutes). Inspired by using surfactants to tune the morphologies of nanostructures, poly (N-vinyl-2-pyrrolidone) (PVP, M_w = 40,000 g/mol) was employed to fabricate ultrathin Bi_2Se_3 NSs. In particular, the favourable absorption surface of PVP is the {0001} planes for the Bi_2Se_3 structure, which could restrain the stacking of QLs along the c axis, as shown in Scheme 1b.[14-15]. By our carefully designed synthesis route, Bi_2Se_3 ultrathin NSs were fabricated, and their TE performance was examined by compressing the NSs into pellets using the spark plasma sintering (SPS). An enhanced TE performance is observed in pellets made of ultrathin Bi_2Se_3 NSs. Their underlying fundamentals are symmetrically investigated, and uncover that such a remarkable improvement in $S^2\sigma$ is ascribed to the optimized Fermi level (E_f) position in ultrathin Bi_2Se_3 NSs with broadened E_g.

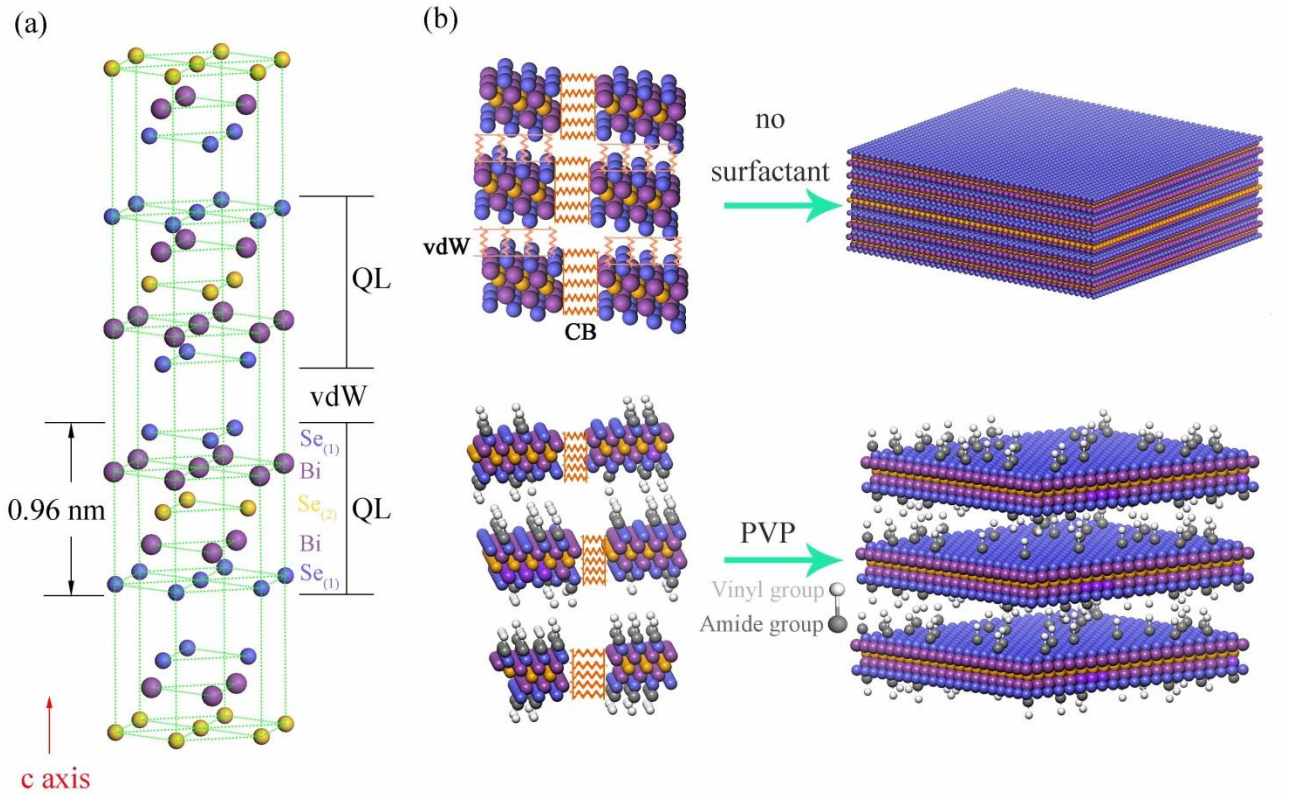

Scheme 1 (a) Bi_2Se_3 rhombohedral crystal structure exhibiting QL connected by the vdW force, (b) morphology evolution of Bi_2Se_3 NSs prepared without and with PVP. In the scheme, vdW and CB is the abbreviation of van der Waals and covalent bonding, respectively.

2. Results and Discussion

The as-synthesized products were firstly baked at 300 °C in the Ar atmosphere for 4 hours to remove the absorbed PVP. Fourier transform infrared spectrum was used to

examine the PVP residuals and the results demonstrate that PVP has almost vanished from the baked samples, as shown in Figure S1. Subsequently, AFM was employed to determine the thickness of baked NSs prepared using different PVP/Bi_2Se_3 molar ratios, namely, 0.0025, 0.0125, 0.025, and 0.05. Figure 1a is a typical AFM image of a NS prepared at a PVP/Bi_2Se_3 molar ratio of 0.0025, and Figure 1b shows the corresponding height profile in which the NS thickness is ca. 13 nm. Through analysing a larger number of baked NSs by AFM (shown in Figure S2), the average thickness is statistically revealed as 13 nm, as shown in Figure S3a. With increasing the PVP/Bi_2Se_3 molar ratio to 0.0125, Bi_2Se_3 NSs with mean thickness of ca.7 nm were obtained, as illustrated in Figure 1c and d, and their thickness distribution is shown in Figure S3b. By further increasing the PVP/Bi_2Se_3 molar ratio to 0.025, thinner Bi_2Se_3 NSs with only several QLs thick can be obtained. Figure 1e and f are an AFM image and the corresponding height profile of a typical NS with a thickness of ca. 4 nm. The histogram of thickness distribution illustrates that NSs with 4 QLs become dominate in this sample (Figure S3c). Figure 1g and h shows the evidence of a single-layered Bi_2Se_3 NS, obtained by raising the PVP/Bi_2Se_3 molar ratio to 0.05. The NS thickness distribution of this case is shown in Figure S3d, suggesting that the average thickness of obtained Bi_2Se_3 NSs is ca.1 nm. Figure 1i plots the variation of the NS thickness as a function of the PVP/Bi_2Se_3 ratio; from which, the thickness of baked Bi_2Se_3 NSs is found to gradually reduce with increasing the PVP/Bi_2Se_3 ratio, indicating that the thickness of Bi_2Se_3 NSs can be well controlled by adjusting the PVP concentration.

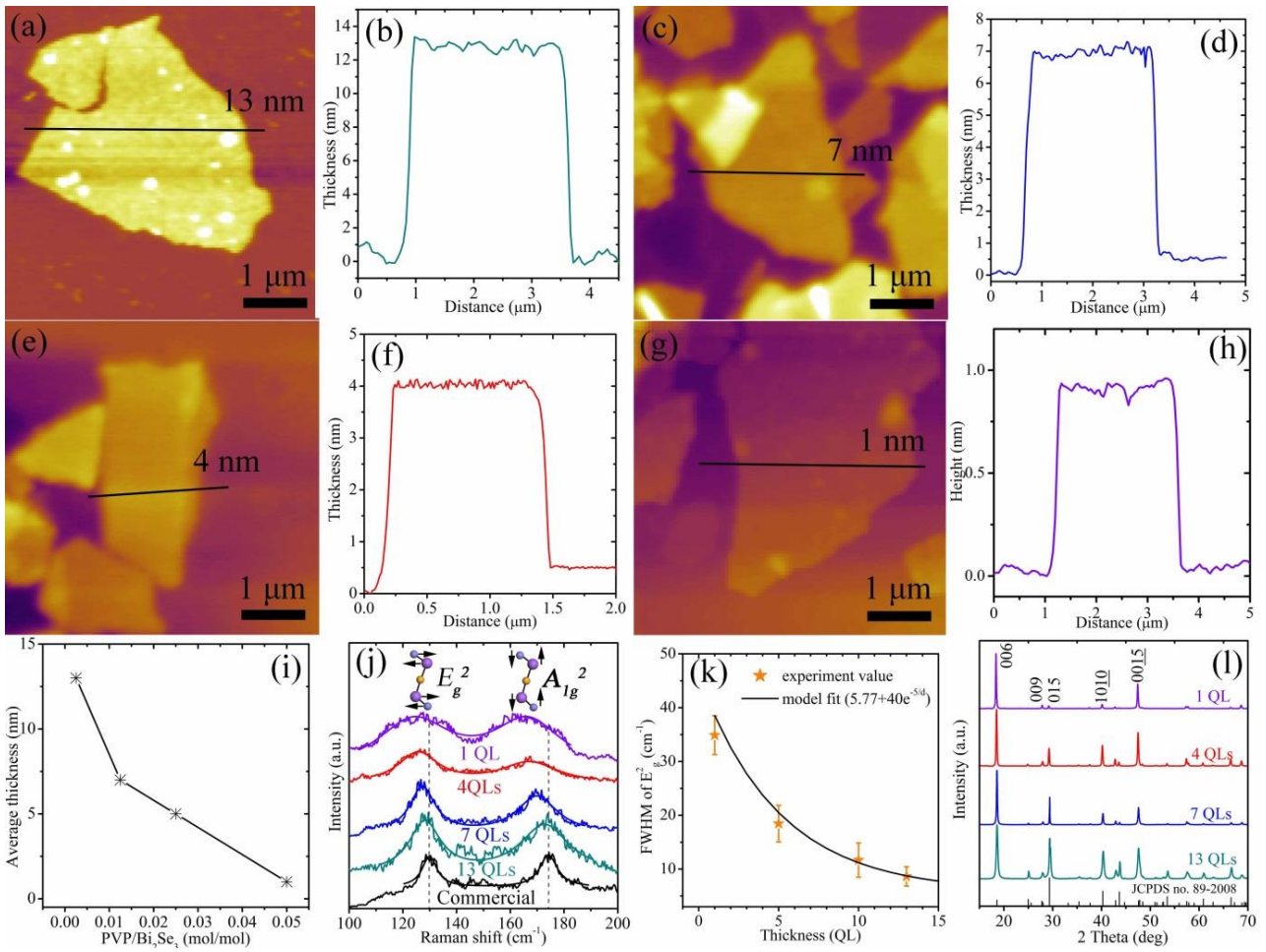

Figure 1 AFM images together with thickness distributions of Bi_2Se_3 NSs fabricated at various PVP/Bi2Se3 molar ratios: (a) (b) 0.0025, (c) (d) 0.0125, (e) (f) (0.025), (g) (h) 0.05. (i) Plot of the average thickness of Bi_2Se_3 NSs as a function of the PVP/Bi_2Se_3 molar ratio, (j) Raman spectra of NSs with various QLs thickness, (k) FWHM of the E_g^2 mode dependence on thickness of Bi_2Se_3 NSs and (l) XRD patterns of the NSs with various average thicknesses.

To further understand the thickness alternation of the synthesized products, Raman spectroscopy was subsequently employed to compare the baked NSs with commercial bulk Bi_2Se_3. Figure 1j shows the Raman spectra, in which two peaks at 131 cm^{-1} and 175 cm^{-1} were detected for the commercial bulk Bi_2Se_3, which can be assigned as E_g^2 (in-plane) and A_{1g}^2 (out-of-plane) modes, respectively.[29] Both E_g^2 and A_{1g}^2 modes of baked Bi_2Se_3 NSs exhibit broadening and shifting towards the low wave number. Such peak shifting and broadening have been observed in other ultrathin Bi_2Se_3 NSs,[30-31] which were attributed to the thickness reduction of Bi_2Se_3 NSs. Additionally, the thickness dependence of the full-

width-at-half-maximum (FWHM) of E_g^2 mode can be simulated by a phenomenological exponential format (FWHM = 5.77+40exp(-5/*d*), with the thickness (*d*)).[32] Figure 1k shows the variation of FWHM for different thicknesses of NSs (marked as stars with error bars) compared with the simulated theoretical values (dark curve) as a function of the NS thickness. As can been seen, the measured values fit well with the theoretical curve, suggesting that the theoretically estimated thicknesses according to the FWHM of E_g^2 modes are consistent with the experimentally statistic thickness determined by AFM examinations.[30-31]

To clarify the crystal structure and their orientation of baked Bi_2Se_3 NSs, XRD investigation was performed and results are shown in Figure 1l. All diffraction peaks can be exclusively indexed as rhombohedral structured Bi_2Se_3 phase (JCPDS no. 89-2008 with lattice parameters of *a* = 4.14 Å and *c* = 28.64 Å).[33] Moreover, (006) and (0015) peaks become much stronger in the obtained Bi_2Se_3 NSs, suggesting that these NSs show preferable orientation along <0001> direction. The fundamental reason is attributed to the large ratio of the lateral size and the thickness of ultrathin Bi_2Se_3 NSs.

To understand the microstructure of as-baked Bi_2Se_3 NSs, scanning electron microscopy (SEM) and transmission electron microscopy (TEM) were applied to determine the morphological and structural characteristics of single-layered Bi_2Se_3 NSs, as an example. Figure 2a is a typical SEM image of these NSs. As can been seen, the obtained Bi_2Se_3 NSs lie evenly on the substrate with a flexible feature. Figure 2b is a TEM image taken from a typical NS supported on the holey carbon film, and shows that the lateral size of the NS is ca.1 μm. The light contrast of the NS (when compared with the thin holey carbon supporting film) indicates that NS is indeed ultrathin. Figure 2c and the inset are a <0001> high-resolution TEM image and its corresponding selected area electron diffraction (SAED) pattern, in which the NS has a high quality crystal structure. Since the TEM specimen was not titled when the high-resolution TEM image was taken, the NS's normal is parallel to the incidental electron beam, so that it can be assigned as the <0001> direction, matched well with the XRD analysis (refer to in Figure 1l). To determine the composition of the NS, energy-dispersive X-ray spectroscopy (EDS) investigation was conducted. Figure 2d is the EDS profile, in which Bi and Se peaks can be identified (note that the C peak is due to the carbon supporting film and Cu is due to the Cu TEM grid). Detailed compositional analysis indicates that compositions of Bi and Se are ca. 40 at% for Bi and ca. 60 at% for Se with

an uncertainty of 1 at%. Figure 2e and f are the corresponding EDS maps of Bi and Se. Based on their uniform contrasts, Bi and Se elements are distributed uniformly in the NS.

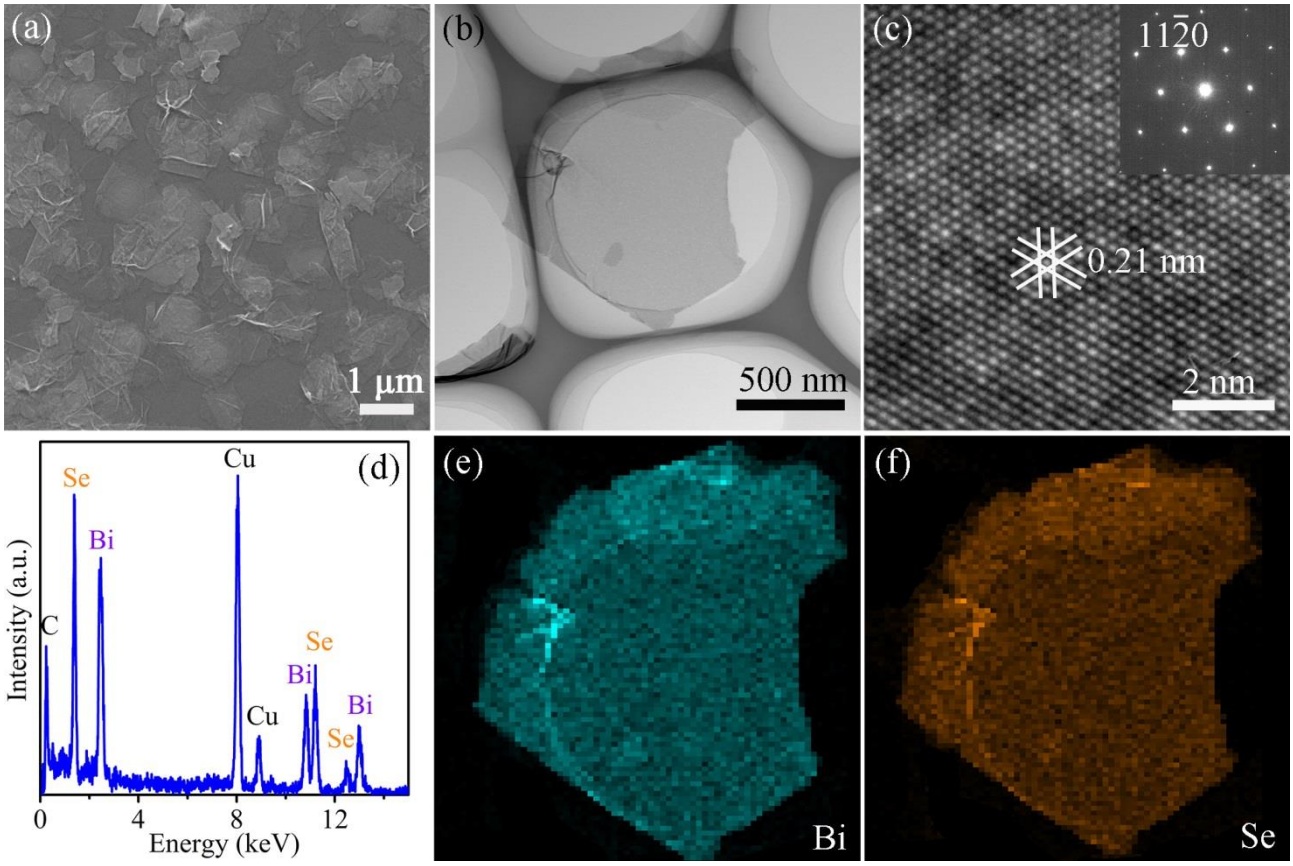

Figure 2 (a) SEM image of ultrathin NSs dispersed on a Si substrate, (b) TEM image of a typical NS, (c) HRTEM image with insert showing corresponding SAED patter, (d) EDS profile and (e - f) EDS mapping for Bi and Se, respectively.

In order to evaluate the TE performance of our Bi_2Se_3 NSs, baked NSs and commercial Bi_2Se_3 powders (for reference) were compressed into pellets by SPS.[34] On the basis of XRD patterns collected from NS-based pellets (see Figure S4), there is no detectable impurity, such as oxidations. Similar to the powder samples, NS-based pellets preserve the preferential orientation along the <0001> direction. The texture fraction of the {0001} planes can be estimated from the intensities of XRD diffraction peaks (shown in Table S1) using the Lotgering method,[35] from which the texture fraction of the pellet comprising of single-layered NSs is ~0.57. This value is comparable with the bulk material processed by hot deformation.[17] The calculated results for all samples are shown in Table S2. Such a high texture will definitely strengthen anisotropic behaviour of Bi_2Se_3 pellets. Therefore, we need to measure σ, S and κ along the same direction. Accordingly, pellets with a diameter of 12 mm and a thickness of 8 mm were prepared (as illustrated in Figure 3a), so that the

measurements of the out-of-plane σ, S and κ can be realised. Similarly, the in-plane TE properties were also measured on the sintered pellet made of ultrathin NSs, and the in-plane TE properties is shown in Figure S5. The in-plane ZT is 0.46, close to the out-of-plane ZT, which will be demonstrated below.

Figure 3b is the plots of σ as a function of temperature for the pellets, and shows σ increases gently and then drops with the temperature and the thinner the NSs, the smaller the measured σ values. The pellet made of single-layered NSs exhibits the lowest σ, fluctuating at around 2.0×10^4 S/m in the entire temperature region. Figure 3c shows the temperature dependent S. As can be seen, negative S indicates the n-type feature of our Bi_2Se_3 NSs, and the peak values for pellets made by thinner NSs shift to the elevated temperature. The peak of S = -155.32 μV/K is achieved at 427 K for the pellet made of single-layered Bi_2Se_3 NSs compared with the peak value of - 90.5 μV/K for the commercial Bi_2Se_3 at 350 K. Figure 3d is the plots of $S^2\sigma$ as a function of temperature, and demonstrates that the thinner the NSs, the higher the measured $S^2\sigma$ values. For the pellet made by single-layered NSs, $S^2\sigma = 4.71\times10^{-4}$ W/mK^2 is reached, doubling the value for the current commercial counterpart. The comparison of Figure 3b – d suggests that the considerably enhanced S in the thinner NSs can compensate the moderately deteriorated σ, and in turn lead to the $S^2\sigma$ improvement.

Figure 3e shows the plots of κ as a function of temperature, which are notably decreased for pellets made of thinner NSs (κ = 0.41 W/mK is found for the pellet made of single-layered NSs). As an advantage of nanostructures, the significantly reduced κ is due to (i) the strengthened scattering for the mid/long wavelength phonons,[36-38] and (ii) the surface structural disorder in NSs with reduced thickness effectively enhancing the scattering of the short wavelength phonons.[23] Moreover, the ultrathin NSs promote the <0001> texture in the SPS pellets, which in turn further enhance the phonon scattering in the direction that is parallel to the sintering press direction.

It is expected that the obtained high $S^2\sigma$ as well as low κ can result in a significant increase in ZT. Indeed, Figure 3f shows such a case. The peak ZT for the pellet composed of single-layered NSs is 0.48, much larger than the previously reported pure Bi_2Se_3 thicker plate-like nanostructures with ZT less than 0.2.[12-13, 39] In comparison with the single-layer Bi_2Se_3 NSs (with ZT = 0.35) prepared by the two-step lithium ionic exfoliation method,[23] our κ is almost identical to their κ. Although our σ decreases slightly, the absolute value of our peak S (-155.32 μV/K) is much larger than that of their peak S (-120.7 μV/K).[23] We

anticipated that the enhanced TE performance of our single-layered Bi_2Se_3 NSs could be attributed to band-structure optimisation,[40] which will be discussed later.

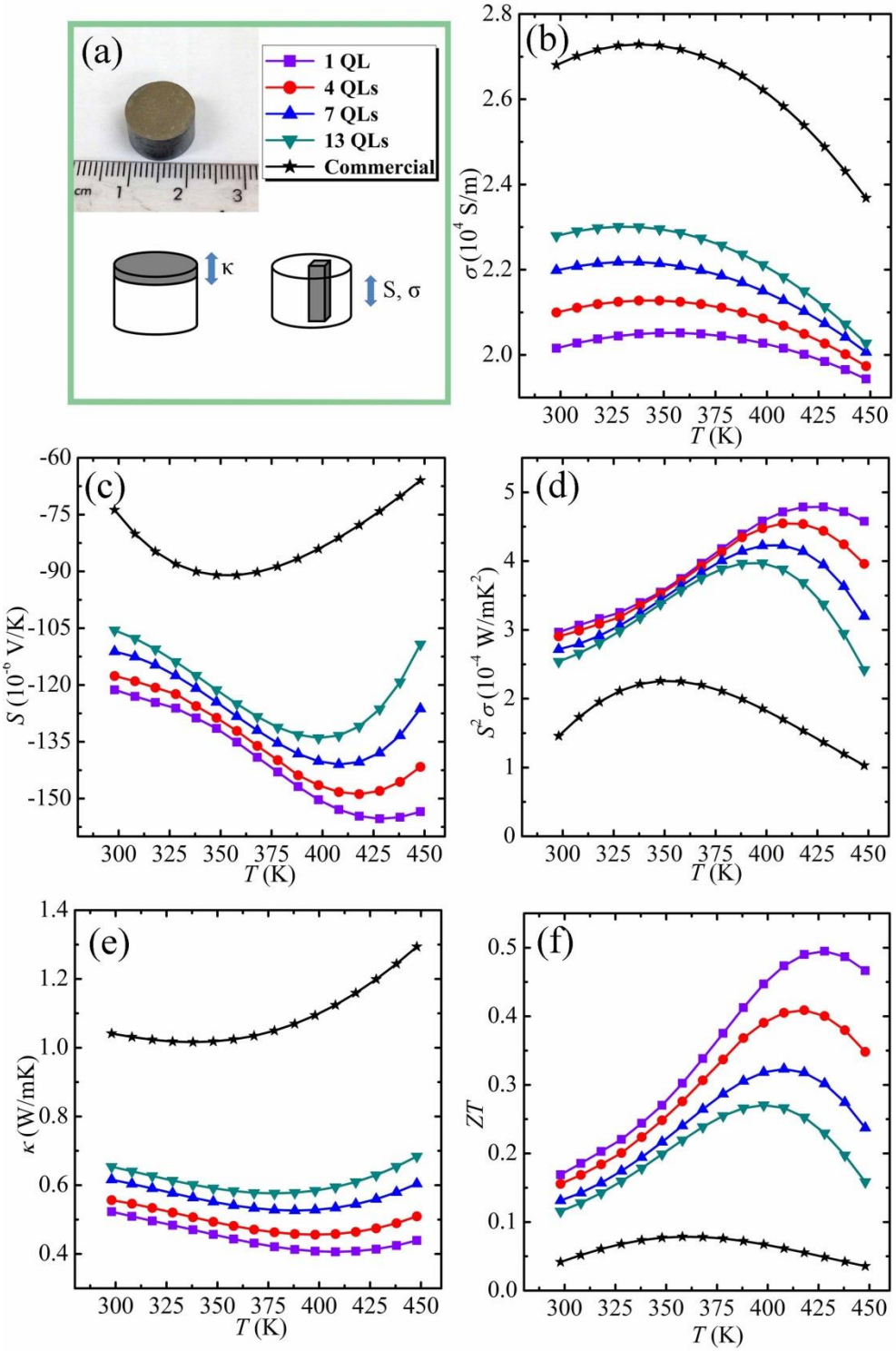

Figure 3 (a) Photograph of a sintered pellet with thermoelectric measurement direction. TE characteristics as a function of temperature for pellets sintered from corresponding as-synthesized NSs as well as commercial Bi_2Se_3: (b) σ, (c) S, (d) $S^2\sigma$, (e) κ, and (f) ZT, respectively.

In order to elucidate the fundamental relationship between *S*, *σ* and band structure, we applied nonparabolic models to simulate the carrier transport properties, in which the energy (*E*) dispersion relation can be given by the Kane description:[41] $E\left(1+E/E_g\right)=\frac{\hbar^2k^2}{2m^*}$. On this basis, the carrier transport properties from individual band can be described by:[42-44]

Seebeck coefficient

$$S=\pm\frac{\kappa_B}{e}\left[\frac{F_{r+1,2}^{1}\left(\eta,\beta\right)}{F_{r+1,2}^{0}\left(\eta,\beta\right)}-\eta\right], \tag{1}$$

and electrical conductivity

$$\sigma=e^2\frac{\tau_0}{2\pi^2m_\sigma^*}\left(\frac{2N^{2/3}m_d^*k_BT}{\hbar^2}\right)^{3/2}F_{r+1,2}^{0}\left(\eta,\beta\right), \tag{2}$$

where $F_{m,k}^{n}\left(\eta,\beta\right)$ has a similar form as the Fermi integral that can be described as:[45]

$$F_{m,k}^{n}\left(\eta,\beta\right)=\int_0^\infty\left[-\frac{\partial f\left(\eta\right)}{\partial\varepsilon}\right]\varepsilon^n\frac{\left(E+\beta\varepsilon^2\right)^m}{\left(1+2\beta\varepsilon\right)^k}d\varepsilon \tag{3}$$

and

$$\beta=\frac{k_BT}{E_g}. \tag{4}$$

In the above equations, *k* is electron wave vector, m_d^* is the density of states effective mass, m_σ^* is the conduction effective mass, *N* is the band degeneracy, k_B is the Boltzmann constant, *ħ* is the reduced Planck constant, ε is the reduced electron energy ($\varepsilon=\frac{E}{k_BT}$), τ_0 is a constant relating to relaxation time, η is the reduced Fermi level (for electrons, $\eta_e=\frac{E_f-E_c}{k_BT}$ with E_c denoting the conduction band edge; for holes, $\eta_h=\frac{E_v-E_f}{k_BT}=\frac{E_c-E_g-E_f}{k_BT}=-1/\beta-\eta_e$ with E_v denoting the valance band edge), *f* is the Fermi - Dirac distribution, and *r* is the characteristics scattering parameter (For most good

TE materials, *r* equals to -1/2, since acoustic phonons dominate the carrier scattering.[40, 46]). To simplify the representation, η will be specialized as the reduced Fermi level for electrons in the bellowing discussion.

Apart from $F_{r+1,2}^{0}(\eta,\beta)$, the other items in Equation (2) is nearly irrelevant to η and β. Therefore, to directly analyse the dependence of carrier transport properties on η and reduced band gap ($\frac{E_g}{k_BT}$, $\frac{E_g}{k_BT}=1/\beta$), we defined the reduced electrical conductivity (σ_r) as

$$\sigma_r = F_{r+1,2}^{0}(\eta,\beta) \quad (5)$$

Considering the contributions from both conduction band and valance band, the total *S* and σ_r can be expressed by

$$S = \frac{S^c\sigma_r^c + S^v\sigma_r^v}{\sigma_r^c + \sigma_r^v}, \text{ and} \quad (6)$$

$$\sigma_r = \sigma_r^c + \sigma_r^v; \quad (7)$$

where superscripts *c* and *v* represent the relevant contributions from the conduction band and the valance band, respectively.

By substituting Equation (1) into Equation (6), and Equation (5) into Equation (7) with respectively calculated η for electrons and holes, we plot *S*, σ_r, as well as $S^2\sigma_r$ as a function of η and $1/\beta$, in Figure 4a – c, respectively. Figure 4a shows that the absolute value of *S* increases with decreasing η, and it increases with increasing $1/\beta$. Figure 4b shows that σ_r increases with increasing η, but is nearly independent on $1/\beta$ when $1/\beta$ is larger than 10. Figure 4c shows that $S^2\sigma_r$ increases with increasing $1/\beta$. Interestingly, $S^2\sigma_r$ has a peak value with variation of η. Quantitatively, $S^2\sigma_r$ peaks locate in the region of η between 0.17 and 0.68 for the studied range of $1/\beta$ (between 1 and 30 at T = 300 K), which are consistent with the recent studies ($S^2\sigma_r$ peaks at η = 0.3 and $1/\beta$=10).[40, 47] Namely, the optimal $E_f - E_c$ is between 0.004 eV and 0.016 eV for E_g ranging from 0.025 eV to 0.75 eV.

Based on the simulation results outlined above, η values for our samples can be deduced. Firstly, $1/\beta$ should be determined. Note that E_g can be obtained from the

reported experimental data,[19, 48] which indicates that E_g for 1 QL, 4 QLs, 7 QLs, 13 QLs and commercial Bi_2Se_3 are 0.5 eV, 0.42 eV, 0.4 eV, 0.35 eV and 0.3 eV, respectively. Consequently, $1/\beta$ ($1/\beta = \frac{E_g}{k_B T}$) for all samples is derived at 300 K. Then η can be determined using the calculated $1/\beta$ and measured S according to the Equation (1) and (4), and the result is shown in Figure 4d. As can be seen, the higher the measured S, the lower the η, suggesting that pellets made of thinner NSs has smaller η. Based on the derived η, σ_r can be determined, as shown in Figure 4e, in which σ_r decreases for pellets made of thinner NSs. Figure 4f shows the plots of $S^2\sigma_r$ as a function of η, illustrating that the enhancement in $S^2\sigma_r$ is due to the decreased η.

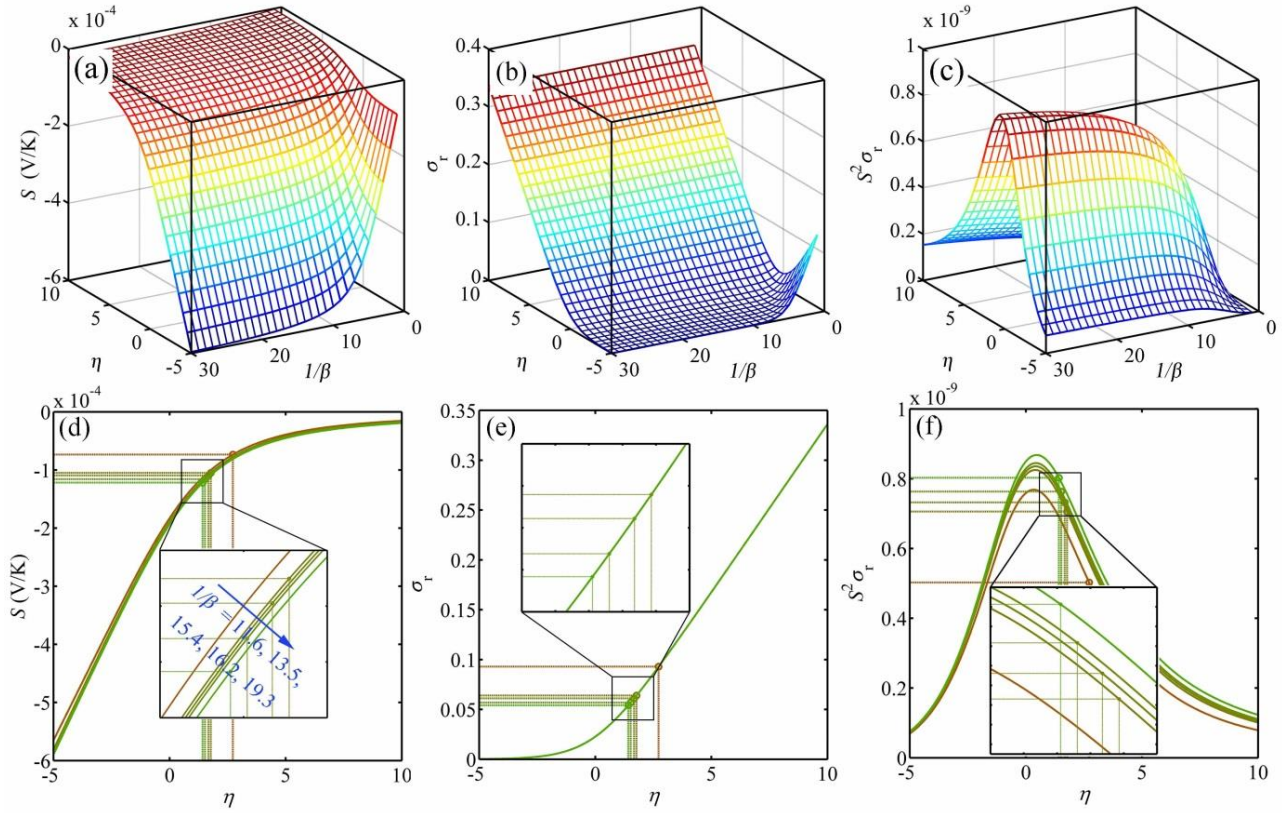

Figure 4 Simulated electronic transport properties as a function of reduced Fermi level and reduced band gap: (a) S, (b) σ_r and (c) $S^2\sigma_r$. (d) Derivation of η for pellets with various $1/\beta$ (11.6, 13.5, 15.4, 16.2 and 19.3 represented by different coloured lines) at room temperature, and calculation of (e) σ_r and (f) $S^2\sigma_r$ based on the estimated η. The inserts amplify the marked areas in (d - f).

Since $E_f - E_c = \eta k_B T$, E_f - E_c can then be calculated using the deduced η for our samples. Figure 5 is the result, in which a positive E_f - E_c can be observed, indicating that E_f is located in the conduction band for all samples.[49-50] Besides, with decreasing the thickness of NSs, E_f - E_c decreases. Moreover, the reduced Fermi level for holes can be subsequently derived, and is shown in Figure S6.

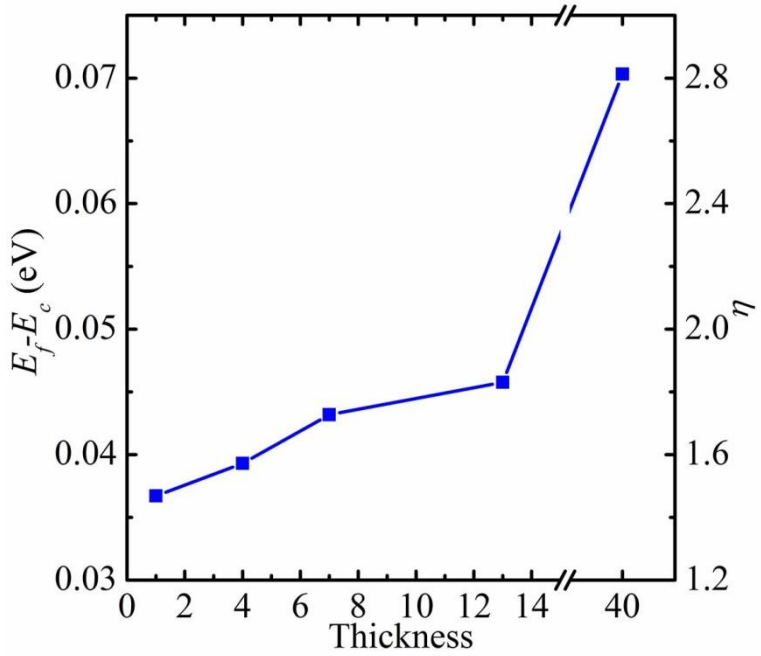

Figure 5 Calculated η for electrons and E_f - E_c for all samples at T = 300 K.

To understand the significantly decreased κ, we monitor κ_e, κ_{amb} and κ_l. According to Wiedemann-Franz law ($\kappa_e = L\sigma T$, where L represents the Lorenz number),[51] we need to derive L first. By considering both conduction band and valance band, L is given by[45]

$$L = \frac{L^c \sigma_r^c + L^v \sigma_r^v}{\sigma_r^c + \sigma_r^v}, \tag{8}$$

where L^i (i = c or v representing contribution from the conduction band or the valance band, respectively) is expressed by[45]

$$L^i = \left(\frac{k_B}{e}\right)^2 \left[\frac{F_{r+1,2}^2(\eta,\beta)}{F_{r+1,2}^0(\eta,\beta)} - \left(\frac{F_{r+1,2}^1(\eta,\beta)}{F_{r+1,2}^0(\eta,\beta)}\right)^2\right]. \tag{9}$$

Note that η for electrons ($\eta = \frac{E_f - E_c}{k_B T}$) and holes ($\eta = -1/\beta - \frac{E_f - E_c}{k_B T}$) should be calculated, respectively. In order to simplify the derivation for η in the entire measured temperature range, we assume that E_g is independent with temperature. Subsequently, η for electrons is calculated based on the measured S, shown in Figure S7. Then the calculated L for all samples is plot in Figure 6a. For NS pellets, L fluctuates from 1.43×10^{-8} to 1.35×10^{-8} V^2/K^2 in the measured temperature region, which are consistent with the reported values for low dimensional TE materials.[52] The average value for commercial counterpart is 1.9×10^{-8} V^2/K^2, which matches well with L for highly degenerate TE materials.[53-54] On this basis, Figure 6b shows the variations of κ_e as a function of T for different pellets, from which κ_e is significantly reduced for pellets made of thinner NSs compared with the bulk counterpart. This is because both L and σ decrease for the Bi_2Se_3 NSs with reduced thickness (refer to Figure 6a and Figure 3b). Moreover, κ_{amb}, is calculated using the reference-outlined method.[55] Figure 6c is the variation of κ_{amb} in the measured temperature region, where κ_{amb} increases with increasing the temperature, while the magnitude of such an increase is remarkably reduced in pellets made of thinner NSs. This indicates that the ambipolar effect is suppressed in our ultrathin Bi_2Se_3 NSs: ambipolar effect emerges at > 360 K for NS pellets compared with at 320 K for commercial counterpart. Since the ambipolar effect is caused by the diffusion of electron-hole pairs within the intrinsic region,[17] the suppressed ambipolar effect suggests that the intrinsic excitation is postponed to the higher temperature. Moreover, S can be offset when both electrons and holes are present, because electrons and holes have opposite contribution on S. Therefore, the suppression of the ambipolar effect can also enhance S,[5] which has been achieved for the pellet made of ultrathin NSs (refer to Figure 3c). By extrapolating the linear relationship between κ_l and $1/T$ demonstrated in the insert of Figure 6c, the variation of κ_l in the whole temperature region can be derived, as shown in Figure 6d. For NS pellets, κ_l is greatly reduced, approximately 50% lower than that of commercial counterparts. Besides, κ_l is further reduced with decreasing the thickness of NSs. As discussed above, the significantly reduction in κ_l is due to the strengthened scattering of long/mid-wavelength and short-wavelength phonons by nanograins and structural disorders, respectively.

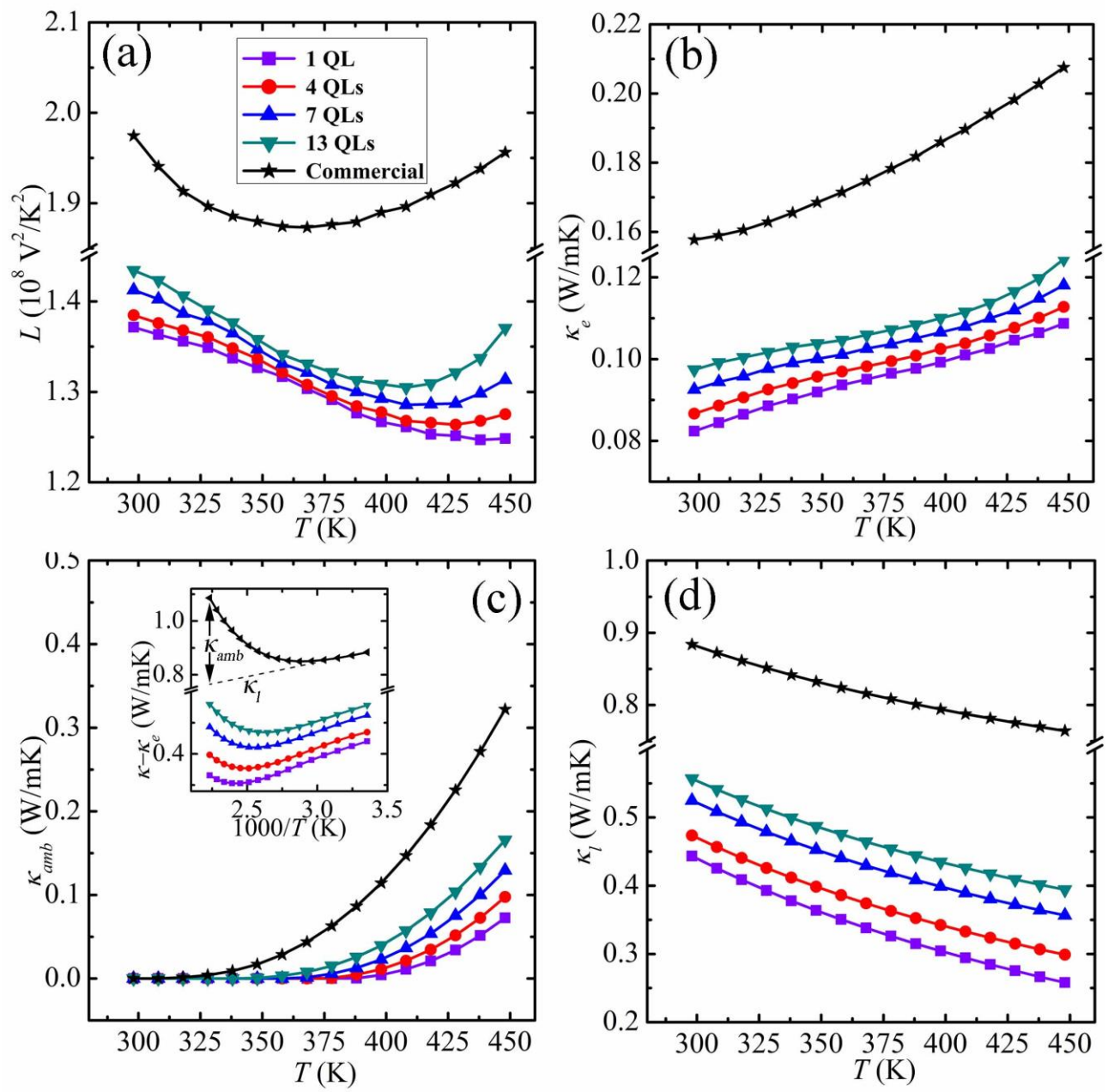

Figure 6 (a) Derived L for the as-prepared samples, (b) κ_e, (c) κ_{amb} with insert showing the inverse temperature dependence of subtracting κ_e from κ and (d) κ_l.

3. Conclusion

In this study, a one-step microwave-stimulated solvothermal method using PVP as surfactant is developed to tune the thickness of Bi_2Se_3 NSs. Examined by AFM and re-confirmed by Raman spectroscopy, highly-crystallized Bi_2Se_3 NSs with average thickness of 1 nm, 4 nm, 7 nm and 13 nm have been fabricated. TE property evaluations show a significantly reduced κ (0.41 W/mK), and enhanced $S^2\sigma$ (4.71×10^{-4} W/mK^2 with S = -155.32 μV/K and σ = 1.96×10^4 S/m) in the pellet composed of single-layered Bi_2Se_3 NSs.

Through the nonparabolic Kane model simulation and analysis, we found that the enhanced $S^2\sigma$ in the as-prepared samples is originated from broadened E_g and optimized E_f - E_c. Moreover, the strengthened phonon scattering, reduced κ_e and the suppressed ambipolar effect lead to the significantly reduced κ. This result indicates that it is possible to further enhance the TE performance of Bi_2Se_3-based binary or ternary phases by reducing the thickness of nanostructures.

4. Experimental Sections

4.1. Materials synthesis and processing

All chemicals were purchased from Sigma Aldrich and used without further purification. In a typical synthesis of uniform ultrathin Bi_2Se_3, we added $Bi(NO_3)_3 \cdot 5H_2O$ (1 mmol, 485.07 mg) and SeO_2 (1.5 mmol, 166.44 mg) into ethylene glycol (40 mL) dissolving with poly(N-vinyl-2-pyrrolidone) (PVP, M_w=40,000) (1 g). The prepared solution was mixed with NaOH solution (5 mol/L, 2 mL), and subsequently stirred vigorously for 30 min at room temperature. The obtained clear solution was finally sealed in a 100 mL teflon vessel, which was exposed to microwaves in the CEM Mars 6 microwave oven at a setting temperature of 230 ˚C for 5 min. After cooled to room temperature, the products were collected by a high-speed centrifugation, washed six times with distilled water and absolute ethanol and finally dried at 60 ˚C for at least 12 hours in vacuum oven. The procedure for thicker Bi_2Se_3 nanosheets was identical to the synthesis of ultrathin nanosheets except for using different PVP dosage.

4.2. Materials Characterizations

The crystal structures of the synthesized products were characterized by X-ray diffraction (XRD), recorded on an X-ray diffractometer equipped with graphite monochromatized, Cu Kα radiation (λ = 1.5418 Å). The morphological, structural, and chemical characteristics of the synthesized products were investigated by scanning electron microscopy (SEM, JEOL 7800) and transmission electron microscopy (TEM, FEI F20) equipped with energy-dispersive X-ray spectroscopy (EDS). The thickness of Bi_2Se_3 NSs was measured by atomic force microscopy (AFM, Cypher S) operated in tapping mode. Raman spectra were detected by a Renishawin Via Raman microscope system with a 514.5 nm Ar laser. The laser power on the sample is 0.5 mW, while the integral time is 10 seconds. Fourier transformation infrared (FTIR) spectra were recorded in the range

4000 - 400 cm^{-1} on a Nicolet FTIR spectrometer in the transmission mode with a spectral resolution of 4 cm^{-1} and 32 scans.

4.3. Fabrication of pellets

As a comparison, Bi_2Se_3 (99.999%, -325 mesh powder) was obtained from Alfa. The as-synthesized nanosheets and the purchased powders were compressed into cylinder-shaped bulk samples by spark plasma sintering (SPS) under 40 MPa and at 250 ˚C for 5 min in vacuum. Measured by an Archimedes method, the densities of all sintered pellets were confirmed to be approximately 91.3%.

4.4. Thermoelectric Performance Measurement

In order to ensure the thermoelectric property measurement was conducted along the same direction. A disk with thickness of around 2 mm was cut from the sintered pellets to measure the thermal conductivity, and a cuboid was cut from the remaining part of the sintered pellet to measure the σ and S.

Thermal conductivity was calculated through $\kappa = DC_p d$, where D, C_p, and d were the thermal diffusivity, specific heat capacity, and density, respectively. Thermal diffusivity was measured by a laser flash method with LFA 457, NETZSCH, while specific heat capacity was obtained from an empirical formula $C_p = 118.61 + 19.26 \times 10^{-3} \cdot T$, where T is temperature.[56]

The electrical conductivity was measured by a four-point method, while Seebeck coefficient was determined by the slope of the voltage difference versus temperature-difference curve. Electrical resistivity and Seebeck coefficient were measured simultaneously on ZEM-3, ULVAC. The uncertainty of the thermoelectric performance measurements (S, σ and D) was around 5%.

Supporting Information

Supporting Information is available from the Wiley Online Library or from the author.

Acknowledgements

This work was financially supported by the Australian Research Council (DP150100056), ZGC thanks QLD government for a smart state future fellowship (2011002414). MH thanks China Scholarship Council for PhD financial supports. The Australian Microscopy & Microanalysis Research Facility is acknowledged for providing characterization facilities.

Reference

(1) Bell, L. E. Cooling, Heating, Generating Power, and Recovering Waste Heat with Thermoelectric Systems. *Science* **2008**, 321, 1457-1461.

(2) Riffat, S. B.; Ma, X. L. Thermoelectrics: a Review of Present and Potential Applications. *Appl. Therm. Eng.* **2003**, 23, 913-935.

(3) Tritt, T. M.; Subramanian, M. A. Thermoelectric Materials, Phenomena, and Applications: a Bird's Eye View. *Mrs. Bull.* **2006**, 31, 188-194.

(4) DiSalvo, F. J. Thermoelectric Cooling and Power Generation. *Science* **1999**, 285, 703-706.

(5) Minnich, A. J.; Dresselhaus, M. S.; Ren, Z. F.; Chen, G. Bulk Nanostructured Thermoelectric Materials: Current Research and Future Prospects. *Energy Environ. Sci.* **2009**, 2, 466-479.

(6) Chen, Z.-G.; Han, G.; Yang, L.; Cheng, L.; Zou, J. Nanostructured Thermoelectric Materials: Current Research and Future Challenge. *Prog. Nat. Sci.* **2012**, 22, 535-549.

(7) Zhang, X. D.; Xie, Y. Recent Advances in Free-Standing Two-Dimensional Crystals with Atomic Thickness: Design, Assembly and Transfer Strategies. *Chem. Soc. Rev.* **2013**, 42, 8187-8199.

(8) Jeong, C.; Kim, R.; Lundstrom, M. S. On the Best Bandstructure for Thermoelectric Performance: a Landauer Perspective. *J. Appl. Phys.* **2012**, 111, 113707-10.

(9) Li, J. F.; Liu, W. S.; Zhao, L. D.; Zhou, M. High-Performance Nanostructured Thermoelectric Materials. *NPG Asia Mater.* **2010**, 2, 152-158.

(10) Han, G.; Chen, Z.-G.; Drennan, J.; Zou, J. Indium Selenides: Structural Characteristics, Synthesis and Their Thermoelectric Performances. *Small* **2014**, 10, 2747-2765.

(11) Zhao, L. D.; Dravid, V. P.; Kanatzidis, M. G. The panoscopic approach to high performance thermoelectrics. *Energy Environ. Sci.* **2014**, 7, 251-268.

(12) Mishra, S. K.; Satpathy, S.; Jepsen, O. Electronic Structure and Thermoelectric Properties of Bismuth Telluride and Bismuth Selenide. *J. Phys-condens. Mat.* **1997**, 9, 461-470.

(13) Hu, L. P.; Zhu, T. J.; Wang, Y. G.; Xie, H. H.; Xu, Z. J.; Zhao, X. B. Shifting up the Optimum Figure of Merit of *p*-Type Bismuth Telluride-Based Thermoelectric Materials for Power Generation by Suppressing Intrinsic Conduction. *NPG Asia Mater.* **2014**, 6, e88.

(14) Bahk, J.-H.; Bian, Z.; Shakouri, A. Electron Energy Filtering by a Nonplanar Potential to Enhance the Thermoelectric Power Factor in Bulk Materials. *Phys. Rev. B* **2013**, 87, 075204-10.

(15) Sakamoto, Y.; Hirahara, T.; Miyazaki, H.; Kimura, S.-i.; Hasegawa, S. Spectroscopic Evidence of a Topological Quantum Phase Transition in Ultrathin Bi_2Se_3 Films. *Phys. Rev. B* **2010**, 81, 165432.

(16) Zhuang, A.; Li, J. J.; Wang, Y. C.; Wen, X.; Lin, Y.; Xiang, B.; Wang, X. P.; Zeng, J. Screw-Dislocation-Driven Bidirectional Spiral Growth of Bi_2Se_3 Nanoplates. *Angew. Chem. Int. Edit.* **2014**, 53, 6425-6429.

(17) Min, Y.; Moon, G. D.; Kim, B. S.; Lim, B.; Kim, J.-S.; Kang, C. Y.; Jeong, U. Quick, Controlled Synthesis of Ultrathin Bi_2Se_3 Nanodiscs and Nanosheets. *J. Am. Chem. Soc.* **2012**, 134, 2872-2875.

(18) Nicolosi, V.; Chhowalla, M.; Kanatzidis, M. G.; Strano, M. S.; Coleman, J. N. Liquid Exfoliation of Layered Materials. *Science* **2013**, 340, 1420-+.

(19) Hong, S. S.; Kundhikanjana, W.; Cha, J. J.; Lai, K.; Kong, D.; Meister, S.; Kelly, M. A.; Shen, Z.-X.; Cui, Y. Ultrathin Topological Insulator Bi_2Se_3 Nanoribbons Exfoliated by Atomic Force Microscopy. *Nano Lett.* **2010**, 10, 3118-3122.

(20) Sun, Y.; Cheng, H.; Gao, S.; Liu, Q.; Sun, Z.; Xiao, C.; Wu, C.; Wei, S.; Xie, Y. Atomically Thick Bismuth Selenide Freestanding Single Layers Achieving Enhanced Thermoelectric Energy Harvesting. *J. Am. Chem. Soc.* **2012**, 134, 20294-20297.

(21) Sun, L. P.; Lin, Z. P.; Peng, J.; Weng, J.; Huang, Y. Z.; Luo, Z. Q. Preparation of Few-Layer Bismuth Selenide by Liquid-Phase-Exfoliation and Its Optical Absorption Properties. *Sci. Rep.* **2014**, 4.

(22) Zhang, Y.; He, K.; Chang, C.-Z.; Song, C.-L.; Wang, L.-L.; Chen, X.; Jia, J.-F.; Fang, Z.; Dai, X.; Shan, W.-Y.; Shen, S.-Q.; Niu, Q.; Qi, X.-L.; Zhang, S.-C.; Ma, X.-C.; Xue, Q.-K. Crossover of the Three-Dimensional Topological Insulator Bi_2Se_3 to the Two-Dimensional Limit. *Nat. Phys.* **2010**, 6, 584-588.

(23) Cheng, P.; Song, C.; Zhang, T.; Zhang, Y.; Wang, Y.; Jia, J.-F.; Wang, J.; Wang, Y.; Zhu, B.-F.; Chen, X.; Ma, X.; He, K.; Wang, L.; Dai, X.; Fang, Z.; Xie, X.; Qi, X.-L.; Liu, C.-X.; Zhang, S.-C.; Xue, Q.-K. Landau Quantization of Topological Surface States in Bi_2Se_3. *Phys. Rev. Lett.* **2010**, 105, 076801.

(24) Zhang, G.; Qin, H.; Teng, J.; Guo, J.; Guo, Q.; Dai, X.; Fang, Z.; Wu, K. Quintuple-Layer Epitaxy of Thin Films of Topological Insulator Bi_2Se_3. *Appl. Phys. Lett.* **2009**, 95, 053114.

(25) Xiao, C.; Li, Z.; Li, K.; Huang, P.; Xie, Y. Decoupling Interrelated Parameters for Designing High Performance Thermoelectric Materials. *Accounts. Chem. Res.* **2014**, 47, 1287-1295.

(26) Li, R. X.; Wang, M. L.; Meng, X. Q.; Wei, Z. M. Effect of the Thickness of Bi_2Se_3 Sheets on the Morphologies of Bi_2Se_3–ZnS Nanocomposites and Improved Photoresponsive Characteristic. *J. Mater. Sci-mater. El* **2013**, 24, 4197-4203.

(27) Kim, Y.; Chen, X.; Wang, Z.; Shi, J.; Miotkowski, I.; Chen, Y. P.; Sharma, P. A.; Lima Sharma, A. L.; Hekmaty, M. A.; Jiang, Z.; Smirnov, D. Temperature Dependence of Raman-Active Optical Phonons in Bi_2Se_3 and Sb_2Te_3. *Appl. Phys. Lett.* **2012**, 100, 071907.

(28) Jana, M. K.; Biswas, K.; Rao, C. N. R. Ionothermal Synthesis of Few-Layer Nanostructures of Bi_2Se_3 and Related Materials. *Chem-eur. J.* **2013**, 19, 9110-9113.

(29) Zhang, J.; Peng, Z.; Soni, A.; Zhao, Y.; Xiong, Y.; Peng, B.; Wang, J.; Dresselhaus, M. S.; Xiong, Q. Raman Spectroscopy of Few-Quintuple Layer Topological Insulator Bi_2Se_3 Nanoplatelets. *Nano Lett.* **2011**, 11, 2407-2414.

(30) Zhang, S. L.; Wu, S. N.; Yan, Y.; Hu, T.; Zhao, J.; Song, Y.; Qu, Q.; Ding, W. Study on the Applied Limitation of the Micro-Crystal Model for Raman Spectra of Nano-Crystalline Semiconductors. *J. Raman. Spectrosc.* **2008**, 39, 1578-1583.

(31) Kong, D.; Randel, J. C.; Peng, H.; Cha, J. J.; Meister, S.; Lai, K.; Chen, Y.; Shen, Z.-X.; Manoharan, H. C.; Cui, Y. Topological Insulator Nanowires and Nanoribbons. *Nano Lett.* **2009**, 10, 329-333.

(32) Soni, A.; Shen, Y.; Yin, M.; Zhao, Y.; Yu, L.; Hu, X.; Dong, Z.; Khor, K. A.; Dresselhaus, M. S.; Xiong, Q. Interface Driven Energy Filtering of Thermoelectric Power in Spark Plasma Sintered $Bi_2Te_{2.7}Se_{0.3}$ Nanoplatelet Composites. *Nano Lett.* **2012**, 12, 4305-4310.

(33) Lotgering, F. K. Topotactical Reactions with Ferrimagnetic Oxides Having Hexagonal Crystal Structures—I. *J. Inorg. Nucl. Chem.* **1959**, 9, 113-123.

(34) Yan, X.; Liu, W.; Wang, H.; Chen, S.; Shiomi, J.; Esfarjani, K.; Wang, H.; Wang, D.; Chen, G.; Ren, Z. Stronger Phonon Scattering by Larger Differences in Atomic Mass and Size in *p*-Type Half-Heuslers $Hf_{1-x}Ti_xCoSb_{0.8}Sn_{0.2}$. *Energy Environ. Sci.* **2012**, 5, 7543-7548.

(35) Zebarjadi, M.; Esfarjani, K.; Dresselhaus, M. S.; Ren, Z. F.; Chen, G. Perspectives on Thermoelectrics: From Fundamentals to Device Applications. *Energy Environ. Sci.* **2012**, 5, 5147-5162.

(36) Poudel, B.; Hao, Q.; Ma, Y.; Lan, Y.; Minnich, A.; Yu, B.; Yan, X.; Wang, D.; Muto, A.; Vashaee, D.; Chen, X.; Liu, J.; Dresselhaus, M. S.; Chen, G.; Ren, Z. High-Thermoelectric Performance of Nanostructured Bismuth Antimony Telluride Bulk Alloys. *Science* **2008**, 320, 634-638.

(37) Kadel, K.; Kumari, L.; Li, W. Z.; Huang, J. Y.; Provencio, P. P. Synthesis and Thermoelectric Properties of Bi_2Se_3 Nanostructures. *Nanoscale Res. Lett.* **2011**, 6, 57.

(38) Min, Y.; Roh, J. W.; Yang, H.; Park, M.; Kim, S. I.; Hwang, S.; Lee, S. M.; Lee, K. H.; Jeong, U. Surfactant-Free Scalable Synthesis of Bi_2Te_3 and Bi_2Se_3 Nanoflakes and Enhanced Thermoelectric Properties of Their Nanocomposites. *Adv. Mater.* **2013**, 25, 1425-9.

(39) Soni, A.; Zhao, Y. Y.; Yu, L. G.; Aik, M. K. K.; Dresselhaus, M. S.; Xiong, Q. H. Enhanced Thermoelectric Properties of Solution Grown $Bi_2Te_{3-x}Se_x$ Nanoplatelet Composites. *Nano Lett.* **2012**, 12, 1203-1209.

(40) Pei, Y.; Wang, H.; Snyder, G. J. Band Engineering of Thermoelectric Materials. *Adv. Mater.* **2012**, 24, 6125-35.

(41) Kane, E. O. Band Structure of Indium Antimonide. *J. Phys. Chem. Solids* **1957**, 1, 249-261.

(42) Kyratsi, T.; Hatzikraniotis, E.; Paraskevopoulos, K. M.; Malliakas, C. D.; Dyck, J. S.; Uher, C.; Kanatzidis, M. G. Structure Inhomogeneities, Shallow Defects, and Charge Transport in the Series of Thermoelectric Materials $K_2Bi_{8-x}SbxSe_{13}$. *J. Appl. Phys.* **2006**, 100, 123704-11.

(43) Popescu, A.; Woods, L. M.; Martin, J.; Nolas, G. S. Model of Transport Properties of Thermoelectric Nanocomposite Materials. *Phys. Rev. B* **2009**, 79, 205302.

(44) Faleev, S. V.; Léonard, F. Theory of Enhancement of Thermoelectric Properties of Materials with Nanoinclusions. *Phys. Rev. B* **2008**, 77, 214304.

(45) Wu, D.; Zhao, L.; Hao, S.; Jiang, Q.; Zheng, F.; Doak, J. W.; Wu, H.; Chi, H.; Gelbstein, Y.; Uher, C.; Wolverton, C.; Kanatzidis, M.; He, J. Origin of the High Performance in GeTe-Based Thermoelectric Materials upon Bi2Te3 Doping. *J. Am. Chem. Soc.* **2014**, 136, 11412-11419.

(46) Young, D. L.; Coutts, T. J.; Kaydanov, V. I.; Gilmore, A. S.; Mulligan, W. P. Direct Measurement of Density-of-States Effective Mass and Scattering Parameter in Transparent Conducting Oxides Using Second-Order Transport Phenomena. *J. Vac. Sci. Technol. A* **2000**, 18, 2978-2985.

(47) Pei, Y.; Gibbs, Z. M.; Balke, B.; Zeier, W. G.; Snyder, G. J. Optimum Carrier Concentration in *n*-Type PbTe Thermoelectrics. *Adv. Energy Mater.* **2014**, 4, 1400486.

(48) Peng, H.; Dang, W.; Cao, J.; Chen, Y.; Wu, D.; Zheng, W.; Li, H.; Shen, Z.-X.; Liu, Z. Topological Insulator Nanostructures for Near-Infrared Transparent Flexible Electrodes. *Nat. Chem.* **2012**, 4, 281-286.

(49) Scanlon, D. O.; King, P. D. C.; Singh, R. P.; de la Torre, A.; Walker, S. M.; Balakrishnan, G.; Baumberger, F.; Catlow, C. R. A. Controlling Bulk Conductivity in Topological Insulators: Key Role of Anti-Site Defects. *Adv. Mater.* **2012**, 24, 2154-2158.

(50) Horák, J.; Stary, Z.; Lošťák, P.; Pancíř, J. Anti-Site Defects in *n*-Bi_2Se_3 Crystals. *J. Phys. Chem. Solids* **1990**, 51, 1353-1360.

(51) Sumithra, S.; Takas, N. J.; Misra, D. K.; Nolting, W. M.; Poudeu, P. F. P.; Stokes, K. L. Enhancement in Thermoelectric Figure of Merit in Nanostructured Bi_2Te_3 with Semimetal Nanoinclusions. *Adv. Energy Mater.* **2011**, 1, 1141-1147.

(52) Wang, X. D.; Wang, Z. M. *Nanoscale thermoelectrics*. Springer: Cham, **2014**; Vol. 16.

(53) Kumar, G. S.; Prasad, G.; Pohl, R. O. Experimental Determinations of the Lorenz Number. *J. Mater. Sci.* **1993**, 28, 4261-4272.

(54) Nolas, G. S.; Sharp, J.; Goldsmid, H. J. *Thermoelectrics: Basic Principles and New Materials Developments*. Springer: Berlin, **2001**.

(55) Liu, W.-S.; Zhang, B.-P.; Li, J.-F.; Zhang, H.-L.; Zhao, L.-D. Enhanced Thermoelectric Properties in $CoSb_{3-x}Te_x$ Alloys Prepared by Mechanical Alloying and Spark Plasma Sintering. *J. Appl. Phys.* **2007**, 102, 103717.

(56) Mills, K. C. *Thermodynamic Data for Inorganic Sulphides, Selenides and Tellurides*. Butterworths: London, **1974**.

Supporting Information

Enhanced Thermoelectric Performance of Ultrathin Bi_2Se_3 Nanosheets through Thickness Control

Min Hong, Zhi-Gang Chen, Lei Yang, Guang Han, and Jin Zou**

M. Hong, Dr Z.-G. Chen, Mr L. Yang, Dr G. Han, Prof. J. Zou.

Materials Engineering, The University of Queensland, Brisbane, QLD 4072, Australia E-mail: j.zou@uq.edu.au,z.chen1@uq.edu.au

Prof. J Zou

Centre for Microscopy and Microanalysis, The University of Queensland, Brisbane, QLD 4072, Australia

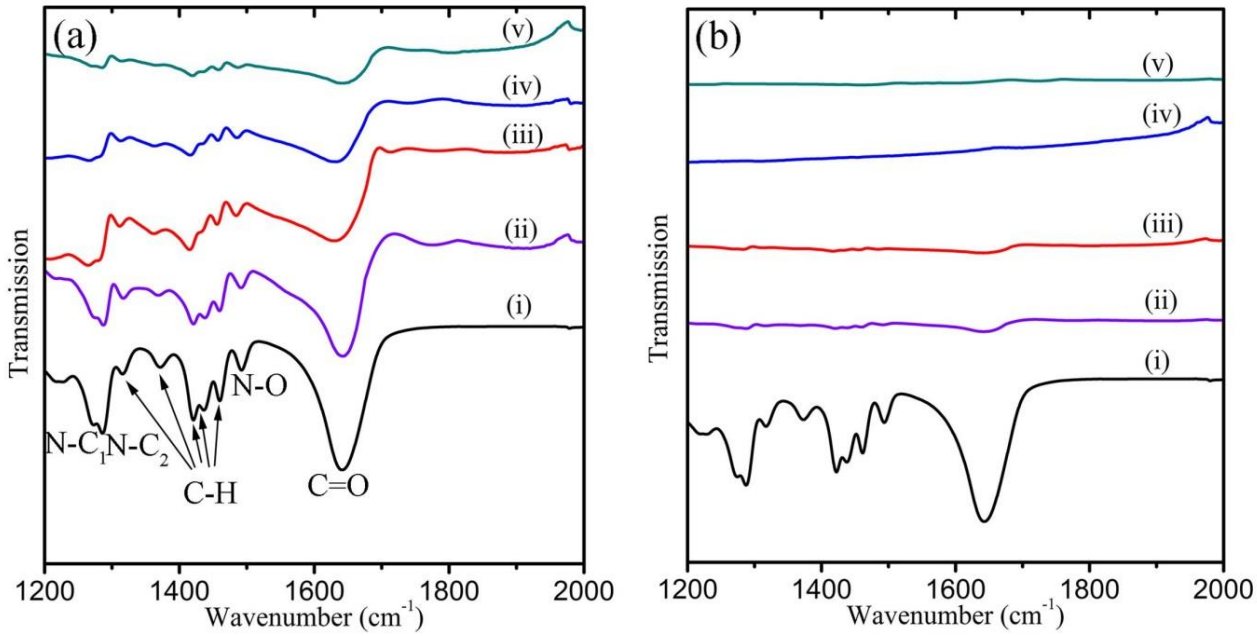

Figure S1 Fourier transform infrared spectrum of (a) samples collected from autoclaves after washed and subsequently dried and (b) samples baked at 300 ˚C for 4 hours. In the two plots, (i) signifies pure PVP as the reference and (ii) (iii) (iv) as well as (v) represent Bi_2Se_3 nanosheets synthesized with various PVP/Bi_2Se_3 molar ratios of 0.0025, 0.0125, 0.025, and 0.05, respectively.

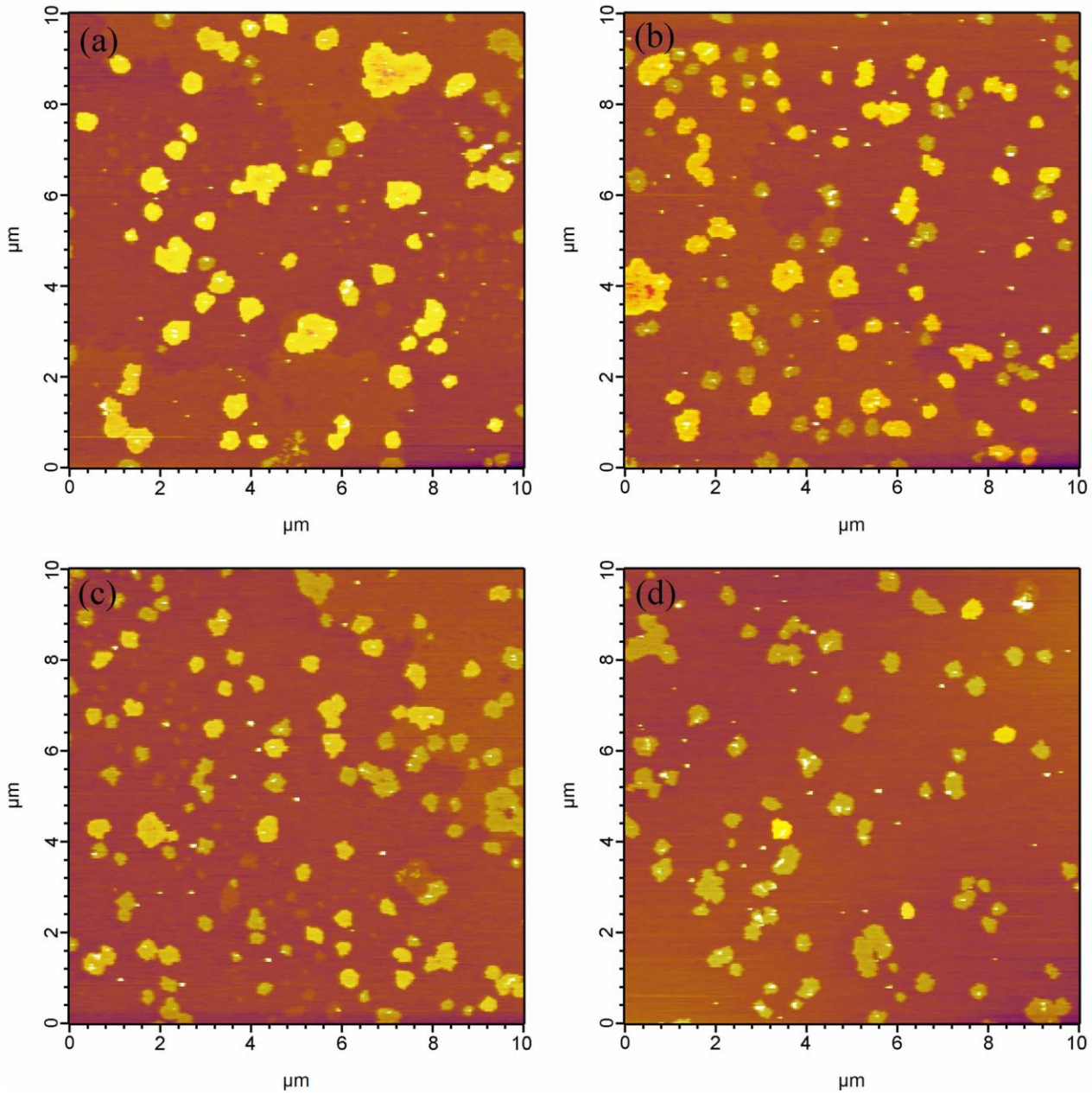

Figure S2 AFM images of numbers of Bi_2Se_3 nanosheets synthesized with various PVP/Bi_2Se_3 molar ratios: (a) 0.0025, (b) 0.0125, (c) 0.025, and (d) 0.05. According to the image contrast, the thickness of nanosheets decreases with increasing the PVP/Bi_2Se_3 molar ratios. After statistically analysing the height profiles of the AFM images, the thickness distribution will be summarized below.

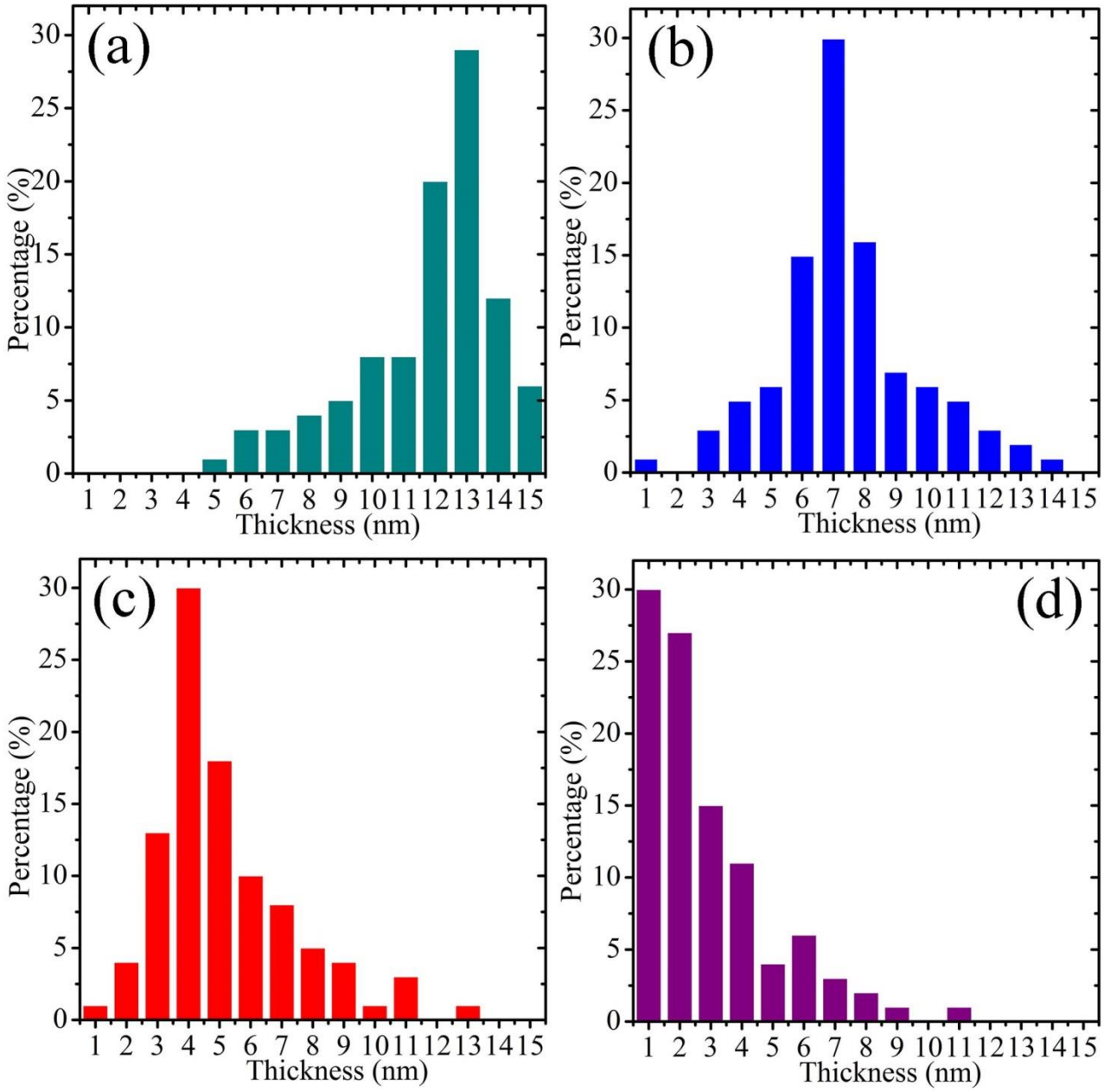

Figure S3 Thickness distributions of Bi_2Se_3 nanosheets synthesized with various PVP/Bi_2Se_3 molar ratios: (a) 0.0025, (b) 0.0125, (c) 0.025 and (d) 0.05.

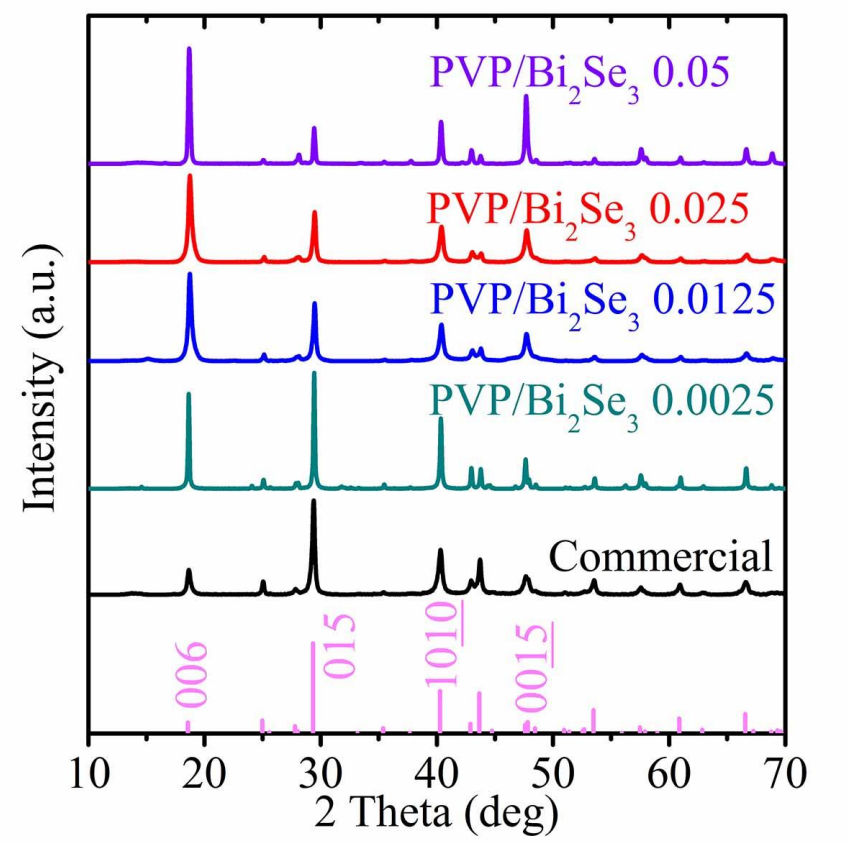

Figure S4 XRD patterns for sintered pellets.

Table S1 Peak intensities of XRD patterns for sintered pellets with Bi_2Se_3 nanosheets and the commercial counterpart

	Bi_2Se_3 (JCPDS 89-2008)	Commercial	13 QLs	7 QLs	4 QLs	1 QL
006	18.3	28.7	88.2	100	100	100
101	16.5	14.8	7.8	7.7	6	2.8
009	2.1	0	4.7	4.1	4.5	6.1
015	100	100	100	73.5	55.5	29.3
018	4.4	2.6	3.4	1.7	1.5	1.1
00,12	0.1	0	1	1	1.1	1.2
10,10	34.4	46	53.6	37.4	38	19.3
01,11	7	9.5	15	9.2	9.4	6
110	30.1	32.9	14.3	10.8	8.2	5
00,15	5.7	17.1	20.9	23.8	25.9	28.5
01,14	0.9	2.3	0.7	1.6	0.7	0.2
205	14.3	13.9	7.3	4.4	3.9	2.3
10,16	3.3	7.8	8.8	8	7.3	3.8
02,10	8.1	9.5	8.1	4.3	3.8	2.5
20,11	1.8	2.1	1.6	2.9	0.9	0.5
11,15	9.8	12.1	14.3	7.2	7.5	4.2
00,21	0.6	1.5	2.3	2.4	2.8	3
01,20	3.5	6.8	6.6	6.8	7.4	4.3
11,18	2.1	2.9	1.7	1.5	1.5	0.5
10,22	3.3	5.8	4	4.2	2.1	1.3
01,23	1.1	2.8	0.9	2.7	0.8	0.6
11,21	1.6	2.8	3.6	3	1.9	1.2
039	1.7	2.3	1.9	1.1	1	0.7

The texture fraction of the (001) planes was estimated from the XRD patterns by the Lotgering method,[1] $f=(P-P_0)/1-P_0$, where $P=\Sigma I(001)/\Sigma I(h\ k\ l)$ and $P_0=\Sigma I^0(001)/\Sigma I^0(h\ k\ l)$ with $I(h\ k\ l)$ and $I^0(h\ k\ l)$ denoting the intensities of ($h\ k\ l$) peaks for textured and the isotropic standard Bi_2Se_3 (JCPDS 29-2008), respectively.

Table S2 Calculated orientation factor of {0001} planes for powder samples and corresponding pellets.

	Commercial	13 QLs	7 QLs	4 QLs	1 QL
Powders	0.26	0.31	0.38	0.56	0.70
Pellets	0.05	0.24	0.34	0.41	0.57

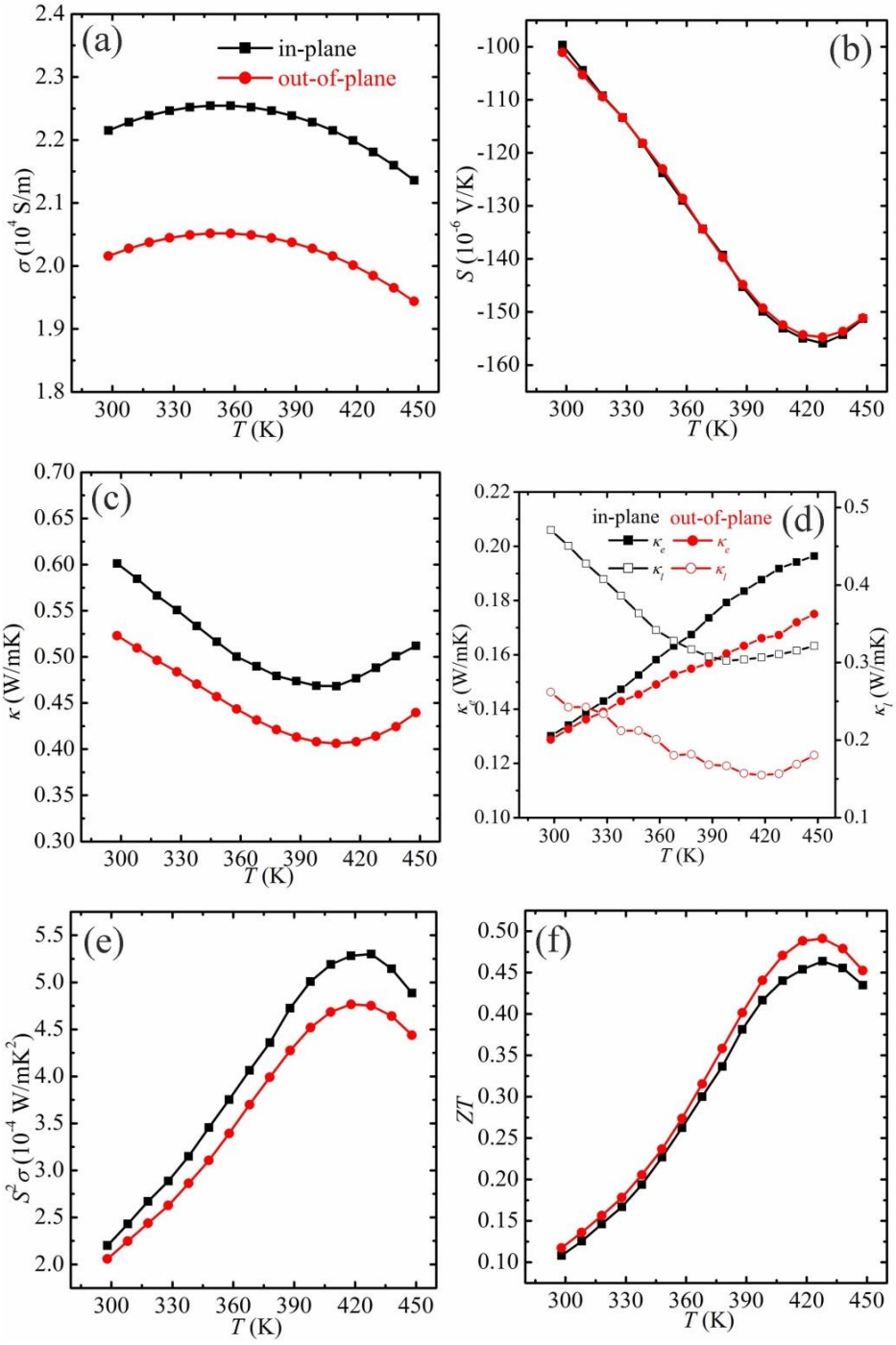

Figure S5 In-plane and out-of-plane thermoelectric characterization of pellets sintered from the ultrathin Bi_2Se_3 nanosheets: (a) electrical conductivity σ, (b) Seebeck coefficient S, (c) thermal conductivity κ, (d) electronic component κ_e and lattice component κ_l thermal conductivity, (e) power factor $S^2\sigma$ and (f) the figure of merit ZT. Compared with the out-of-plane thermoelectric properties, the in-plane electrical conductivity increases, and the in-plane thermal conductivity unfavourably increases, while the in-plane Seebeck coefficient is similar. As a consequence, the in-plane peak ZT is ca. 0.46, which is close to the out-of-plane maximum ZT value (0.48).

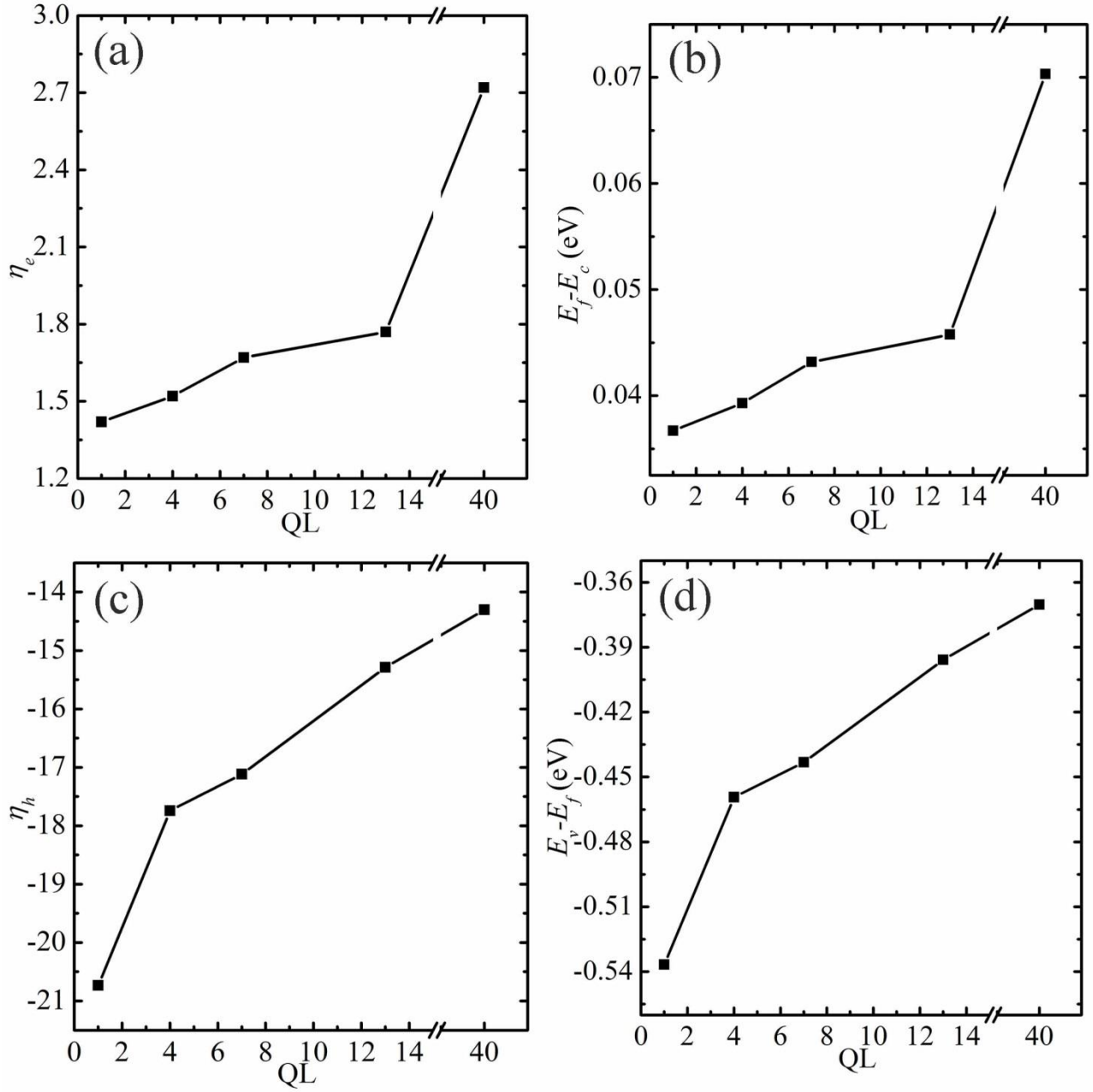

Figure S6 (a) Calculated reduced Fermi level for electrons (η_e), (b) $E_f - E_c$, (c) calculated reduced Fermi level for holes (η_h), and (d) $E_v - E_f$. The calculated reduced Fermi level for electrons and holes are at T = 300 K.

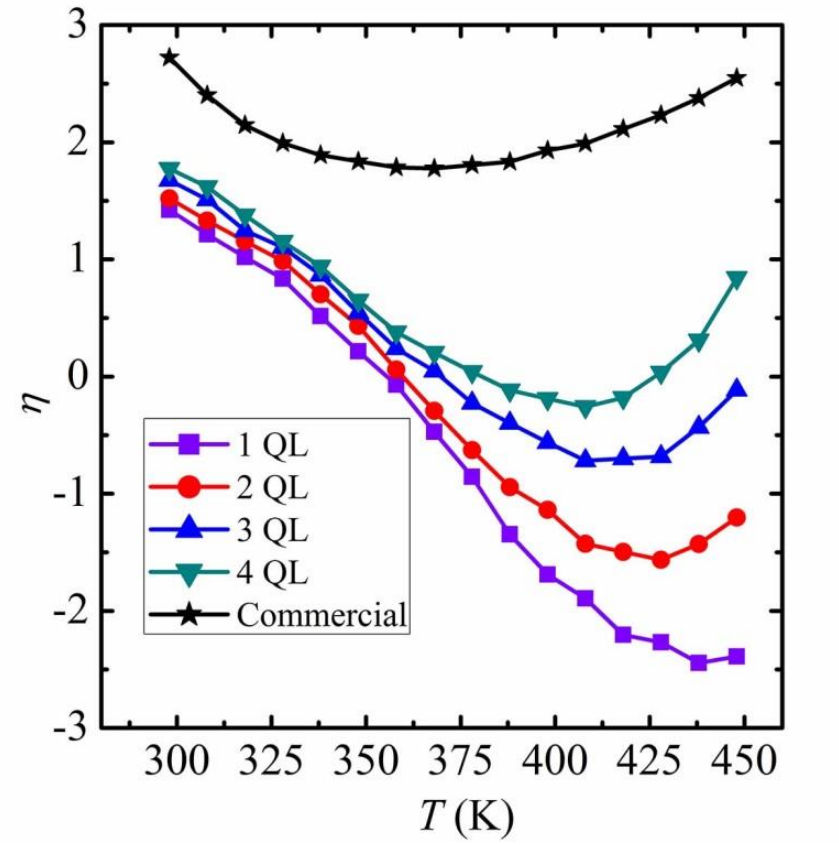

Figure S7 Calculated η for pellets made of nanosheets and commercial Bi_2Se_3 at the measured temperature range with the assumption that E_g does not change with temperature rising.

Reference

(1) Lotgering, F. K. Topotactical Reactions with Ferrimagnetic Oxides Having Hexagonal Crystal Structures—I. *J. Inorg. Nucl. Chem.* **1959**, 9, 113-123.

5

Enhancing Thermoelectric Performance of Hierarchical Te-Bi_2Te_3 Nanostructures through Rational Design

5.1 Introduction

Nanostructuring can achieve lower compared with the bulk counterparts, and therefore higher *ZT* can be obtained. Here, we design a hierarchical nanostructures assembled with well-aligned Bi_2Te_3 nanoplates using Te nanotubes as templates to further reduce the thermal conductivity by a facile microwave-assisted solvothermal synthesis. From the comparison of their thermoelectric performance and theoretical calculations with simple Bi_2Te_3 nanostructures, we found that Te/Bi_2Te_3 hierarchical nanostructures exhibits higher figure-of-merit due to the optimized reduced Fermi level and enhanced phonon scattering, as well as the suppressed bipolar conduction. This study provides an effective approach to enhance thermoelectric performance of Bi_2Te_3 based nanostructures by rationally designing the nanostructures.

5.2 Journal Publication

The results in Chapter 5 are included as it appears in *Nanoscale* **2016**, 8. http://pubs.rsc.org/en/Content/ArticleLanding/2016/NR/C6NR00719H#!divAbstract

Enhancing Thermoelectric Performance of Bi_2Te_3-based Nanostructures through Rational Structure Design

Min Hong[a], Zhi-Gang Chen[*a], Lei Yang[a] and Jin Zou[*ab]

a. Materials Engineering, University of Queensland, Brisbane, QLD 4072, Australia.

b. Centre for Microscopy and Microanalysis, University of Queensland, Brisbane, QLD 4072, Australia

Email: j.zou@uq.edu.au, z.chen1@uq.edu.au.

Nanostructuring has been successfully employed to enhance the thermoelectric performance of Bi_2Te_3 due to their obtained low thermal conductivity. In order to further reduce the thermal conductivity, we design a hierarchical nanostructures assembled with well-aligned Bi_2Te_3 nanoplates using Te nanotubes as templates by a facile microwave-assisted solvothermal synthesis. From the comparisons of their thermoelectric performance and theoretical calculations with simple Bi_2Te_3 nanostructures, we found that Te/Bi_2Te_3 hierarchical nanostructures exhibits higher figure-of-merit due to the optimized reduced Fermi level and enhanced phonon scattering, as well as the suppressed bipolar conduction. This study provides an effective approach to enhance thermoelectric performance of Bi_2Te_3 based nanostructures by rationally designing the nanostructures.

1. Introduction

Considering the environmental pollution caused by the consumption of fossil fuels and the rising demand of energy depletion, it is necessary to develop green sustainable energy sources and energy harvesting technologies.[1] Thermoelectric materials, enabling the direct conversion between heat and electricity, provide an alternative solution to these crises.[2] The energy conversion efficiency of a thermoelectric material is gauged by the dimensionless figure of merit, $ZT = S^2\sigma T/\kappa$, where S, σ, κ and T are the Seebeck coefficient, electrical conductivity, thermal conductivity (including electronic component κ_e, lattice component κ_l, and bipolar component κ_{bi}), and the working temperature, respectively.[3-5] However, the current low ZT values, especially for n-type (with free

electrons) thermoelectric materials, significantly hinder the commercialization of thermoelectric devices, which demand the synergistic development of both n-type and p-type (with free holes) thermoelectric elements.[6,7]

Bi_2Te_3 and the family of similar compounds are the promising thermoelectric candidates at room temperature region.[8-10] Because of their six-fold valley degeneracy, the narrow energy gap and layered crystal structure, Bi_2Te_3 potentially meets the criteria of high power factor ($S^2\sigma$) and low κ.[11] Compared with bulk counterpart, nanostructured Bi_2Te_3 can achieve much lower κ, and provides promising possibilities to manipulate the thermoelectric properties.[12] Especially, rhombohedral structured Bi_2Te_3 nanoplates, as two-dimensional nanostructures,[13-15] exhibit strengthened phonon scattering due to the dense grain boundaries after sintered into pellets.[16] To further strengthen the phonon scattering, we can assemble the randomly orientated nanoplates in the form of well-aligned hierarchical nanostructures.[17]

Inspired by our previous study on epitaxial growth of T-shaped Te/Bi_2Te_3 heteronanojunctions,[18] we explored the fabrication of the hierarchical nanostructures by using the one-dimensional Te nanostructures as templates. One-dimensional Te nanostructures, including nanowires[19] and nanotubes[20,21] have been reported to be synthesized by the wet chemical method. Compared with nanowires, nanotubes show even lower κ due to the existence of tube channels.[22] Because of the potential lattice match between trigonal structured Te (a_{Te} = 4.45 Å, c_{Te} = 5.92 Å)[23] and rhombohedral structured Bi_2Te_3 (a_{Bi2Te3} = 4.38 Å, c_{Bi2Te3} = 30.49 Å)[24], i.e. $a_{Te} \approx a_{Bi2Te3}$, $c_{Te} \approx 1/5\ c_{Bi2Te3}$, it is anticipated a small lattice mismatch of {11$\bar{2}$0} plane for Te and Bi_2Te_3 (< 2%),[25] so that {11$\bar{2}$0} planes of Te nanotubes can serve as templates for the epitaxial growth of Bi_2Te_3 nanoplates, as demonstrated in the atomic models of Te/Bi_2Te_3 heteronanojunctions (refer to Figure 1a and b). Using this crystallographic relationship, Te/Bi_2Te_3 hierarchical nanostructures can be formed on Te nanostructures. F*or layered* Bi_2Te_3 single crystals, κ *is anisotropic and its value* along the *c*-axis is only ~50% of that on the *a*-*b* plane,[26] so that massive studies have explored the advantage of well-aligned Bi_2Te_3 *layered* nanostructures to reduce κ.[7,19,27] Therefore, this hierarchical nanostructures is expected to result in significantly enhanced phonon scattering, as schematically illustrated in Figure 1c. On the other hand, the crystalline nature of Te nanotube walls may enhance σ.[22,28]

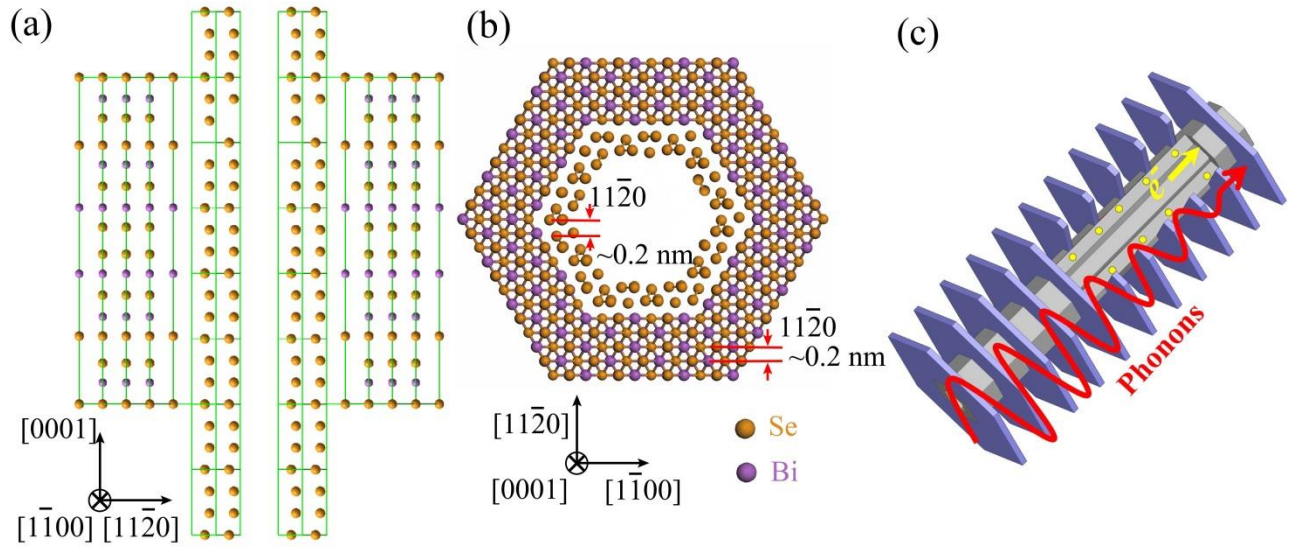

Figure 1 Schematic atomic models for Te/Bi_2Te_3 hierarchical nanostructures showing the crystallographic relationship along (a) [1$\bar{1}$00] and (b) [0001]. (c) Schematic demonstrating the advantages of the hierarchical nanostructure in strengthening phonon scattering and ensuring high electrical conductivity.

In this study, we employed a microwave-assisted solvothermal method to synthesize Te/Bi_2Te_3 hierarchical nanostructures using Te nanotubes as templates. To confirm the superiority of Te/Bi_2Te_3 hierarchical nanostructures in enhancing thermoelectric efficiency, highly uniform Bi_2Te_3 nanoplates were also investigated as a reference. Through the comparison of the morphology-dependent thermoelectric performance, we fundamentally studied the structural effects on tuning thermoelectric properties.

2. Experimental

Materials Synthesis and Processing

In this study, analytical grade $Bi(NO_3)_3 \cdot 5H_2O$, Na_2TeO_3, ethylene glycol, poly(N-vinyl-2-pyrrolidone) (PVP, M_w = 4000), and NaOH solution were used as precursors.

The synthesis of the Te/Bi_2Te_3 hierarchical nanostructures was carried out in two steps. The first step is to synthesize Te nanotubes as the precursors, following by the second step - synthesis of Te/Bi_2Te_3 hierarchical nanostructures. In the first step, we added 332.4 mg Na_2TeO_3 and 0.2 g PVP into 40 mL ethylene glycol. The solutions were stirred vigorously for 30 min at room temperature. Subsequently, the obtained clear solutions were sealed in a 100 mL teflon vessel, which was heated in a CEM Mars-6 microwave oven at 230 ˚C for 5 min. After naturally cooled to room temperature, the as-synthesized

Te nanotubes were collected by a high-speed centrifugation, washed six times with distilled water and absolute ethanol and finally dried at 60 ˚C for 12 h in a vacuum oven. In the second step, the obtained Te nanotubes were mixed with $Bi(NO_3)_3 \cdot 5H_2O$ into 40 mL ethylene glycol with a mole ratio of 2:3, and with NaOH solution (5 mol/L, 2 mL). After stirring for ~30 min, the mixed solution was transferred into the teflon vessels again, and heated in the CEM Mars-6 microwave oven at 230 ˚C for 5 min. Through washing, centrifuging and drying, we obtained the final nanopowders.

As a comparison, pure Bi_2Te_3 nanoplates were also synthesized. During the synthesis, 485.1 mg $Bi(NO_3)_3 \cdot 5H_2O$, 332.4 mg Na_2TeO_3 and 0.2 g PVP were mixed with 40 mL ethylene glycol and NaOH solution (5 mol/L, 2mL). After being stirred vigorously, the obtained clear solutions were sealed in the teflon vessel, and heated in the CEM Mars-6 microwave oven at 230 ˚C for 5 min. After naturally cooled to room temperature, the synthesized products were collected by a high-speed centrifugation, washed six times with distilled water and absolute ethanol, and finally dried at 60 ˚C for at least 12 h in a vacuum oven.

Materials Characterizations

The phase purities of the as-synthesized products were examined by the X-ray diffractometer (XRD) equipped with graphite monochromatized, Cu *Kα* radiation (*λ* = 1.5418 Å). The morphological, structural, and compositional characteristics of the synthesized products were investigated by scanning electron microscopy (SEM, JEOL 7800) and transition electron microscopy (TEM, FEI F20), equipped with EDS for compositional analysis.

Fabrication of Pellets

The as-synthesized Te/Bi_2Te_3 hierarchical nanostructures and Bi_2Te_3 nanoplates were compressed by the spark plasma sintering (SPS) under 40 MPa and at 250 ˚C for 5 min in vacuum into pellets with a diameter of 12.5 mm and a thickness of 2 mm. The densities (d) of sintered pellets were measured by an Archimedes method, and confirmed to be over 90%.

Thermoelectric Performance Measurement

Thermal diffusivity (D) of sintered pellets was measured by a laser flash method (LFA 457, NETZSCH), and κ was calculated through $\kappa = DC_pd$, where C_p is the specific heat

capacity. C_p is obtained from empirical formulas C_{pBT} = 108.06+5.53×$10^{-2}T$ $JK^{-1}mol^{-1}$ for Bi_2Te_3.[29] σ and S were measured simultaneously on a ZEM-3, ULVAC. The uncertainties of the thermoelectric performance measurements (S, σ and D) were estimated as ~5% for each.

3. Results and discussion

Figure 2a is the X-ray diffraction (XRD) pattern collected from the as-synthesized Te/Bi_2Te_3 nanopowders with the inset showing its enlarged view of 2θ in the range of 34° – 43°. As can be seen, the diffraction peaks can be indexed as the rhombohedral structured Bi_2Te_3 phase with lattice parameters of a = 4.38 Å and c = 30.49 Å (JCPDS No. 89-2009)[24] and the trigonal structured Te phase with lattice parameters of a = 4.45 Å and c = 5.92 Å (JCPDS No. 36-1452).[23] It should be noted that no Bi contamination was detected in the as-prepared samples, although our samples contain excessive Bi^{3+} (dissolved from $Bi(NO_3)_3$). We believe that the excessive Bi^{3+} was still in the solvent after the synthesis that was washed away during the post synthesis process. Figure 2b is a SEM image, and shows that the majority (> 90%) of synthesized products are rod-like nanostructures. Figure 2c is a TEM image of a typical rod-like nanostructure, in which the feature of a hierarchical nanostructure is seen — many parallel nanoplates are linked by a nanotube (as a stem). Their crystallographic relationship was further analyzed using selected area electron diffraction (SAED) and high resolution TEM (HRTEM). Figure 2d is a SAED pattern taken from the circled area of such hierarchical nanostructure showing superimposed [$1\bar{1}00$] zone-axis diffraction patterns of a trigonal structured Te phase and a rhombohedral structured Bi_2Te_3 phase, from which the crystallographic relationship between the Te nanotube and the Bi_2Te_3 nanoplates can be determined as $[0001]_{Te}$ // $[0001]_{Bi2Te3}$ and $[11\bar{2}0]_{Te}$ // $[11\bar{2}0]_{Bi2Te3}$. Figure 2e and f are the corresponding HRTEM images taken from the arrowed nanotube body and the nanoplate edge, respectively, which further suggests the coexistence of a high-crystalline trigonal structured Te nanotube stem and rhombohedral structured Bi_2Te_3 nanoplate. EDS was applied to examine the compositions of the nanotube and nanoplates. Figure 2g shows the EDS profiles collected respectively from the labeled areas in Figure 2c, suggesting that the nanotube is indeed Te, while the nanoplates are composed of Bi and Te with a mole ratio of approximately 2:3. To understand the structural characteristics of Te/Bi_2Te_3 hierarchical nanostructures, we examined structures of Te nanotubes after first step synthesis (an example is shown in the Supporting Information), which demonstrated that the obtained

nanotubes have their lengths of 2 - 6 μm and diameters of 100 - 200 nm. Our extensive TEM investigations of Te/Bi_2Te_3 hierarchical nanostructures indicate that the lateral size and thickness of the epitaxially grown Bi_2Te_3 nanoplates are relatively independent to the diameters of Te nanotubes.

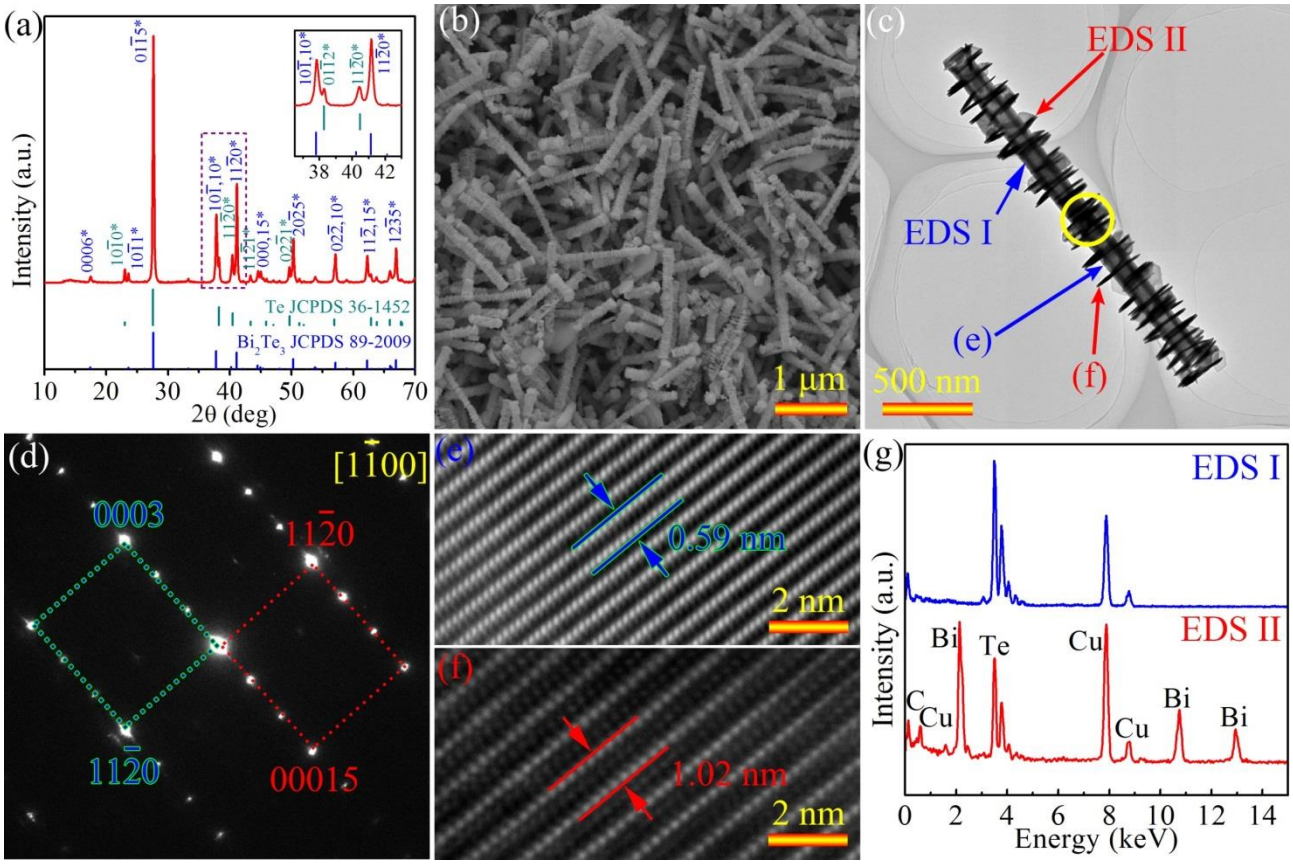

Figure 2 (a) XRD patterns collected from as-synthesized Te/Bi2Te3 nanopowders with inset showing its enlarged view. (b) Low-magnification SEM image showing a large amount of hierarchical nanostructures. (c) TEM image of a typical Te/Bi2Te3 hierarchical nanostructure. (d) The [1$\bar{1}$00] zone-axis SAED. (e) and (f) HRTEM images respectively taken from the arrowed areas in (c). (g) EDS profiles respectively taken from the arrowed areas in (c).

As a comparison, Bi_2Te_3 nanoplates were also synthesized and characterized. Figure 3a is a XRD pattern of as-prepared Bi_2Te_3 nanoplates, confirming Bi_2Te_3 nanoplates are highly pure rhombohedral structured Bi_2Te_3 phase. Figure 3b is the low-magnification SEM image of as-synthesized Bi_2Te_3 hexagonal-shaped nanoplates that have uniform morphology with their lateral size of ~1μm. The inset of Figure 3b is the high-magnification SEM image showing the side-view of several nanoplates, from which the nanoplate thickness of ~ 20 nm can be revealed. Figure 3c is the TEM image of a typical nanoplate

with lateral size of ~1μm, in accordance with the size determined by SEM (refer to Figure 3b). Figure 3d is the [0001] zone-axis SAED pattern and Figure 3e is the corresponding HRTEM image with a lattice spacing of 0.22 nm, which matches well with the *d* value of the $\{11\bar{2}0\}$ planes of rhombohedral structured Bi_2Te_3.[30] Figure 3f shows the EDS profile, indicating that the elemental ratio of Bi and Te is approximately 2:3 (note that Cu and C peaks are caused by the TEM Cu grid with C supporting films).

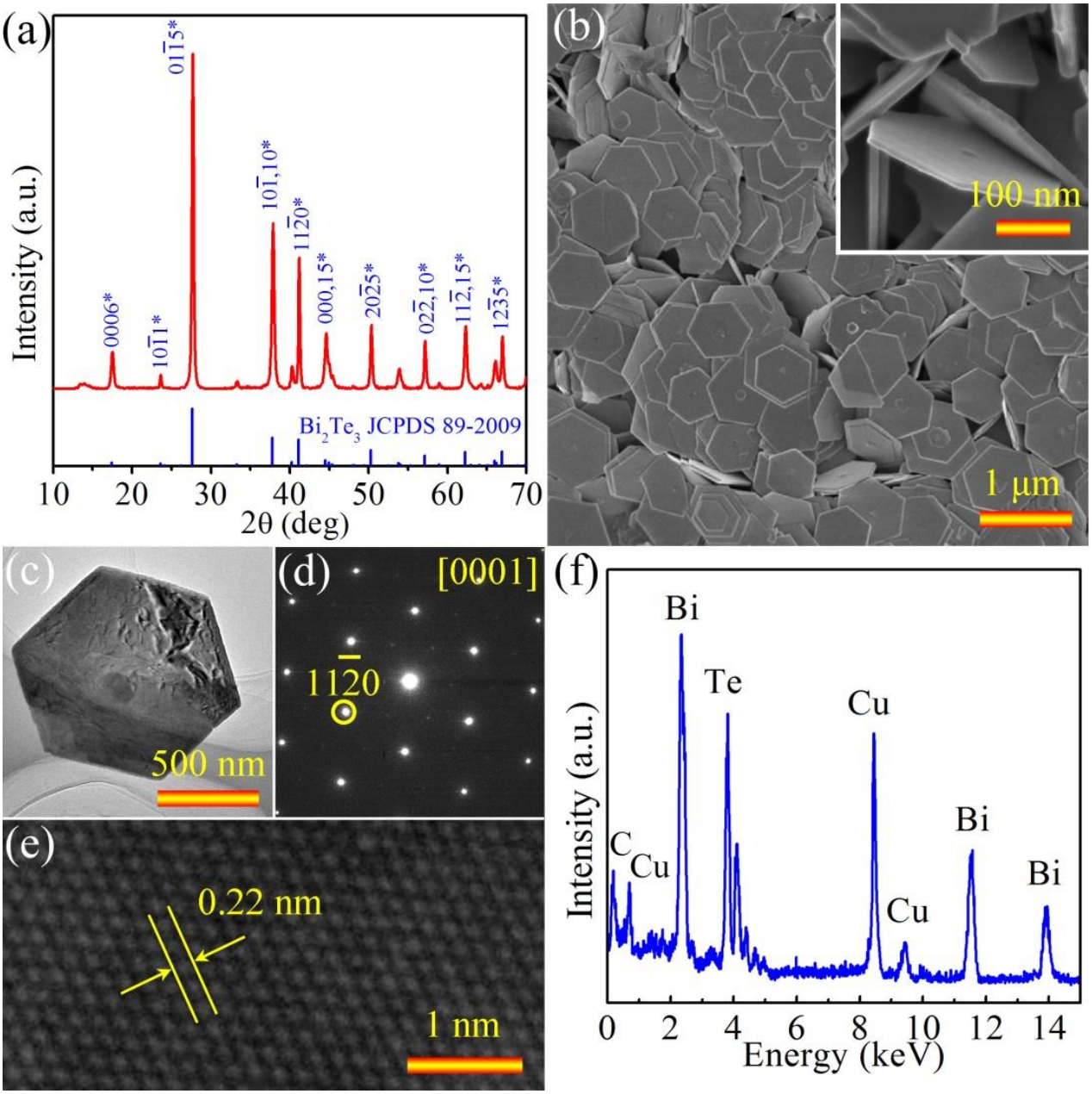

Figure 3 (a) XRD pattern taken from the as-synthesized Bi_2Te_3 nanopowders (b) Low-magnification SEM image with inset of side-view high-magnification SEM image. (c) TEM image of a typical Bi_2Te_3 nanoplate. (d), (e), and (f) Corresponding SAED pattern, HRTEM image, and EDS profile, respectively.

In order to evaluate their thermoelectric performance, we examined sintered pellets made from Te/Bi_2Te_3 hierarchical nanostructures and Bi_2Te_3 nanoplates. Figure 4a presents σ and S as a function of temperature, indicated by the left-hand side and the right-hand side y-axis, respectively. As can be seen, σ declines from ~8×10^4 Sm^{-1} to ~5×10^4 Sm^{-1} with increasing the temperature for both Bi_2Te_3 and Te/Bi_2Te_3 based pellets; however the declining trend in Te/Bi_2Te_3 is mitigated. In the case of S, its negative sign for both Bi_2Te_3 and Te/Bi_2Te_3 cases indicates their n-type feature. Specifically, S for Bi_2Te_3 ranges from -150 μVK^{-1} to -170 μVK^{-1}, while that for Te/Bi_2Te_3 fluctuates between -165 μVK^{-1} and -182 μVK^{-1} in the studied temperature range. Moreover, the absolute value of S increases first and then decreases with increasing the temperature. The decrease in |S| should be caused by the bipolar conduction,[31] and the peak of |S| for Te/Bi_2Te_3 shifts towards the higher temperature, suggesting that the bipolar conduction is suppressed at the higher temperature. Based on the measured σ and S, we can calculate $S^2\sigma$, and plotted in Figure 4b as a function of temperature. As can be seen, the peak $S^2\sigma$ of 19.2×10^{-4} $Wm^{-1}K^{-2}$ for Te/Bi_2Te_3 is larger than that of 18×10^{-4} $Wm^{-1}K^{-2}$ for Bi_2Te_3, and the peak $S^2\sigma$ for Te/Bi_2Te_3 shifts to higher temperature. This is due to the suppressed bipolar conduction and the mitigated declining trend in σ with increasing the temperature in Te/Bi_2Te_3 (refer to Figure 4a).

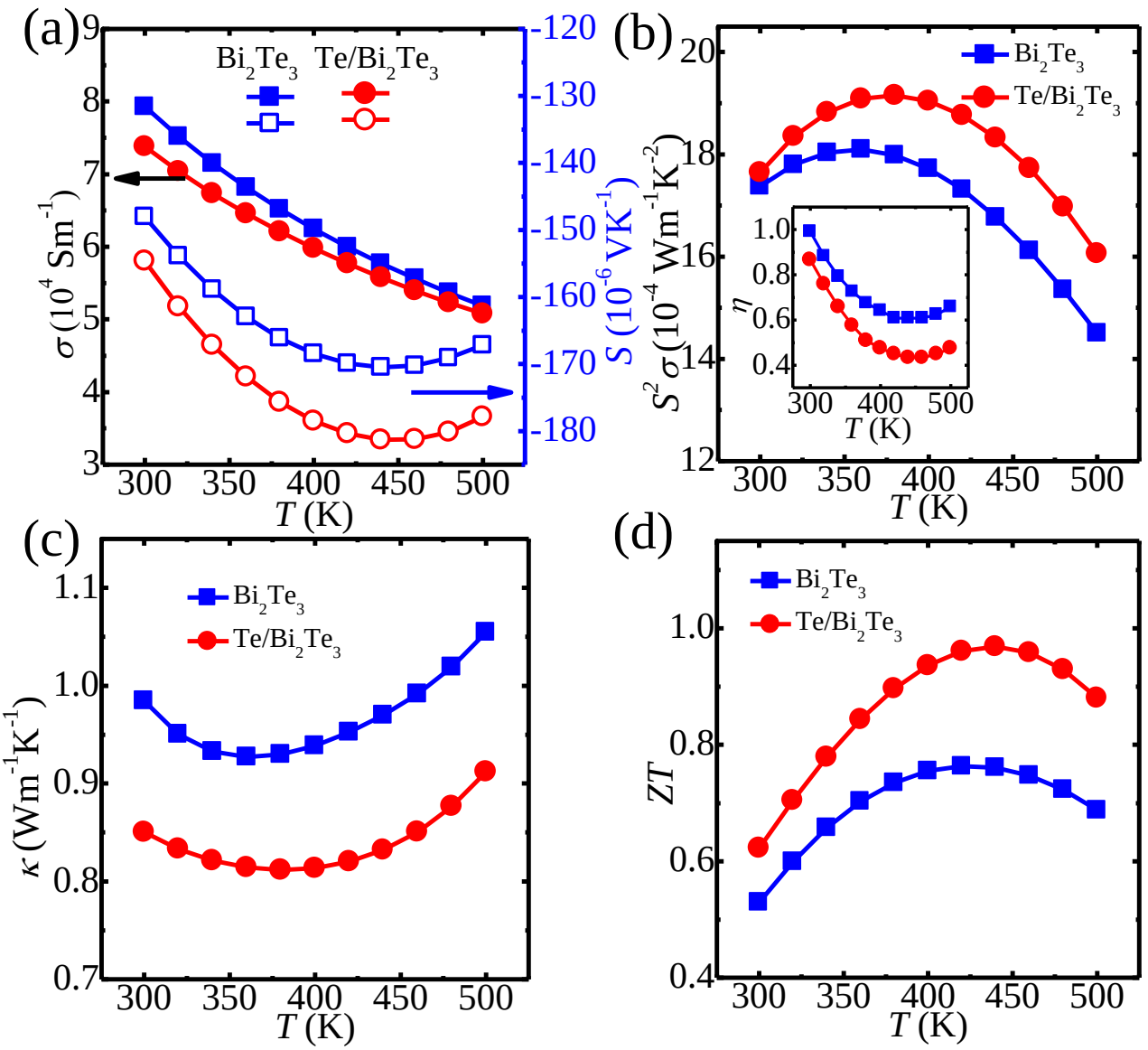

Figure 4 Thermoelectric properties of Te/Bi_2Te_3 hierarchical nanostructures compared with Bi_2Te_3 nanoplates (a) σ and S, (b) $S^2\sigma$ with inset showing calculated η, (c) κ and (d) ZT.

To understand the enhanced $S^2\sigma$, we calculated the reduced Fermi level (η=Ef/kBT, with E_f representing the Fermi level and k_B is the Boltzmann constant) based on the measured S by using the following equation[32]

$$S = -\frac{k_B}{e}\left[\frac{2F_1(\eta)}{F_0(\eta)} - \eta\right], \quad (1)$$

with the generalized Fermi integral

$$F_i(\eta) = \int_0^\infty \frac{\varepsilon^i}{1+\exp(\varepsilon-\eta)} d\varepsilon \ ; \quad (2)$$

where *e* is the elementary charge. The inset of Figure 4b plots the variation of η with temperature for both Bi_2Te_3 and Te/Bi_2Te_3 in which η for Te/Bi_2Te_3 is smaller than that for Bi_2Te_3.

According to our previous study,[33] to maximize $S^2\sigma$, the Fermi level should locate near the conduction band edge for n-type thermoelectric materials. Compared with Bi_2Te_3, η for Te/Bi_2Te_3 is closer to its conduction band edge, so that an enhanced $S^2\sigma$ for Te/Bi_2Te_3 can be anticipated. The η decline for Te/Bi_2Te_3 nanostructures can be ascribed to the excessive Te (provided by Te nanotube stems), which might suppress the Te vacancies in epitaxially grown Bi_2Te_3 nanoplates. Although Te vacancies in Bi_2Te_3 are generally unavoidable (giving n-type transport feature), the Te vacancies lead to the Fermi level resides deep in the conduction band. However, by adding more Te, Te vacancies in in Bi_2Te_3 can be supressed; leading to the shift of the Fermi level towards to valance band in our Te/Bi_2Te_3 nanostructures. Figure 4c plots κ versus temperature, from which κ in Te/Bi_2Te_3 shows ~20% reduction than that for Bi_2Te_3. Due to the enlarged $S^2\sigma$ and simultaneously decreased κ, ZT for Te/Bi_2Te_3 is enhanced, as shown in Figure 4d. ZT for Te/Bi_2Te_3 reaches ~1, much larger than that of ~ 0.75 for Bi_2Te_3.

From above discussion, one of the critical reasons for enhanced ZT is the significantly decreased κ. To clarify the underlying principle, we studied the contributions of κ from electrons, phonons and bipolar conduction. According to the Wiedemann-Franz law,[34] κ_e can be expressed as

$$\kappa_e = L\sigma T \ , \tag{3}$$

where L is the Lorenz number. Employing the single Kane band model, L can be determined by[35]

$$L = \left(\frac{k_B}{e}\right)^2 \left[\frac{3F_2(\eta)}{F_0(\eta)} - \left(\frac{2F_2(\eta)}{F_0(\eta)}\right)^2\right] \tag{4}$$

Through inputting the determined η (refer to the inset of Fig 4b) into Equation (4), we can calculate L. The results are shown in Figure 5a, in which L fluctuates around 1.6×10^{-8} V^2K^{-2} for both samples, matching with reported values for nanostructured thermoelectric systems.[36] On this basis, Figure 5b plots the calculated κ_e over the studied temperature, where κ_e is reduced in Te/Bi_2Te_3 due to its smaller σ and *L* over Bi_2Te_3. By subtracting κ_e from κ, we can study the variation of κ_l, although there is a κ_{bi} contribution at high

temperature. Figure 4b shows the obtained temperature dependent κ-κ_e, which suggests that κ_l in Te/Bi_2Te_3 is significantly decreased. This is because Te/Bi_2Te_3 hierarchical nanostructures have the well-aligned nanoplates attached on the body surface, which lead to stronger phonon scattering compared with the randomly orientated Bi_2Te_3 nanoplates.[37] Moreover, κ_{bi} is calculated using the reference-outlined method.[38] Specifically, by extrapolating the linear relationship between κ_l and 1/T demonstrated in the insert of Figure 5c, we can obtain κ_l in the entire studied temperature range, and finally, though subtracting κ_l from κ-κ_e, we can obtain κ_{bi}. Figure 5d shows the determined κ_{bi} as a function of temperature. As can be seen, κ_{bi} for Te/Bi_2Te_3 is reduced; suggesting that the bipolar conduction in Te/Bi_2Te_3 has been indeed suppressed, which is consistent with the peak of S for Te/Bi_2Te_3 shifting to the high temperature (refer to Figure 4a). To understand this, we note that the band gap difference between Te (0.33 eV)[39] and Bi_2Te_3 (0.15 eV) [40] may lead to an extra energy offset between the conduction and valance bands for the Te/Bi_2Te_3 nanostructures. In addition, our Bi_2Te_3 nanoplates in Te/Bi_2Te_3 are generally thinner than the normal Bi_2Te_3 nanoplates, leading to the enlargement of band gap of our thinner Bi_2Te_3 nanoplates.[41] As a consequence, the bipolar conduction should be suppressed in our Te/ Bi_2Te_3 nanostructures.

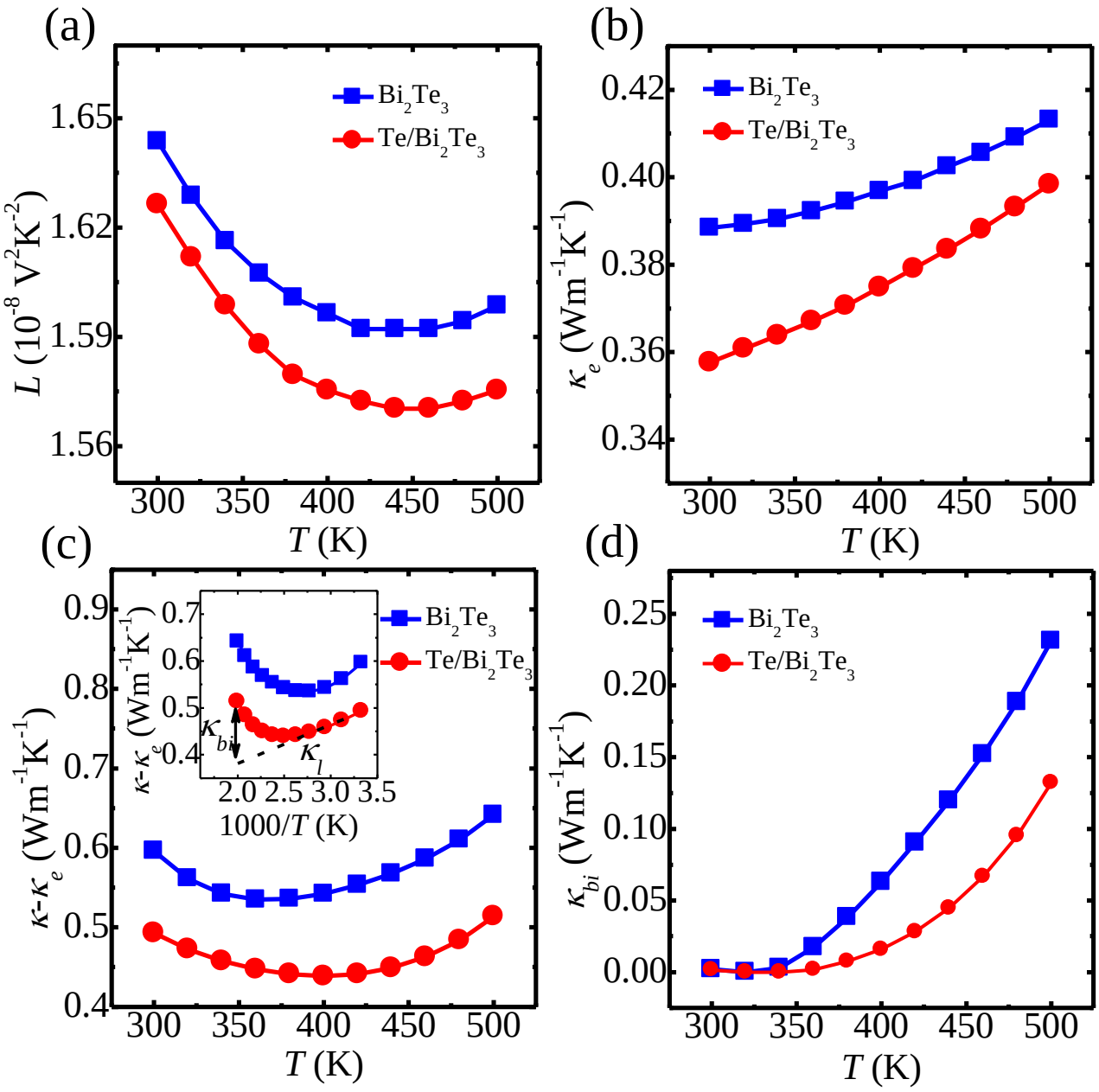

Figure 5 (a) Calculated temperature dependent (a) L, (b) κ_e, (c) κ - κ_e with inset showing the inverse temperature dependence of κ - κ_e, and (d) κ_{bi}.

4. Conclusion

We successfully fabricated Te/Bi_2Te_3 hierarchical nanostructures using Te nanotubes as templates by the facile microwave-assisted solvothermal method. Through systematic morphological, structural and compositional characterizations, structural quality and the epitaxial growth of well-aligned Bi_2Te_3 nanoplates on Te nanotube stems are verified. The thermoelectric properties measured from their sintered pellets indicate an increased ZT ≈ 1 when compared with their pure Bi_2Te_3 nanoplates with ZT ≈ 0.75. Our modelling studies

suggest that the enhanced ZT of our Te/Bi_2Te_3 hierarchical nanostructures is caused by the optimized reduced Fermi level, the strengthened phonon scatterings, and the suppressed bipolar conduction. This study provides an effective approach to enhance thermoelectric efficiency by designing rational nanostructures.

Acknowledgements

This work was financially supported by the Australian Research Council. MH thanks the China Scholarship Council for providing a PhD stipend. The Australian Microscopy & Microanalysis Research Facility is acknowledged for providing characterization facilities.

Reference

(1) Tritt, T. M.; Subramanian, M. A. Thermoelectric Materials, Phenomena, and Applications: a Bird's Eye View. *Mrs. Bull.* **2006**, 31, 188-194.

(2) Snyder, G. J.; Toberer, E. S. Complex Thermoelectric Materials. *Nat. Mater.* **2008**, 7, 105-114.

(3) Chen, Z.-G.; Han, G.; Yang, L.; Cheng, L.; Zou, J. Nanostructured Thermoelectric Materials: Current Research and Future Challenge. *Prog. Nat. Sci.* **2012**, 22, 535-549.

(4) Yang, L.; Chen, Z.-G.; Han, G.; Hong, M.; Zou, Y.; Zou, J. High-Performance Thermoelectric Cu_2Se Nanoplates through Nanostructure Engineering. *Nano Energy* **2015**, 16, 367-374.

(5) Han, G.; Chen, Z.-G.; Yang, L.; Hong, M.; Drennan, J.; Zou, J. Rational Design of Bi_2Te_3 Polycrystalline Whiskers for Thermoelectric Applications. *ACS Appl. Mater. Interf.* **2014**, 7, 989-995.

(6) DiSalvo, F. J. Thermoelectric Cooling and Power Generation. *Science* **1999**, 285, 703-706.

(7) Chang, H.-C.; Chen, C.-H.; Kuo, Y.-K. Great Renhancements in the Tthermoelectric Ppower Ffactor of BiSbTe Nnanostructured Ffilms with Wwell-Oordered Iinterfaces. *Nanoscale* **2013**, 5, 7017-7025.

(8) Poudel, B.; Hao, Q.; Ma, Y.; Lan, Y.; Minnich, A.; Yu, B.; Yan, X.; Wang, D.; Muto, A.; Vashaee, D.; Chen, X.; Liu, J.; Dresselhaus, M. S.; Chen, G.; Ren, Z. High-Thermoelectric

Performance of Nanostructured Bismuth Antimony Telluride Bulk Alloys. *Science* **2008**, 320, 634-638.

(9) Mehta, R. J.; Zhang, Y.; Karthik, C.; Singh, B.; Siegel, R. W.; Borca-Tasciuc, T.; Ramanath, G. A New Class of Doped Nanobulk High Figure-of-Merit Thermoelectrics by Scalable Bottom-up Assembly. *Nat. Mater.* **2012**, 11, 233-240.

(10) Hong, M.; Chen, Z. G.; Yang, L.; Zou, J. BixSb2−xTe3 nanoplates with enhanced thermoelectric performance due to sufficiently decoupled electronic transport properties and strong wide-frequency phonon scatterings. *Nano Energy* **2016**, 20, 144-155.

(11) Rowe, D. M. *CRC handbook of thermoelectrics*. CRC Press: New York, **1995**.

(12) Finefrock, S. W.; Yang, H.; Fang, H.; Wu, Y. Thermoelectric Properties of Solution Synthesized Nanostructured Materials. *Annu. Rev. Chem. Biomol. Eng.* **2015**, 6, 247-266.

(13) Zhang, Y.; Hu, L. P.; Zhu, T. J.; Xie, J.; Zhao, X. B. High Yield Bi_2Te_3 Single Crystal Nanosheets with Uniform Morphology via a Solvothermal Synthesis. *Cryst. Growth Des.* **2013**, 13, 645-651.

(14) Tsai, H.-W.; Wang, T.-H.; Chan, T.-C.; Chen, P.-J.; Chung, C.-C.; Yaghoubi, A.; Liao, C.-N.; Diau, E. W.-G.; Chueh, Y.-L. Fabrication of large-scale single-crystal bismuth telluride (Bi2Te3) nanosheet arrays by a single-step electrolysis process. *Nanoscale* **2014**, 6, 7780-7785.

(15) Guo, L.; Yan, H.; Moore, Q.; Buettner, M.; Song, J.; Li, L.; Araujo, P. T.; Wang, H.-T. Elastic properties of van der Waals epitaxy grown bismuth telluride 2D nanosheets. *Nanoscale* **2015**, 7, 11915-11921.

(16) Soni, A.; Shen, Y.; Yin, M.; Zhao, Y.; Yu, L.; Hu, X.; Dong, Z.; Khor, K. A.; Dresselhaus, M. S.; Xiong, Q. Interface Driven Energy Filtering of Thermoelectric Power in Spark Plasma Sintered $Bi_2Te_{2.7}Se_{0.3}$ Nanoplatelet Composites. *Nano Lett.* **2012**, 12, 4305-4310.

(17) Lu, W. G.; Ding, Y.; Chen, Y. X.; Wang, Z. L.; Fang, J. Y. Bismuth Telluride Hexagonal Nanoplatelets and Their Two-Step Epitaxial Growth. *J. Am. Chem. Soc.* **2005**, 127, 10112-10116.

(18) Cheng, L.; Chen, Z.-G.; Yang, L.; Han, G.; Xu, H.-Y.; Snyder, G. J.; Lu, G.-Q.; Zou, J. T-Shaped Bi_2Te_3-Te Heteronanojunctions: Epitaxial Growth, Structural Modeling, and Thermoelectric Properties. *J. Phys. Chem. C* **2013**, 117, 12458-12464.

(19) Fang, H.; Wu, Y. Telluride Nanowire and Nanowire Heterostructure-Based Thermoelectric Eenergy Harvesting. *J. Mater. Chem. A* **2014**, 2, 6004-6014.

(20) Mayers, B.; Xia, Y. Formation of Tellurium Nanotubes Through Concentration Depletion at the Surfaces of Seeds. *Adv. Mater.* **2002**, 14, 279-282.

(21) Kim, B.; Park, B.-K. Synthesis of Self-Aligned Tellurium Nanotubes by a Sodium Thiosulfate-Assisted Polyol Method. *Electronic Materials Letters* **2012**, 8, 33-36.

(22) Rowe, D. M. *Thermoelectrics Handbook : Macro to Nano*. CRC Press: Hoboken, **2005**.

(23) Song, J.-M.; Lin, Y.-Z.; Zhan, Y.-J.; Tian, Y.-C.; Liu, G.; Yu, S.-H. Superlong High-Quality Tellurium Nanotubes: Synthesis, Characterization, and Optical Property. *Cryst. Growth Des.* **2008**, 8, 1902-1908.

(24) Nakajima, S. The crystal structure of Bi2Te3−xSex. *J. Phys. Chem. Solids* **1963**, 24, 479-485.

(25) Mi, J. L.; Lock, N.; Sun, T.; Christensen, M.; Sondergaard, M.; Hald, P.; Hng, H. H.; Ma, J.; Iversen, B. B. Biomolecule-Assisted Hydrothermal Synthesis and Self-Assembly of Bi_2Te_3 Nanostring-Cluster Hierarchical Structure. *ACS Nano* **2010**, 4, 2523-2530.

(26) Carle, M.; Pierrat, P.; Lahalle-Gravier, C.; Scherrer, S.; Scherrer, H. Transport Properties of *n*-Type $Bi_2(Te_{1-x}Se_x)_3$ Single Crystal Solid Solutions (x = 0.05). *J. Phys. Chem. Solids* **1995**, 56, 201-209.

(27) Shi, W.; Yu, S.; Liu, P.; Fan, W. Hydrothermal Synthesis and Thermoelectric Transport Properties of Sb_2Te_3-Te_X Heterogeneous Nanostructures. *CrystEngComm* **2013**, 15, 2978-2985.

(28) Liu, W.; Yan, X.; Chen, G.; Ren, Z. Recent Advances in Thermoelectric Nanocomposites. *Nano Energy* **2012**, 1, 42-56.

(29) Mills, K. C. *Thermodynamic Data for Inorganic Sulphides, Selenides and Tellurides*. Butterworths: London, **1974**.

(30) Cheng, L.; Chen, Z.-G.; Ma, S.; Zhang, Z.-D.; Wang, Y.; Xu, H.-Y.; Yang, L.; Han, G.; Jack, K.; Lu, G.; Zou, J. High Curie Temperature $Bi_{1.85}Mn_{0.15}Te_3$ Nanoplates. *J. Am. Chem. Soc.* **2012**, 134, 18920-18923.

(31) Wang, S.; Tan, G.; Xie, W.; Zheng, G.; Li, H.; Yang, J.; Tang, X. Enhanced Thermoelectric Properties of $Bi_2(Te_{1-x}Se_x)_3$-Based Compounds as *n*-Type Legs for Low-Temperature Power Generation. *J. Mater. Chem.* **2012**, 22, 20943-20951.

(32) Chen, C. L.; Wang, H.; Chen, Y. Y.; Day, T.; Snyder, G. J. Thermoelectric Properties of *p*-Type Polycrystalline SnSe Doped with Ag. *J. Mater. Chem. A* **2014**, 2, 11171-11176.

(33) Hong, M.; Chen, Z.-G.; Yang, L.; Han, G.; Zou, J. Enhanced Thermoelectric Performance of Ultrathin Bi_2Se_3 Nanosheets through Thickness Control. *Adv. Electron. Mater.* **2015**, 1, 1500025.

(34) Sootsman, J. R.; Chung, D. Y.; Kanatzidis, M. G. New and Old Concepts in Thermoelectric Materials. *Angew. Chem. Int. Edit.* **2009**, 48, 8616-8639.

(35) Zhu, T.; Gao, H.; Chen, Y.; Zhao, X. Ioffe-Regel Limit and Lattice Thermal Conductivity Reduction of High Performance $(AgSbTe_2)_{15}(GeTe)_{85}$ Thermoelectric Materials. *J. Mater. Chem. A* **2014**, 2, 3251-3256.

(36) Zhao, L.; Lo, S. H.; He, J.; Li, H.; Biswas, K.; Androulakis, J.; Wu, C.-I.; Hogan, T. P.; Chung, D.-Y.; Dravid, V. P.; Kanatzidis, M. G. High Performance Thermoelectrics from Earth-Abundant Materials: Enhanced Figure of Merit in PbS by Second Phase Nanostructures. *J. Am. Chem. Soc.* **2011**, 133, 20476-20487.

(37) Zhao, X. B.; Ji, X. H.; Zhang, Y. H.; Zhu, T. J.; Tu, J. P.; Zhang, X. B. Bismuth Telluride Nanotubes and the Effects on the Thermoelectric Properties of Nanotube-Containing Nanocomposites. *Appl. Phys. Lett.* **2005**, 86.

(38) Liu, W.-S.; Zhang, B.-P.; Li, J.-F.; Zhang, H.-L.; Zhao, L.-D. Enhanced Thermoelectric Properties in $CoSb_{3-x}Te_x$ Alloys Prepared by Mechanical Alloying and Spark Plasma Sintering. *J. Appl. Phys.* **2007**, 102, 103717.

(39) Anzin, V. B.; Eremets, M. I.; Kosichkin, Y. V.; Nadezhdinskii, A. I.; Shirokov, A. M. Measurement of the Energy Gap in Tellurium under Pressure. *Phys. Status Solidi A* **1977**, 42, 385-390.

(40) Greenaway, D. L.; Harbeke, G. Band Structure of Bismuth Telluride, Bismuth Selenide and Their Respective Alloys. *J. Phys. Chem. Solids* **1965**, 26, 1585-1604.

(41) Yazyev, O. V.; Moore, J. E.; Louie, S. G. Spin Polarization and Transport of Surface States in the Topological Insulators Bi_2Se_3 and Bi_2Te_3 from First Principles. *Phys. Rev. Lett.* **2010**, 105, 266806.

Supporting Information

Enhancing Thermoelectric Performance of Bi_2Te_3-based Nanostructures through Rational Structure Design

Min Hong[a], Zhi-Gang Chen[*a], Lei Yang[a] and Jin Zou[*ab]

c. Materials Engineering, University of Queensland, Brisbane, QLD 4072, Australia.

d. Centre for Microscopy and Microanalysis, University of Queensland, Brisbane, QLD 4072, Australia

Email: j.zou@uq.edu.au, z.chen1@uq.edu.au

Fig. S1 is the XRD pattern of as-syntehsized nanopowders. As can be seen, all peaks can be assigned to the trigonal structured Te (JCPDS No. 36-1452), suggesting no detectable impurities in the product. Fig. S2 low-magnification SEM image of Te nanopowders, from which randomly aligned one-dimensional nanotubes with smooth surface can be seen, and their length ranges from ~ 2 to 6 μm. The inset of Fig. S2 exhibits the cross-sectional view, demonstrating the hollow hexagonal prism structure of the nanotubes, with a diameter of ~200 nm and a wall thickness of ~30 nm.

Fig. S3a is the TEM image of a typical nanotube, and Fig. S3b is the energy dispersive spectroscopy profile confirming the nanotube is Te (Note that the Cu peak is due to the Cu TEM grid). The Te nanotube shows a dark solid area in the middle of this tubular structure, which stems from the initially formed Te seeds during the growth of Te nanotubes.[1] To understand the crystal structure and the growth direction of the nanotube, we employed the high resolution TEM (HRTEM). Fig. S3c and d are the HRTEM image and the corresponding selected area electron diffraction (SAED) pattern, which reveals the high quality single-crystalline feature of as-synthesized nanotubes. In addition, the zone axis is determined to be $[\bar{1}2\bar{1}0]$, and lattice spacings of ~0.39 and 0.59 nm respectively corresponding to $(10\bar{1}0)$ and (0001) planes for trigonal Te are identified. To exclusively determine the growth direction, we took another set of $[1\bar{1}00]$ zone-axis HRTEM and

SAED, as shown in Fig. S3e and f. To obtain these images, we tilted the nanotube along the axis direction with ~30°. Considering both HRTEM and SAED, (0001) and $(11\bar{2}0)$ planes can be identified. On this basis, we can conclude that the growth direction of as-synthesized Te nanotubes is along [0001].

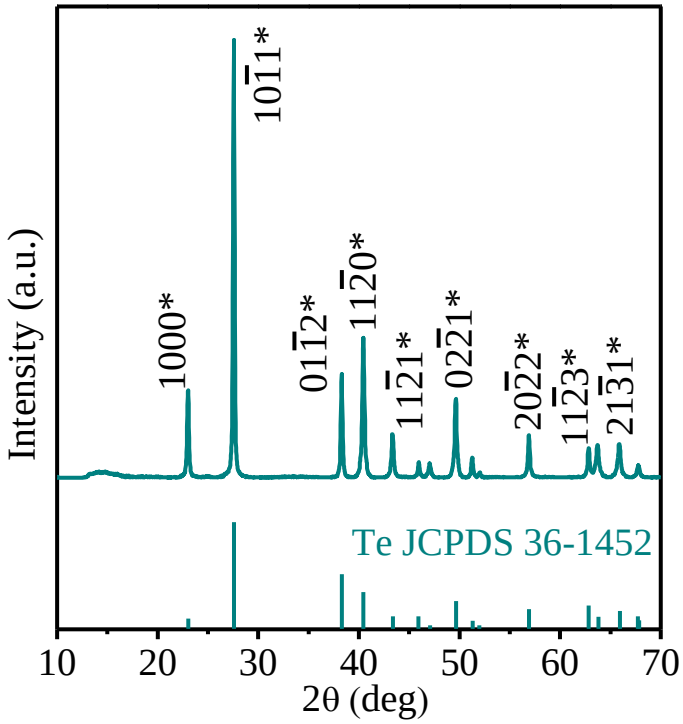

Fig. S1 XRD pattern of as-synthesized Te nanotubes.

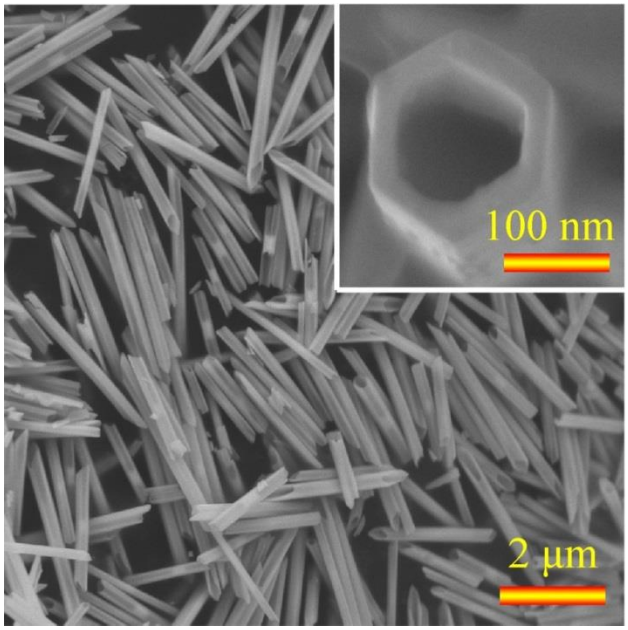

Fig. S2 Low-magnification SEM image of as-synthesized Te nanotubes with inset showing the cross-section view of a typical nanotube.

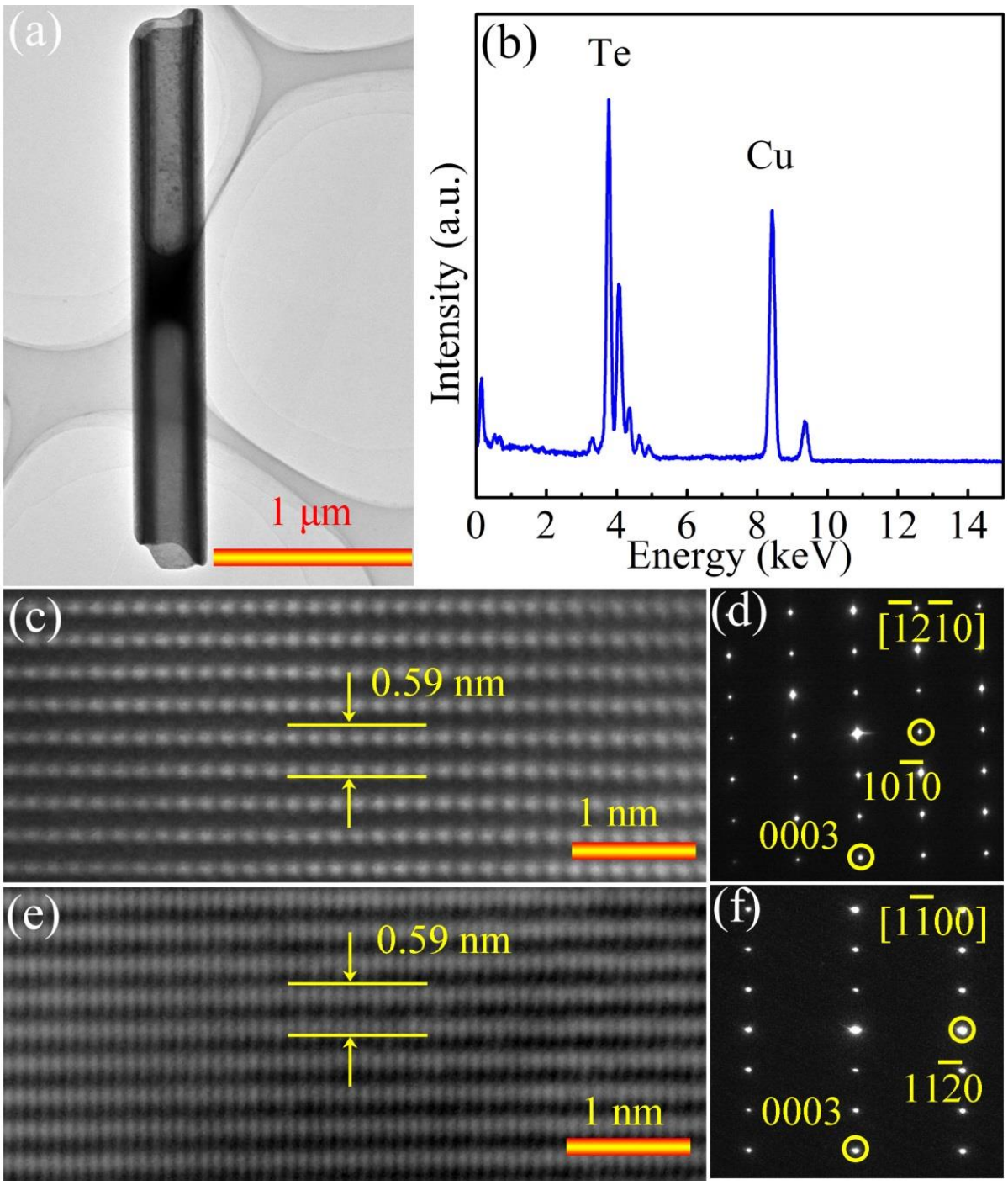

Fig. S3 (a) TEM image of a typical Te nanotube. (b) EDS profile taken from this Te nanotube. (c) HRTEM, and (d) corresponding [$\bar{1}2\bar{1}0$] zone-axis SAED pattern. (e) HRTEM, and (f) corresponding [$1\bar{1}00$] zone-axis SAED pattern.

Reference

(1) Mayers, B.; Xia, Y. Formation of Tellurium Nanotubes Through Concentration Depletion at the Surfaces of Seeds. *Adv. Mater.* **2002**, 14, 279-282.

6

$Bi_xSb_{2-x}Te_3$ Nanoplates with Enhanced Thermoelectric Performance due to Sufficiently Decoupled Electronic Transport Properties and Strong Wide-Frequency Phonon Scatterings

6.1 Introduction

The main challenging for enhancing $S^2\sigma$ is the reversely co-related S and σ, and sufficiently decoupling S and σ can achieve a net increase in $S^2\sigma$. Here, we newly introduced a variable (λE_{def} — the dimensionless λ representing the square root of ratio between the initial effective mass and the free electron mass, and E_{def} representing the deformation potential) to serve as the decoupling factor. Through the simulation studies, we found that reducing λE_{def} and simultaneously optimizing the reduced Fermi level (η) are the key to enhance $S^2\sigma$. Based on these findings, we employed a rapid microwave-assisted solvothermal method to fabricate $Bi_xSb_{2-x}Te_3$ nanoplates, securing an enhanced $S^2\sigma$ of 28.3×10^{-4} $Wm^{-1}K^{-2}$. In addition, we obtained an ultra-low thermal conductivity of 0.7 $Wm^{-1}K^{-1}$, and the reason for this is the broadened frequency phonon scattering caused by point defects, dislocations and grain boundaries. As a consequence, ZT of 1.2 was obtained.

6.2 Journal Publication

The results in Chapter 5 are included as it appears in *Nano Energy* **2016**, 20.

http://www.sciencedirect.com/science/article/pii/S2211285515004851

$Bi_xSb_{2-x}Te_3$ Nanoplates with Enhanced Thermoelectric Performance due to Sufficiently Decoupled Electronic Transport Properties and Strong Wide-Frequency Phonon Scatterings

Min Hong,[a] Zhi G. Chen,[,a] Lei Yang,[a] and Jin Zou[*,a,b]*

a Materials Engineering, University of Queensland, Brisbane, QLD 4072, Australia

b Centre for Microscopy and Microanalysis, University of Queensland, Brisbane, QLD 4072, Australia

Email: j.zou@uq.edu.au, z.chen1@uq.edu.au.

Abstract

Thermoelectric materials enable the direct conversion between heat and electricity, offering a sustainable technology to overcome the upcoming energy crisis. P-type $Bi_xSb_{2-x}Te_3$ systems potentially satisfy the criteria (*i.e.* large power-factor, and low thermal conductivity) for thermoelectric applications. Nanostructuring has been considered as an effective approach to enhance the thermoelectric performance. Here, we employed a rapid microwave-assisted solvothermal method to fabricate $Bi_xSb_{2-x}Te_3$ nanoplates, securing a peak figure-of-merit of 1.2, caused by the obtained high power-factor of 28.3×10^{-4} $Wm^{-1}K^{-2}$ and ultra-low thermal conductivity of 0.7 $Wm^{-1}K^{-1}$. Based on the single Kane band model with a newly introduced variable (λE_{def} — the dimensionless λ representing the square root of ratio between the initial effective mass and the free electron mass, and E_{def}

representing the deformation potential) to serve as the decoupling factor, we found that $Bi_xSb_{2-x}Te_3$ nanoplates with tunable compositions can decrease λE_{def} and simultaneously optimize the reduced Fermi level to ultimately enhance the power-factor. Moreover, detailed structural characterizations reveal dense grain boundaries and dislocations in our nanostructures. These two phonon scattering sources in conjunction with the inherently existed Bi-Sb lattice disorders lead to a strong wide-frequency phonon scattering, and consequently result in a significantly decreased thermal conductivity. This study provides strategic guidance to develop high-performance thermoelectric materials by nanostructuring and compositional engineering to achieve ultra-low thermal conductivity and to maximize the power-factor.

Keywords

$Bi_xSb_{2-x}Te_3$ nanoplates; Microwave-assisted solvothermal; Thermoelectric; Decoupling factor; Phonon scattering

1. Introduction

Thermoelectric technology, realizing the direct solid-state energy conversion between heat and electricity, can be an alternative solution to the energy crisis and environment pollution caused by the excessive usage of fossil fuels [1]. The thermoelectric efficiency is evaluated by the dimensionless figure-of-merit, $ZT = S^2\sigma T/\kappa$, where S, σ, κ and T are respectively the Seebeck coefficient, electrical conductivity, thermal conductivity (including electronic component κ_e and lattice component κ_l), and the working temperature [2]. The enhancement in ZT simultaneously requires a high power factor ($S^2\sigma$) and a low κ [3]. To achieve a large $S^2\sigma$, narrow-band gap semiconductors with compromised S and σ are preferred [4,5]; and to obtain a low κ, these semiconductors should be composed of heavy elements with strong lattice anharmonicity [6] or with complex structures [7]. Therefore, V-VI based semiconductors [8,9]. Half-Heusler alloys [10] and Zintl phases [11] have been widely studied as thermoelectric applications.

For the low temperature (200 K - 400 K) power-generation and refrigeration applications, bismuth telluride (Bi_2Te_3) based alloys are the dominant candidates [12]. To enhance their thermoelectric performance, tuning compositions [13,14] and/or developing novel material fabrication methods [15,16] have been the two key research activities. Tuning compositions by forming ternary phases (i.e. n-type $Bi_2Te_{3-x}Se_x$ and p-type $Bi_xSb_{2-x}Te_3$), coupled with

doping extra elements, can not only control the types and densities of point defects and/or enlarge their band gaps to achieve high $S^2\sigma$, but can also reduce κ_l due to the strengthened phonon scattering by point defects [17,18]. Developing novel material preparation methods aims to reduce the grain size of bulk thermoelectric systems so as to decrease κ_l [19]. However, since grain boundaries and point defects are only effective to respectively block the propagations of low- and high-frequency phonons, it is necessary to introduce additional phonon scattering mechanisms to further reduce κ_l [20]. For this reason, dislocations responsible for scattering mid-frequency phonons were introduced in bulk $Bi_{0.5}Sb_{1.5}Te_3$ system prepared by the Te-rich metal spun [15] and in the $Bi_2Te_{2.7}Se_{0.3}$ ingot processed by hot deformation [21]; from which record-high *ZT* values were achieved. Inspired by these breakthroughs, nanostructured ternary systems with dense grain boundaries and dislocations should be favorable to obtain a high *ZT*. As a typical bottom-up assembly approach to fabricate nanostructures with better control over the size, structure, and morphology [22], solvothermal synthesis is effective to fabricate nanostructured Bi_2Te_3 [23,24], Bi_2Se_3 [25], Sb_2Te_3 [26,27] and their corresponding ternary systems [28,29]. However, the traditional solvothermal method is time-consuming and the possible residuals of surfactants can be detrimental for their thermoelectric properties [30].

In this study, we employed a microwave-assisted surfactant-free solvothermal method. In order to understand the impact of the Bi concentration on *S* and σ modifications, nanostructured $Bi_xSb_{2-x}Te_3$ samples with x ranging from 0 to 0.6 were fabricated. The localized super heating mechanism of microwave irradiation enables to fabricate large-scale nanostructures within a short period of time. To evaluate the thermoelectric performance, the as-synthesized $Bi_xSb_{2-x}Te_3$ nanopowders were compressed into pellets by spark plasma sintering (SPS), from which a peak *ZT* of 1.2 was achieved in the pellet composed of $Bi_{0.5}Sb_{1.5}Te_3$ nanostructures. The fundamentals for the enhanced thermoelectric properties of $Bi_xSb_{2-x}Te_3$ pellets were explored by the single Kane model [31], and the achieved ultra-low κ was clarified by our detailed transmission electron microscopy (TEM) investigations, coupled with theoretical calculations on phonon transport using the Callaway model [32].

2. Materials and methods

Synthesis method: All chemicals were purchased from Sigma Aldrich and used without further purification. In the synthesis of $Bi_xSb_{2-x}Te_3$ with a designed yield of 1 mmol, we added $SbCl_3$ (2-x mmol), $Bi(NO_3)_3{\cdot}5H_2O$ (x mmol), Na_2TeO_3 (3 mmol) and NaOH solution

(5 mol/L, 2 mL) into ethylene glycol (40 mL). The prepared solution was stirred vigorously for 30 min. The formed clear solution was finally sealed in a 100 mL teflon vessel. CEM Mars 6 microwave oven was employed with a setting temperature of 230 ˚C holding for 10 min. After cooled to room temperature, the as-synthesized products were washed, centrifuged, and finally dried at 60 ˚C for 12 hours in vacuum oven.

Characterization: The phase purities of as-synthesized and sintered products were characterized by XRD, recorded on an X-ray diffractometer equipped with graphite monochromatized, Cu Kα radiation (λ = 1.5418 Å). Their morphological, structural, and chemical characteristics of the synthesized products were investigated by SEM (JEOL 7800) and TEM (FEI F20, equipped with EDS for compositional analysis). Compositions of the sintered samples were examined using the wave length dispersive X-ray spectrometry (WDX) in the JEOL JXA-8200 electron probe microanalysis (EPMA).

Fabrication of nanostructured pellets: The as-synthesized nanoplate powders were compressed by SPS under 40 MPa and at 250 ˚C for 5 min in vacuum. The densities of all sintered pellets were measured by an Archimedes method, from which the densities can be confirmed to be ~ 95%.

Measurement of thermoelectric properties: Thermal diffusivity (*D*) was measured by a laser flash method (LFA 457, NETZSCH), and thermal conductivity *κ* was calculated through $\kappa = DC_{p_x}d$, where C_{px} and *d* are the specific heat capacity, and density, respectively. C_{px} is obtained from empirical formulas $C_{P_{ST}} = 120.3 + 28.0\times10^{-3}T$ $JK^{-1}mol^{-1}$ for Sb_2Te_3 [33] and $C_{P_{BT}} = 108.06 + 5.53\times10^{-2}T$ $JK^{-1}mol^{-1}$ for Bi_2Te_3 [34], respectively. C_{px} for $Bi_2Te_{3-x}Se_x$ was then estimated using the Vegard's law of $C_P = C_{P_{ST}}(3-x) + C_{P_{BT}}x$, since the difference between $C_{P_{ST}}$ and $C_{P_{BT}}$ is small. *σ* and *S* were measured simultaneously on a ZEM-3, ULVAC. The uncertainty of the thermoelectric performance measurements (*S*, *σ* and *D*) was estimated as ~ 5%.

3. Results and discussion

Characterizations of $Bi_xSb_{2-x}Te_3$ nanoplates

Figure 1a is X-ray diffraction (XRD) patterns of as-synthesized $Bi_xSb_{2-x}Te_3$ powders with different nominal Bi concentrations (i.e. x = 0, 0.3, 0.4, 0.5 and 0.6). From which, the obtained diffraction peaks can be exclusively indexed as the rhombohedral structured

Sb_2Te_3 phase with lattice parameters of *a* = 4.264 Å and *c* = 30.458 Å (JCPDS No. 71-0393) [35]. Figure 1b presents the enlarged view of 015* diffraction peaks. As can be seen, they systematically shift to the low 2θ angle with increasing the Bi concentration, suggesting an extension of lattice parameters in $Bi_xSb_{2-x}Te_3$ due to Bi atoms replacing Sb sites in the lattice. The calculated lattice parameters of *a* and *c* based on the XRD patterns follow a linear increasing trend with increasing the Bi concentration, which matches well with the Vegard's law [36] (see Figure S1) and the reported ternary $Bi_xSb_{2-x}Te_3$ [28]. To analyze the composition of as-synthesized nanostructures, energy-dispersive X-ray spectroscopy (EDS) was employed, and the obtained EDS profiles are shown in Figure S2. Detailed compositional analysis indicates that elemental ratios of Sb, Bi, and Te are close to the nominal values.

To understand the morphological and structural characteristics of as-synthesized nanostructures, TEM was applied. As a representative example, as-synthesized $Bi_{0.5}Sb_{1.5}Te_3$ powders have been carefully studied and presented in Figure 1c-f. Figure 1c displays a TEM image of a nanoplate with the lateral size of ~1 μm, which agrees with the size distribution revealed by the low-magnification scanning electron microscope (SEM) image shown in Figure S3. Figure 1d is a corresponding selected area electron diffraction (SAED) pattern, and Figure 1e is a corresponding <001> zone-axis high-resolution TEM (HRTEM) image, indicating the single-crystal nature with high crystallinity. Figure 1f is an EDS profile taken from such a nanoplate, in which Sb, Bi, and Te peaks can be identified (the Cu peaks are due to the Cu TEM grid). The elemental mappings in the insets suggest that Sb, Bi, and Te distribute uniformly in the nanoplate. On the basis of above characterization and analysis, we can conclude that pure $Bi_xSb_{2-x}Te_3$ ternary nanoplates have been successfully fabricated by our facile microwave-assisted solvothermal method.

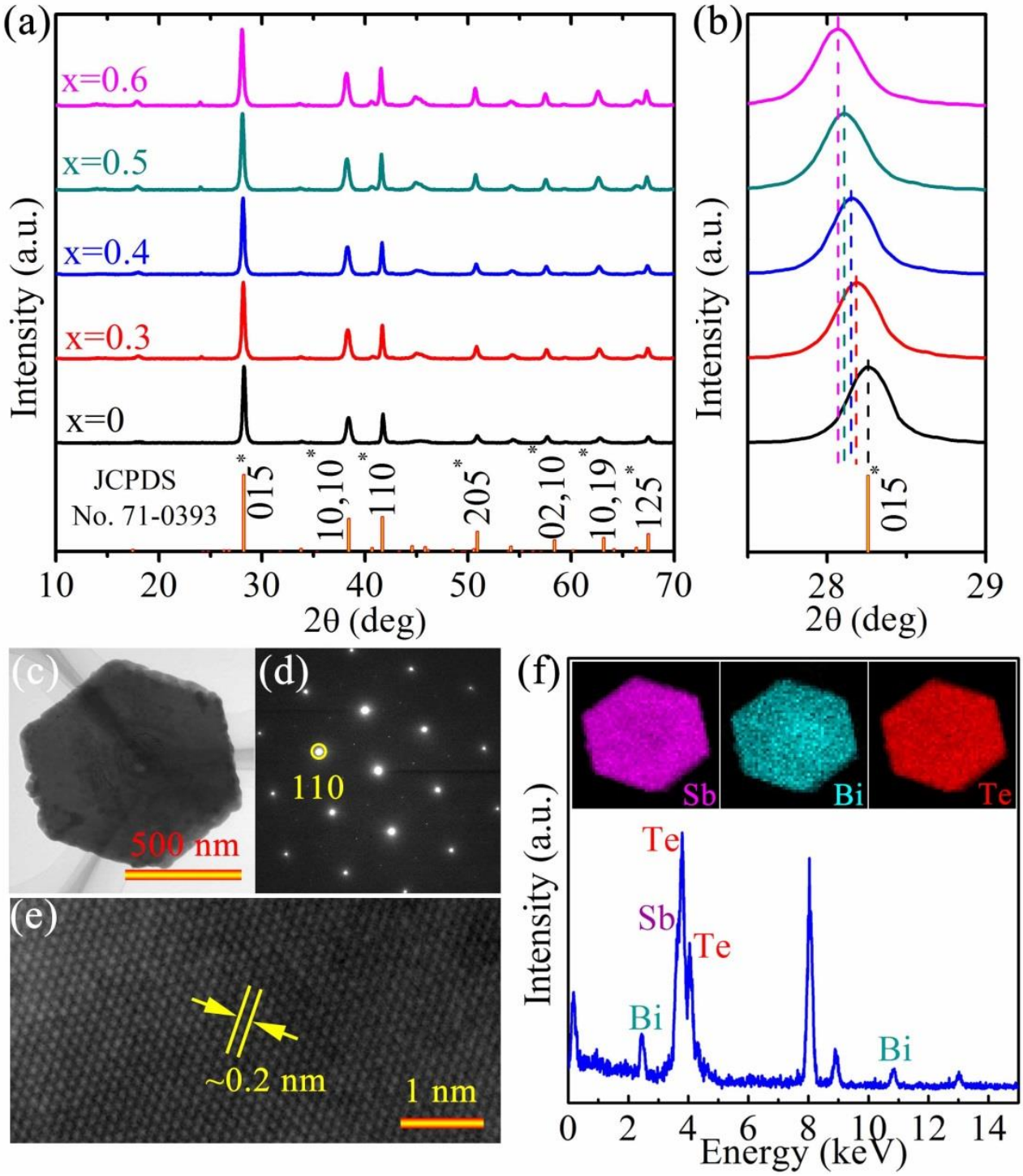

Figure 1 (a) XRD patterns of as-synthesized $Bi_xSb_{2-x}Te_3$ nanoplates with x = 0, 0.3, 0.4. 0.5 and 0.6. (b) Enlarged 015* diffraction peaks for different samples showing their systematic shift toward to the low 2θ angle. (c) TEM image of a typical $Bi_{0.5}Sb_{1.5}Te_3$ (d) SAED pattern. (e) Corresponding HRTEM image. (f) EDS profile with insets showing elemental mappings.

Thermoelectric performance evaluation

To evaluate the thermoelectric performance of our as-synthesized $Bi_xSb_{2-x}Te_3$ nanoplates, they were compressed into pellets by SPS. To examine the compositions of sintered pellets, we applied the electron probe microanalysis (EPMA), which suggests that the elemental ratios of pellets are close to the corresponding nominal stoichiometric proportions (see Figure 2a). To clarify the phase purities, we employed XRD to analyze the pellets. Figure 2b shows the corresponding XRD patterns, from which no detectable impurities or contaminations are observed. Based on the intensities of obtained diffraction peaks, the texture fraction of the sintered pellets ranging from 0.05 - 0.11 can be estimated by the Lotgering method (refer to Table S1) [37]. Due to the as-estimated low texture fractions of our sintered pellets, the anisotropic behaviors of their thermoelectric properties are expected to be weakened. To confirm this prediction, both in-plane (perpendicular to the pressing direction) and out-of-plane (parallel to the pressing direction) thermoelectric properties of the $Bi_{0.5}Sb_{1.5}Te_3$ pellet were measured, and results are shown in Figure S4. As can be seen, thermoelectric properties along the two directions only differ slightly, resulting in almost identical *ZT* values along the two perpendicular directions. Therefore, only the out-of-plane thermoelectric properties of other samples were presented.

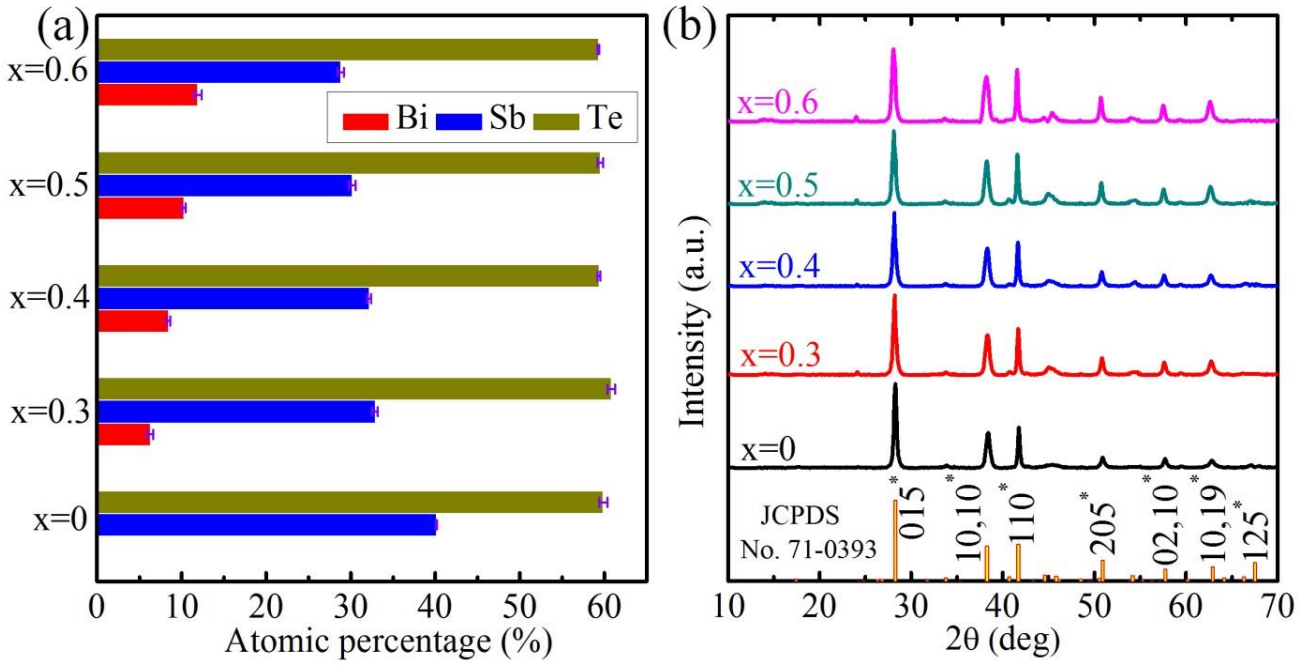

Figure 2 (a) Composition analysis of sintered $Bi_xSb_{2-x}Te_3$ pellets using EPMA. (b) XRD patterns taken from sintered pellets.

Figure 3a shows the composition-dependent σ as a function of temperature. As can be seen, σ decreases monotonically with increasing the temperature for all samples and roughly follows a relationship of $T^{-1.5}$, suggesting that acoustic phonons dominate the carrier scattering [21]. Moreover, σ reduces with increasing the Bi concentration. In particular, the pellet made of Sb_2Te_3 nanoplates exhibits the highest σ, ranging from 3.9×10^4 to 8.5×10^4 Sm^{-1} in the entire temperature region, while the $Bi_{0.6}Sb_{1.4}Te_3$ pellet shows the lowest σ, fluctuating from 3.0×10^4 to 6.0×10^4 Sm^{-1}. Figure 3b shows the variations of S with the temperature. The positive sign of S indicates the p-type nature for our $Bi_xSb_{2-x}Te_3$ pellets [38], and S increases gently first and then decreases with increasing the temperature. Moreover, in contrast to the continually reduced σ with increasing the Bi concentration, S increases with increasing the Bi concentration. Specifically, S reaches to the maximum value of 205 μVK^{-1} in the $Bi_{0.6}Sb_{1.4}Te_3$ pellet compared with that of only 168 μVK^{-1} for Sb_2Te_3 pellet. Such an opposite variation trend in σ and S results in diverse $S^2\sigma$ found in different samples. Figure 3c presents the plots of $S^2\sigma$ as a function of temperature, from which the highest $S^2\sigma$ of 28.3×10^{-4} $Wm^{-1}K^{-2}$ is secured in the $Bi_{0.5}Sb_{1.5}Te_3$ pellet, compared with that of 21.5×10^{-4} $Wm^{-1}K^{-2}$ and 26.6×10^{-4} $Wm^{-1}K^{-2}$ for the Sb_2Te_3 and $Bi_{0.4}Sb_{1.6}Te_3$ pellets, respectively.

Figure 3d is the plots of κ as a function of temperature, in which the lowest κ of 0.68 $Wm^{-1}K^{-1}$ can be found in the $Bi_{0.6}Sb_{1.4}Te_3$ pellet. As can be seen, the nanoplate pellets show lower κ than that (~1 $Wm^{-1}K^{-1}$) in their $Bi_xSb_{2-x}Te_3$ counterparts prepared by ball-milling plus hot-pressing method.[19,39] Also our achieved lowest κ is comparable to that of the $Bi_xSb_{2-x}Te_3$ pellets fabricated by the melt-spun plus SPS sintering method [16] and the newly developed Te-rich melt-spun plus SPS sintering method [15]. It is well known that κ is mainly contributed by electrons and phonons [40]. Based on the Wiedemann-Franz law [41], κ_e can be calculated using $\kappa_e = L\sigma T$, where L represents the Lorenz number and can be derived from Equation S5 with the determined η (discussed later), shown in Figure S5. On this basis, the calculated κ_e is plotted in the inset of Figure 3e, indicating that the reduced κ_e is due to the simultaneously decreased σ and L (refer to Figure 3a and Figure S5). Figure 3e shows the composition-dependent κ - κ_e, which is predominantly contributed by κ_l despite of a small amount of bipolar effect component at high temperature. As can be seen, κ_l is remarkably reduced. In addition to the inherently strong anharmonicity in Sb_2Te_3 crystals (strengthening the Umklapp phonon-phonon scattering) [42], the significant

suppression in κ_l should be the consequence of strengthened wide-frequency phonon scatterings caused by multi-scale scattering sources (discussed later).

Due to the obtained high $S^2\sigma$ as well as low κ, significantly enhanced *ZT* values are expected. Figure 3f is the *ZT* plots as a function of temperature, in which a peak *ZT* of 1.2 at 320 K is achieved in the $Bi_{0.5}Sb_{1.5}Te_3$ pellet. Through comparing this figure with the reported *ZT* for $Bi_xSb_{2-x}Te_3$ nanostructures prepared by wet-chemical methods (refer to Figure 4) [28,43-46], we can conclude that our obtained *ZT* of 1.2 represents one of the highest values.

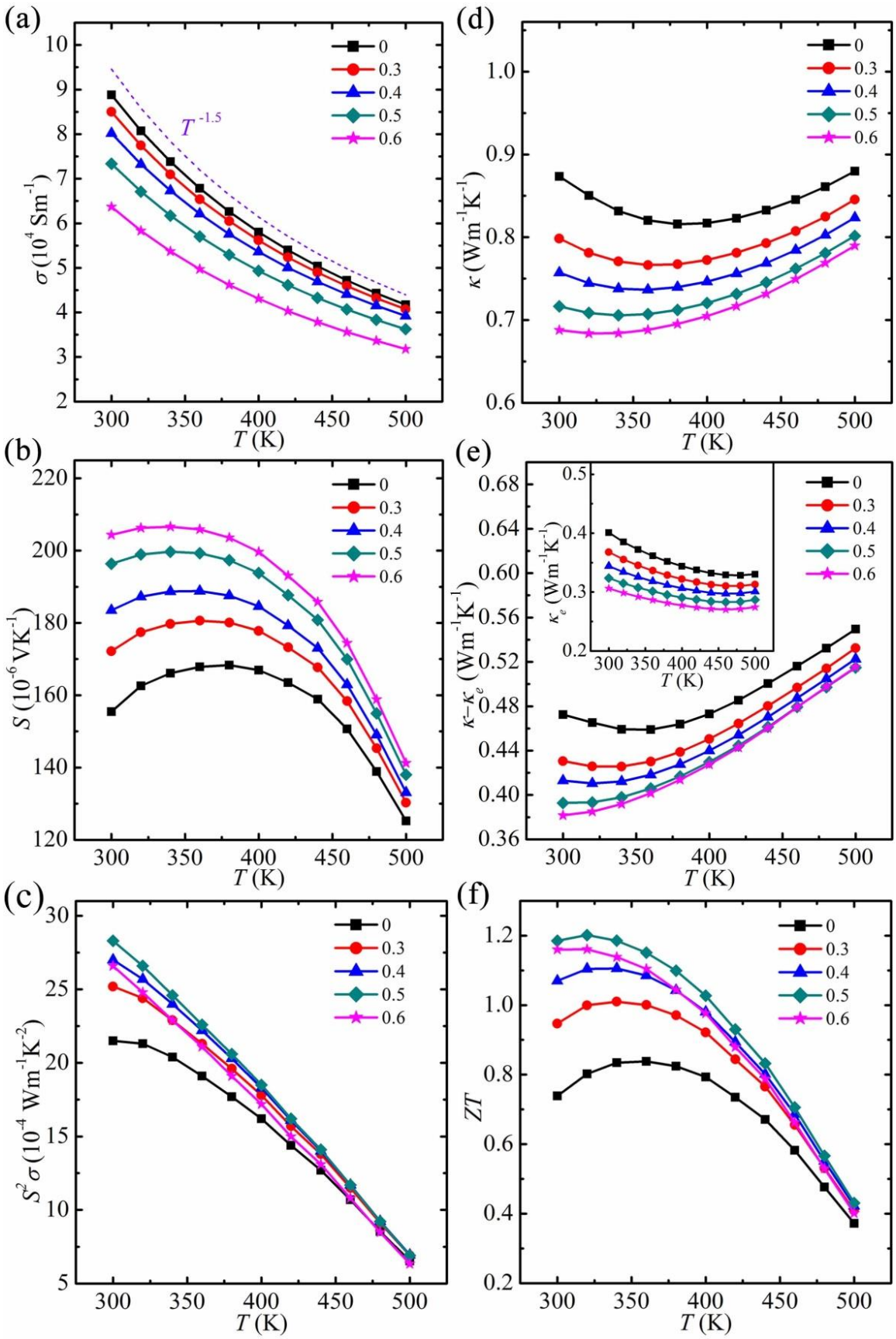

Figure 3 Thermoelectric characteristics of sintered $Bi_xSb_{2-x}Te_3$ pellets: (a) σ, (b) S, (c) $S^2\sigma$ (d) κ, (e) κ - κ_e with inset showing κ_e and (f) ZT, respectively.

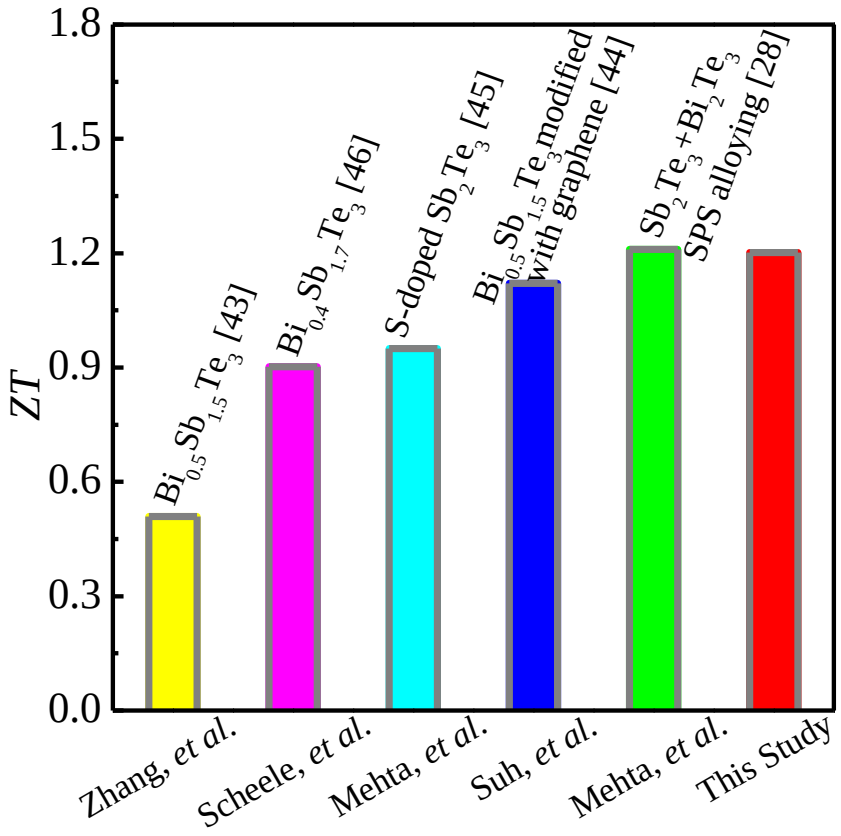

Figure 4 The comparison of our obtained peak *ZT* with the reported values for $Bi_xSb_{2-x}Te_3$ nanostructures [28,43-46].

Understanding the enhanced $S^2\sigma$

To understand the electronic transport properties of our sintered $Bi_xSb_{2-x}Te_3$ pellets, we applied the single Kane model [47]. Note that the thermoelectric performance of our sintered pellets is confirmed to be isotropic due to the extremely low texture fraction; therefore it is applicable to use the isotropic Kane model to simulate our obtained thermoelectric properties. In addition, the parabolic model has been widely used to study the theoretical/experimental thermoelectric properties of Bi_2Te_3 systems, although it is also isotropic [14,18,48]. The parabolic model is the simplified formation of the Kane model by assuming band gap (E_g) equaling infinite. Because most of the thermoelectric materials are semiconductors with narrow E_g, the Kane model is more appropriate to study their corresponding thermoelectric properties. On this basis, the thermoelectric properties are given by

Seebeck coefficient

$$S = \frac{k_B}{e}\left[\frac{F_{1,2}^{1}(\eta,\beta)}{F_{1,2}^{0}(\eta,\beta)} - \eta\right], \tag{1}$$

electrical conductivity

$$\sigma = \frac{3e^2 N_v \hbar C_l}{\pi m_I^* E_{def}^2} F_{1,2}^{0}(\eta,\beta), \tag{2}$$

with the generalized Fermi integral

$$F_{m,k}^{n}(\eta,\beta) = \int_0^\infty \left[-\frac{\partial f(\eta)}{\partial \varepsilon}\right] \varepsilon^n \frac{\left(\varepsilon + \beta\varepsilon^2\right)^m}{\left(1+2\beta\varepsilon\right)^k} d\varepsilon\ , \tag{3}$$

where $\eta = \frac{E_v - E_f}{k_B T}$ (E_v is the top of valance band and E_f is the Fermi level) is the reduced Fermi level, $\beta = \frac{k_B T}{E_g}$ is the reciprocal reduced band gap, k_B is Boltzmann constant, e is the elementary charge, N_v is the band degeneracy, $\hbar$ is the reduced Planck constant, C_l is the combination of elastic constants, m_I^* is the inertial effective mass, and E_{def} is the deformation potential, respectively [31].

By assuming $m_I^* = \lambda^2 m_0$ with a dimensionless λ and the free electron mass m_0, we can re-write Equation (2) as

$$\sigma = \frac{3e^2 N_v \hbar C_l}{\pi\left(\lambda E_{def}\right)^2 m_0} F_{1,2}^{0}(\eta,\beta) \tag{4}$$

According to Equation (1) and (4), with a given E_g at a constant temperature (leading to a fixed β), S is a function of η only, whereas σ is functions of both η and λE_{def}. Therefore, the introduction of λE_{def} can be used to decouple S and σ. For $Bi_{0.5}Sb_{1.5}Te_3$ with E_g of ~0.2 eV at 300 K [49], the variation of S and σ with η can be calculated by setting λE_{def} = 12.5 eV (the value determined for our $Bi_{0.5}Sb_{1.5}Te_3$ pellet — discussed later), as shown in Figure 5a. With decreasing η, S increases, while σ decreases, which results in a first increase and then decrease trend in $S^2\sigma$ (see Figure 5b). As proposed in our previous studies [2], the E_g dependent optimal reduced Fermi level (η^{opt}) can be defined to correspond to the peak $S^2\sigma$. For our $Bi_{0.5}Sb_{1.5}Te_3$ with E_g = 0.2 eV [49], η^{opt} is determined to be ~0.2, suggesting that

$Bi_{0.5}Sb_{1.5}Te_3$ with high thermoelectric performance should be slightly degenerated to maximize $S^2\sigma$, as illustrated in the inset of Figure 5b. By simultaneously varying η and λE_{def}, we can study the overall effects of both η and λE_{def} on $S^2\sigma$. Figure 5c shows the dependence of $S^2\sigma$ on both η and λE_{def}, from which, $S^2\sigma$ can be enhanced by reducing λE_{def} and/or optimizing η towards η^{opt}. Figure 5d shows the corresponding two-dimensional plots of calculated $S^2\sigma$ as a function λE_{def} by evenly selecting η values in the range of -2 to 3, and the inset displays the enlarged view of the squared frame. As can be seen, $S^2\sigma$ increases significantly with reducing λE_{def}, and follows a trend of $\left(\lambda E_{def}\right)^{-2}$, because λE_{def} with an index of 2 exists in the denominator of Equation (4). Moreover, although optimizing η towards η^{opt} leads to an increased $S^2\sigma$, with η gradually approaching η^{opt} at a fixed step (for instance, $\Delta\eta$ = ~0.25), the magnitude of such an increase in $S^2\sigma$ decreases. On this basis, when η has been sufficiently optimized (i.e. Fermi level locates near by the top of valance band for p-type thermoelectric materials), reducing λE_{def} becomes the key to enhance $S^2\sigma$.

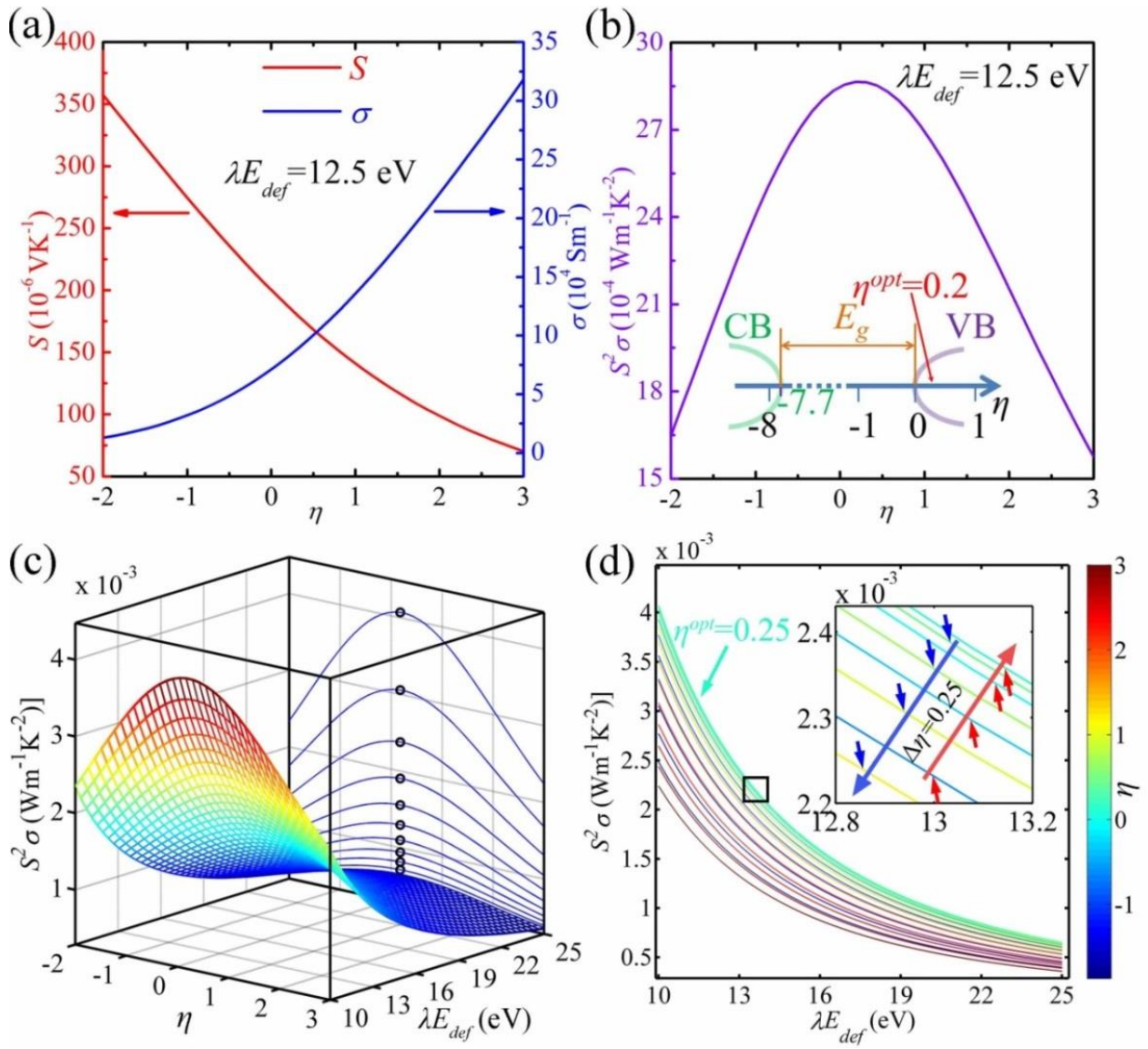

Figure 5 (a) Calculated S and σ as a function of η for λE_{def} = 12.5 eV at 300 K. (b) The corresponding η dependent $S^2\sigma$, with inset illustrating the variation of η in the band structure. (c) Two-dimensional array of calculated $S^2\sigma$ as a function η and λE_{def} at 300 K. (d) Corresponding plots of $S^2\sigma$ as a function λE_{def} by evenly selecting 20 η values in the range of -2 to 3 indicated as the color bar, with inset showing the enlarged view of the squared frame.

To understand our achieved high $S^2\sigma$, their related η and λE_{def} are calculated. For a given material system, the monotonic decreasing relationship between S and η shown in Figure 4a indicates that η can be exclusively determined from the measured S. Figure 6a shows calculated curves of S as a function of η according to Equation (1), and the measured S data points. The comparison between the measured data points and the correspondingly calculated curves allows to exclusively determine η values for our pellets

over the studied temperature range. Since σ is a function of both η and λE_{def} at a given temperature, λE_{def} can be determined based on the measured σ and the previously determined η. Figure 6b shows the calculated curves of σ versus both η and λE_{def} based on Equation (4), and determined λE_{def} values (red circles) that fit perfectly with the theoretical plots. In the these calculations, the composition-dependent E_g over the entire temperature range is obtained from Ref. [49], which has intensively studied the composition-dependent E_g for $Bi_xSb_{2-x}Te_3$ systems. Specifically, E_g values at 300 K for $Bi_xSb_{2-x}Te_3$ with (x = 0, 0.3, 0.4, 0.5, 0.6 and 1) can be respectively estimated as 0.28 eV, 0.24 eV, 0.21 eV, 0.2 eV and 0.19 eV, and the composition-independent temperature coefficient is -1.5×10^{-4} eVK^{-1}. Based on these careful calculations, determined η and λE_{def} can be plotted as a function of temperature for our $Bi_xSb_{2-x}Te_3$ pellets, and the results are shown in Figure 6c and d. From these figures, we can explore the impact of η and λE_{def} on the experimental $S^2\sigma$. Figure 6e plots the measured $S^2\sigma$ versus determined λE_{def} data points at 300 K, in which a clear tendency is demonstrated: the smaller the λE_{def}, the larger the $S^2\sigma$. Note that each data point corresponds to a different η value. To verify the impact of the determined η on measured $S^2\sigma$, Figure 6e also includes the theoretical curves of $S^2\sigma$ as a function of λE_{def} calculated with composition-dependent η^{opt} for each $Bi_xSb_{2-x}Te_3$. Since there is a diverse η^{opt} value for each $Bi_xSb_{2-x}Te_3$ due to the different E_g, we need to compare the data points with their relevant $S^2\sigma$ versus λE_{def} theoretical curves. Interestingly, all measured data points locate in left-hand side of the corresponding curve, suggesting that there exists a difference between the determined η and η^{opt} for a given composition. Because η^{opt} corresponds to peak $S^2\sigma$, reducing this difference can increase $S^2\sigma$ to its peak value. As discussed above, the overall $S^2\sigma$ enhancement depends upon λE_{def} as well as η, it is necessary for both parameters to be synergistically controlled. Figure 6f presents the determined data points of λE_{def} versus η, with vertical lines indicating the composition-dependent η^{opt}. By taking both Figure 6e and f into account, we can conclude that simultaneously reducing both λE_{def} and $|\eta - \eta^{opt}|$ is achieved in our $Bi_xSb_{2-x}Te_3$ through tuning Bi concentration, and therefore an enlarged $S^2\sigma$ is obtained in $Bi_{0.5}Sb_{1.5}Te_3$. To verify the feasibility of this conclusion, we examined the reported thermoelectric properties for $Bi_xSb_{2-x}Te_3$ systems. Two representative examples synthesized by conventional wet chemical method are presented in Figure 6e and f, including pure $Bi_xSb_{2-x}Te_3$ [43] and $Bi_{0.5}Sb_{1.5}Te_3$ modified with graphene of various volume ratios (y%) [44]. As can be seen, reducing λE_{def} and $|\eta - \eta^{opt}|$ leading to high $S^2\sigma$ is also applied.

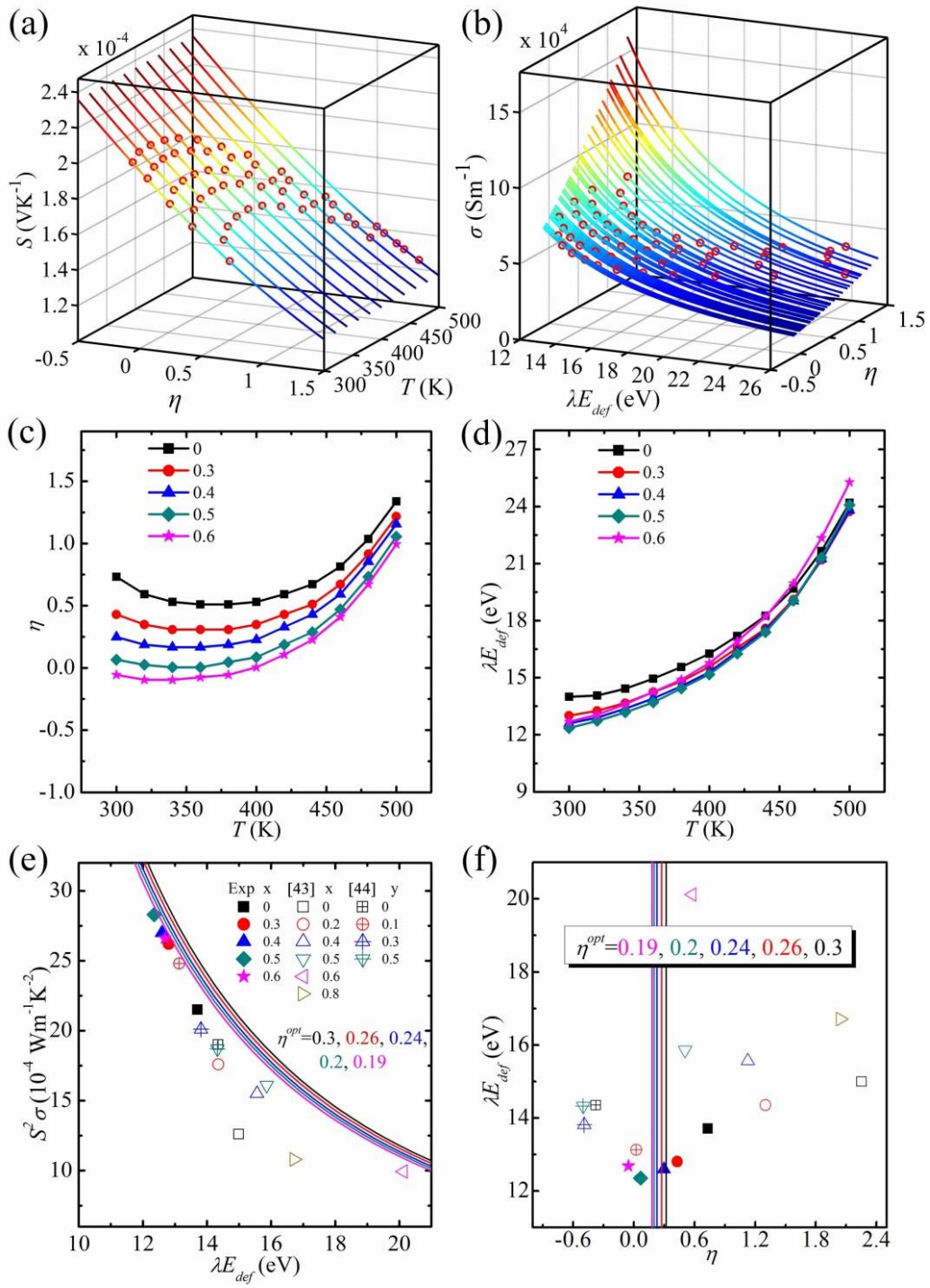

Figure 6 (a) Theoretical plots of S varying with η and temperature compared with measured data points. (b) Theoretical plots of σ as a function of λE_{def} and η compared with measured data points. Determined η (c) and λE_{def} (d) as a function of temperature for sintered $Bi_xSb_{2-x}Te_3$ pellets. (e) Theoretical plots of $S^2\sigma$ versus λE_{def} for different η^{opt} with experimental data points for comparison. (f) Determined λE_{def} versus η data points compared with different η^{opt}. In (e) and (f), the literature data from $Bi_xSb_{2-x}Te_3$ systems [43] and $Bi_{0.5}Sb_{1.5}Te_3$ modified with graphene (y vol%) [44] are marked for comparison.

Analyzing the ultra-low κ

To understand the impact of microstructures on our obtained lowest κ_l, TEM was applied to investigate the $Bi_{0.5}Sb_{1.5}Te_3$ pellet. Figure 7a is a low-magnification TEM image, revealing their multi-grain feature. Figure 7b is the corresponding grain size distribution histogram, from which the average grain size is found to be ~ 900 nm. The inset of Figure 7b is a high angle annular dark-field image with the EDS line scans, reflecting the composition homogeneity of this multi-grained pellet. To further verify the grain boundaries, HRTEM was applied. Figure 7c is a HRTEM image of two neighboring grains with a clear grain boundary, and Figure 7d shows a ~15 nm grain surrounded by other relatively larger grains (a large fraction of grain boundaries is seen). Figure 7e is a HRTEM image and shows several dislocations (marked as arrows). Figure 7f is an inverse fast Fourier transform (FFT) image taken from the frame in Figure 7e, and clearly shows the dislocation cores. Figure 7g - i are FFT patterns taken from areas framed in Figure 7e, in which Figure 7g and h show individual set of diffraction patterns, while Figure 7i shows the superimposed diffraction patterns with a misorientation of ~3°, caused by these dislocations [50]. The observed dense grain boundaries and dislocations are believed to be responsible for the reduction in κ_l.

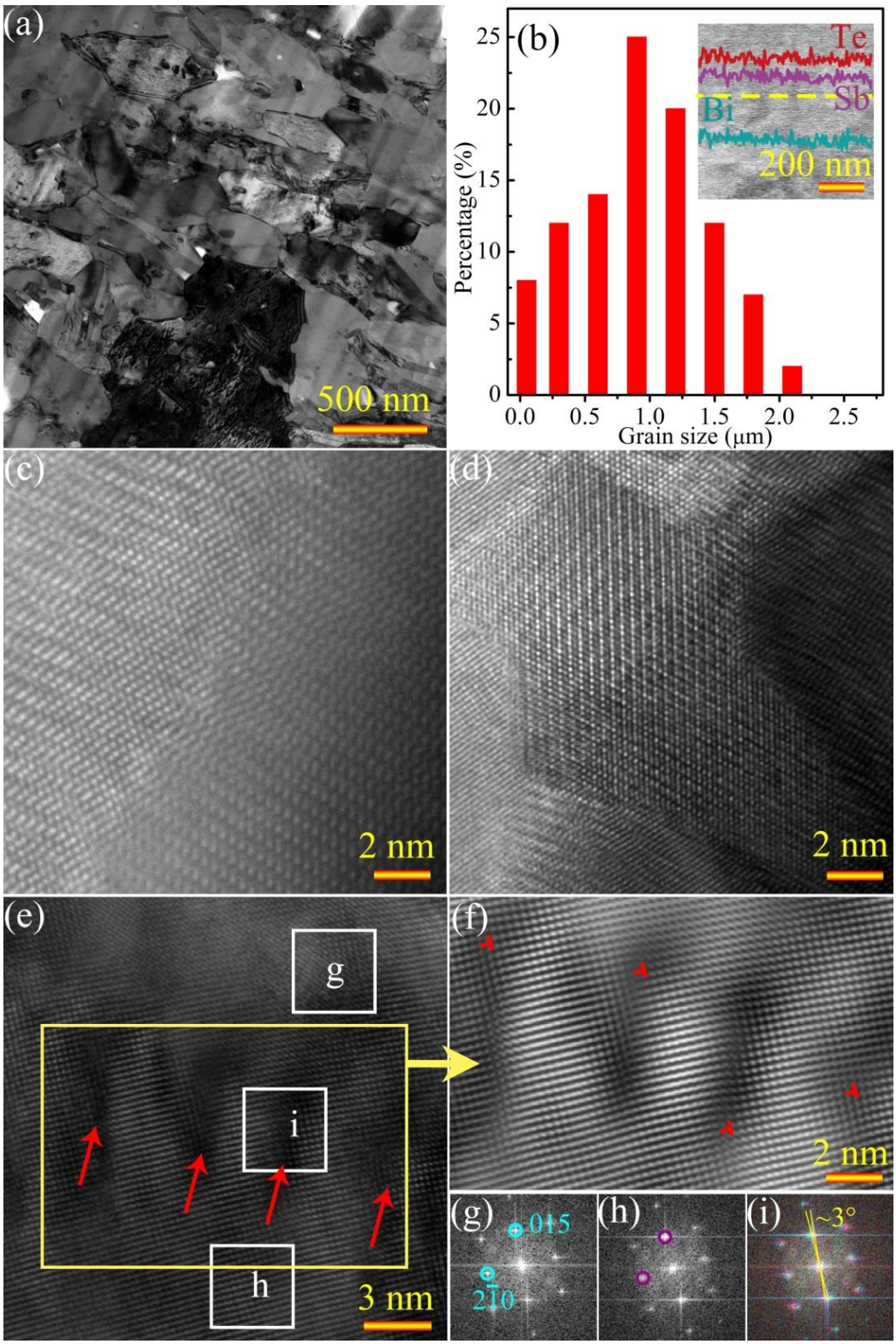

Figure 7 (a) Low-magnification TEM image of the $Bi_{0.5}Sb_{1.5}Te_3$ pellet. (b) Corresponding grain size distribution histogram with inset showing the high angle annular dark-field image and EDS line scans. (c) and (d) HRTEM images showing clear grain boundaries. (e) HRTEM image of a typical area with dislocations. (f) Corresponding IFFT image showing dislocation cores. (g) - (i) FFT patterns taken from different regions in (e).

To numerically study the impacts of the observed grain boundaries and dislocations on reducing κ_l, we investigate the phonon transport by considering various phonon scattering mechanisms, i.e. phonon-phonon Umklapp (U) scattering, and electron-phonon (E) scattering, grain boundary (B) scattering, point defect (PD) scattering, and dislocation (D) scattering. The details of the phonon relaxation time regarding various scattering processes are discussed in Section 7 of the Supplementary material. Based on the phonon relaxation time, the spectral lattice thermal conductivity (κ_s) was calculated. Figure S6 shows the calculation results, from which grain boundaries, dislocations and point defects respectively scatter phonons with low-, mid- and high- frequencies. Therefore, in order to reduce κ_l, it is necessary to produce multi-scale phonon scattering sources. In this regard, we note that the integration of κ_s with respect to the whole phonon frequency (ω) is κ_l, namely [51]

$$\kappa_l = \frac{k_B}{2\pi^2 \upsilon}\left(\frac{k_B T}{\hbar}\right)^3 \int_0^{\frac{\theta_D}{T}} \tau_{tot} \frac{z^4 \exp(z)}{\left[\exp(z)-1\right]^2} dz \tag{5}$$

where θ_D is the Debye temperature, $\upsilon = \left[\frac{1}{3}\left(\frac{1}{\upsilon_L^3}+\frac{2}{\upsilon_T^3}\right)\right]^{-1/3}$ is the sound velocity with υ_L and υ_T respectively denoting the longitudinal and transverse sound velocities, τ_{tot} is the total relaxation time, and $z = \frac{\hbar\omega}{k_B T}$ is the reduced phonon frequency.

Based on Equation (5) and the physical parameters listed in Table S2, we calculated κ_l for our $Bi_{0.5}Sb_{1.5}Te_3$ pellet by models considering U+E+B+PD and U+E+B+PD+D, and fit the calculated κ_l curves with our experimental data points over the entire temperature range. Figure 8a shows the calculated results, from which the U+E+B+PD+D model (red curve) can match well with the experimental κ - κ_e before the appearance of the bipolar effect, whereas the U+E+B+PD model (blue curve) with the same physical parameters gives κ_l much larger than the experimental κ -κ_e. For a given material system with a determined grain size, the strength of U, E and B phonon scattering mechanisms are nearly constant, while that of PD depending on the point defect scattering parameter (Γ) is variable. To study whether the achieved ultra-low κ - κ_e can be explained by strong PD, we re-calculated the κ_s and κ_l using the U+E+B+PD model with Γ = 1 (note that Γ = 1 is much larger than the reported values in thermoelectric systems) [52,53]. Figure 8b shows the

obtained ω dependent κ_s at 300 K using the U+E+B+PD+D model with Γ = 0.16 (red curve) and using the U+E+B+PD model with both Γ =0.16 (blue curve) and Γ = 1 (dash blue curve). As can be seen, although increasing Γ to 1 enables a significant decrease in κ_s, area (i) is larger than area (ii), suggesting that, at 300 K, corresponding κ_l determined by the U+E+B+PD model with Γ = 1 is still larger than that determined by the U+E+B+PD+D model with Γ = 0.16. Correspondingly, in Figure 8a, κ_l (dash blue curve) determined by the U+E+B+PD model with Γ = 1 is larger than that (red curve) determined by the U+E+B+PD+D. Therefore, only the U+E+B+PD+D model is applicable to quantitatively predict our experimental κ - κ_e for the $Bi_{0.5}Sb_{1.5}Te_3$ pellet. Based on these discussions, we can conclude that the significant reduction in κ for our samples is due to the enhanced scattering of phonons with wide frequencies by multi-scale scattering sources.

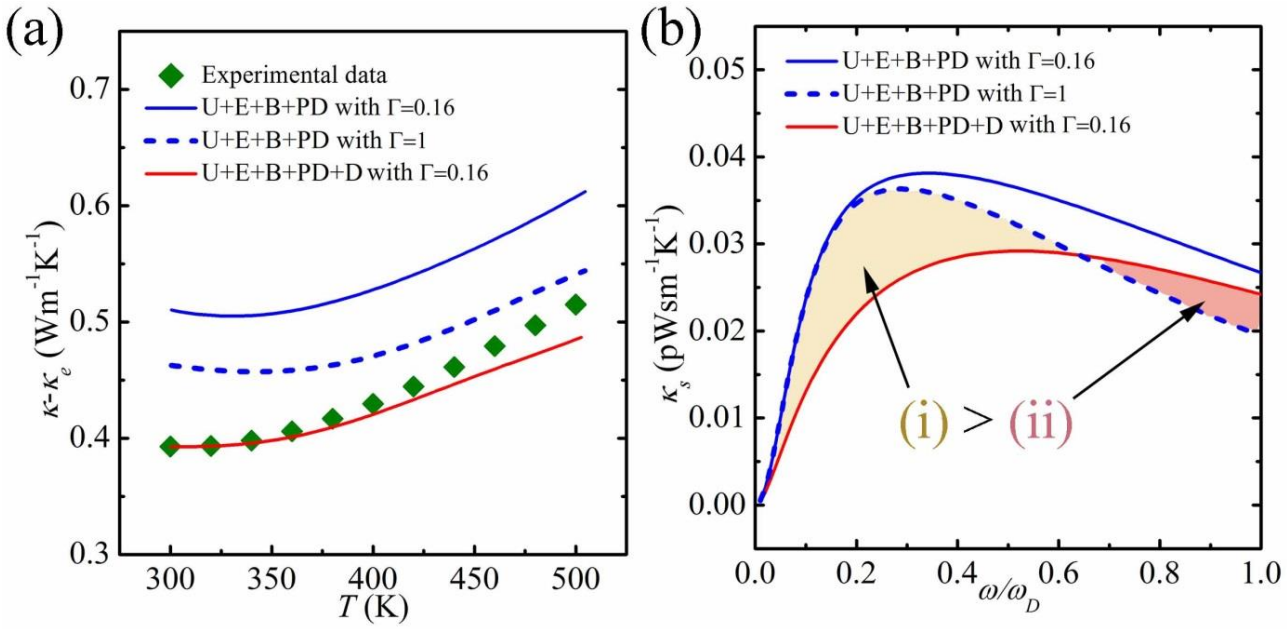

Figure 8 (a) Measured κ - κ_e data points for the $Bi_{0.5}Sb_{1.5}Te_3$ pellet compared with calculated κ_l determined by different models. (b) Calculated κ_s based on models of U+E+B+PD, and U+E+B+PD+D with different Γ values.

4. Conclusion

We successfully fabricated $Bi_xSb_{2-x}Te_3$ (with x = 0, 0.3, 0.4, 0.5 and 0.6) nanoplates using the microwave-assisted solvothermal method. Thermoelectric performance of the pellets sintered from these as-synthesized $Bi_xSb_{2-x}Te_3$ nanoplates depends strongly upon the Bi concentration, and a peak ZT of 1.2 was achieved from the $Bi_{0.5}Sb_{1.5}Te_3$ pellet. Based on the composition dependent $S^2\sigma$, we performed profound simulation studies

using the single Kane model. We found the decoupling factor, namely λE_{def} for S and σ with contradictory relationship. On this basis, $S^2\sigma$ can be enhanced by reducing λE_{def}, when η has been sufficiently optimized. Through comparing our experimental data with the simulation results, we confirmed that through tuning the Bi concentration in nanostructured $Bi_xSb_{2-x}Te_3$, η can be optimized and λE_{def} can be reduced, leading to peak $S^2\sigma$. Moreover, based on our comprehensive TEM investigations and theoretical calculations using the Callaway model, the achieved ultra-low κ is due to the high-density grain boundaries and dislocations, coupled with the inherently existed Sb-Bi lattice disorders that can remarkably strengthen the scattering of phonons with wide frequencies.

Acknowledgements

This work was financially supported by the Australian Research Council, ZGC thanks QLD government for a smart state future fellowship (2011002414). MH thanks the China Scholarship Council for providing a PhD stipend. The Australian Microscopy & Microanalysis Research Facility is acknowledged for providing characterization facilities.

References

(1) Biswas, K.; He, J.; Blum, I. D.; Wu, C. I.; Hogan, T. P.; Seidman, D. N.; Dravid, V. P.; Kanatzidis, M. G. High-Performance Bulk Thermoelectrics with All-Scale Hierarchical Architectures. *Nature* **2012**, 489, 414-418.

(2) Hong, M.; Chen, Z.-G.; Yang, L.; Han, G.; Zou, J. Enhanced Thermoelectric Performance of Ultrathin Bi_2Se_3 Nanosheets through Thickness Control. *Adv. Electron. Mater.* **2015**, 1, 1500025.

(3) Minnich, A. J.; Dresselhaus, M. S.; Ren, Z. F.; Chen, G. Bulk Nanostructured Thermoelectric Materials: Current Research and Future Prospects. *Energy Environ. Sci.* **2009**, 2, 466-479.

(4) Sofo, J. O.; Mahan, G. D. Optimum Band Gap of a Thermoelectric Material. *Phys. Rev. B* **1994**, 49, 4565-4570.

(5) Goldsmid, H. J.; Douglas, R. W. The Use of Semiconductors in Thermoelectric Refrigeration. *Brit. J. Appl. Phys.* **1954**, 5, 386-390.

(6) Lee, Y.; Lo, S.-H.; Chen, C.; Sun, H.; Chung, D.-Y.; Chasapis, T. C.; Uher, C.; Dravid, V. P.; Kanatzidis, M. G. Contrasting Role of Antimony and Bismuth Dopants on The Thermoelectric Performance of Lead Selenide. *Nat. Commun.* **2014**, 5.

(7) Snyder, G. J.; Toberer, E. S. Complex Thermoelectric Materials. *Nat. Mater.* **2008**, 7, 105-114.

(8) Polvani, D. A.; Meng, J. F.; Chandra Shekar, N. V.; Sharp, J.; Badding, J. V. Large Improvement in Thermoelectric Properties in Pressure-Tuned p-Type $Sb_{1.5}Bi_{0.5}Te_3$. *Chem. Mater.* **2001**, 13, 2068-2071.

(9) Fang, H.; Yang, H.; Wu, Y. Thermoelectric Properties of Silver Telluride–Bismuth Telluride Nanowire Heterostructure Synthesized by Site-Selective Conversion. *Chem. Mater.* **2014**, 26, 3322-3327.

(10) Fu, C.; Zhu, T.; Liu, Y.; Xie, H.; Zhao, X. Band Engineering of High Performance p-Type FeNbSb Based Half-Heusler Thermoelectric Materials for Figure of Merit ZT > 1. *Energy Environ. Sci.* **2015**, 8, 216-220.

(11) Alam, H.; Ramakrishna, S. A review on the Enhancement of Figure of Merit from Bulk to Nano-Thermoelectric Materials. *Nano Energy* **2013**, 2, 190-212.

(12) Zhang, Y.; Stucky, G. D. Heterostructured Approaches to Efficient Thermoelectric Materials. *Chem. Mater.* **2014**, 26, 837-848.

(13) Soni, A.; Zhao, Y. Y.; Yu, L. G.; Aik, M. K. K.; Dresselhaus, M. S.; Xiong, Q. H. Enhanced Thermoelectric Properties of Solution Grown $Bi_2Te_{3-x}Se_x$ Nanoplatelet Composites. *Nano Lett.* **2012**, 12, 1203-1209.

(14) Hu, L. P.; Zhu, T. J.; Wang, Y. G.; Xie, H. H.; Xu, Z. J.; Zhao, X. B. Shifting up the Optimum Figure of Merit of *p*-Type Bismuth Telluride-Based Thermoelectric Materials for Power Generation by Suppressing Intrinsic Conduction. *NPG Asia Mater.* **2014**, 6, e88.

(15) Kim, S. I.; Lee, K. H.; Mun, H. A.; Kim, H. S.; Hwang, S. W.; Roh, J. W.; Yang, D. J.; Shin, W. H.; Li, X. S.; Lee, Y. H.; Snyder, G. J.; Kim, S. W. Dense Dislocation Arrays Embedded in Grain Boundaries for High-Performance Bulk Thermoelectrics. *Science* **2015**, 348, 109-114.

(16) Xie, W.; Tang, X.; Yan, Y.; Zhang, Q.; Tritt, T. M. Unique Nanostructures and Enhanced Thermoelectric Performance of Melt-Spun BiSbTe Alloys. *Appl. Phys. Lett.* **2009**, 94, 102111.

(17) Hu, L.; Zhu, T.; Liu, X.; Zhao, X. Point Defect Engineering of High-Performance Bismuth-Telluride-Based Thermoelectric Materials. *Adv. Funct. Mater.* **2014**, 24, 5211–5218.

(18) Liu, W.-S.; Zhang, Q.; Lan, Y.; Chen, S.; Yan, X.; Zhang, Q.; Wang, H.; Wang, D.; Chen, G.; Ren, Z. Thermoelectric Property Studies on Cu-Doped *n*-Type $Cu_xBi_2Te_{2.7}Se_{0.3}$ Nanocomposites. *Adv. Energy Mater.* **2011**, 1, 577-587.

(19) Poudel, B.; Hao, Q.; Ma, Y.; Lan, Y.; Minnich, A.; Yu, B.; Yan, X.; Wang, D.; Muto, A.; Vashaee, D.; Chen, X.; Liu, J.; Dresselhaus, M. S.; Chen, G.; Ren, Z. High-Thermoelectric Performance of Nanostructured Bismuth Antimony Telluride Bulk Alloys. *Science* **2008**, 320, 634-638.

(20) Kim, P.; Shi, L.; Majumdar, A.; McEuen, P. L. Thermal Transport Measurements of Individual Multiwalled Nanotubes. *Phys. Rev. Lett.* **2001**, 87, 215502.

(21) Hu, L.; Wu, H.; Zhu, T.; Fu, C.; He, J.; Ying, P.; Zhao, X. Tuning Multiscale Microstructures to Enhance Thermoelectric Performance of *n*-Type Bismuth-Telluride-Based Solid Solutions. *Adv. Energy Mater.* **2015**, 5, 1500411.

(22) Cheng, L.; Chen, Z.-G.; Ma, S.; Zhang, Z.-D.; Wang, Y.; Xu, H.-Y.; Yang, L.; Han, G.; Jack, K.; Lu, G.; Zou, J. High Curie Temperature $Bi_{1.85}Mn_{0.15}Te_3$ Nanoplates. *J. Am. Chem. Soc.* **2012**, 134, 18920-18923.

(23) Han, G.; Chen, Z.-G.; Yang, L.; Hong, M.; Drennan, J.; Zou, J. Rational Design of Bi_2Te_3 Polycrystalline Whiskers for Thermoelectric Applications. *ACS Appl. Mater. Interf.* **2014**, 7, 989-995.

(24) Mi, J. L.; Lock, N.; Sun, T.; Christensen, M.; Sondergaard, M.; Hald, P.; Hng, H. H.; Ma, J.; Iversen, B. B. Biomolecule-Assisted Hydrothermal Synthesis and Self-Assembly of Bi_2Te_3 Nanostring-Cluster Hierarchical Structure. *ACS Nano* **2010**, 4, 2523-2530.

(25) Sun, Y.; Cheng, H.; Gao, S.; Liu, Q.; Sun, Z.; Xiao, C.; Wu, C.; Wei, S.; Xie, Y. Atomically Thick Bismuth Selenide Freestanding Single Layers Achieving Enhanced Thermoelectric Energy Harvesting. *J. Am. Chem. Soc.* **2012**, 134, 20294-20297.

(26) Min, Y.; Moon, G. D.; Kim, C.-E.; Lee, J.-H.; Yang, H.; Soon, A.; Jeong, U. Solution-Based Synthesis of Anisotropic Metal Chalcogenide Nanocrystals and Their Applications. *J. Mater. Chem. C* **2014**, 2, 6222-6248.

(27) Mehta, R. J.; Karthik, C.; Singh, B.; Teki, R.; Borca-Tasciuc, T.; Ramanath, G. Seebeck Tuning in Chalcogenide Nanoplate Assemblies by Nanoscale Heterostructuring. *ACS Nano* **2010**, 4, 5055-5060.

(28) Mehta, R. J.; Zhang, Y.; Karthik, C.; Singh, B.; Siegel, R. W.; Borca-Tasciuc, T.; Ramanath, G. A New Class of Doped Nanobulk High Figure-of-Merit Thermoelectrics by Scalable Bottom-up Assembly. *Nat. Mater.* **2012**, 11, 233-240.

(29) Lu, W. G.; Ding, Y.; Chen, Y. X.; Wang, Z. L.; Fang, J. Y. Bismuth Telluride Hexagonal Nanoplatelets and Their Two-Step Epitaxial Growth. *J. Am. Chem. Soc.* **2005**, 127, 10112-10116.

(30) Zhang, Y.; Wang, H.; Kräemer, S.; Shi, Y.; Zhang, F.; Snedaker, M.; Ding, K.; Moskovits, M.; Snyder, G. J.; Stucky, G. D. Surfactant-Free Synthesis of Bi_2Te_3−Te Micro−Nano Heterostructure with Enhanced Thermoelectric Figure of Merit. *ACS Nano* **2011**, 5, 3158-3165.

(31) Pei, Y.; Gibbs, Z. M.; Balke, B.; Zeier, W. G.; Snyder, G. J. Optimum Carrier Concentration in *n*-Type PbTe Thermoelectrics. *Adv. Energy Mater.* **2014**, 4, 1400486.

(32) Callaway, J.; von Baeyer, H. Effect of Point Imperfections on Lattice Thermal Conductivity. *Phys. Rev.* **1960**, 120, 1149-1154.

(33) Pashinkin, A. S.; Malkova, A. S.; Mikhailova, M. S. The Heat Capacity of Solid Antimony Telluride Sb_2Te_3. *Russ. J. Phys. Chem.* **2008**, 82, 878-879.

(34) Mills, K. C. *Thermodynamic Data for Inorganic Sulphides, Selenides and Tellurides.* Butterworths: London, **1974**.

(35) Anderson, T. L.; Krause, H. B. Refinement of The Sb_2Te_3 and Sb_2Te_2Se Structures and Their Relationship to Nonstoichiometric $Sb_2Te_{3-y}Se_y$ Compounds. *Acta. Crystallogr. B* **1974**, 30, 1307-1310.

(36) Denton, A. R.; Ashcroft, N. W. Vegard's Law. *Phys. Rev. A* **1991**, 43, 3161-3164.

(37) Lotgering, F. K. Topotactical Reactions with Ferrimagnetic Oxides Having Hexagonal Crystal Structures—I. *J. Inorg. Nucl. Chem.* **1959**, 9, 113-123.

(38) Zhang, Q.; Ai, X.; Wang, L.; Chang, Y.; Luo, W.; Jiang, W.; Chen, L. Improved Thermoelectric Performance of Silver Nanoparticles-Dispersed Bi2Te3 Composites Deriving from Hierarchical Two-Phased Heterostructure. *Adv. Funct. Mater.* **2015**, 25, 966-976.

(39) Ma, Y.; Hao, Q.; Poudel, B.; Lan, Y. C.; Yu, B.; Wang, D. Z.; Chen, G.; Ren, Z. F. Enhanced Thermoelectric Figure-of-Merit in p-Type Nanostructured Bismuth Antimony Tellurium Alloys Made from Elemental Chunks. *Nano Lett.* **2008**, 8, 2580-2584.

(40) Chen, Z.-G.; Han, G.; Yang, L.; Cheng, L.; Zou, J. Nanostructured Thermoelectric Materials: Current Research and Future Challenge. *Prog. Nat. Sci.* **2012**, 22, 535-549.

(41) Zhao, L.; Lo, S. H.; He, J.; Li, H.; Biswas, K.; Androulakis, J.; Wu, C.-I.; Hogan, T. P.; Chung, D.-Y.; Dravid, V. P.; Kanatzidis, M. G. High Performance Thermoelectrics from Earth-Abundant Materials: Enhanced Figure of Merit in PbS by Second Phase Nanostructures. *J. Am. Chem. Soc.* **2011**, 133, 20476-20487.

(42) Lee, S.; Esfarjani, K.; Luo, T.; Zhou, J.; Tian, Z.; Chen, G. Resonant Bonding Leads to Low Lattice Thermal Conductivity. *Nat. Commun.* **2014**, 5, 3525.

(43) Zhang, C.; Peng, Z.; Li, Z.; Yu, L.; Khor, K. A.; Xiong, Q. Controlled Growth of Bismuth Antimony Telluride $Bi_xSb_{2-x}Te_3$ Nanoplatelets and Their Bulk Thermoelectric Nanocomposites. *Nano Energy* **2015**, 15, 688-696.

(44) Suh, D.; Lee, S.; Mun, H.; Park, S.-H.; Lee, K. H.; Wng Kim, S.; Choi, J.-Y.; Baik, S. Enhanced Thermoelectric Performance of $Bi_{0.5}Sb_{1.5}Te_3$-Expanded Graphene Composites by Simultaneous Modulation of Electronic and Thermal Carrier Transport. *Nano Energy* **2015**, 13, 67-76.

(45) Mehta, R. J.; Zhang, Y.; Zhu, H.; Parker, D. S.; Belley, M.; Singh, D. J.; Ramprasad, R.; Borca-Tasciuc, T.; Ramanath, G. Seebeck and Figure of Merit Enhancement in Nanostructured Antimony Telluride by Antisite Defect Suppression through Sulfur Doping. *Nano Lett.* **2012**, 12, 4523-4529.

(46) Scheele, M.; Oeschler, N.; Veremchuk, I.; Reinsberg, K.-G.; Kreuziger, A.-M.; Kornowski, A.; Broekaert, J.; Klinke, C.; Weller, H. ZT Enhancement in Solution-Grown $Sb_{(2-x)}$BixTe3 Nanoplatelets. *ACS Nano* **2010**, 4, 4283-4291.

(47) Ravich, Y. I.; Efimova, B. A.; Smirnov, I. A. *Semiconducting Lead Chalcogenides*. Plenum Press: **1970**.

(48) Hicks, L.; Dresselhaus, M. Effect of Quantum-Well Structures on the Thermoelectric Figure of Merit. *Phys. Rev. B* **1993**, 47, 12727-12731.

(49) Sehr, R.; Testardi, L. R. The Optical Properties of p-Type Bi_2Te_3-Sb_2Te_3 Alloys between 2–15 Microns. *J. Phys. Chem. Solids* **1962**, 23, 1219-1224.

(50) Jo, J.; Yoo, H.; Park, S.-I.; Park, J. B.; Yoon, S.; Kim, M.; Yi, G.-C. High-Resolution Observation of Nucleation and Growth Behavior of Nanomaterials Using a Graphene Template. *Adv. Mater.* **2014**, 26, 2011-2015.

(51) Xie, H.; Wang, H.; Pei, Y.; Fu, C.; Liu, X.; Snyder, G. J.; Zhao, X.; Zhu, T. Beneficial Contribution of Alloy Disorder to Electron and Phonon Transport in Half-Heusler Thermoelectric Materials. *Adv. Funct. Mater.* **2013**, 23, 5123-5130.

(52) Klemens, P. G. Thermal Resistance due to Point Defects at High Temperatures. *Phys. Rev.* **1960**, 119, 507-509.

(53) Klemens, P. G. The Scattering of Low-Frequency Lattice Waves by Static Imperfections. *P. Roy. Soc. A* **1955**, 68, 1113-1128.

Supporting Information

$Bi_xSb_{2-x}Te_3$ Nanoplates with Enhanced Thermoelectric Performance due to Sufficiently Decoupled Electronic Transport Properties and Strong Wide-Frequency Phonon Scatterings

Min Hong,[a] Zhi G. Chen,[,a] Lei Yang,[a] and Jin Zou[*,a,b]*

a Materials Engineering, University of Queensland, Brisbane, QLD 4072, Australia

b Centre for Microscopy and Microanalysis, University of Queensland, Brisbane, QLD 4072, Australia

Email: j.zou@uq.edu.au, z.chen1@uq.edu.au.

1. Lattice parameter calculation

The lattice parameters (*a* and *c*) for rhombohedral structure can be calculated by [1]

$$\frac{1}{d_{hkl}^2} = \frac{4}{3}\left(\frac{h^2 + hk + k^2}{a^2}\right) + \frac{l^2}{c^2} \quad \text{(S1)}$$

where *hkl* are the index of the $\{hkl\}$ atomic planes, and d_{hkl} is the corresponding interplanar spacing, determined from XRD patterns. Therefore, *a* and *c* for $Bi_xSb_{2-x}Te_3$ nanoplates can be determined, as shown in Figure S1. From which, the variation of *a* and *c* follows the Vegard's law.

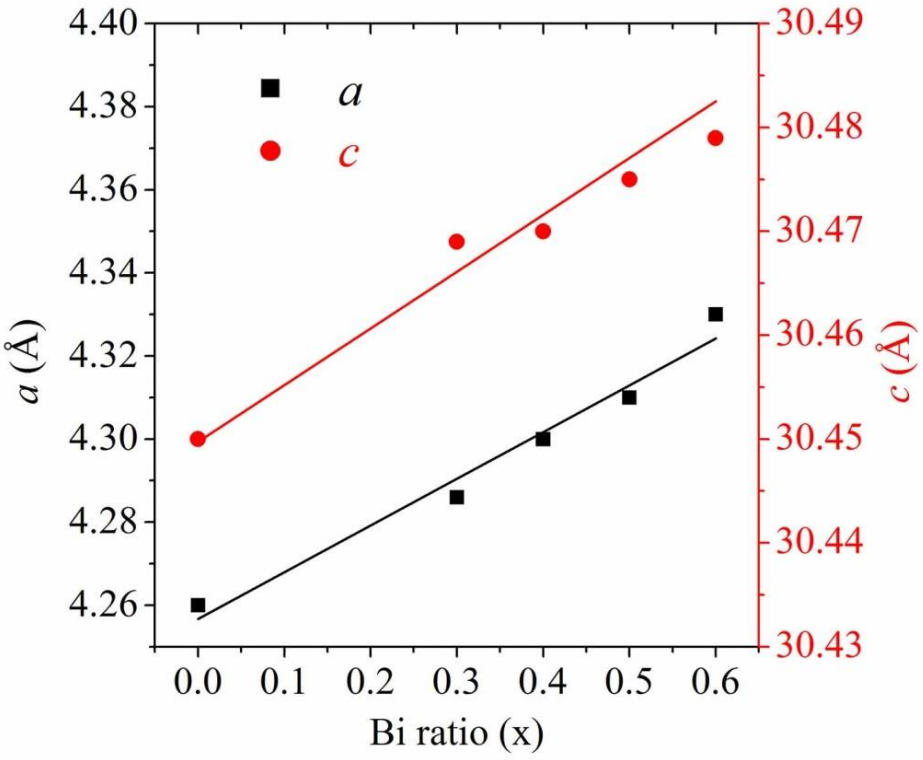

Figure S1 Determined lattice parameters as a function of the Bi concentration for different as-prepared $Bi_xSb_{2-x}Te_3$ nanoplates.

2. Chemical composition determined by EDS

The chemical compositions of as-synthesized $Bi_xSb_{2-x}Te_3$ nanoplates were examined by TEM equipped with EDS, and Figure S2 shows collected EDS profiles. The quantitative analysis of these EDS profiles indicates that the compositions of as-synthesized $Bi_xSb_{2-x}Te_3$ nanoplates are close to the nominal ratios (refer to Figure S2).

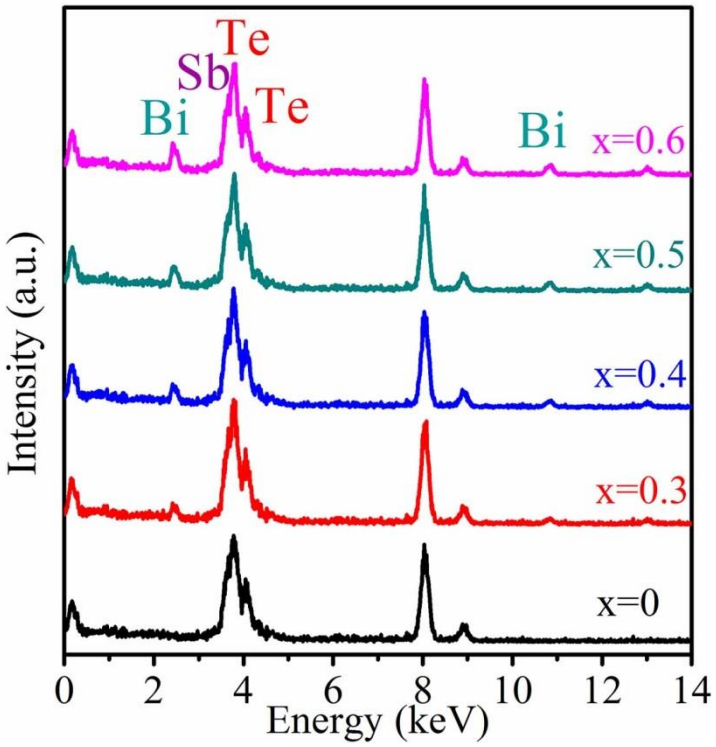

Figure S2 EDS profiles of as-synthesized $Bi_xSb_{2-x}Te_3$ nanoplates.

3. Size distribution of $Bi_xSb_{2-x}Te_3$ nanoplates

To clarify the size distribution of as-synthesized $Bi_xSb_{2-x}Te_3$ nanoplates, SEM investigations were employed. Figure S3 shows SEM images taken from as-synthesized $Bi_xSb_{2-x}Te_3$ nanoplates, from which the size distribution can be statistically estimated to be ~1 μm for all $Bi_xSb_{2-x}Te_3$ nanoplates, with a slight tendency of size decreasing with increasing the Bi concentration.

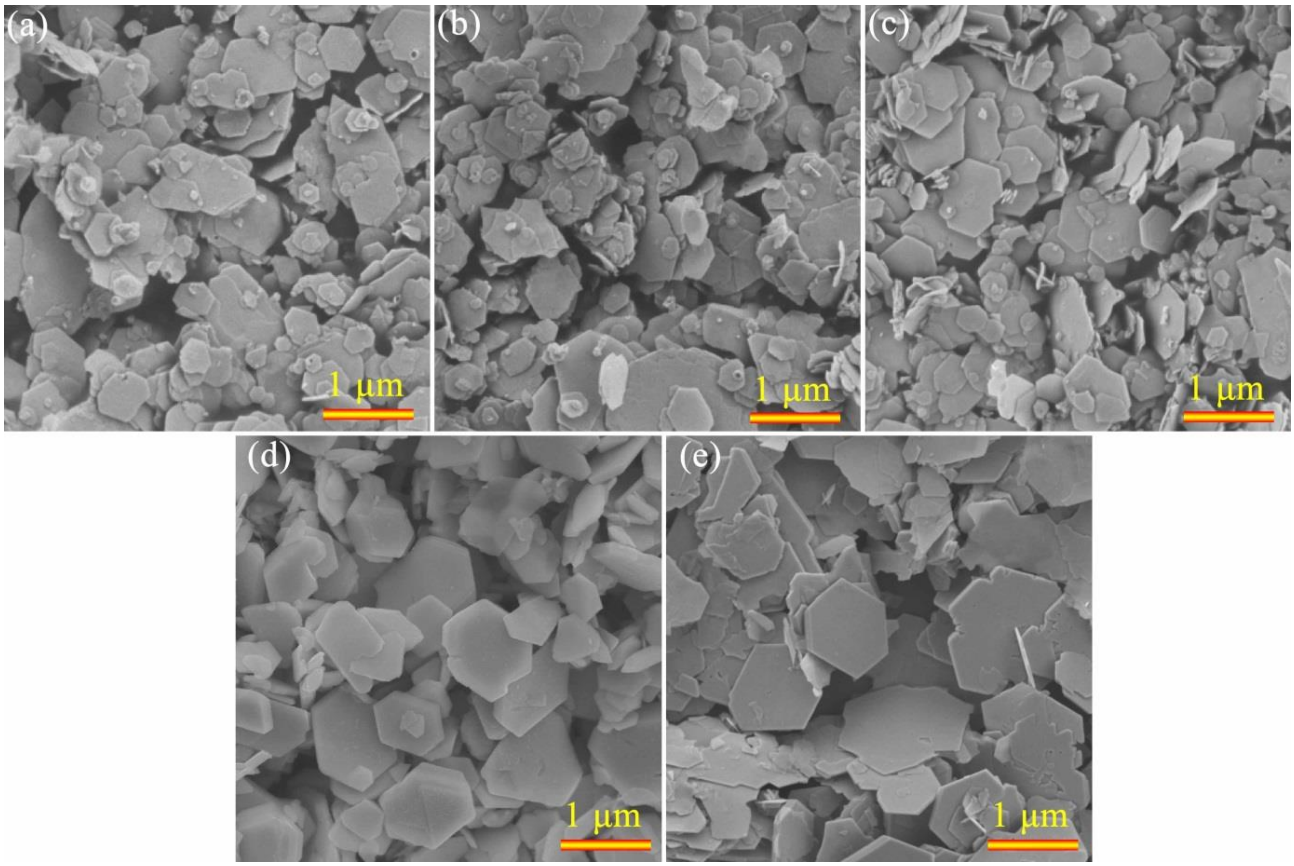

Figure S3 SEM image taken from as-synthesized nanoplates with composition of (a) Sb_2Te_3, (b) $Bi_{0.3}Sb_{1.7}Te_3$, (c) $Bi_{0.4}Sb_{1.6}Te_3$, (d) $Bi_{0.5}Sb_{1.5}Te_3$ and (e) $Bi_{0.6}Sb_{1.4}Te_3$.

4. Determination of texture fraction

Based on the XRD patters for the powder and pellet samples, the corresponding texture fraction (f_{00l}) can be determined by the Lotgering method [2]:

$$f_{00l} = \frac{P_{00l} - P_0}{1 - P_0} \quad \text{(S2)}$$

with

$$P_{00l} = \frac{\sum I_{00l}}{\sum I_{hkl}} \quad \text{(S3)}$$

and

$$P_0 = \frac{\sum I^0_{00l}}{\sum I^0_{hkl}} \quad \text{(S4)}$$

where I_{hkl} and I^0_{hkl} are the intensities of (*hkl*) diffraction peaks for the textured and for the randomly oriented samples. Based on the obtained experimental XRD patterns compared with standard PDF card (JCPDS No. 71-0393), f_{00l} can be determined for all $Bi_xSb_{2-x}Te_3$ pellets.

Table S1 Determined texture fraction of {001} planes for as-synthesized $Bi_xSb_{2-x}Te_3$ nanoplates and corresponding pellets.

x	0	0.3	0.4	0.5	0.6
nanoplates	0.06	0.07	0.05	0.04	0.07
Pellets	0.05	0.07	0.06	0.05	0.10

5. Thermoelectric properties measured along both in-plane and out-of-plane directions

Figure S4 plots the thermoelectric properties measured from the $Bi_{0.5}Sb_{1.5}Te_3$ pellet along both in-plane (perpendicular to the pressing direction) and out-of-plane (parallel to the pressing direction) directions, from which similar thermoelectric properties can be witnessed along the two directions.

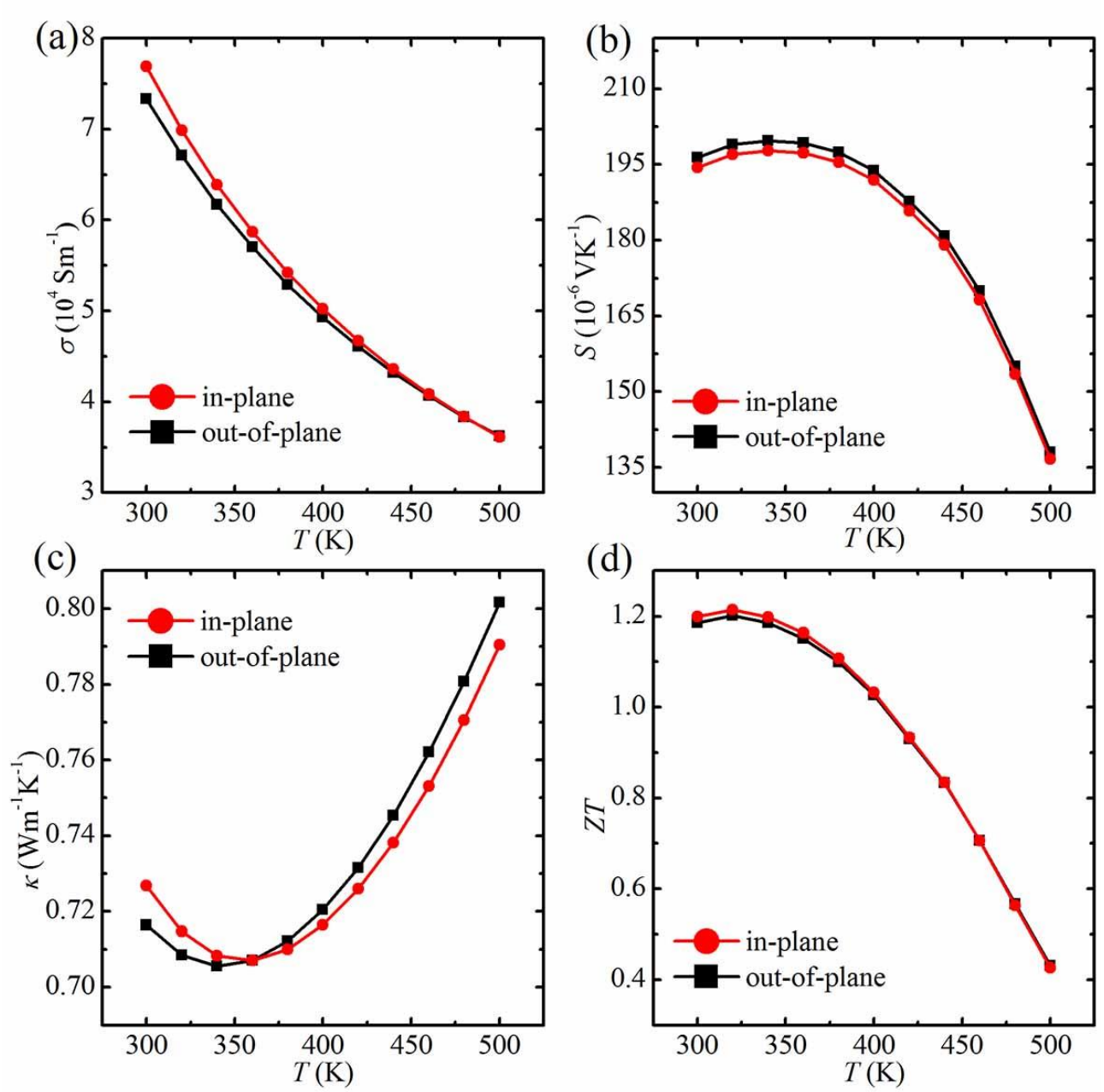

Figure S4 The in-plane and out-of-plane measurements of (a) electrical conductivity σ, (b) Seebeck coefficient S, (c) power factor $S^2\sigma$, and (d) figure of merit ZT for the $Bi_{0.5}Sb_{1.5}Te_3$ pellet.

6. Determination of Lorenz number (*L*)

According to Ref. [3], *L* can be determined by

$$L = \left(\frac{k_B}{e}\right)^2 \left[\frac{F_{1,2}^2(\eta,\beta)}{F_{1,2}^0(\eta,\beta)} - \left(\frac{F_{1,2}^1(\eta,\beta)}{F_{1,2}^0(\eta,\beta)}\right)^2\right] \quad \text{(S5)}$$

with the generalized Fermi integral

$$F_{m,k}^n(\eta,\beta) = \int_0^\infty \left[-\frac{\partial f(\eta)}{\partial \varepsilon}\right] \varepsilon^n \frac{\left(\varepsilon + \beta\varepsilon^2\right)^m}{\left(1+2\beta\varepsilon\right)^k} d\varepsilon \quad \text{(S6)}$$

where k_B is Boltzmann constant, e is the elementary charge, $\eta = \frac{E_v - E_f}{k_B T}$ (E_v is the top of valance band and E_f is the Fermi level) is the reduced Fermi level, $\beta = \frac{k_B T}{E_g}$ (E_g is the band gap), using the determined η shown in Figure 4c, the relationship between *L* and temperature can be plotted for different compositions, as shown in Figure S5.

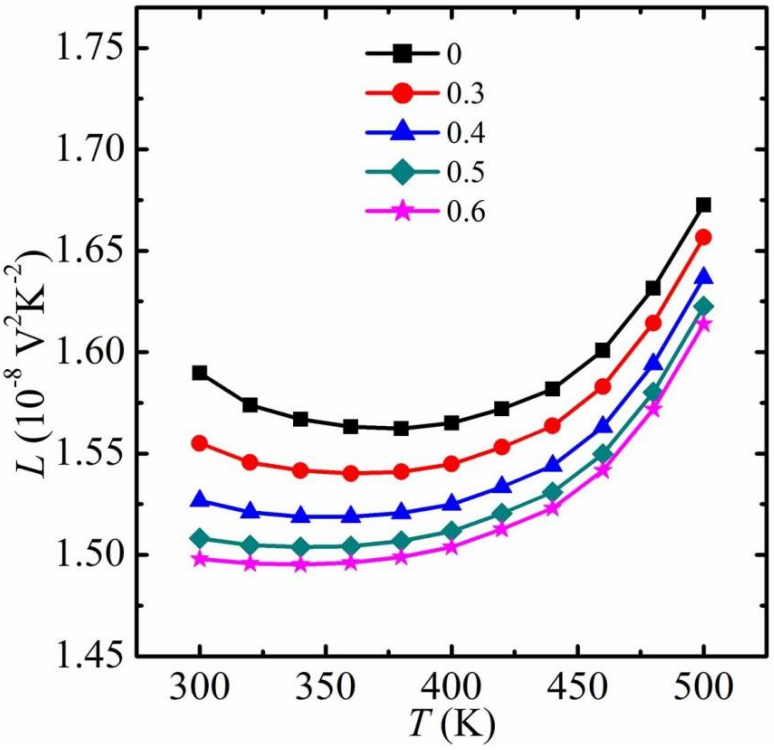

Figure S5 Plots of temperature-depended Lorenz number for all $Bi_xSb_{2-x}Te_3$ pellets.

7. Phonon relaxation time of various scattering mechanisms

According to Refs [4,5], we have

Umklapp phonon scattering (U)

$$\tau_U^{-1} = \frac{\hbar\gamma^2\omega^2 T}{\bar{M}\upsilon^2\theta_D}\exp\left(-\frac{\theta_D}{3T}\right), \quad \text{(S7)}$$

Electron phonon scattering (E)

$$\tau_E^{-1} = \frac{E_{def}^2 m^* \omega^2}{2\pi\hbar^3\rho\upsilon_{\|}}, \quad \text{(S8)}$$

Point defect phonon scattering (PD)

$$\tau_{PD}^{-1} = \frac{\bar{V}\omega^4}{4\pi\upsilon^3}\Gamma, \text{ and} \quad \text{(S9)}$$

Grain boundary phonon scattering (B)

$$\tau_B^{-1} = \frac{\upsilon}{d}, \quad \text{(S10)}$$

where $\hbar$ is reduced Planck constant, γ is the Grüneisen parameter, w is phonon frequency, $\overline{M}$ is the average mass, $\upsilon = \left[\frac{1}{3}\left(\frac{1}{\upsilon_L^3}+\frac{2}{\upsilon_T^3}\right)\right]^{-1/3}$ is the sound velocity with υ_L and υ_T respectively denoting the longitudinal and transverse sound velocities, θ_D is the Debye temperature, E_{def} is the acoustic phonon deformation potential, m^* is the effective mass of charger carrier, ρ is the sample density, $\bar{V}$ is the average atomic volume, Γ is the point defect scattering parameter, and d is the grain size, respectively.

In addition, relaxation time of strained dislocation scattering can be estimated by [4]

Dislocation core phonon scattering (DC)

$$\tau_{DC}^{-1} = N_D\frac{\bar{V}^{4/3}}{\upsilon^2}\omega^3, \text{ and} \quad \text{(S11)}$$

Dislocation strain phonon scattering (DS)

$$\tau_{DS}^{-1} = 0.6B_D^2 N_D \left(\gamma + \Delta\gamma\right)^2 \omega \left\{ \frac{1}{2} + \frac{1}{24}\left(\frac{1-2r}{1-r}\right)^2 \left[1 + \sqrt{2}\left(\frac{\upsilon_L}{\upsilon_T}\right)\right]^2 \right\} \quad \text{(S12)}$$

where N_D is the dislocation density, B_D is the effective Burger's vector, r is the Poisson's ratio and $\Delta\gamma$ is the change in γ due to the dislocation strain, as given by[4]

$$\Delta\gamma = \frac{V_{ST} c_0 K}{k_B T_a}\left(\gamma\alpha^2 - \alpha\beta\right) \quad \text{(S13)}$$

with

$$\alpha = \frac{V_{BT} - V_{ST}}{V_{ST}}, \text{ and} \quad \text{(S14)}$$

$$\beta = \frac{M_{ST} - M_{BT}}{2M_{ST}} \quad \text{(S15)}$$

where c_0 is the concentration of Bi_2Te_3 in $Bi_xSb_{2-x}Te_3$, K is the bulk modulus of Sb_2Te_3, T_a is the sample sintering temperature, V_{BT} and V_{ST} are the atomic volume of Bi_2Te_3 and Sb_2Te_3, and M_{BT} and M_{ST} are the atomic mass of Bi_2Te_3 and Sb_2Te_3, respectively.

According to the Matthiessen rule, the total scattering relaxation time τ_{tot} can be given different models, namely

U+E model

$$\tau_{tot}^{-1} = \tau_U^{-1} + \tau_E^{-1} \quad \text{(S16)}$$

U+E +B model

$$\tau_{tot}^{-1} = \tau_U^{-1} + \tau_E^{-1} + \tau_B^{-1} \quad \text{(S17)}$$

U+E+B+PD model

$$\tau_{tot}^{-1} = \tau_U^{-1} + \tau_E^{-1} + \tau_{PD}^{-1} + \tau_B^{-1} \quad \text{(S18)}$$

U+E+B+PD+D model

$$\tau_{tot}^{-1} = \tau_U^{-1} + \tau_E^{-1} + \tau_{PD}^{-1} + \tau_B^{-1} + \tau_{DC}^{-1} + \tau_{DS}^{-1} \quad \text{(S19)}$$

To determine which phonons contribute dominantly to the thermal conductivity, the spectral lattice thermal conductivity (κ_s) is used,[6] which can be expressed as

$$\kappa_s = \frac{k_B}{2\pi^2 \upsilon}\left(\frac{k_B T}{\hbar}\right)^3 \tau_{tot} \frac{z^4 \exp(z)}{\left[\exp(z)-1\right]^2} \quad \text{(S20)}$$

where k_B is the Boltzmann constant, $\hbar$ is the reduced Plank constant, and $z = \frac{\hbar\omega}{k_B T}$ is the reduced phonon frequency. Figure S6 shows the calculated κ_s for the $Bi_{0.5}Sb_{1.5}Te_3$ pellet based on models of U+E, U+E+B, U+E+B+PD, and U+E+B+PD+D with physical parameters in Table S2. As can be seen, the introduction of grain boundaries, point defects and dislocations can reduce κ_l contributed by low-frequency, high-frequency and mid-frequency phonons, respectively.

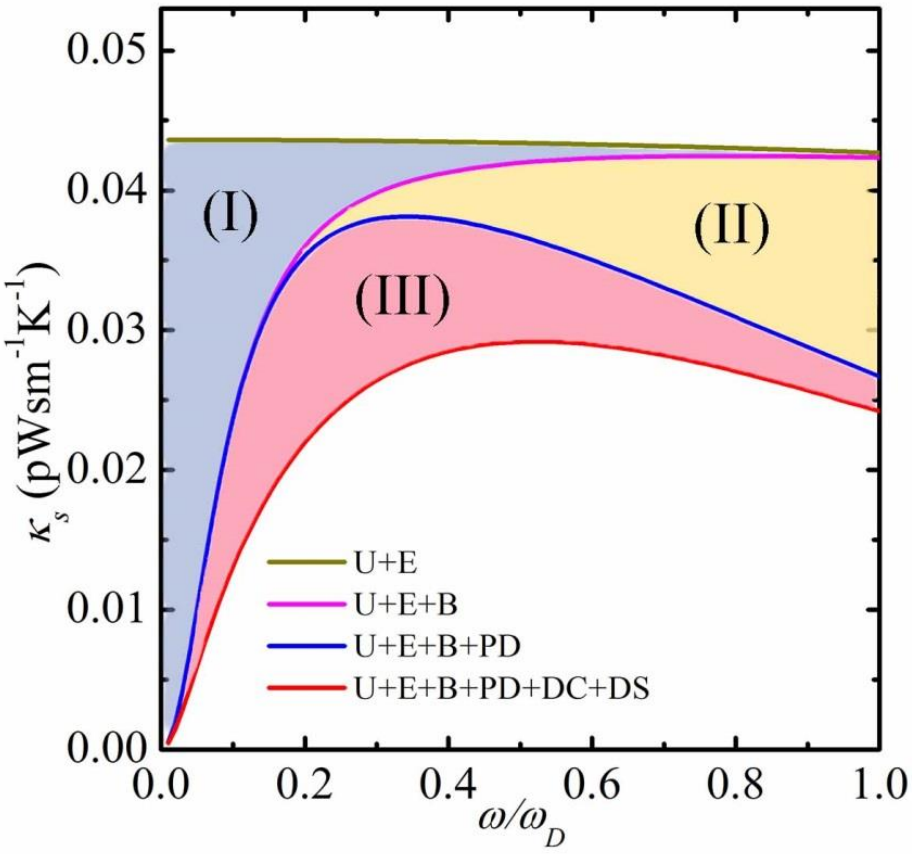

Figure S6 Calculated κ_s for $Bi_{0.5}Sb_{1.5}Te_3$ based on models of U+E, U+E+B, U+E+B+PD, and U+E+B+PD+D. Areas (I), (II) and (III) represent the reduction in κ_l due to the strengthened phonon scattering by introducing grain boundaries, point defects and dislocations, respectively.

8. Physical properties used to calculate κ_l based on various phonon scattering processes

Table S2 Physical properties regarding the phonon transport properties.

Parameters	Values
Debye temperature θ_D (K)	165*
Longitudinal sound velocity υ_L (ms^{-1})	2884*
Transverse sound velocity υ_T (ms^{-1})	1780*
Sound velocity υ (ms^{-1})	2147*
Atomic mass of Bi_2Te_3 M_{BT} (kg)	2.79×10^{-25}
Atomic mass of Sb_2Te_3 M_{ST} (kg)	2.07×10^{-25}
Atomic volume of Bi_2Te_3 V_{BT} (m^3)	3.40×10^{-29}
Atomic volume of Sb_2Te_3 V_{ST} (m^3)	3.13×10^{-29}
Sample density ρ of Bi_2Te_3 (g cm^{-3})	7.6
Sample density ρ of $Bi_{0.5}Sb_{1.5}Te_3$ (g cm^{-3})	6.6
Grain size d for $Bi_{0.5}Sb_{1.5}Te_3$ (nm)	900 (Exp)
Point defect scattering parameter Γ	0.16 (fitted)
Dislocation density N_D of $Bi_{0.5}Sb_{1.5}Te_3$ (cm^{-2})	1.5×10^{11} (Exp)
Magnititude of Burger's vector B_D of $Bi_{0.5}Sb_{1.5}Te$ (Å)	11.6 (fitted)
Poisson's ratio r	0.24*
Grüneisen parameter γ	2.3*
Bulk modulus K (GPa)	44.8*

*Data attracted from Refs [4,7,8].

References

(1) Cullity, B. D.; Stock, S. R. *Elements of X-ray Diffraction*. Prentice Hall: London, **2001**; Vol. 3rd.

(2) Lotgering, F. K. Topotactical Reactions with Ferrimagnetic Oxides Having Hexagonal Crystal Structures—I. *J. Inorg. Nucl. Chem.* **1959**, 9, 113-123.

(3) Pei, Y.; LaLonde, A. D.; Wang, H.; Snyder, G. J. Low Effective Mass Leading to High Thermoelectric Performance. *Energy Environ. Sci.* **2012**, 5, 7963-7969.

(4) Kim, S. I.; Lee, K. H.; Mun, H. A.; Kim, H. S.; Hwang, S. W.; Roh, J. W.; Yang, D. J.; Shin, W. H.; Li, X. S.; Lee, Y. H.; Snyder, G. J.; Kim, S. W. Dense Dislocation Arrays Embedded in Grain Boundaries for High-Performance Bulk Thermoelectrics. *Science* **2015**, 348, 109-114.

(5) Xie, H.; Wang, H.; Pei, Y.; Fu, C.; Liu, X.; Snyder, G. J.; Zhao, X.; Zhu, T. Beneficial Contribution of Alloy Disorder to Electron and Phonon Transport in Half-Heusler Thermoelectric Materials. *Adv. Funct. Mater.* **2013**, 23, 5123-5130.

(6) Toberer, E. S.; Zevalkink, A.; Snyder, G. J. Phonon Engineering through Crystal Chemistry. *J. Mater. Chem.* **2011**, 21, 15843-15852.

(7) Jenkins, J.; Rayne, J.; Ure, R. Elastic Moduli and Phonon Properties of Bi_2Te_3. *Phys. Rev. B* **1972**, 5, 3171-3184.

(8) Chen, X.; Zhou, H. D.; Kiswandhi, A.; Miotkowski, I.; Chen, Y. P.; Sharma, P. A.; Lima Sharma, A. L.; Hekmaty, M. A.; Smirnov, D.; Jiang, Z. Thermal Expansion Coefficients of Bi_2Se_3 and Sb_2Te_3 Crystals from 10 K to 270 K. *Appl. Phys. Lett.* **2011**, 99, 261912.

7

n-Type $Bi_2Te_{3-x}Se_x$ Nanoplates with Enhanced Thermoelectric Efficiency Driven by Wide-Frequency Phonon Scattering and Synergistic Carrier Scattering

7.1 Introduction

For most of thermoelectric semiconductors, acoustic phonons dominate the charger carrier scattering, which leads to the significantly reduced carrier mobility and electrical conductivity at high temperature. If we can intensify the carrier scattering by other mechanism, such as ionic impurities, we are able to weaken the decreasing trend of carrier mobility with increasing temperature. Here, we employed the microwave-assisted solvothermal synthesis to successfully fabricate $Bi_2Te_{3-x}Se_x$ nanoplates. The pellets sintered from the nanoplates show enhanced ZT, accompanied with the significantly reduced κ and shifting of $S^2\sigma$ to high temperature. Through intensive TEM investigations and modeling studies, the achieved low κ can be ascribed to the wide frequency phonon scattering. The infrared reflectance spectroscopy indicated that band gap in the as-prepared nanoplates has been increased, which leads to the suppressed bipolar conduction. Moreover, the derived scattering exponent from the infrared reflectance spectra suggested that a mixed carrier scattering mechanisms existed in our nanoplates, which resulted in the weakened decreasing rate of carrier mobility with temperature.

7.2 Journal Publication

The results in Chapter 7 are included as it appears in *ACS Nano* **2016**, 10.

http://pubs.acs.org/doi/abs/10.1021/acsnano.6b01156

n-Type $Bi_2Te_{3-x}Se_x$ Nanoplates with Enhanced Thermoelectric Efficiency Driven by Wide-Frequency Phonon Scatterings and Synergistic Carrier Scatterings

Min Hong,[†] Thomas C. Chasapis,[‡,§] Zhi-Gang Chen,[*,†] Lei Yang,[†] Mercouri G. Kanatzidis,[§] G. Jeffrey Snyder[*,‡] and Jin Zou[*,†,∥]

[†]Materials Engineering, University of Queensland, Brisbane, QLD 4072, Australia
[‡]Department of Materials Science and Engineering, Northwestern University, Evanston, Illinois 60208, USA

[§]Department of Chemistry, Northwestern University, Evanston, Illinois 60208, USA

[∥]Centre for Microscopy and Microanalysis, University of Queensland, Brisbane, QLD 4072, Australia

E-mail: j.zou@uq.edu.au, z.chen1@uq.edu.au, and jeff.snyder@northwestern.edu

Abstract

Driven by the prospective applications of thermoelectric materials, massive efforts have been dedicated to enhancing the conversion efficiency. The latter is governed by the figure of merit (ZT), which is proportional to the power factor ($S^2\sigma$) and inversely proportional to the thermal conductivity (κ). Here, we demonstrate the synthesis of high-quality ternary $Bi_2Te_{3-x}Se_x$ nanoplates using a microwave-assisted surfactant-free solvothermal method. The obtained *n*-type $Bi_2Te_{2.7}Se_{0.3}$ nanostructures exhibit a high ZT of 1.23 at 480 K measured from the corresponding sintered pellets, in which a remarkably low κ and a shift of peak $S^2\sigma$ to high temperature are observed. By detailed electron microscopy investigations, coupled with theoretical analysis on phonon transports, we propose that the achieved κ reduction is attributed to the strong wide-frequency phonon scatterings. The shifting of peak $S^2\sigma$ to high temperature is due to the weakened temperature dependent transport properties governed by the synergistic carrier scatterings and the suppressed bipolar effects by enlarging the band gap.

Keywords: $Bi_2Te_{3-x}Se_x$ nanoplates, thermoelectric, synergistic carrier scatterings, wide-frequency phonon scattering

1. Introduction

With the capability of directly converting heat into electricity, thermoelectric materials can potentially mitigate the energy crisis and environmental problems *via* capturing energy from waste, environmental or mechanical heat sources, and then transforming into an exploitable form. Energy conversion efficiency of a thermoelectric material is evaluated by the dimensionless figure of merit, $ZT = S^2\sigma T/\kappa$, where S, σ, κ, and T are respectively the Seebeck coefficient, electrical conductivity, thermal conductivity (including electronic component κ_e, lattice component κ_l, and bipolar component κ_{bi}), and the working temperature.[1] So far, significant progress has been made in enhancing ZT *via* increasing the power factor ($S^2\sigma$) by resonant state doping,[2] minority carrier blocking,[3] band convergence,[4] reversible phase transition,[5] and quantum confinement,[6] and/or reducing κ by nanostructuring,[7-9] hierarchical architecturing,[10-12] and matrix with nano-precipitate.[13]

Bi_2Te_3-based alloys have been studied extensively as representative materials for thermoelectric applications near room temperature.[14,15] However, there are at least three issues impeding Bi_2Te_3-based materials to serve as more widely useable thermoelectric devices. Firstly, their *ZT* values deteriorate severely at temperature over 450 K, predominately due to the bipolar effect.[16] Enlarging the band gap (E_g) suppresses the bipolar conduction.[17] Alternatively, synergistic carrier scatterings (a mixture of multi carrier scatterings) can be introduced to weaken the dependence of carrier mobility (μ) on temperature in order to slow down the *ZT* deteriorating rate at relatively high temperature.[18] Secondly, due to the unavoidable Te vacancies in pure *n*-type Bi_2Te_3, the Fermi level (E_f) resides deep in the conduction band, and in turn resulting in a decreased $S^2\sigma$.[19] By incorporating Se in Bi_2Te_3, anion vacancies can be tuned, so an enhanced $S^2\sigma$ can be achieved.[20] Finally, introducing grain boundaries through nanostructuring can substantially reduce κ. However the current fabrication methods, such as ball milling[21] and melt spinning,[22] are relatively ineffective and costly. Compared with ball milling and melt spinning, solvothermal synthesis allows better control over the size, structure, and morphology of the nanograins. Nevertheless, the removal of surfactants is generally time consuming and incomplete, and restricts production yield, and most importantly, the residual surfactants can affect their final thermoelectric performance.[1]

In this study, we demonstrate a microwave-assisted surfactant-free solvothermal approach to synthesize gram-level $Bi_2Te_{3-x}Se_x$ nanoplates within a very short period of time. The fabricated products show a high *ZT* of 1.23 at 480 K in the *n*-type pellets sintered from $Bi_2Te_{2.7}Se_{0.3}$ nanoplates. The significantly enhanced *ZT* mainly arises from the remarkably reduced κ over the entire temperature and the preserved high $S^2\sigma$ at elevated temperature. Microstructure evolution in the sintered pellets examined by the advanced electron microscopy, coupled with theoretical calculations on phonon transports uncovered the underlying principles related to the significant reduction in κ. Moreover, the fundamental reason of $S^2\sigma$ shifting to elevated temperature was clarified by diffuse reflectance infrared Fourier transform spectroscopy.

2. Results and discussion

Characterization of as-synthesized nanopowders. Figure 1a is X-ray diffraction (XRD) patterns of as-synthesized $Bi_2Te_{3-x}Se_x$ products with different nominal Se contents

(*i.e.* 0.0, 0.1, 0.2, 0.3, 0.4, 0.5, 0.6, 0.7, and 1.0), in which the diffraction peaks of as-synthesized Bi_2Te_3 products can be exclusively indexed as the rhombohedral Bi_2Te_3 phase with lattice parameters of a = 4.38 Å and c = 30.49 Å (JCPDS No. 89-2009).[23] Figure 1b presents the enlarged view of the $01\bar{1}5^*$ diffraction peak shifting for different Se containing samples. The calculated lattice parameters of a and c display linear decreases with increasing the Se content, which are consistent with the Vegard's law (see Figure S1 in the Supporting Information) and previous studies.[24,25] To determine the composition of the obtained samples, we conducted the energy-dispersive X-ray spectroscopy (EDS) investigation within a transmission electron microscope (TEM), and results are shown in Figure S2, which indicates that elemental ratios of Bi, Te, and Se are close to the nominal values. To further verify the compositional variation of as-synthesized products, we performed Raman spectroscopy. Figure 1c shows the Raman spectra, in which two peaks assigned as E_g^2 (in-plane) and A_{1g}^2 (out-of-plane) modes at 103 cm^{-1} and 134 cm^{-1} are detected for the binary Bi_2Te_3 sample, as illustrated in Figure 1d.[26] Moreover, both E_g^2 and A_{1g}^2 modes shift to the high wave number for the Se containing samples. Figure 1e summarizes the Raman shift of E_g^2 and A_{1g}^2 modes as a function of the Se content. Such shifts can be ascribed to the Se substitution in Te sites, which modifies the lattice vibrations and the electron-phonon interactions within $Bi_2Te_{3-x}Se_x$ structure.[25]

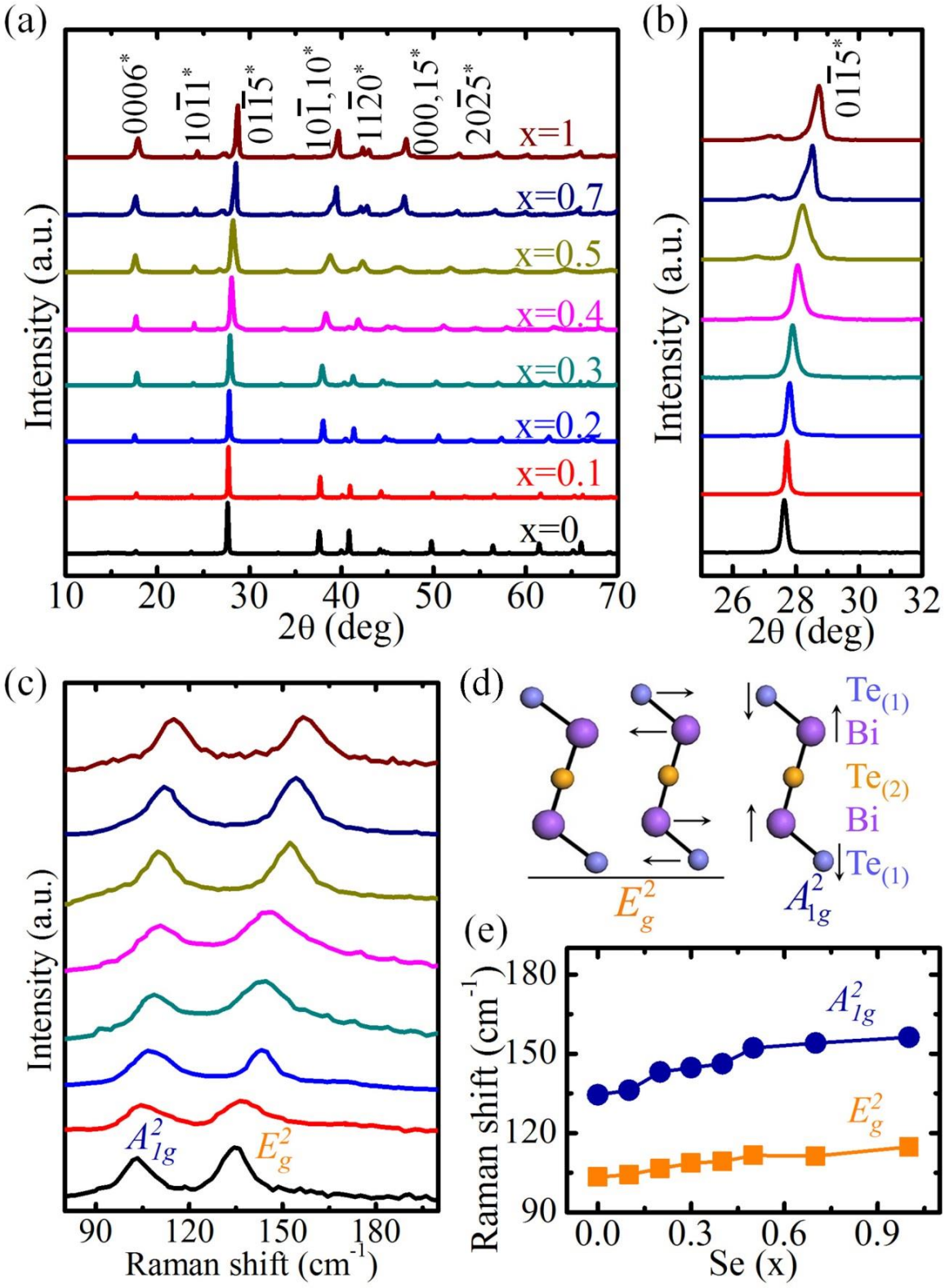

Figure 1 (a) XRD patterns of as-synthesized $Bi_2Te_{3-x}Se_x$ nanoplates with x ranging from 0 to 1. (b) Enlarged XRD patterns showing the systematic shift of the $01\bar{1}5$* peak. (c) Raman spectra of $Bi_2Te_{3-x}Se_x$ nanostructures. (d) Schematic diagrams for the two Raman-active modes. (e) Measured E_g^2 and A_{1g}^2 peak positions as a function of the Se content.

To understand the morphological and structural characteristics, we performed TEM investigations. As a representative example, the detailed microstructures of as-synthesized $Bi_2Te_{2.7}Se_{0.3}$ powders are presented. Figure 2a shows a TEM image of a single nanoplate with lateral size of ~1 μm, which agrees with the size distribution revealed by scanning electron microscopy (SEM) investigation (refer to Figure S3a). As a comparison, we present the SEM images of $Bi_2Te_{2.7}Se_{0.3}$ products synthesized with poly(N-vinyl-2-pyrrolidone) (PVP, M_w=40,000) serving as the surfactant (refer to Figure S3b). As can be seen, such products are in the form of uniform hexagonal nanoplates with clear edges, caused by the capping effect of PVP to stabilize the surface energy of their side walls.[27] Additionally, nanoplates prepared without and with PVP show the similar thicknesses of ~30 nm. Figure 2b and c respectively show the selected area electron diffraction (SAED) pattern and the <0001> zone-axis high-resolution TEM (HRTEM) image, suggesting that the nanoplate has high structural quality. Figure 2d is the EDS profile, in which Bi, Te, and Se peaks can be identified (note that the Cu peaks come from the Cu TEM grid), and the inset exhibits the EDS maps of Bi, Te, and Se, which clearly demonstrate that all elements are uniformly distributed in this nanoplate. Based on the comprehensive characterizations outlined above, we can conclude that Se atoms have successfully substituted Te sites to form pure ternary $Bi_2Te_{3-x}Se_x$ phases.

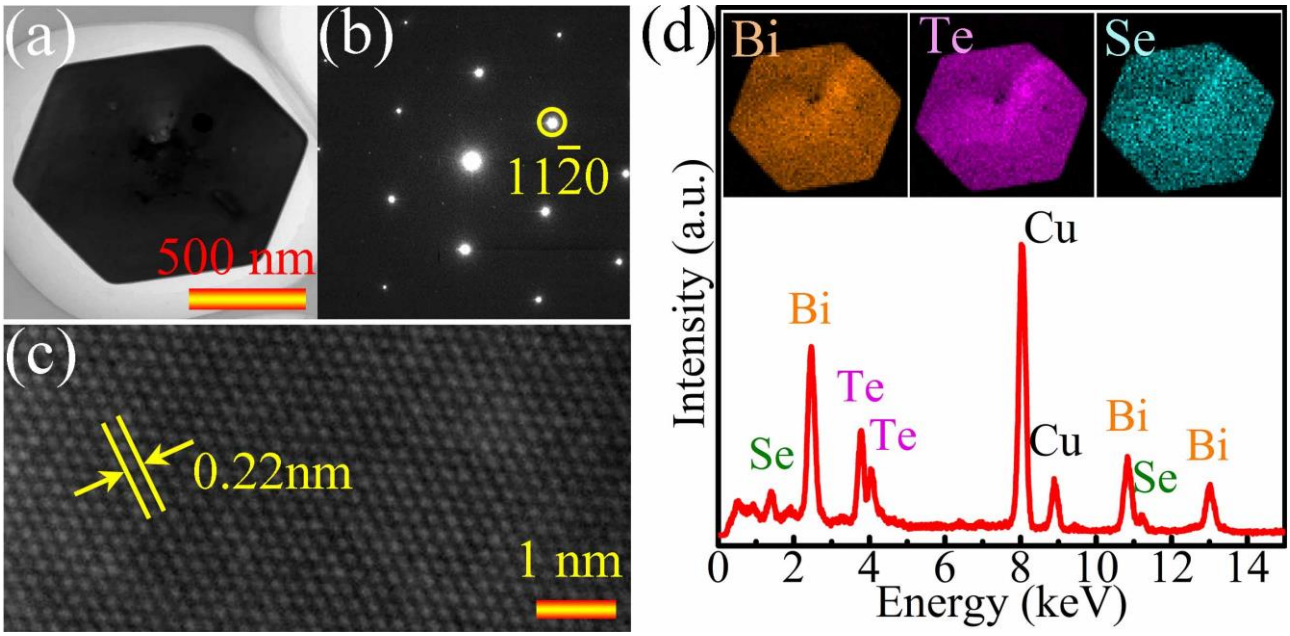

Figure 2 (a) TEM image of a typical $Bi_2Te_{2.7}Se_{0.3}$ nanoplate. (b) SAED pattern. (c) HRTEM image. (d) EDS profile with EDS mappings of Bi, Te and Se.

Thermoelectric performance evaluation. In order to evaluate their thermoelectric performance, we compressed as-synthesized $Bi_2Te_{3-x}Se_x$ nanoplates into pellets with a diameter of ~12.5 mm by spark plasma sintering (SPS). Due to the anisotropic behavior of Bi_2Te_3-based materials,[16] both in-plane (vertical to the pressing direction) and out-of-plane (parallel to the pressing direction) S, σ, κ, and ZT for the $Bi_2Te_{2.7}Se_{0.3}$ pellets were measured. Figure 3a illustrates the sample preparations for the measurement of the thermoelectric properties along two directions. Specifically, two pellets were sintered with different thicknesses for each Se content. The thin pellet with a thickness of ~ 2 mm was used to measure the out-of-plane κ directly. After that, it was polished into rectangular shape along the radial direction with a dimension of approximately 2×3×10 mm to measure the in-plane S and σ. The thick pellet with a thickness of ~10 mm was polished into a rectangular shape along the axis direction with a dimension of approximately 2×10×10 mm to measure the in-plane κ. Subsequently, this large rectangular shape was further polished into a smaller rectangle with a dimension of approximately 2×3×10 mm for the measurement of the out-of-plane S and σ. Prior to measure the thermoelectric performance, the phase purities of sintered samples were confirmed by XRD (Figure S6). Moreover, we applied the electron probe microanalysis (EPMA) to examine the compositions of sintered samples by randomly selecting 5 spots for each sample. Figure 3b shows the results, from which the compositions are close to the nominal values. Figure S7 and S8 summarizes the obtained thermoelectric properties respectively for $Bi_2Te_{2.7}Se_{0.3}$ and Bi_2Te_2Se from both directions, in which the obtained thermoelectric properties along the two directions are nearly identical. Since the in-plane and out-of-plane S and σ are measured from sintered pellets with different thickness, it is necessary to cross check the data along both these directions from a single sintered pellet. To achieve this, we prepared a 12 mm thick pellet and cut it into two sections, one with thickness of ~4 mm and other one with thickness of ~8 mm, as illustrated in Figure S9a. The in-plane S and σ were measured from the thin pellet (polished into a rectangle shape along the radial direction), and the out-of-plane S and σ were measured from the thick pellet (polished into rectangle shape along the axial direction). Figures S9b and c illustrate that the measurements along both these directions are almost identical.

To understand the weakened anisotropic feature, we employed the Lotgering method[28] to estimate the texture fraction of the $\{000l\}$ planes for the as-sintered pellets and a value of ~0.06 with a variation of 0.03 – 0.11 was obtained (see Table S1). This small texture

fraction agrees well with the nearly isotropic thermoelectric properties measured in our pellets. Although the anisotropy is very pronounced in $Bi_2Te_{3-x}Se_x$ single crystal,[29] it has been confirmed such anisotropic behavior in polycrystalline $Bi_2Te_{3-x}Se_x$ can be weakened, resulting in nearly isotropic *ZT* values along both in-plane and out-of-plane directions.[24] In our nanostructured materials, the texture fraction is smaller than the bulk polycrystalline counterpart; supporting our obtained near-isotropic thermoelectric properties. For this reason, we only measured the out-of-plane thermoelectric properties for pellets with other compositions.

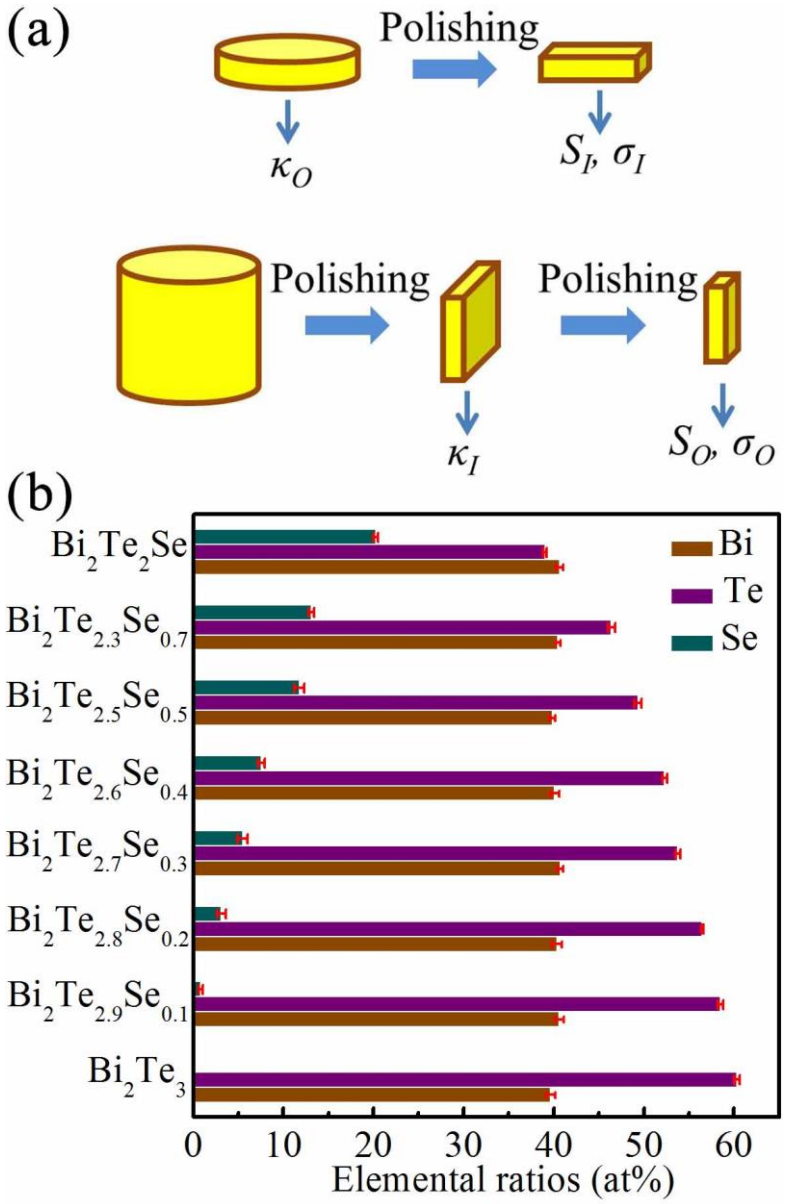

Figure 3 (a) Schematic illustration of the preparation of sintered samples for measuring in-plane (S_I, σ_I and κ_I) and out-of-plane (S_O, σ_O and κ_O) thermoelectric properties. (b) Compositions of sintered $Bi_2Te_{3-x}Se_x$ pellets determined by EPMA.

Figure 4a shows the composition dependent σ, which decreases monotonically with increasing the temperature for all pellets. Moreover, with increasing the Se content, σ decreases and then increases. As can be seen, the pellet made of $Bi_2Te_{2.7}Se_{0.3}$ nanoplates exhibits the lowest σ, ranging from 5.9×10^4 to 4.7×10^4 Sm^{-1} in the entire temperature region. Figure 4b is the variation of S with the temperature. The negative sign of S for all $Bi_2Te_{3-x}Se_x$ pellets suggests their n-type nature, and the peak value shifts to high temperature in the ternary phases. Specifically, a peak of S = -198 μVK^{-1} is achieved at 460 K for the $Bi_2Te_{2.7}Se_{0.3}$ pellet compared with that of -173 μVK^{-1} for Bi_2Te_3 at 420 K and -154 μVK^{-1} for Bi_2Te_2Se at 480 K. With increasing the Se content, σ and S display an opposite variation trend, which leads to a diverse $S^2\sigma$, as shown in Figure 4c. As can be seen, the $Bi_2Te_{2.7}Se_{0.3}$ pellet exhibits the highest $S^2\sigma$ of 19×10^{-4} $Wm^{-1}K^{-2}$ at 440 K.

Figure 4d shows the plots of κ *versus* temperature. These nanoplate-based pellets exhibit considerably reduced κ compared with the bulk systems (refer to Figure S10).[30] Specifically, the Bi_2Te_3 and Bi_2Te_2Se pellets respectively exhibit κ as low as 0.92 and 0.98 $Wm^{-1}K^{-1}$ compared with the lowest κ of ~1.7 and ~2.0 $Wm^{-1}K^{-1}$ found in their bulk counterparts with the identical compositions.[31] More importantly, κ drops and then rises with increasing the Se content, and the lowest value reaches 0.69 $Wm^{-1}K^{-1}$ in the $Bi_2Te_{2.7}Se_{0.3}$ pellet. In fact, κ is the sum of κ_e, κ_l, and κ_{bi}.[32] Therefore, by subtracting κ_e from κ (the calculation of κ_e is discussed in Section 7 of the Supporting Information), we can obtain κ_l (namely, $\kappa_l = \kappa - \kappa_e$) if κ_{bi} is sufficiently small. Figure 4e shows the variation of κ_l, which is significantly reduced. Despite the inherently strong anharmonicity in Bi_2Te_3 crystals (strengthening the Umklapp phonon-phonon scattering),[33] the significant suppression in κ_l may be due to the wide-frequency phonon scatterings caused by multi scattering pathways (discussed later).

Due to the high $S^2\sigma$ as well as low κ, a significantly enhanced ZT is expected, as shown in Figure 4f. A peak ZT of 1.23 at the relatively high temperature of 480 K is achieved in our pellet made of $Bi_2Te_{2.7}Se_{0.3}$ nanoplates, owing to the $S^2\sigma$ peak shifting to higher temperature and the pronounced reduction of κ.

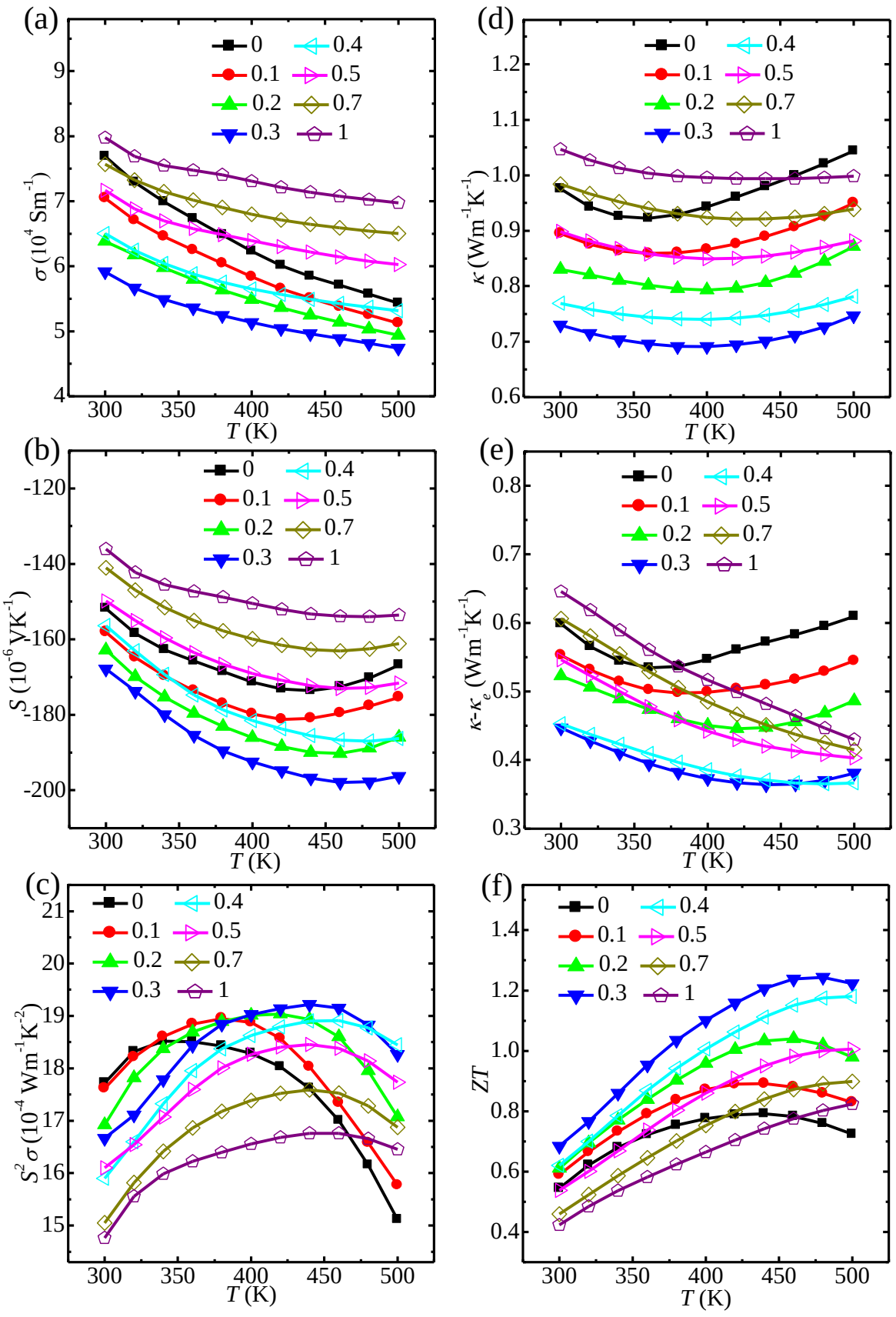

Figure 4 Thermoelectric characteristics of pellets sintered from $Bi_2Te_{3-x}Se_x$ nanoplates: (a) σ, (b) S, (c) $S^2\sigma$ (d) κ, (e) κ-κ_e and (f) ZT, all as a function of temperature, respectively.

Microstructures in sintered pellets. Based on above discussion, we conclude that the enhanced peak *ZT* is mainly due to the significantly reduced κ_l. To understand the impact of microstructures on our remarkably low κ, we analyzed the structural characteristics of the nanostructured pellets using electron microscopy. Figure S12 are SEM images taken from pellets made from nanoplates with different compositions, and show their sub-μm grain sizes. Since the $Bi_2Te_{2.7}Se_{0.3}$ pellet shows the lowest κ, we investigate this pellet in more details. Figure 5a presents the EBSD image taken from the $Bi_2Te_{2.7}Se_{0.3}$ pellet, suggesting the widely-distributed grain sizes with random crystallographic orientations, which further confirms the nearly isotropic behavior of measured thermoelectric properties. Figure 5b is a typical TEM image, revealing the multi-grain feature. To further verify the grain boundaries, HRTEM was employed. Figure 5c and d demonstrate a couple of examples, from which grain boundaries appear clearly. To examine the structural evolution within the grains, HRTEM investigations were performed. Figure 5e shows an example with inset presenting the fast Fourier transformation (FFT) pattern. Figure 5f depicts the inversed FFT image filtered by $01\bar{1}5$* and $2\bar{1}\bar{1}0$* reflections, from which many dislocations can be observed (marked by T), and their density was estimated as ~1.7×10^{11} cm^{-2} (confirmed from extensive HRTEM analyses). Since, as presented earlier, as-synthesized nanoplates have high-crystallinity, the dislocations observed in the sintered pellets must be generated due to the mechanical deformation during the sintering process. Such a high density of dislocations and grain boundaries, coupled with point defects,[34] can greatly enhance phonon scattering so as to effectively reduce κ.

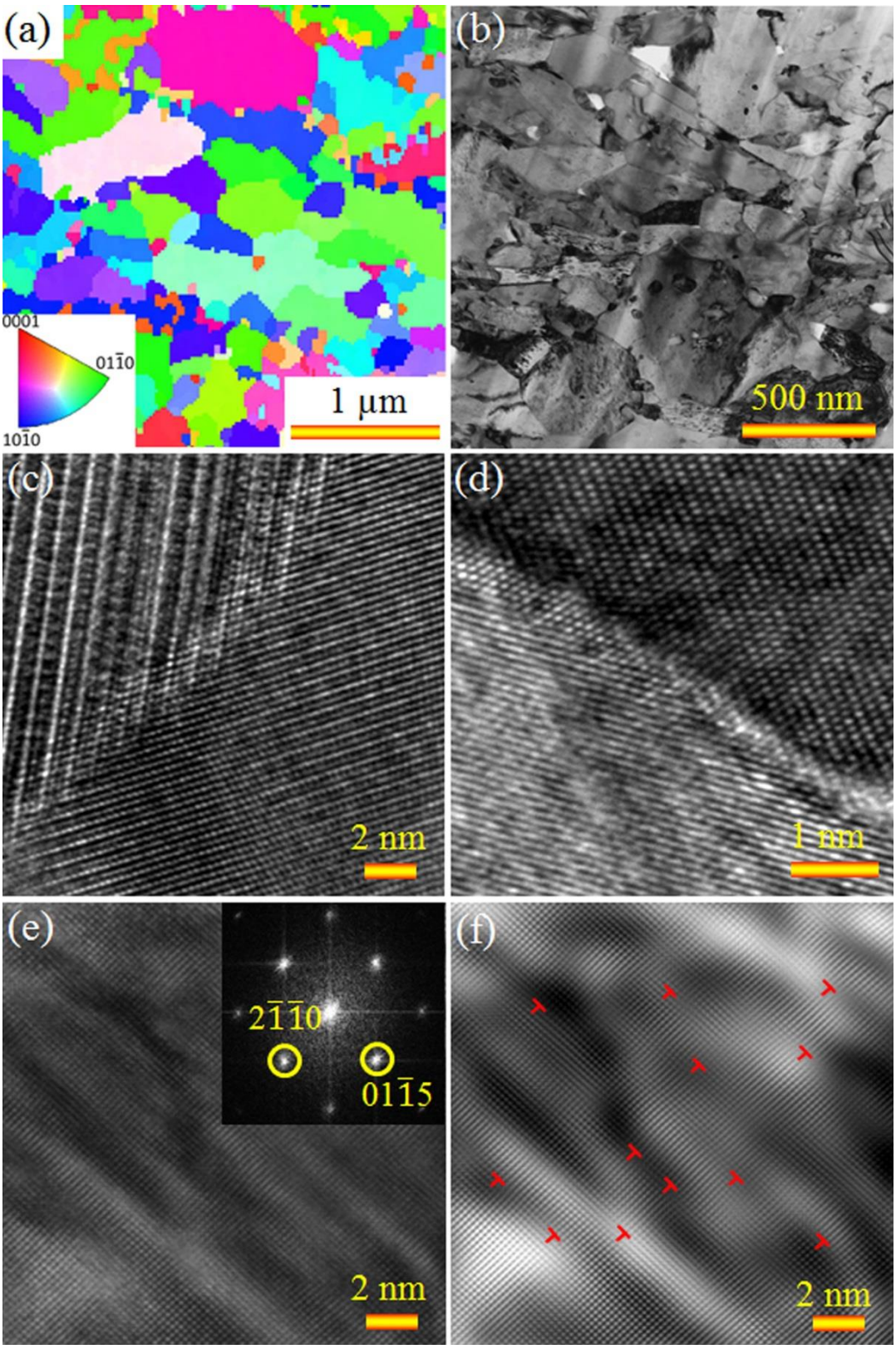

Figure 5 (a) EBSD and (b) TEM images of the sintered $Bi_2Te_{2.7}Se_{0.3}$ pellet. (c) and (d) HRTEM images showing grain boundaries. (e) HRTEM image taken from a typical inner grain area and inset showing the FFT pattern. (f) The corresponding inversed FFT image showing high-density dislocations.

Theoretical studies on phonon transport. To quantitatively understand the obtained lowest κ_l, we examined the phonon transport by considering various phonon scattering mechanisms, including Umklapp processes (U), electrons (E), grain boundaries (B), point defects (PD), and dislocations (D) composed of dislocation cores (DC) and dislocation strains (DS) (The details of phonon transport calculations are shown in Section 10 of the Supporting Information).

Since the integral of the spectral lattice thermal conductivity (κ_s) with respect to the phonon frequency equals to κ_l,[35] we can clarify which kind of phonons contributes to κ_l by evaluating κ_s. Based on Equation S10 with the physical parameters listed in Table S2 of the Supporting Information, we calculated κ_s for our $Bi_2Te_{2.7}Se_{0.3}$ nanostructures. Figure 6a shows the phonon frequency (ω) dependent κ_s, determined respectively by models considering different scattering mechanisms at 300 K, including U+E, U+E+B, U+E+B+PD, U+E+B+PD+D. As can be seen, compared with the U+E model (considering scatterings from the Umklapp processes and electrons only), the introduction of grain boundaries in the U+E+B model gives lower κ_s, and the low-frequency Area (I) in Figure 6a represents the reduction in κ_l caused by grain boundaries. Similarly, the high-frequency Area (II) and the mid-frequency Area (III) in Figure 6a represent the further reductions in κ_l resulted from point defects and dislocations, respectively. Based on this, we conclude that grain boundaries, dislocations and point defects are effective to scatter low-, medium-, and high-frequency phonons, respectively, as illustrated in Figure 6b.

As mentioned above, the obtained κ_l in our nanostructured Bi_2Te_3 systems are lower than that for the ingot and the ball milling counterparts. To verify the underlying reasons, we compared κ_l for our $Bi_2Te_{2.7}Se_{0.3}$ nanostructures with the reported values for ingots[31] and ball milling samples[30] with the same composition. Since ingots and ball milling samples exhibit a very low density of dislocations,[36] D scattering can be negligible compared with the B and PD scatterings. Based on U+E+B and U+E+PD models with the fitted grain size and point defect scattering parameter (Γ) given in Table S3, we calculated κ_s components corresponding to the respective introduction of B or PD scatterings at 300 K to understand their individual contributions. Figure 6c shows the calculated κ_s. Compared with the ingot case, the ball milling case contains stronger B and PD scatterings, and nanostructuring leads to the strongest B and PD scatterings. Although the fitted grain size and Γ may vary within a small magnitude, the variation trend of B and PD scatterings in these three cases remains.

Furthermore, we calculated κ_l over the entire temperature range. Figure 6d shows the calculated κ_l against the experimental data. As can be seen, the calculated κ_l plots using the U+E+B+PD model match well with the experimental data of κ - κ_e for ingot and ball milling samples, respectively. It should be noted that the deviation between the calculated κ_l and the experimental data is mainly due to increased κ_{bi} in κ - κ_e at high temperature. This is because κ includes κ_e, κ_l, and κ_{bi}, which means that κ - κ_e equals to κ_l + κ_{bi}, rather than κ_l; especially when the bipolar effect is notable at high temperature. In Figure 6d, the calculated κ_l does not include κ_{bi}, resulting in the calculated κ_l deviating from the κ - κ_e at relatively high temperature. For our nanostructures, the U+E+B+PD+D model can quantitatively predict the experimental data. Moreover, the minimum of calculated κ_l plots (corresponding to the possible peak *ZT*) tends to move towards the high temperature in the sequence of ingot, balling milling, and nanostructuring samples. This is probably due to the enhanced B, PD or D scatterings, which may shift the low κ_l to high temperature. Similar phenomena have also been observed experimentally,[14,31,37,38] in which the temperature dependent κ_l generally shows the lowest value at higher temperature when the B and/or PD scatterings are enhanced.

Based on above discussions, the achieved ultra-low κ_l in our $Bi_2Te_{2.7}Se_{0.3}$ pellet can be explained by the existence of dislocations providing wide-frequency phonon scatterings.

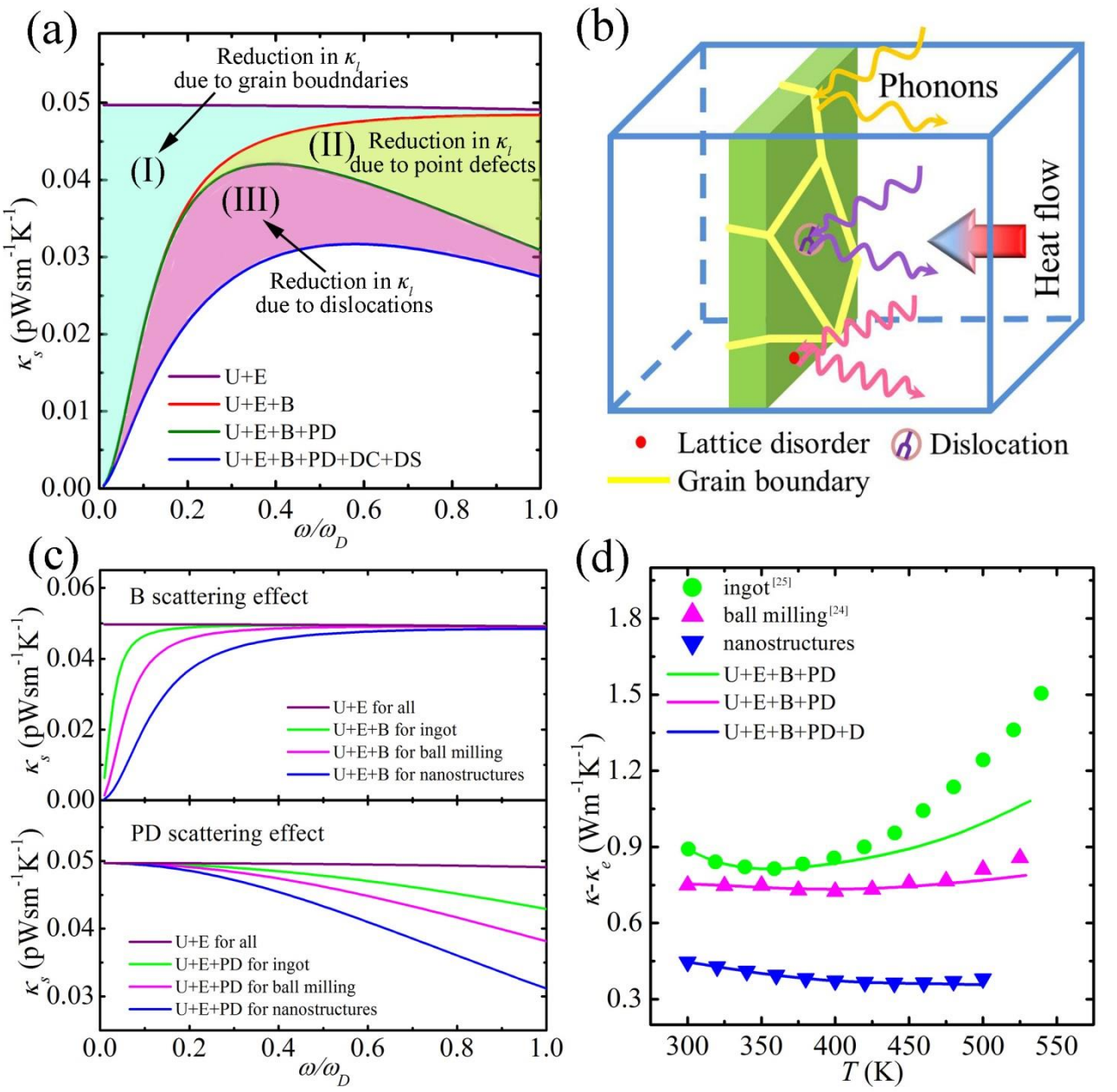

Figure 6 (a) Calculated room-temperature κ_s for our $Bi_2Te_{2.7}Se_{0.3}$ pellet with various phonon scatterings. (b) Schematic diagram illustrating the scattering of wide-frequency phonons by various sources. (c) The effects of solely introducing grain boundaries or point defects on reducing κ_s for the ingot sample,[31] ball milling,[30] and our nanostructures with the same composition of $Bi_2Te_{2.7}Se_{0.3}$. (d) The measured data points of κ - κ_e for the three samples, compared with calculated κ_l as a function of temperature.

Transport properties determined by Hall effect. Figure S14 plots the measured Hall coefficient (R_H) as a function of temperature. From which, Hall carrier concentration (n_H)

and Hall carrier mobility (μ_H) over the measured temperature range can be obtained. Figure 7a shows the composition dependent n_H, which is nearly independent of temperature, but shows decreasing and then increasing trend with increasing the Se content (x) in $Bi_2Te_{3-x}Se_x$. It is well documented that n_H in $Bi_2Te_{3-x}Se_x$ is determined by the antisite defects (providing holes) and vacancies (providing electrons).[20] With increasing the Se content, n_H decreases for x < 0.3, indicating that antisite defects contribute more holes than the electrons from vacancies, while n_H increases for x > 0.3, in which vacancies dominate over antisite defects. Figure 7b shows the composition dependent μ_H over the studied temperature range. As can be seen, μ_H is strongly related to the doping level, and is peaked at $Bi_2Te_{2.7}Se_{0.3}$. The peak at x = 0.3 reflects the minimum in the n_H shown in Figure 7a. The increase of μ_H might be related to relaxed scattering mechanisms, as well as modification of the band structure, *i.e.* the effective mass. In this regard, we note that the charger carrier scattering is very complicated, including point defects.[39,40] With increasing the Se content, point defects scattering becomes strong. However, other carrier scattering mechanisms may also change. We anticipate that the increase of μ_H found in our nanostructured pellets for x < 0.3 is caused the relaxed carrier scatterings from other sources. On the other hand, the band structure could be modified by the Se doping. Kohler *et al.*[41] and Prokofieva *et al.*[42] have proposed a complex conduction band structure for $Bi_2Te_{3-x}Se_x$. Upon alloying, possible modification of the conduction band extrema may give rise to variation of the electron mobility. Our calculations based on single parabolic model suggest that the Se content dependent effective mass reaches to the minimum for $Bi_2Te_{2.7}Se_{0.3}$, which should also be responsible for the observed maximum μ_H in $Bi_2Te_{2.7}Se_{0.3}$ (refer to Figure S16).

In addition, μ_H decreases with increasing the temperature, following a power law of $T^{-0.5}$ – $T^{-0.1}$ for all samples. Because acoustic phonon scattering predicts $T^{-1.5}$, the variation of μ_H indicates that other carrier scattering mechanisms could be present (such as optical phonons, ionized impurities, and/or other scattering mechanism).[39] These other types of carrier scatterings lead to μ_H being less temperature dependent, compared with the acoustic phonon dominated carrier scatterings. This should assist the $S^2\sigma$ peak shifting to higher temperature (refer to Figure 4c).

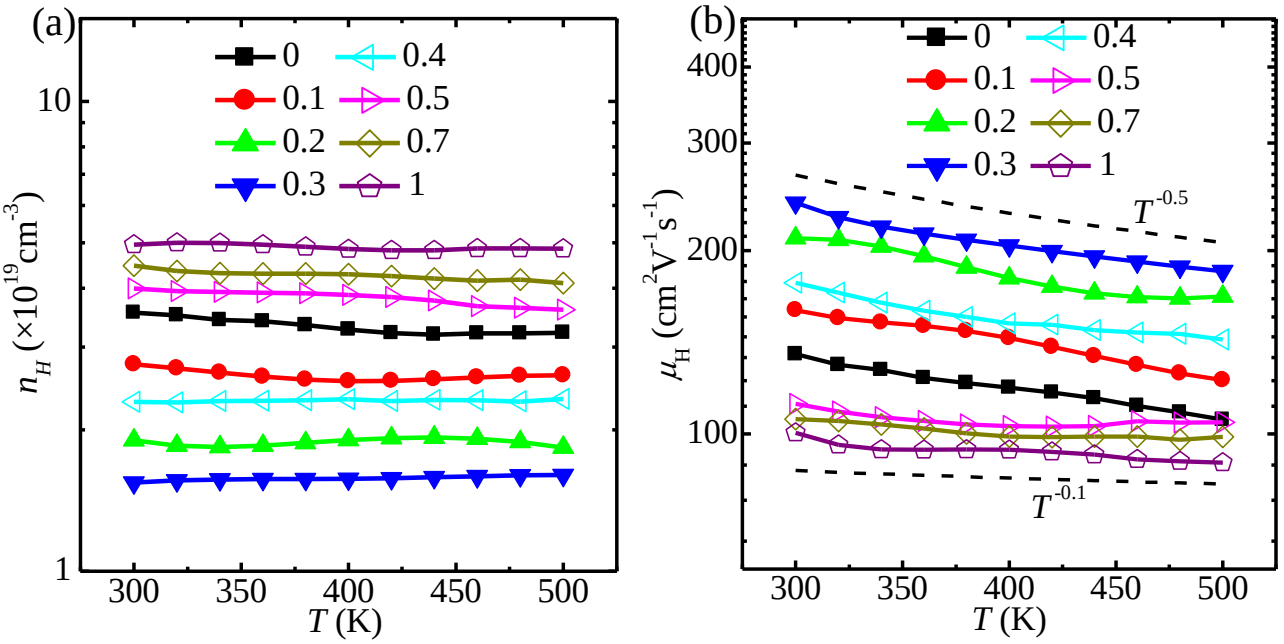

Figure 7 Composition dependent n_H (a) and μ_H (b) over the measured temperature range for different sintered $Bi_2Te_{3-x}Se_x$ pellets.

Understanding the thermoelectric properties through optical diffuse reflectance. To understand the observed thermoelectric behavior, we determine the carrier scattering type(s) and the optical energy gap ($E_{g,opt}$) of as-synthesized $Bi_2Te_{3-x}Se_x$ nanoplates with different Se contents using diffuse reflectance infrared Fourier transform spectroscopy (DRIFTS). Figure S17 shows the normalized Kubelka-Munk function of as-synthesized nanoplates. To determine the carrier scattering type(s), we fit the corresponding free carrier absorption tails (α_{FC}) *versus* photon energy ($\hbar\omega$) using the equation of $\alpha_{FC} = \alpha_0 + C(\hbar\omega)^{-r}$,[41] in which α_0 is the background correction term, C is the fitting coefficient, and r is the scattering exponent that depends on the carrier scattering type(s). The details of extraction method for r are discussed in Section 12 of the Supporting Information. Figure 8a shows the composition dependent r, in which r increases from ~1.8 to a peak of ~3 at x = 0.4 and then decreases to a plateau of ~1.5 for x > 1.2. Expected r values for different carrier scattering types can be calculated, namely, r = 1.5 for the acoustic phonon scattering, r = 2.5 for the optical phonon scattering, and r = 3 (or 3.5) for the ionized impurity scattering.[42-44] By comparing the experimental r with the calculated values for different carrier scattering types, we find that a mixture of carrier scattering mechanisms likely occurs in our $Bi_2Te_{3-x}Se_x$ ($0 \le x \le 1$) nanoplates. Since the data are collected from

nanostructures, it is necessary to compare them with their bulk commercial ingots. Therefore, bulk $Bi_2Te_{3-x}Se_x$ materials were mechanically ground (MG) and their corresponding *r* values were determined and outlined in Figure 8a. As can be seen, for MG $Bi_2Te_{3-x}Se_x$ powders, the variation of *r* with the Se content is smooth and *r* is in the range of 1.4 – 1.7, suggesting that acoustic phonons dominate the carrier scattering in the MG powders. In fact, transport studies in other nanostructured thermoelectrics, such as PbTe[45-47] and Bi_2Te_3,[48] also suggested higher *r* over their relevant bulk analogs due to an additional scattering of charge carriers by grain boundaries and interfaces. For our $Bi_2Te_{3-x}Se_x$ nanoplates with possible point defects, the existences of micro-scale grain boundaries and dislocations have been confirmed by our TEM studies. These complicated multi-scale micro/nano structures affect the carrier transport behavior, leading to mixed carrier scatterings in our nanoplates. It has been reported that the grain boundaries preferentially scatter minority carriers;[49] therefore, the bipolar conduction can also be effectively reduced.

Furthermore, from the Kubelka-Munk function shown in Figure S17, we can also derive $E_{g,opt}$ for our $Bi_2Te_{3-x}Se_x$ nanoplates. Since Bi_2Te_3 is an indirect band gap semiconductor while Bi_2Se_3 is a direct one,[50] and $Bi_2Te_{2.7}Se_{0.3}$ shows a transition between them,[51] the determination of $E_{g,opt}$ should depend on the corresponding composition (for detailed discussion see Section 12 of the Supporting Information). Figure 8b shows determined $E_{g,opt}$ for our nanoplates, in which $E_{g,opt}$ increases from ~0.2 to ~0.32 eV when x changes from 0 to 2.8. In comparison, the reported $E_{g,opt}$ for bulk $Bi_2Te_{3-x}Se_x$ counterparts were also shown in Figure 8b as the purple plot,[50] in which, for $0 \le x \le 1$ (the composition region in this study), the obtained $E_{g,opt}$ of nanostructures are larger. The higher $E_{g,opt}$ values of the $Bi_2Te_{3-x}Se_x$ nanoplates may be explained by the electron doping (in the same composition regime the bulk samples were found non-degenerate) and the Burstein-Moss shift of the Fermi level within the conduction band.[41] The $E_{g,opt}$ increase upon alloying results in a reduction of the bipolar conduction — leading to a reduced κ, and extending high thermoelectric efficiency to elevated temperature.[17,52]

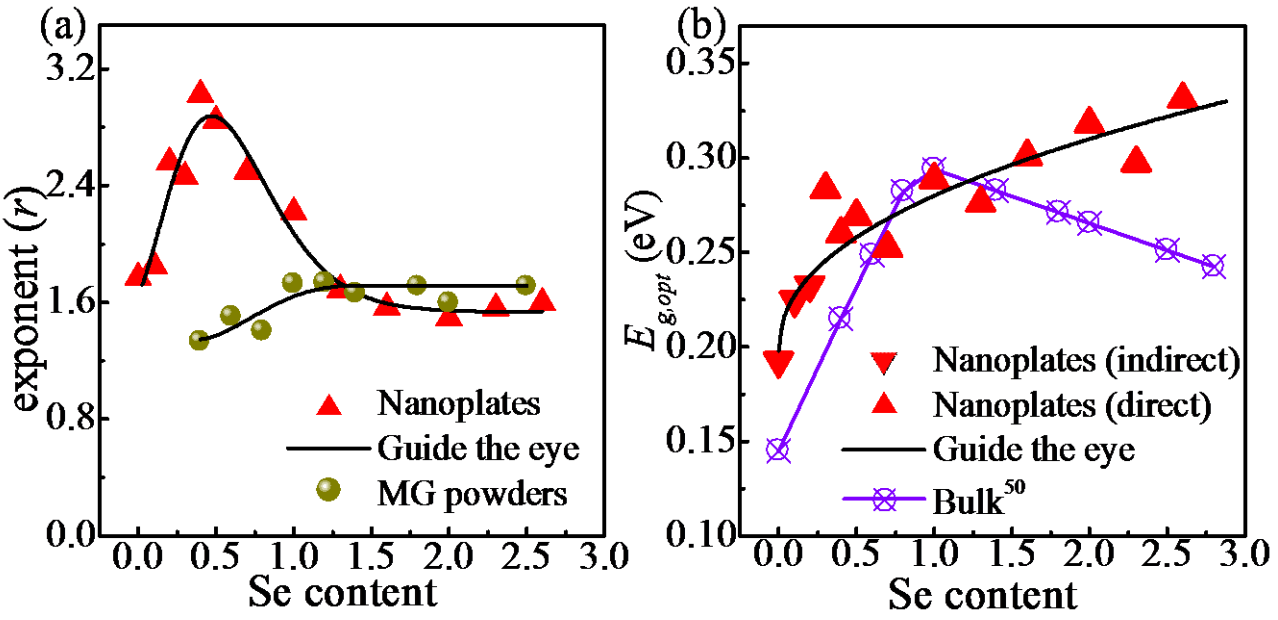

Figure 8 (a) Scattering exponent *r* derived from optical absorption for the $Bi_2Te_{3-x}Se_x$ nanoplates compared to MG samples. (b) $E_{g,opt}$ for the $Bi_2Te_{3-x}Se_x$ nanoplates compared with that for bulk counterparts.[50]

3. Conclusion

In this study, we successfully fabricate high-purity and crystalline $Bi_2Te_{3-x}Se_x$ nanoplates by a microwave-assisted solvothermal method without using surfactants. A high *ZT* of ~1.23 at 480 K for the *n*-type Bi_2Te_3-based thermoelectric material is achieved from the sintered $Bi_2Te_{2.7}Se_{0.3}$ nanoplates, which is due to the significantly reduced κ and the peak $S^2\sigma$ shifting to high temperature compared to the conventional material. Through detailed structural investigations by SEM/TEM and theoretical modeling, the obtained ultra-low κ is understood as due to strong wide-frequency phonon scatterings by multi-scale scattering sources. The shifting of $S^2\sigma$ to higher temperature is a result of increased $E_{g,opt}$ and the complex carrier scatterings, which respectively suppress the bipolar effect and weaken the dependence of transport properties on temperature. This study provides an alternative insight on the design of high-performance thermoelectric materials by nanostructuring.

4. Experimental method

Material synthesis and processing. All chemicals were purchased from Sigma Aldrich and used without further purification. In the synthesis of $Bi_2Te_{2.7}Se_{0.3}$, we added $Bi(NO_3)_3{\cdot}5H_2O$ (1 mmol, 485.07 mg), Na_2TeO_3 (1.35 mmol, 299.12 mg), and Na_2SeO_3

(0.15 mmol, 25.94 mg) into ethylene glycol (40 mL) mixed with NaOH solution (5 mol/L, 2 mL). After stirred for ~30 min, the obtained clear solution was sealed in a 100 mL Teflon vessel, which was heated in a CEM Mars 6 microwave oven at a setting temperature of 230 ˚C for 5 min. After cooled to room temperature, the synthesized products were collected by a high-speed centrifugation, washed six times with distilled water and absolute ethanol and finally dried at 60 ˚C for 12 hours in vacuum oven. The procedure for other samples was identical to the synthesis of $Bi_2Te_{2.7}Se_{0.3}$ except for using different precursor ratios.

Material characterizations. The phase purity of the synthesized products were characterized by XRD equipped with graphite monochromatized, Cu Kα radiation (λ = 1.5418 Å). The morphological, structural, and chemical characteristics of the nanopowders were investigated by SEM (JEOL 7800) and TEM (FEI F20, equipped with EDS). Raman spectra were detected by a Renishawin Via Raman microscope system with a 514.5 nm Ar laser. The laser power was 0.5 mW, and the integral time was 10 seconds. Composition analysis of sintered samples was conducted using wave length dispersive X-ray spectrometry in the JEOL JXA-8200 EPMA. The EBSD investigation and TEM specimen preparation for sintered pellet were performed using focused ion beam (FIB) under low current in FEI Scios.

Thermoelectric performance and Hall effect measurement. The nanopowders were compressed by SPS under 40 MPa and at 250 ˚C for 5 min under vacuum into pellets with diameter of ~12.5 mm, and measured by an Archimedes method the densities of all sintered pellets were confirmed to be approximately 92.6%. For each composition, we sintered two pellets with different heights of ~2 and 10 mm under the same sintering conditions to measure S, σ and κ along the same direction.

Thermal diffusivity (D) was measured by a laser flash method (LFA 457, NETZSCH), and κ was calculated through $\kappa=DC_pd$, where C_p and d are the specific heat capacity, and density, respectively. C_p was obtained from empirical formulas, *i.e.* $C_{pBT} = 108.06+5.53\times10^{-2}T$ $JK^{-1}mol^{-1}$ for Bi_2Te_3 and $C_{pBS} = 118.61+1.92\times10^{-2}T$ $JK^{-1}mol^{-1}$ for Bi_2Se_3, respectively.[53] C_p for $Bi_2Te_{3-x}Se_x$ was estimated by $C_p = [C_{pBT}(3-x)+C_{pBS}x]/3$, since the difference between C_{pBT} and C_{pBS} is small. σ and S were measured simultaneously on a ZEM-3, ULVAC. The uncertainty of the thermoelectric performance measurements (S, σ, and D) was estimated as ~ 5%.

Hall coefficient R_H was measured using the Van der Pauw method in a magnetic field up to ±2*T*.[54] n_H and μ_H were respectively calculated using $n_H = 1/(eR_H)$ and $\mu_H = \sigma R_H$.

Optical property measurement. Room temperature optical diffuse reflectance measurements were conducted in the mid-IR range 0 – 0.7 eV (400 – 6000 cm^{-1}) using a Nicolet 6700 FT-IR spectrometer. A silver mirror was used as background. The absorption spectra (α/s) were obtained by the Kubelka – Munk function relating the diffuse reflectance (R) with the absorption coefficient (α) and the scattering coefficient (s) through (a/s) = $(1-R)^2/2R$.[55]

Associated content

Supporting Information: Lattice parameter calculation, chemical composition determination using EDS, SEM images and size distribution of different nanoplates, XRD of sintered pellets and their texture fractions, in-plane and out-of-plane thermoelectric properties for $Bi_2Te_{2.7}Se_{0.3}$ and Bi_2Te_2Se based pellet, comparisons of our ZT, κ_e and κ-κ_e with reported data, calculation of κ_e, grain size determined by SEM for the sintered pellets, calculation of κ_l, Hall coefficient, and optical properties. This material is available free of charge *via* the Internet at http://pubs.acs.org.

Author information

Corresponding Authors

* Email: j.zou@uq.edu.au

* Email: z.chen1@uq.edu.au

* Email: jeff.snyder@northwestern.edu

Notes

The authors declare no competing financial interest.

Acknowledgements

This work was financially supported by the Australian Research Council. M.H. acknowledges the China Scholarship Council for providing the PhD stipend, and the Graduate School of University of Queensland for providing the travel award. The Australian Microscopy & Microanalysis Research Facility is acknowledged for providing characterization facilities. G.J.S. and T.C.C. acknowledge the Solid-State Solar-Thermal

Energy Conversion Center (S3TEC-EFRC), funded by the U.S. Department of Energy, Office of Science, Basic Energy Sciences under Award # DE-SC0001299. M.G.K. acknowledges support from the Department of Energy, Office of Science, Basic Energy Sciences under grant DE-SC0014520.

References

(1) Chen, Z.-G.; Han, G.; Yang, L.; Cheng, L.; Zou, J. Nanostructured Thermoelectric Materials: Current Research and Future Challenge. *Prog. Nat. Sci.* **2012**, 22, 535-549.

(2) Heremans, J. P.; Jovovic, V.; Toberer, E. S.; Saramat, A.; Kurosaki, K.; Charoenphakdee, A.; Yamanaka, S.; Snyder, G. J. Enhancement of Thermoelectric Efficiency in PbTe by Distortion of the Eectronic Density of States. *Science* **2008**, 321, 554-557.

(3) Yang, H.; Bahk, J.-H.; Day, T.; Mohammed, A. M. S.; Snyder, G. J.; Shakouri, A.; Wu, Y. Enhanced Thermoelectric Properties in Bulk Nanowire Heterostructure-Based Nanocomposites through Minority Carrier Blocking. *Nano Lett.* **2015**, 15, 1349-1355.

(4) Pei, Y.; Shi, X.; LaLonde, A.; Wang, H.; Chen, L.; Snyder, G. J. Convergence of Electronic Bands for High Performance Bulk Thermoelectrics. *Nature* **2011**, 473, 66-69.

(5) Zhao, L.; Lo, S. H.; Zhang, Y.; Sun, H.; Tan, G.; Uher, C.; Wolverton, C.; Dravid, V. P.; Kanatzidis, M. G. Ultralow Thermal Conductivity and High Thermoelectric Figure of Merit in SnSe Crystals. *Nature* **2014**, 508, 373-377.

(6) Dresselhaus, M. S.; Chen, G.; Tang, M. Y.; Yang, R. G.; Lee, H.; Wang, D. Z.; Ren, Z. F.; Fleurial, J. P.; Gogna, P. New Directions for Low-Dimensional Thermoelectric Materials. *Adv. Mater.* **2007**, 19, 1043-1053.

(7) Kanatzidis, M. G. Nanostructured Thermoelectrics: The New Paradigm? *Chem. Mater.* **2010**, 22, 648-659.

(8) Son, J. S.; Choi, M. K.; Han, M.-K.; Park, K.; Kim, J.-Y.; Lim, S. J.; Oh, M.; Kuk, Y.; Park, C.; Kim, S.-J.; Hyeon, T. *n*-Type Nanostructured Thermoelectric Materials Prepared from Chemically Synthesized Ultrathin Bi_2Te_3 Nanoplates. *Nano Lett.* **2012**, 12, 640-647.

(9) Zhang, G.; Kirk, B.; Jauregui, L. A.; Yang, H.; Xu, X.; Chen, Y. P.; Wu, Y. Rational Synthesis of Ultrathin *n*-Type Bi_2Te_3 Nanowires with Enhanced Thermoelectric Properties. *Nano Lett.* **2012**, 12, 56-60.

(10) Han, G.; Chen, Z.-G.; Yang, L.; Hong, M.; Drennan, J.; Zou, J. Rational Design of Bi_2Te_3 Polycrystalline Whiskers for Thermoelectric Applications. *ACS Appl. Mater. Interf.* **2014**, 7, 989-995.

(11) Fang, H.; Feng, T.; Yang, H.; Ruan, X.; Wu, Y. Synthesis and Thermoelectric Properties of Compositional-Modulated Lead Telluride–Bismuth Telluride Nanowire Heterostructures. *Nano Lett.* **2013**, 13, 2058-2063.

(12) Fang, H.; Yang, H.; Wu, Y. Thermoelectric Properties of Silver Telluride–Bismuth Telluride Nanowire Heterostructure Synthesized by Site-Selective Conversion. *Chem. Mater.* **2014**, 26, 3322-3327.

(13) Biswas, K.; He, J.; Blum, I. D.; Wu, C. I.; Hogan, T. P.; Seidman, D. N.; Dravid, V. P.; Kanatzidis, M. G. High-Performance Bulk Thermoelectrics with All-Scale Hierarchical Architectures. *Nature* **2012**, 489, 414-418.

(14) Liu, W.-S.; Zhang, Q.; Lan, Y.; Chen, S.; Yan, X.; Zhang, Q.; Wang, H.; Wang, D.; Chen, G.; Ren, Z. Thermoelectric Property Studies on Cu-Doped *n*-Type $Cu_xBi_2Te_{2.7}Se_{0.3}$ Nanocomposites. *Adv. Energy Mater.* **2011**, 1, 577-587.

(15) Finefrock, S. W.; Yang, H.; Fang, H.; Wu, Y. Thermoelectric Properties of Solution Synthesized Nanostructured Materials. *Annu. Rev. Chem. Biomol. Eng.* **2015**, 6, 247-266.

(16) Hu, L. P.; Zhu, T. J.; Wang, Y. G.; Xie, H. H.; Xu, Z. J.; Zhao, X. B. Shifting up the Optimum Figure of Merit of *p*-Type Bismuth Telluride-Based Thermoelectric Materials for Power Generation by Suppressing Intrinsic Conduction. *NPG Asia Mater.* **2014**, 6, e88.

(17) Minnich, A. J.; Dresselhaus, M. S.; Ren, Z. F.; Chen, G. Bulk Nanostructured Thermoelectric Materials: Current Research and Future Prospects. *Energy Environ. Sci.* **2009**, 2, 466-479.

(18) Wang, S.; Yang, J.; Wu, L.; Wei, P.; Zhang, W.; Yang, J. On Intensifying Carrier Impurity Scattering to Enhance Thermoelectric Performance in Cr-Doped $Ce_yCo_4Sb_{12}$. *Adv. Funct. Mater.* **2015**, 25, 6660–6670.

(19) Pei, Y.; Gibbs, Z. M.; Balke, B.; Zeier, W. G.; Snyder, G. J. Optimum Carrier Concentration in *n*-Type PbTe Thermoelectrics. *Adv. Energy Mater.* **2014**, 4, 1400486.

(20) Hu, L.; Zhu, T.; Liu, X.; Zhao, X. Point Defect Engineering of High-Performance Bismuth-Telluride-Based Thermoelectric Materials. *Adv. Funct. Mater.* **2014**, 24, 5211–5218.

(21) Lan, Y.; Minnich, A. J.; Chen, G.; Ren, Z. Enhancement of Thermoelectric Figure-of-Merit by a Bulk Nanostructuring Approach. *Adv. Funct. Mater.* **2010**, 20, 357-376.

(22) Xie, W.; Wang, S.; Zhu, S.; He, J.; Tang, X.; Zhang, Q.; Tritt, T. M. High Performance Bi_2Te_3 Nanocomposites Prepared by Single-Element-Melt-Spinning Spark Plasma Sintering. *J. Mater. Sci.* **2013**, 48, 2745-2760.

(23) Nakajima, S. The Crystal Structure of $Bi_2Te_{3-x}Se_x$. *J. Phys. Chem. Solids* **1963**, 24, 479-485.

(24) Yan, X.; Poudel, B.; Ma, Y.; Liu, W. S.; Joshi, G.; Wang, H.; Lan, Y.; Wang, D.; Chen, G.; Ren, Z. F. Experimental Studies on Anisotropic Thermoelectric Properties and Structures of *n*-Type $Bi_2Te_{2.7}Se_{0.3}$. *Nano Lett.* **2010**, 10, 3373-3378.

(25) Soni, A.; Zhao, Y. Y.; Yu, L. G.; Aik, M. K. K.; Dresselhaus, M. S.; Xiong, Q. H. Enhanced Thermoelectric Properties of Solution Grown $Bi_2Te_{3-x}Se_x$ Nanoplatelet Composites. *Nano Lett.* **2012**, 12, 1203-1209.

(26) Richter, W.; Kohler, H.; Becker, C. R. A Raman and Far-Infrared Investigation of Phonons in Rhombohedral V2-VI3 Compounds Bi_2Te_3, Bi_2Se_3, Sb_2Te_3 and $Bi_2(Te_{1-x}Se_x)_3$ ($0<x<1$), $(Bi_{1-y}Sb_y)_2Te_3$ ($0<y<1$). *Phys. Status. Solidi. B* **1977**, 84, 619-628.

(27) Peng, X. Mechanisms for the Shape-Control and Shape-Evolution of Colloidal Semiconductor Nanocrystals. *Adv. Mater.* **2003**, 15, 459-463.

(28) Lotgering, F. K. Topotactical Reactions with Ferrimagnetic Oxides Having Hexagonal Crystal Structures—I. *J. Inorg. Nucl. Chem.* **1959**, 9, 113-123.

(29) Carle, M.; Pierrat, P.; Lahalle-Gravier, C.; Scherrer, S.; Scherrer, H. Transport Properties of *n*-Type $Bi_2(Te_{1-x}Se_x)_3$ Single Crystal Solid Solutions ($x = 0.05$). *J. Phys. Chem. Solids* **1995**, 56, 201-209.

(30) Liu, W.; Lukas, K. C.; McEnaney, K.; Lee, S.; Zhang, Q.; Opeil, C. P.; Chen, G.; Ren, Z. Studies on the Bi_2Te_3-Bi_2Se_3-Bi_2S_3 System for Mid-Temperature Thermoelectric Energy Conversion. *Energy Environ. Sci.* **2013**, 6, 552-560.

(31) Wang, S.; Tan, G.; Xie, W.; Zheng, G.; Li, H.; Yang, J.; Tang, X. Enhanced Thermoelectric Properties of $Bi_2(Te_{1-x}Se_x)_3$-Based Compounds as *n*-Type Legs for Low-Temperature Power Generation. *J. Mater. Chem.* **2012**, 22, 20943-20951.

(32) Hong, M.; Chen, Z. G.; Yang, L.; Zou, J. $Bi_xSb_{2-x}Te_3$ Aanoplates with Enhanced Thermoelectric Performance due to Sufficiently Decoupled Electronic Transport Properties and Strong Wide-Frequency Phonon Scatterings. *Nano Energy* **2016**, 20, 144-155.

(33) Lee, S.; Esfarjani, K.; Luo, T.; Zhou, J.; Tian, Z.; Chen, G. Resonant Bonding Leads to Low Lattice Thermal Conductivity. *Nat. Commun.* **2014**, 5, 3525.

(34) Kim, S. I.; Lee, K. H.; Mun, H. A.; Kim, H. S.; Hwang, S. W.; Roh, J. W.; Yang, D. J.; Shin, W. H.; Li, X. S.; Lee, Y. H.; Snyder, G. J.; Kim, S. W. Dense Dislocation Arrays Embedded in Grain Boundaries for High-Performance Bulk Thermoelectrics. *Science* **2015**, 348, 109-114.

(35) Zhu, T. J.; Fu, C. G.; Xie, H. H.; Liu, Y. T.; Feng, B.; Xie, J.; Zhao, X. B. Lattice Thermal Conductivity and Spectral Phonon Scattering in FeVSb-Based Half-Heusler Compounds. *EPL* **2013**, 104, 46003.

(36) Lan, Y.; Poudel, B.; Ma, Y.; Wang, D.; Dresselhaus, M. S.; Chen, G.; Ren, Z. Structure Study of Bulk Nanograined Thermoelectric Bismuth Antimony Telluride. *Nano Lett.* **2009**, 9, 1419-1422.

(37) Wang, H.; Bahk, J.-H.; Kang, C.; Hwang, J.; Kim, K.; Kim, J.; Burke, P.; Bowers, J. E.; Gossard, A. C.; Shakouri, A.; Kim, W. Right Sizes of Nano- and Microstructures for High-Performance and Rigid Bulk Thermoelectrics. *Proc. Natl. Acad. Sci. USA* **2014**, 111, 10949-10954.

(38) Hu, L.; Wu, H.; Zhu, T.; Fu, C.; He, J.; Ying, P.; Zhao, X. Tuning Multiscale Microstructures to Enhance Thermoelectric Performance of *n*-Type Bismuth-Telluride-Based Solid Solutions. *Adv. Energy Mater.* **2015**, 5, 1500411.

(39) Huang, B. L.; Kaviany, M. Ab initio and Molecular Dynamics Predictions for Electron and Phonon Transport in Bismuth Telluride. *Phys. Rev. B* **2008**, 77, 125209.

(40) Appel, J. Electron-Electron Scattering and Transport Phenomena in Nonpolar Semiconductors. *Phys. Rev.* **1961**, 122, 1760-1772.

(41) Gibbs, Z. M.; LaLonde, A.; Snyder, G. J. Optical Band Gap and the Burstein-Moss Effect in Iodine Doped PbTe Using Diffuse Reflectance Infrared Fourier Transform Spectroscopy. *New J. Phys.* **2013**, 15, 075020.

(42) Walukiewicz, W.; Lagowski, L.; Jastrzebski, L.; Lichtensteiger, M.; Gatos, H. C. Electron Mobility and Free Carrier Absorption in GaAs - Determination of the Compensation Ratio. *J. Appl. Phys.* **1979**, 50, 899-908.

(43) Pankove, J. I. *Optical Processes in Semiconductors*. Dover: New York, **1971**.

(44) Fan, H. Y. Infra-Red Absorption in Semiconductors. *Rep. Prog. Phys.* **1956**, 19, 107.

(45) Kishimoto, K.; Koyanagi, T. Preparation of Sintered Degenerate *n*-Type PbTe with a Small Grain Size and Its Thermoelectric Properties. *J. Appl. Phys.* **2002**, 92, 2544-2549.

(46) Sootsman, J. R.; Kong, H.; Uher, C.; D'Angelo, J. J.; Wu, C.-I.; Hogan, T. P.; Caillat, T.; Kanatzidis, M. G. Large Enhancements in the Thermoelectric Power Factor of Bulk PbTe at High Temperature by Synergistic Nanostructuring. *Angew. Chem. Int. Edit.* **2008**, 47, 8618-8622.

(47) Heremans, J. P.; Thrush, C. M.; Morelli, D. T. Thermopower Enhancement in Lead Telluride Nanostructures. *Phys. Rev. B* **2004**, 70, 115334.

(48) Lukyanova, L. N.; Yu, A. B.; Danilov, V. A.; Usov, O. A.; Volkov, M. P.; Kutasov, V. A. Thermoelectric and Galvanomagnetic Properties of Bismuth Chalcogenide Nanostructured Heteroepitaxial Films. *Semicond. Sci. Tech.* **2015**, 30, 015011.

(49) Wang, S.; Yang, J.; Toll, T.; Yang, J.; Zhang, W.; Tang, X. Conductivity-Limiting Bipolar Thermal Conductivity in Semiconductors. *Sci. Rep.* **2015**, 5, 10136.

(50) Greenaway, D. L.; Harbeke, G. Band Structure of Bismuth Telluride, Bismuth Selenide and Their Respective Alloys. *J. Phys. Chem. Solids* **1965**, 26, 1585-1604.

(51) Veis, A. N.; Luk'yanova, L. N.; Kutasov, V. A. Band Gap and Type of Optical Transitions at the Interband Absorption Edge in Solid Solutions Based on Bismuth Telluride. *Phys. Solid State* **2012**, 54, 2182-2188.

(52) Gibbs, Z. M.; Kim, H.-S.; Wang, H.; Snyder, G. J. Band Gap Estimation from Temperature Dependent Seebeck Measurement—Deviations from the $2e|S|_{max}T_{max}$ Relation. *Appl. Phys. Lett.* **2015**, 106, 022112.

(53) Mills, K. C. *Thermodynamic Data for Inorganic Sulphides, Selenides and Tellurides*. Butterworths: London, **1974**.

(54) Borup, K. A.; Toberer, E. S.; Zoltan, L. D.; Nakatsukasa, G.; Errico, M.; Fleurial, J.-P.; Iversen, B. B.; Snyder, G. J. Measurement of the Electrical Resistivity and Hall Coefficient at High Temperatures. *Rev. Sci. Instrum.* **2012**, 83, 123902.

(55) Philips-Invernizzi, B.; Dupont, D.; Caze´, C. Bibliographical Review for Reflectance of Diffusing Media. *Opt. Eng.* **2001**, 40, 1082-1092.

Supporting Information

n-Type $Bi_2Te_{3-x}Se_x$ Nanoplates with Enhanced Thermoelectric Efficiency Driven by Wide-Frequency Phonon Scatterings and Synergistic Carrier Scatterings

Min Hong,[†] Thomas C. Chasapis,[‡,§] Zhi-Gang Chen,[*,†] Lei Yang,[†] Mercouri G. Kanatzidis,[§] G. Jeffrey Snyder[*,‡] and Jin Zou[*,†,||]

[†]Materials Engineering, University of Queensland, Brisbane, QLD 4072, Australia
[‡]Department of Materials Science and Engineering, Northwestern University, Evanston, Illinois 60208, USA

[§]Department of Chemistry, Northwestern University, Evanston, Illinois 60208, USA

[||]Centre for Microscopy and Microanalysis, University of Queensland, Brisbane, QLD 4072, Australia

E-mail: j.zou@uq.edu.au, z.chen1@uq.edu.au, and jeff.snyder@northwestern.edu

1. Determination of Lattice Parameters

It is well known that the relationship between the lattice spacing of the atomic planes (d_{hkil}) and its lattice parameters (*a* and *c*) for rhombohedral structure can be calculated by[1]

$$\frac{1}{d_{hkl}^2} = \frac{4}{3}\left(\frac{h^2 + hk + k^2}{a^2}\right) + \frac{l^2}{c^2}, \qquad \text{(S1)}$$

where *hkil* are the index of the {*hkil*} atomic planes. Since d_{hkil} can be measured from XRD patterns, different *a* and *c* can be determined for different $Bi_2Te_{3-x}Se_x$ samples. By using the changes of $000\underline{15}^*$ and $01\bar{1}5^*$ in their 2θ, the corresponding *c* and *a* can be

determined. Figure S1 shows the determined *a* and *c* as a function of the Se content, in which the measured variation of lattice parameters follow the Vegard's law.

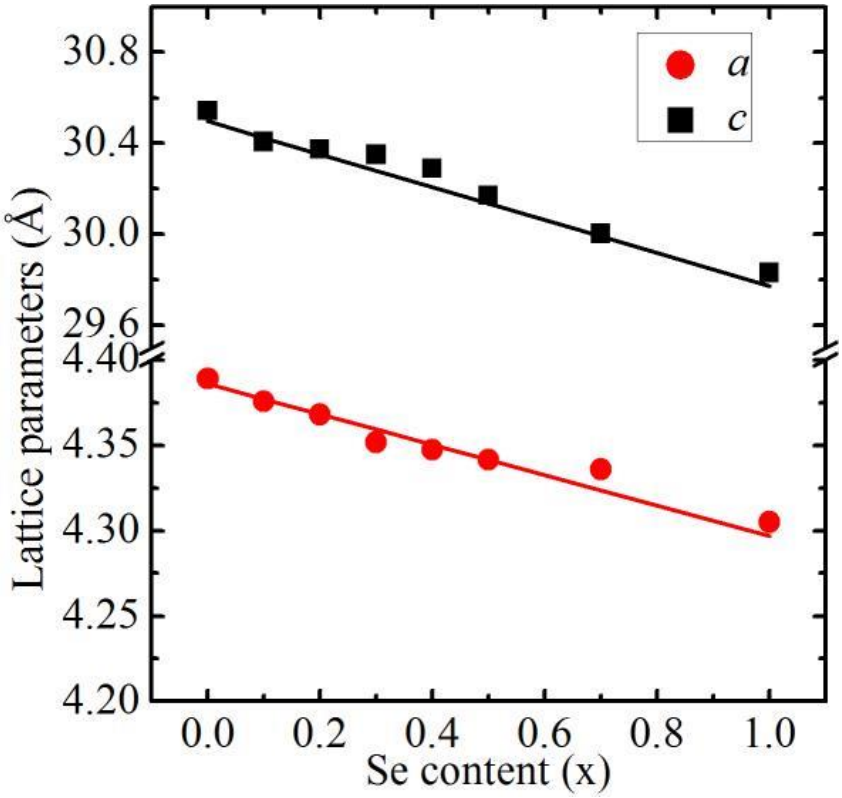

Figure S1 Determined lattice parameters as a function of the Se content for different as-prepared $Bi_2Te_{3-x}Se_x$ nanoplates.

2. Chemical Composition Determination Using EDS

The chemical compositions of different as-synthesized $Bi_2Te_{3-x}Se_x$ nanoplates were determined by EDS (equipped in TEM). Figure S2 shows the EDS profiles corresponding to different x, in which the variations of the Bi, Te, and Se peaks can be seen for samples with $0 < x \leq 1$ (note that the Cu peaks are originated from the Cu TEM grids). Detailed quantitative analysis indicates that elemental ratios of Bi, Te, and Se are close to the nominal compositions.

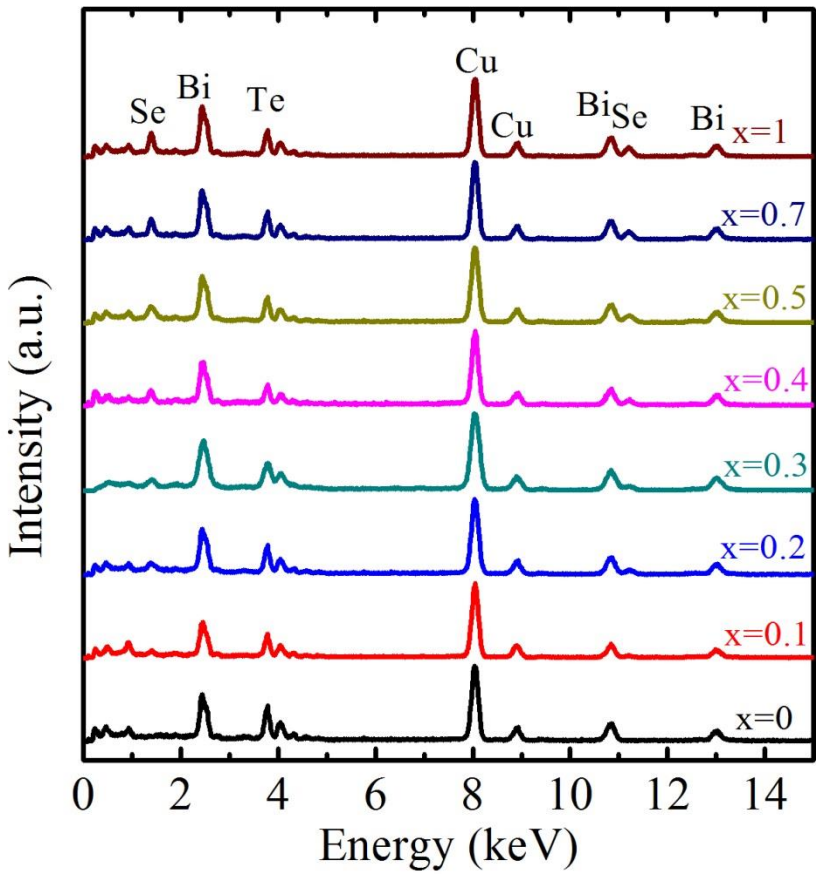

Figure S2 EDS profiles of as-synthesized $Bi_2Te_{3-x}Se_x$ nanostructures.

3. SEM Characterization of $Bi_2Te_{2.7}Se_{0.3}$ Nanostructures Prepared with and without PVP

Figure S3a and b are SEM images of $Bi_2Te_{2.7}Se_{0.3}$ nanoplates synthesized without surfactant and with poly(N-vinyl-2-pyrrolidone) (PVP, M_w=40,000) serving as the surfactant, respectively. As can be seen, the $Bi_2Te_{2.7}Se_{0.3}$ nanoplates synthesized with PVP is more uniform, and their edges and corners are clearer, compared with the nanoplates synthesized without PVP. The thicknesses of the two kinds of nanoplates are nearly identical (~ 30nm).

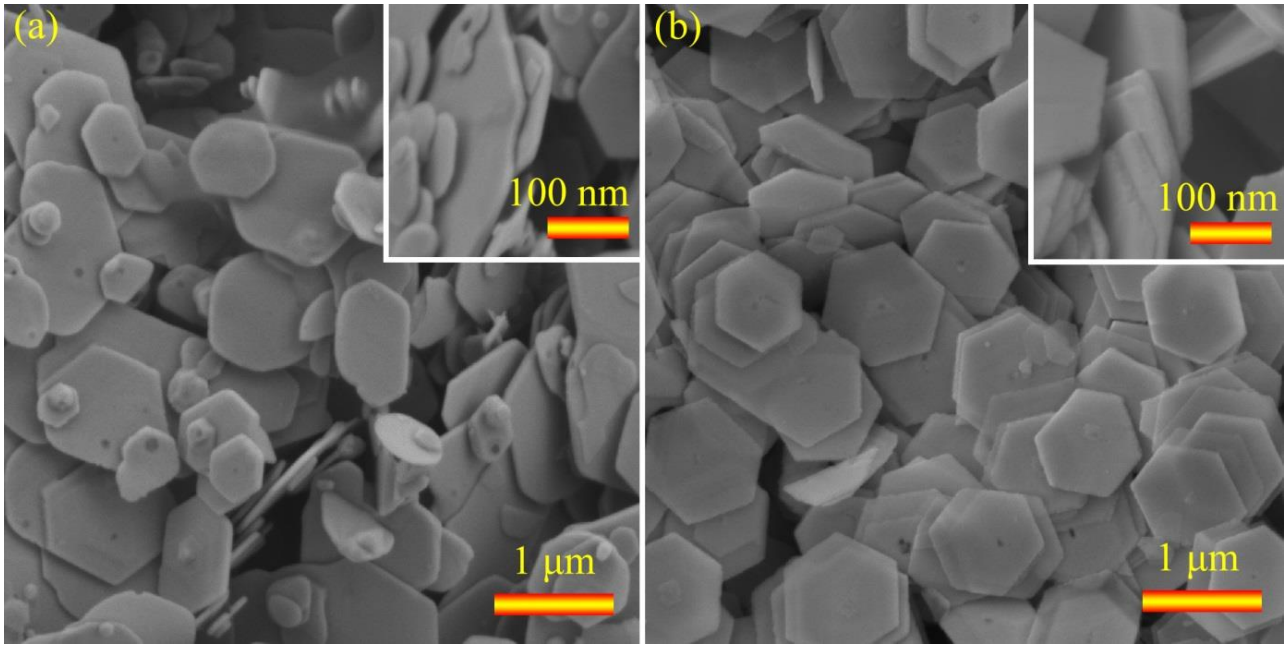

Figure S3 SEM images of $Bi_2Te_{2.7}Se_{0.3}$ nanoplates prepared (a) without and (b) with PVP. The insets show the thicknesses of the nanoplates

4. Size Distribution of as-Synthesized $Bi_2Te_{3-x}Se_x$ Nanoplates

To examine the size distribution of as-synthesized $Bi_2Te_{3-x}Se_x$ nanoplates, SEM characterization was employed. Figure S4 summarizes SEM images of as-synthesized nanoplates. Based on this, lateral size distributions were obtained and shown in Figure S5, from which the majority size of nanoplates for all compositions is in the range of ~1 µm.

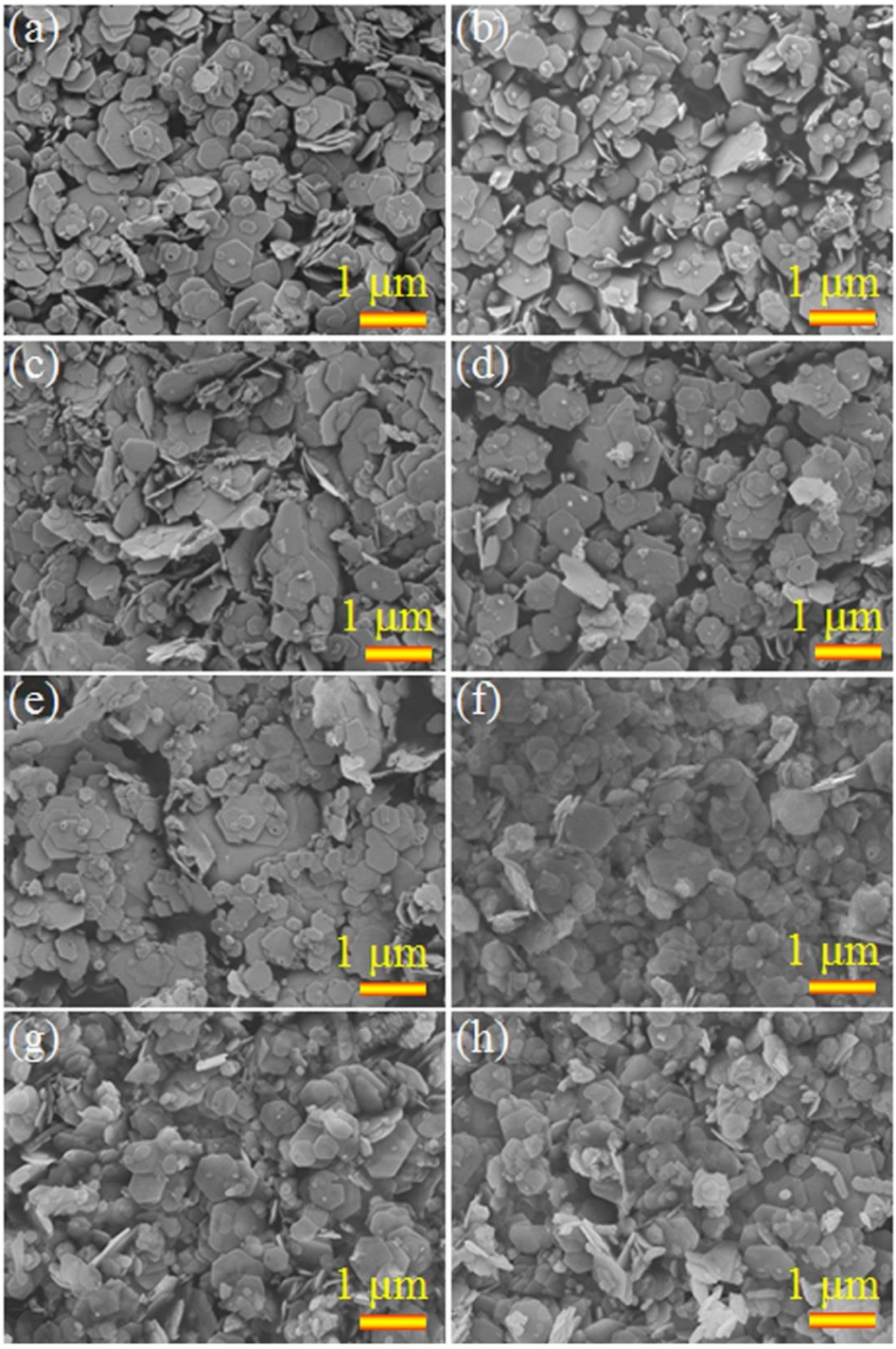

Figure S4 SEM images of $Bi_2Te_{3-x}Se_x$ nanoplates: (a) x = 0, (b) x = 0.1, (c) x = 0.2, (d) x = 0.3, (e) x = 0.4, (f) x = 0.5, (g) x = 0.7, and (h) x = 1.

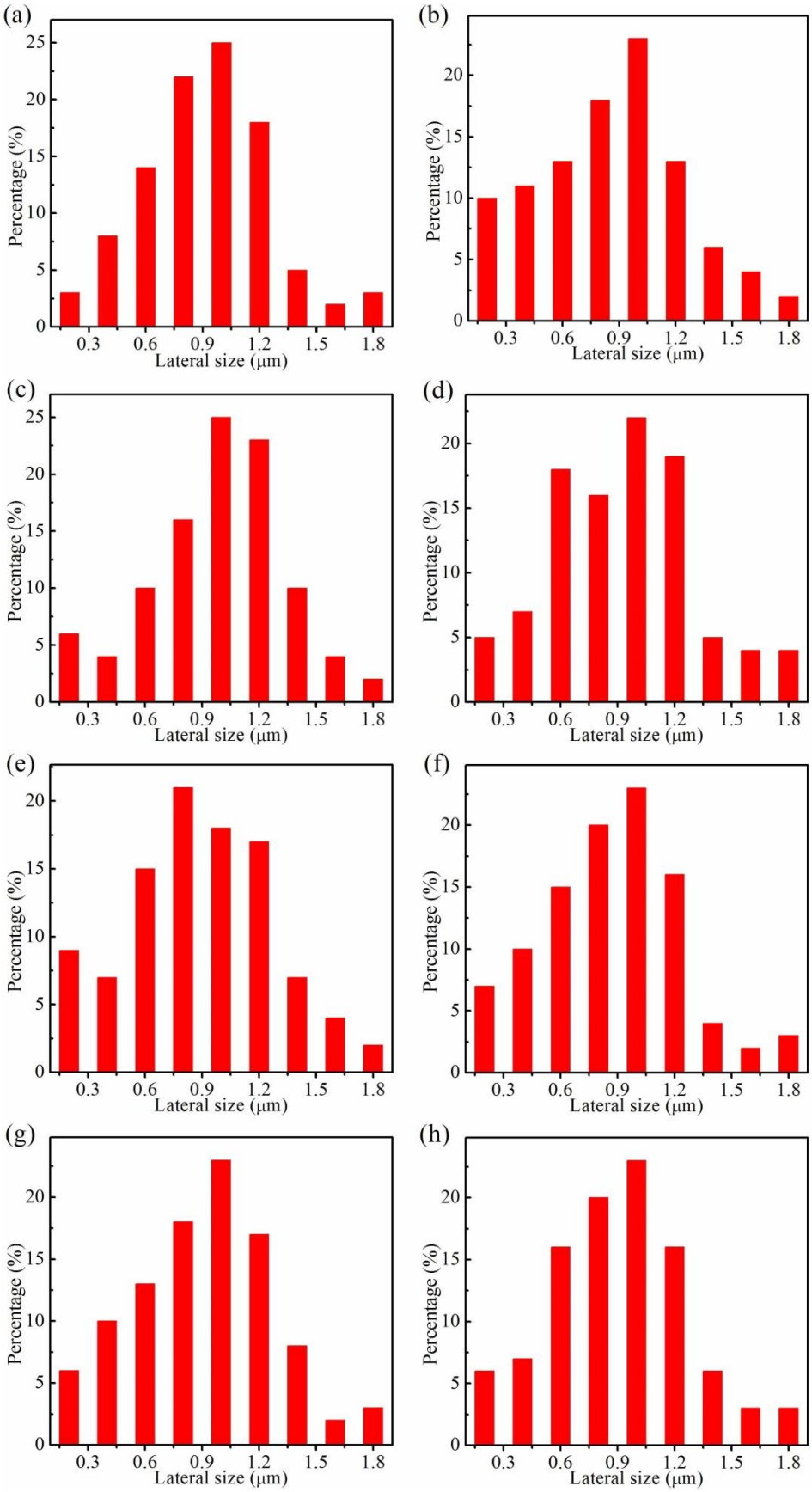

Figure S5 Statistical lateral size distributions of $Bi_2Te_{3-x}Se_x$ nanoplates: (a) x = 0, (b) x = 0.1, (c) x = 0.2, (d) x = 0.3, (e) x = 0.4, (f) x = 0.5, (g) x = 0.7, and (h) x = 1.

5. XRD Patters of the Sintered Pellets and the Determination of Texture Fraction

Spark plasma sintering was used to prepare pellets for measuring their thermoelectric properties. Figure S6 shows XRD patterns taken from the pellets sintered from $Bi_2Te_{3-x}Se_x$ nanoplates with different Se contents. As can be seen, there is no impurity in all sintered samples.

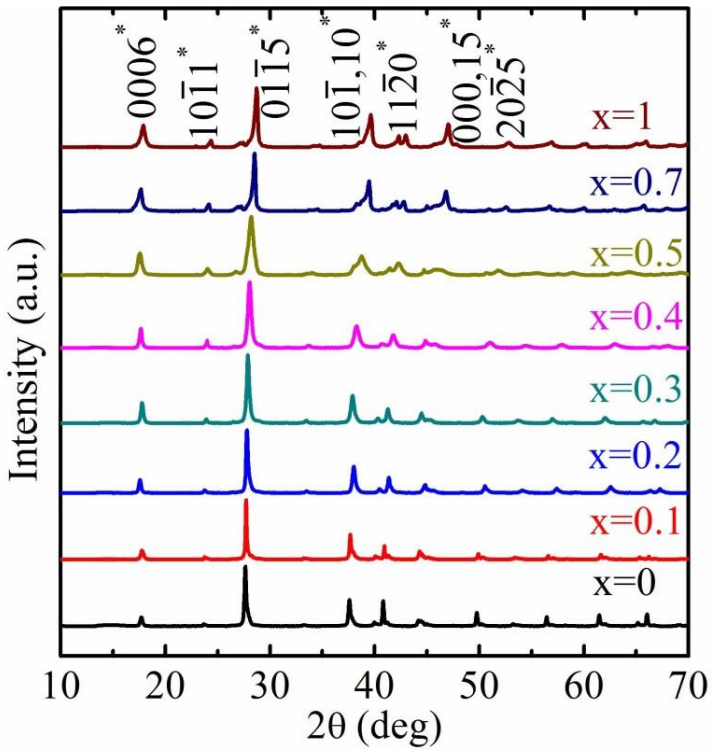

Figure S6 XRD patterns taken from pellets sintered from different $Bi_2Te_{3-x}Se_x$ nanostructures.

In fact, from XRD patterns of these pellets, their texture fraction (f_{hkil}) can be determined. In this study, f_{000l} (using the {000*l*} planes) is estimated by the Lotgering method:[2]

$$f_{000l} = \frac{P_{000l} - P_0}{1 - P_0} \quad , \tag{S2}$$

with

$$P_{000l} = \frac{\sum I_{000l}}{\sum I_{hkil}} \quad , \tag{S3}$$

and

$$P_0 = \frac{\sum I^0_{000l}}{\sum I^0_{hkil}} \quad , \tag{S4}$$

where I_{hkil} and I^{0}_{hkil} are the intensities of *hkil** diffraction peaks for our pellets and the standard values obtained from the PDF card (JCPDS No. 89-2009). Table S1 summarizes the determined texture fraction.

Table S1 Texture fractions determined using the *000l** reflections for $Bi_2Te_{3-x}Se_x$ nanoplates and corresponding pellets.

x	0	0.1	0.2	0.3	0.4	0.5	0.7	1
Nanoplates	0.04	0.05	0.03	0.06	0.05	0.08	0.11	0.10
Pellets	0.03	0.06	0.07	0.04	0.08	0.07	0.11	0.11

6. Thermoelectric performance evaluation

To clarify the anisotropic behavior of the pellet sintered from $Bi_2Te_{2.7}Se_{0.3}$ nanoplates, thermoelectric properties were measured along in-plane and out-of-plane directions, respectively. Figure S7 shows the measurement results, in which S, σ and κ are almost identical along the two directions, indicating an isotropic nature of thermoelectric properties in our pellets, which agrees with the obtained small f_{000l} (refer to Table S1). Since f_{000l} for Bi_2Te_2Se is the largest, we also measured the thermoelectric properties for this composition along two directions, as shown in Figure S8. As can be seen, the anisotropy for Bi_2Te_2Se is slightly higher than that for $Bi_2Te_{2.7}Se_{0.3}$.

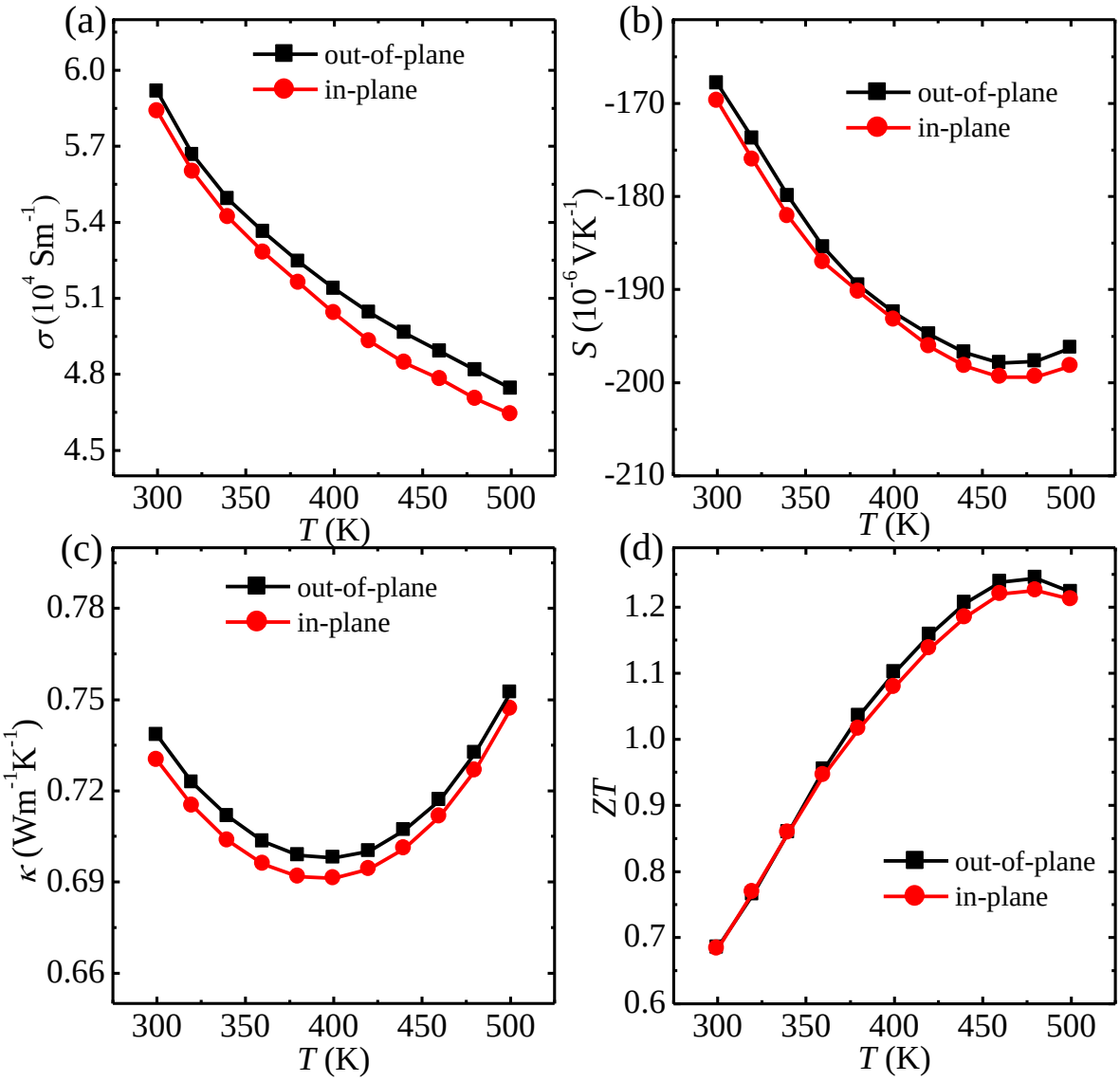

Figure S7 In-plane and out-of-plane thermoelectric characteristics of the sintered $Bi_2Te_{2.7}Se_{0.3}$ pellet: (a) σ, (b) S, (c) κ, and (d) ZT; all as a function of temperature.

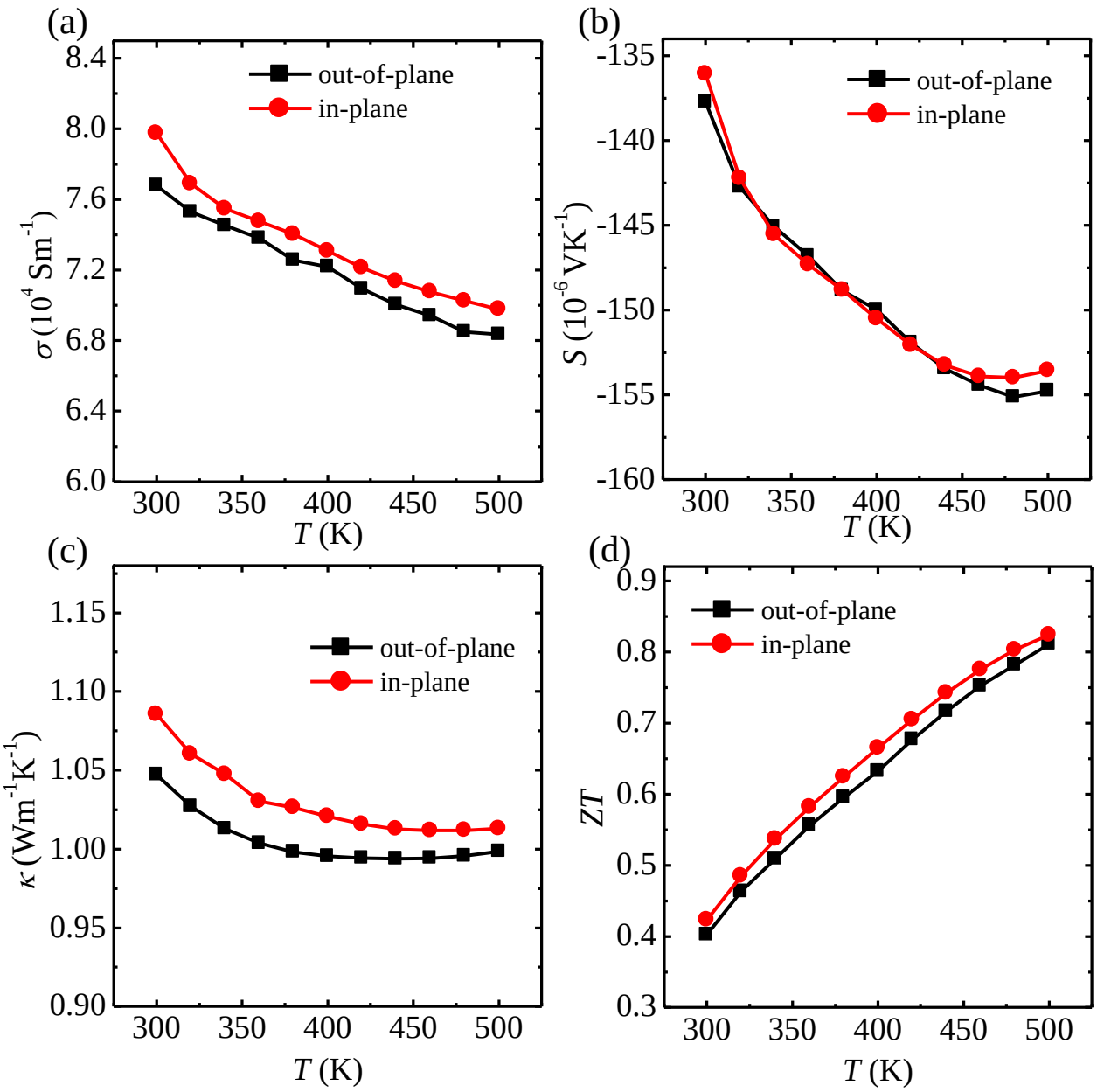

Figure S8 In-plane and out-of-plane thermoelectric characteristics of the sintered Bi_2Te_2Se pellet: (a) σ, (b) S, (c) κ, and (d) ZT; all as a function of temperature.

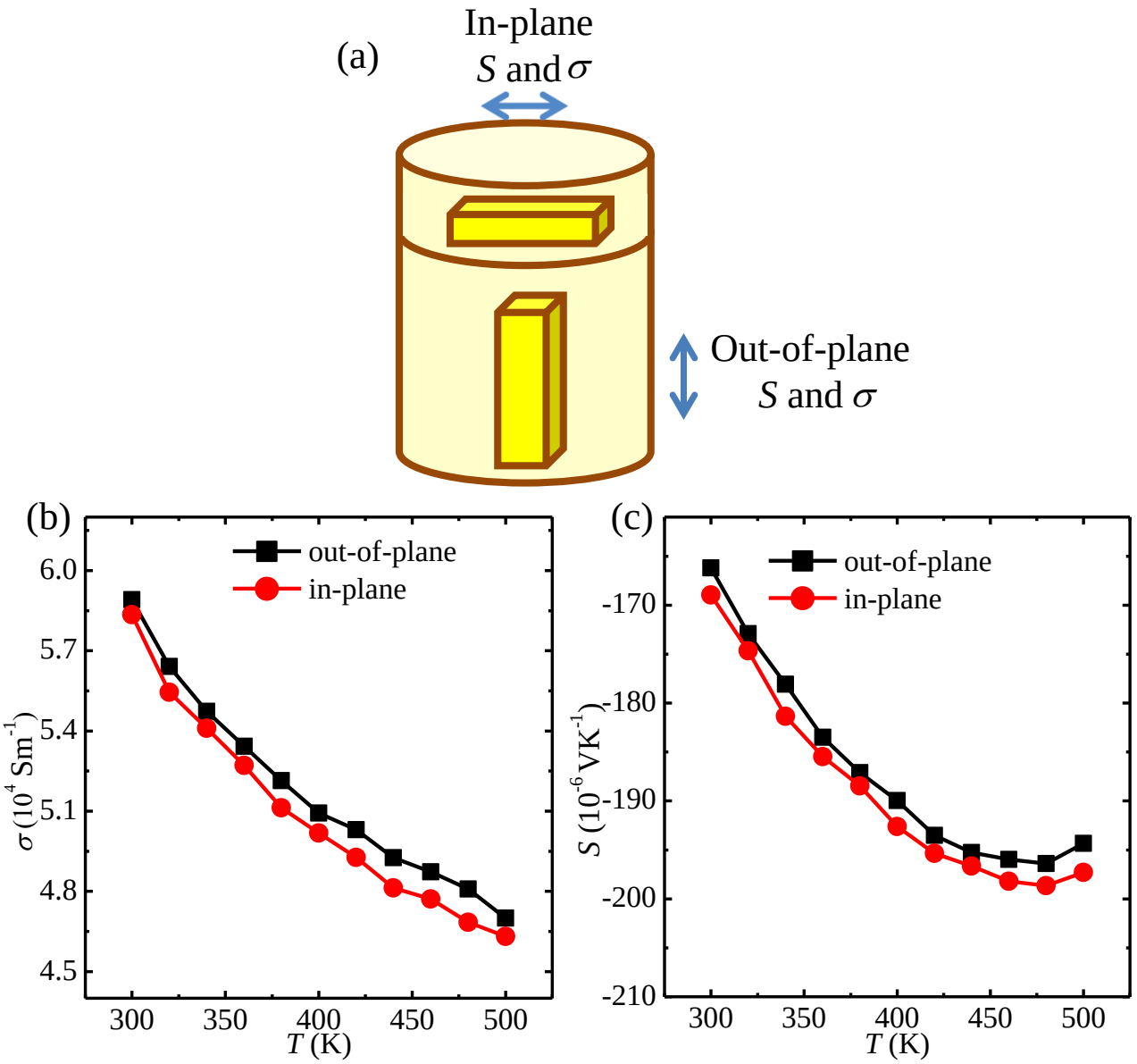

Figure S9 (a) Schematic illustrating the processing method of sintered pellet for measuring the in-plane and the out-of-plane *S* and *σ*. (b) and (c) The measured in-plane and out-of-plane *S* and *σ*, respectively.

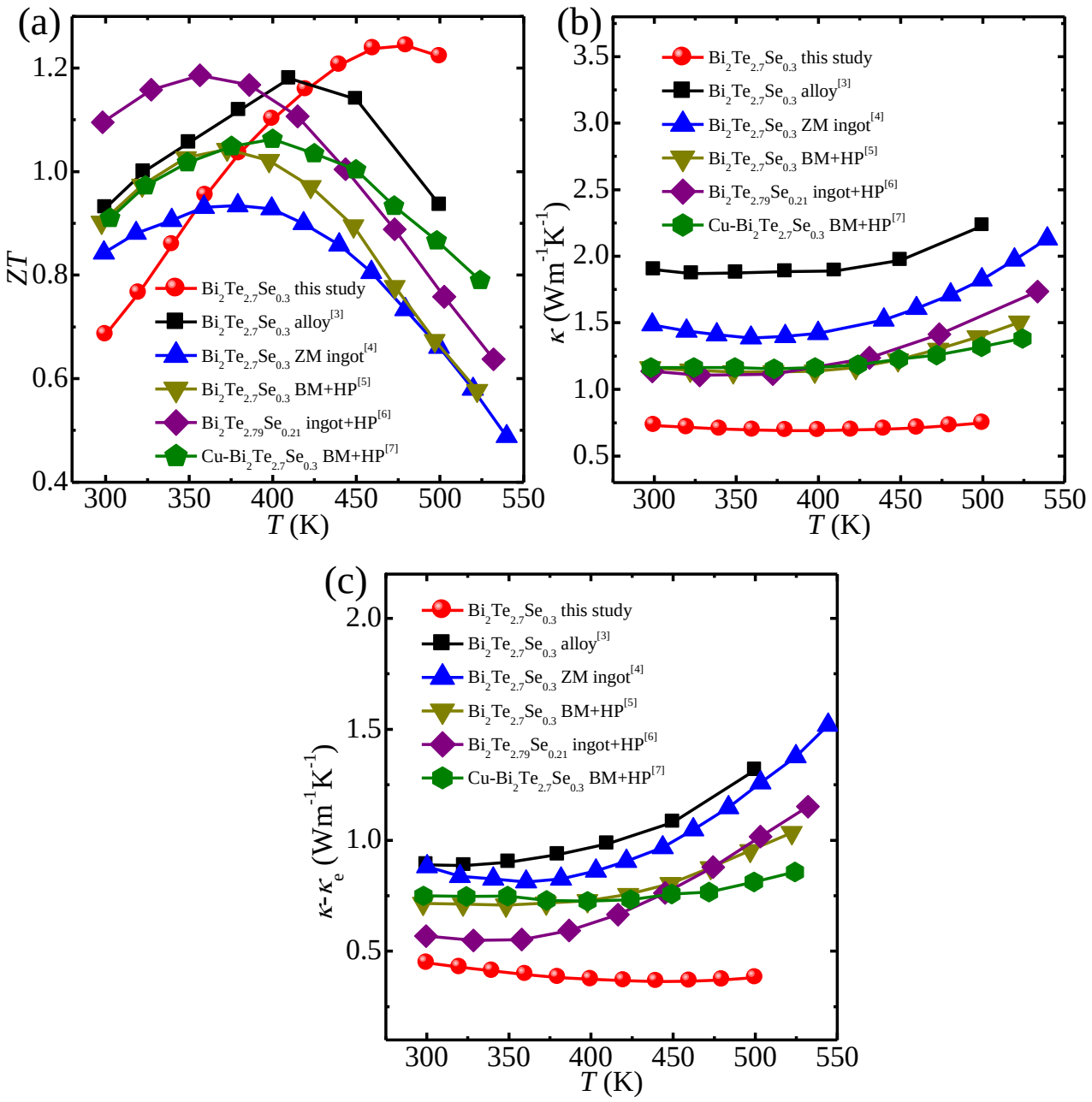

Figure S10 The temperature dependent (a) *ZT*, (b) κ, and (c) κ - κ_e of *n*-type $Bi_2Te_{2.7}Se_{0.3}$ for this study compared with $Bi_2Te_{2.7}Se_{0.3}$ alloy Bridgman-Stockbarger method,[3] $Bi_2Te_{2.7}Se_{0.3}$ zone melting (ZM) ingot,[4] $Bi_2Te_{2.7}Se_{0.3}$ ball milling (BM) plus two-step dc-hot pressing (HP),[5] $Bi_2Te_{2.79}Se_{0.21}$ ingot with two-step hot pressing,[6] and Cu-$Bi_2Te_{2.7}Se_{0.3}$ ball milling plus dc-hot pressing.[7]

7. Calculation of Electronic Thermal Conductivity

According to the Wiedemann-Franz law,[8] κ_e can be expressed as

$$\kappa_e = L\sigma T \ , \tag{S5}$$

where L is the Lorenz number. Employing the single parabolic band model, L can be determined by

$$L = \left(\frac{k_B}{e}\right)^2 \left[\frac{3F_2(\eta)}{F_0(\eta)} - \left(\frac{2F_1(\eta)}{F_0(\eta)}\right)^2\right] , \tag{S6}$$

with

$$F_x = \int_0^\infty \frac{\varepsilon^x}{1+\exp(\varepsilon-\eta)^x} d\varepsilon , \tag{S7}$$

in which e is free electron charge, k_B is the Boltzmann constant, and η is the reduced Fermi level. The determination of η is based on the measured S, which is expressed as[9]

$$S = \frac{k_B}{e}\left[\frac{2F_1(\eta)}{F_0(\eta)} - \eta\right] . \tag{S8}$$

From Equation (S8), S varies only with η. Our previous study has revealed the monotonic relation between S and η.[10] Therefore, based on the measured S, we can determine the corresponding η, shown in Figure S11a. Based on Equation (S6) with the determined η, L can be determined, and their values are shown in Figure S11b. By substituting the determined L and measured σ over the entire studied temperature into Equation (S5), κ_e can be calculated, which are shown in Figure S11c.

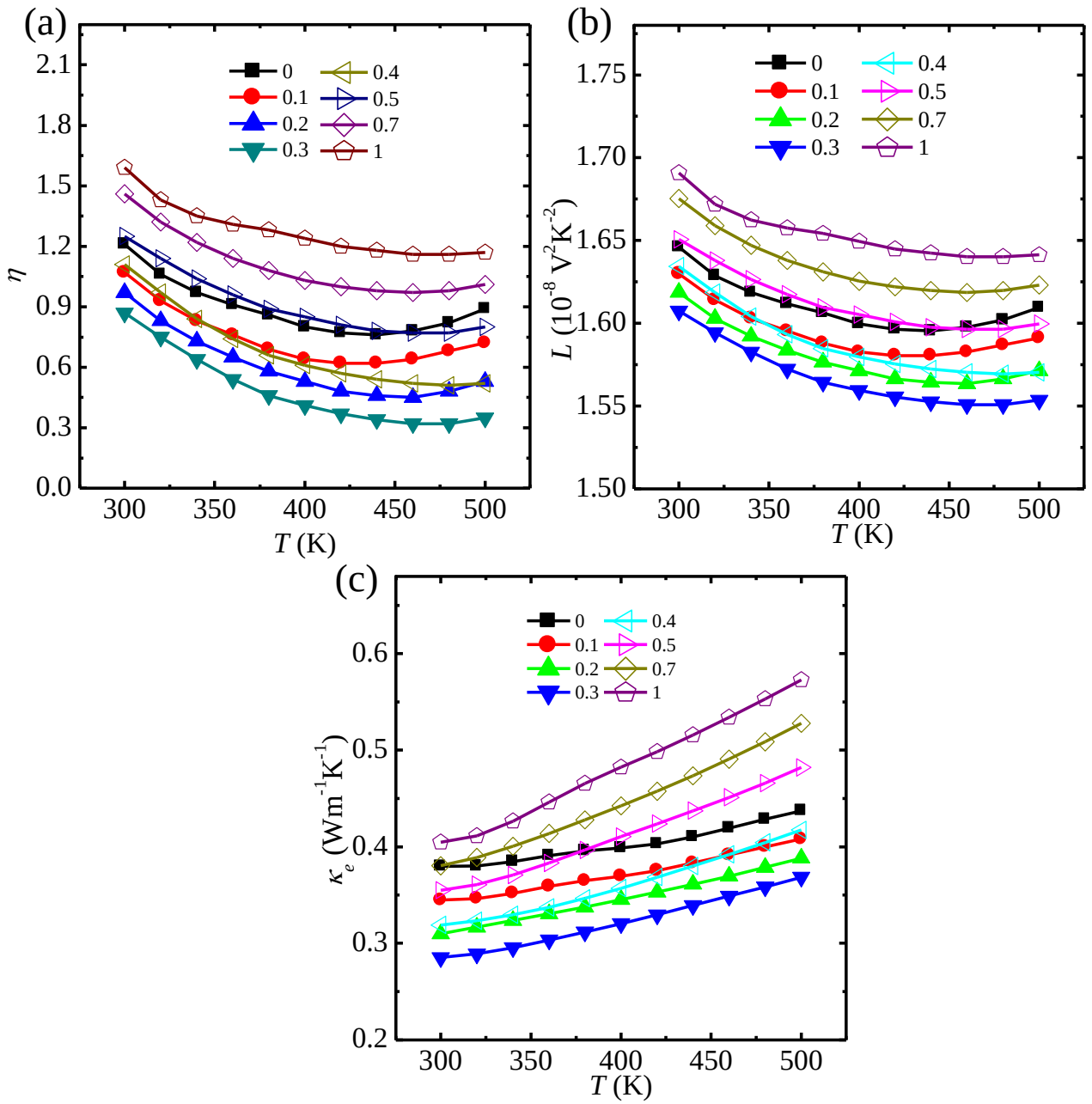

Figure S11 Composition dependent (a) η, (b) L, and (c) κ_e as a function of temperature.

8. SEM Characterization of Sintered Pellets

SEM was employed to understand the grain size distributions of sintered $Bi_2Te_{3-x}Se_x$ pellets, and results are shown in Figure S12. As can be seen, the grain size is in the range of ~ 1 μm, suggesting that SPS sintering did not cause notable crystal growth.

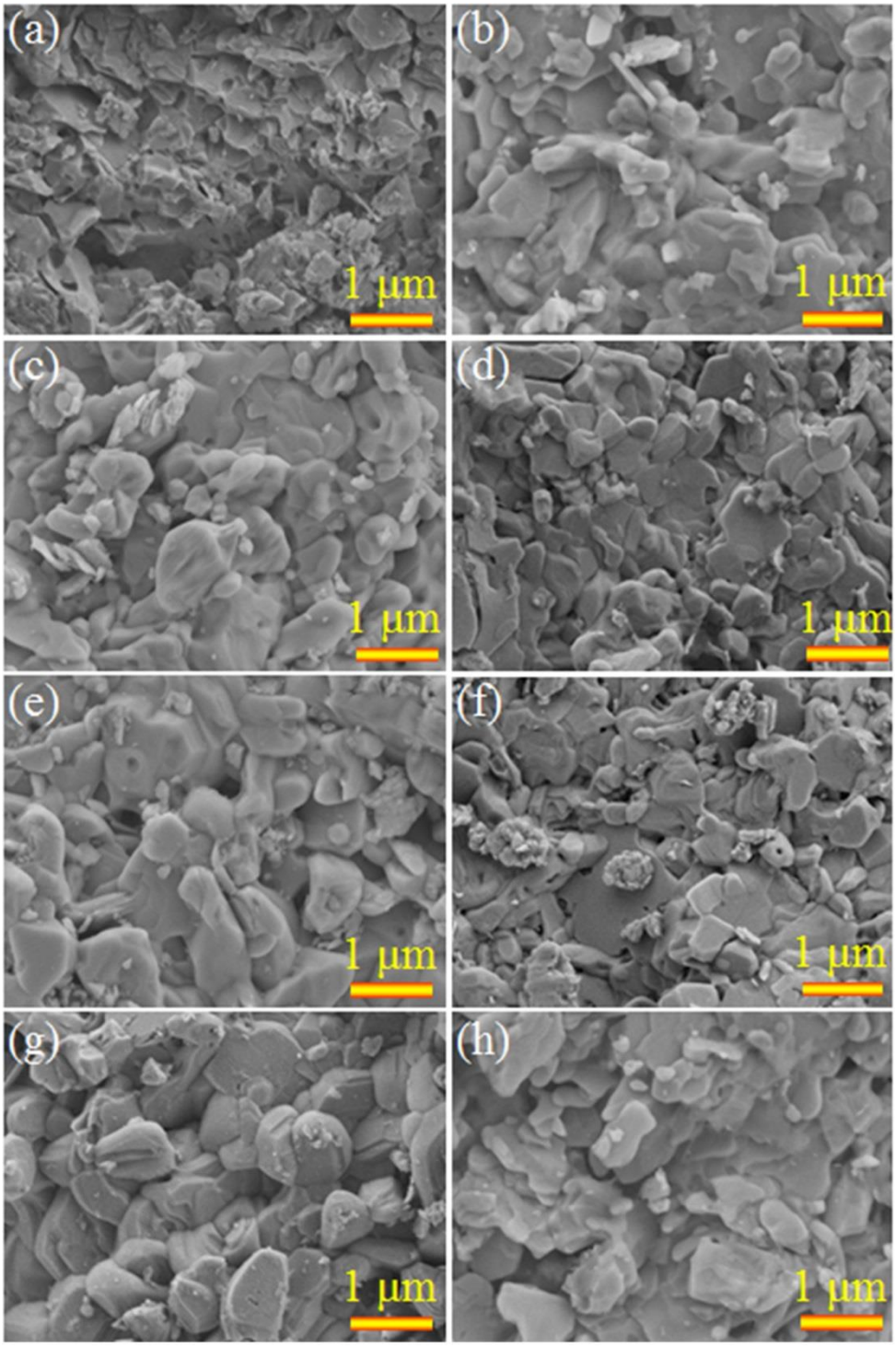

Figure S12 SEM images of sintered pellets made of $Bi_2Te_{3-x}Se_x$: (a) x = 0, (b) x = 0.1, (c) x = 0.2, (d) x = 0.3, (e) x = 0.4, (f) x = 0.5, (g) x = 0.7, and (h) x = 1.

9. Out-of-plane EBSD Image and the Grain Size Distribution

To further confirm the random orietation feature, we provided another EBSD image along the out-of-plane direction, shown in Figure S13a. By taking into account both in-plane and out-of-plane EBSD images, we obtained the statistical grain size distribution of $Bi_2Te_{2.7}Se_{0.3}$, shown in Figure S13b. As can be seen, the average grain size is ~800 nm.

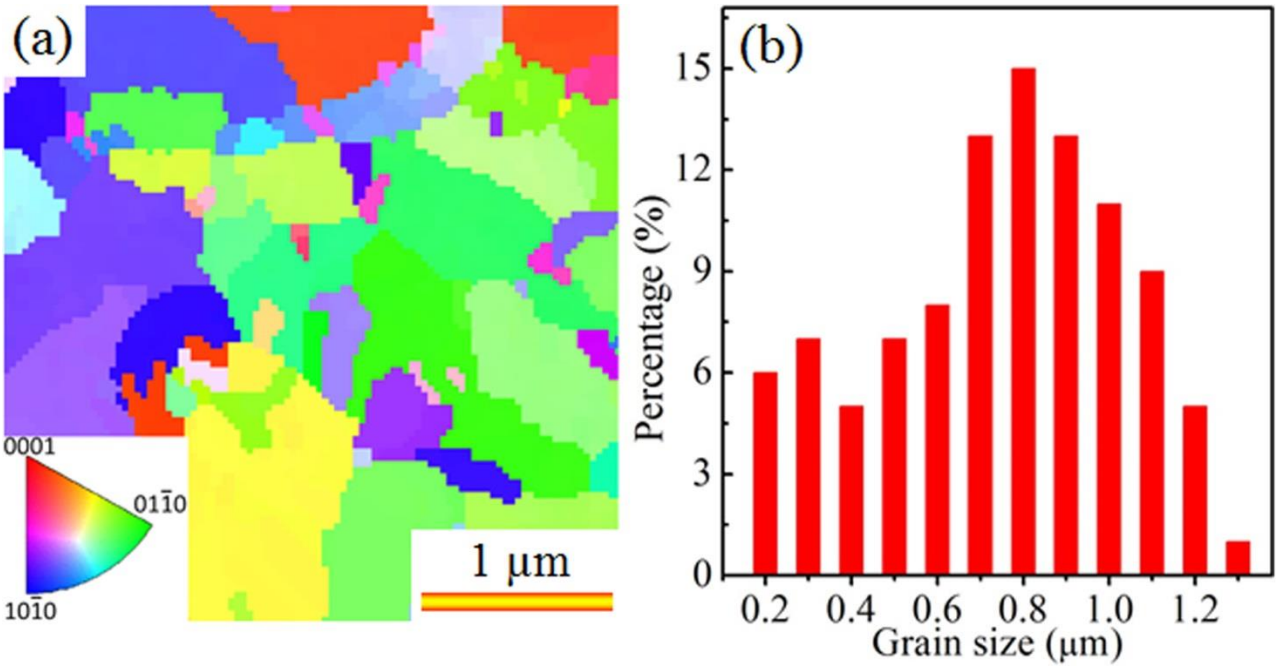

Figure S13 (a) EBSD image of $Bi_2Te_{2.7}Se_{0.3}$ along the out-of-plane direction. (b) Statistical grain size distribution of $Bi_2Te_{2.7}Se_{0.3}$ by taking into account both the in-plane (refer to Figure 5a of Main Manuscript) and out-of-plane EBSD images.

10. Calculation of Lattice Thermal Conductivity

According to the Debye-Callaway model,[11,12] κ_l can be calculated by

$$\kappa_l = \frac{k_B}{2\pi^2 \upsilon}\left(\frac{k_B T}{\hbar}\right)^3 \int_0^{\frac{\theta_D}{T}} \tau_{tot} \frac{z^4 \exp(z)}{\left[\exp(z)-1\right]^2} dz \tag{S9}$$

The integrand item in conjunction with the coefficient of Equation (S9) is the spectral lattice thermal conductivity (κ_s),[13] namely

$$\kappa_s = \frac{k_B}{2\pi^2 \upsilon}\left(\frac{k_B T}{\hbar}\right)^3 \tau_{tot} \frac{z^4 \exp(z)}{\left[\exp(z)-1\right]^2} \tag{S10}$$

In the above equations, $z = \frac{\hbar\omega}{k_B T}$ (with ω denoting the phonon frequency) is the reduced phonon frequency, $\hbar$ is the reduced Plank constant, θ_D is the Debye temperature, $\upsilon = \left[\frac{1}{3}\left(\frac{1}{\upsilon_L^3} + \frac{2}{\upsilon_T^3}\right)\right]^{-1/3}$ (with υ_L and υ_T respectively denoting the longitudinal and transverse sound velocities) is the sound velocity, and τ_{tot} is the total relaxation time. The phonon scattering pathways generally include phonon-phonon Umklapp (U), electron-phonon (E), point defects (PD), and grain boundaries (B).[13,14] The relevant phonon relaxation times are given by

Umklapp phonon scattering

$$\tau_U^{-1} = \frac{\hbar\gamma^2\omega^2 T}{\bar{M}\upsilon^2\theta_D}\exp\left(-\frac{\theta_D}{3T}\right), \tag{S11}$$

Electron phonon scattering

$$\tau_E^{-1} = \frac{E_{def}^2 m^* \omega^2}{2\pi\hbar^3\rho\upsilon_{\|}}, \tag{S12}$$

Point defect phonon scattering

$$\tau_{PD}^{-1} = \frac{\bar{V}\omega^4}{4\pi\upsilon^3}\Gamma \text{ , and} \tag{S13}$$

Grain boundary phonon scattering

$$\tau_B^{-1} = \frac{\upsilon}{d}, \tag{S14}$$

where γ is the Grüneisen parameter, $\bar{M}$ is the average mass, E_{def} is the acoustic phonon deformation potential, m^* is the effective mass of charger carrier ($m^* = 1.2m_0$ with m_0 representing the free electron mass),[4] ρ is the sample density, $\bar{V}$ is the average atomic volume, Γ is the point defect scattering parameter, and d is the grain size, respectively.

For a material with dislocations, the scattering caused by the dislocations (D) should be considered, which includes dislocation core (DC) and dislocation strain (DS).[15] Relaxation time of dislocation scattering can be considered as

dislocation core phonon scattering

$$\tau_{DC}^{-1} = N_D \frac{\bar{V}^{4/3}}{\upsilon^2}\omega^3 \text{ , and} \tag{S15}$$

dislocation strain phonon scattering

$$\tau_{DS}^{-1} = 0.6B_D^2 N_D \left(\gamma + \Delta\gamma\right)^2 \omega \left\{\frac{1}{2} + \frac{1}{24}\left(\frac{1-2r}{1-r}\right)^2 \left[1 + \sqrt{2}\left(\frac{\upsilon_{\parallel}}{\upsilon_{\perp}}\right)\right]^2\right\} , \tag{S16}$$

where N_D is the dislocation density, B_D is the effective Burger's vector, r is the Poisson's ratio and $\Delta\gamma$ is the change in γ due to the dislocation strain, as given by

$$\Delta\gamma = \frac{V_{BT}c_0 K}{k_B T_a}\left(\gamma\alpha^2 - \alpha\beta\right) , \tag{S17}$$

with

$$\alpha = \frac{V_{BS} - V_{BT}}{V_{BT}} \text{ , and} \tag{S18}$$

$$\beta = \frac{M_{BT} - M_{BS}}{2M_{BT}} , \tag{S19}$$

where c_0 is the concentration of Bi_2Se_3 in $Bi_2Te_{3-x}Se_x$, K is the bulk modulus of Bi_2Te_3, T_a is the sample sintering temperature, V_{BS} and V_{BT} are the atomic volume of Bi_2Se_3 and Bi_2Te_3, and M_{BS} and M_{BT} are the atomic mass of Bi_2Se_3 and Bi_2Te_3.

According to the Matthiessen rule,[15] the total scattering relaxation time τ_{tot} can be given by U+E+PD+B mode

$$\tau_{tot}^{-1} = \tau_U^{-1} + \tau_E^{-1} + \tau_{PD}^{-1} + \tau_B^{-1} \text{ , and} \tag{S20}$$

U+E+PD+B+D model

$$\tau_{tot}^{-1} = \tau_U^{-1} + \tau_E^{-1} + \tau_{PD}^{-1} + \tau_B^{-1} + \tau_{DC}^{-1} + \tau_{DS}^{-1} \quad . \tag{S21}$$

By inputting physical parameters listed in Table S2 into above equations, κ_l can be calculated by models of U+E+PD+B and U+E+PD+B+D.

Table S2 Physical properties used to calculate κ_l based on various phonon scattering processes.

Parameters	Values
Debye temperature θ_D (K)	164[16]
Longitudinal sound velocity υ_L (ms^{-1})	2800[16]
Transverse sound velocity υ_T (ms^{-1})	1600[16]
Sound velocity υ (ms^{-1})	1778
Average atomic mass of Bi_2Te_3 M_{BT} (kg)	2.66×10^{-25}
Average atomic mass of Bi_2Se_3 M_{BS} (kg)	2.18×10^{-25}
Average atomic volume of Bi_2Te_3 V_{BT} (m^3)	3.48×10^{-29}
Average atomic volume of Bi_2Se_3 V_{BS} (m^3)	3.19×10^{-29}
Sample density ρ of Bi_2Te_3 (g cm^{-3})	7.6
Sample density ρ of $Bi_2Te_{2.7}Se_{0.3}$ (g cm^{-3})	7.1
Grain size d for $Bi_2Te_{2.7}Se_{0.3}$ (nm)	800 (Exp)
Point defect scattering parameter Γ	0.18 (fitted)
Dislocation density N_D of $Bi_2Te_{2.7}Se_{0.3}$ (cm^{-2})	1.7×10^{11} (Exp)
Magnititude of Burger's vector B_D of $Bi_2Te_{2.7}Se_{0.3}$ (Å)	12 (fitted)
Poisson's ratio r	0.4[17]
Grüneisen parameter γ	1.5[18]
Bulk modulus K (GPa)	37.4[16]

Table S3 Grain size (*d*) and point defect scattering parameter (Γ) for the reported ingot, reported ball milling and our nanostrucutred $Bi_2Te_{2.7}Se_{0.3}$.

	Ingot[4]	Ball milling[19]	Nanostructures
d (μm)	75 (fitted)	10 (fitted)	0.8 (Exp)
Γ	0.07 (fitted)	0.12 (fitted)	0.18 (fitted)

11. Hall Coefficient (R_H)

To determined Hall carrier concentration (n_H) and Hall carrier mobility (μ_H), we measured Hall coefficient R_H using the Van der Pauw method in a magnetic field up to ±2T.[20] Figure S14 plots the measured results, in which the negative sign of measured R_H suggests the *n*-type feature for our pellets, which is consistent with the conclusion made from measured *S*. For simplicity, we use the absolute value of measured R_H to calculated n_H and μ_H by[20]

$$n_H = \frac{1}{e|R_H|}, \text{ and} \tag{S22}$$

$$\mu_H = \sigma|R_H| \ . \tag{S23}$$

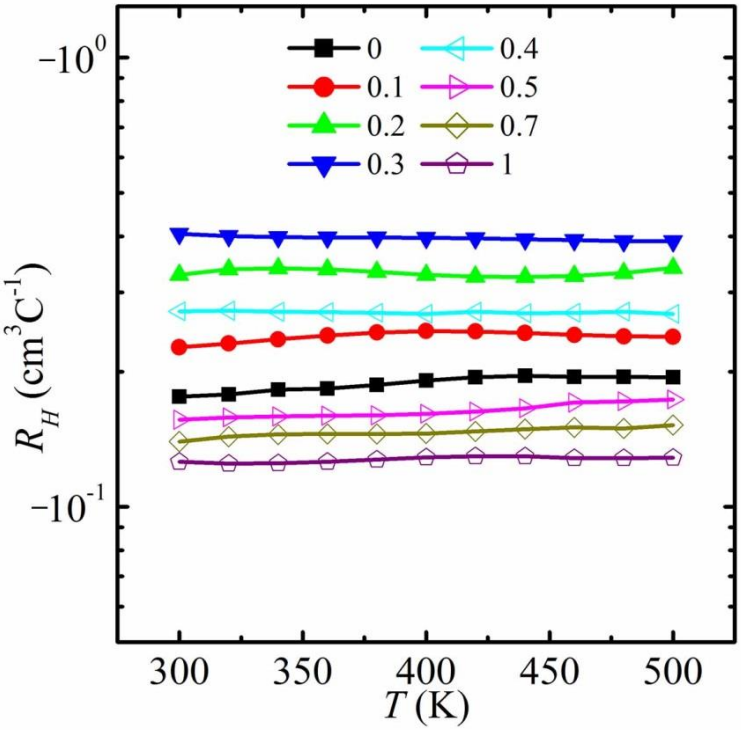

Figure S14 Measured Hall coefficient (R_H) for sintered $Bi_2Te_{3-x}Se_x$ pellets as a function of temperature.

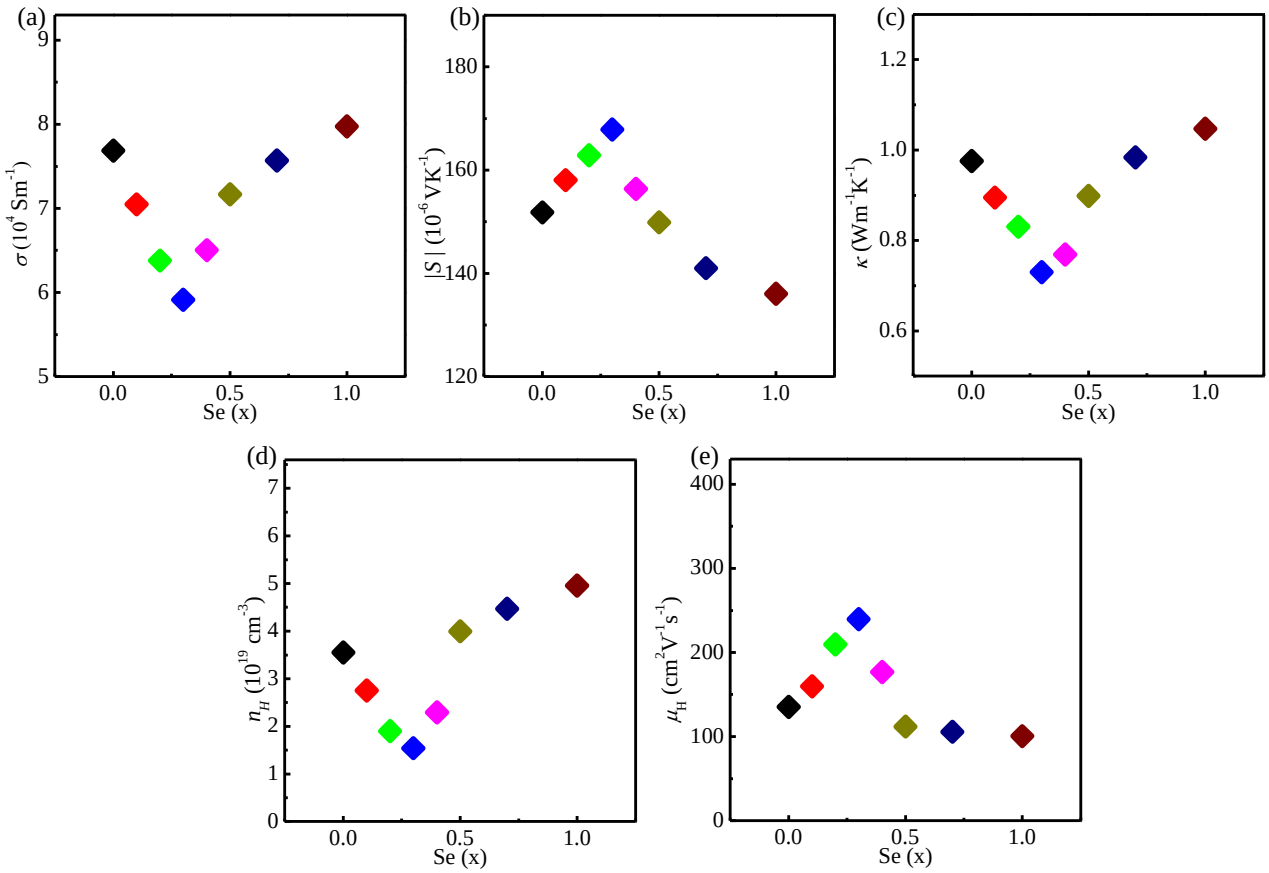

Figure S15 Se content dependent (a) σ, (b) S, (c) κ, (d) n_H, and (e) μ_H κ for our $Bi_2Te_{3-x}Se_x$ nanostructures at 300 K.

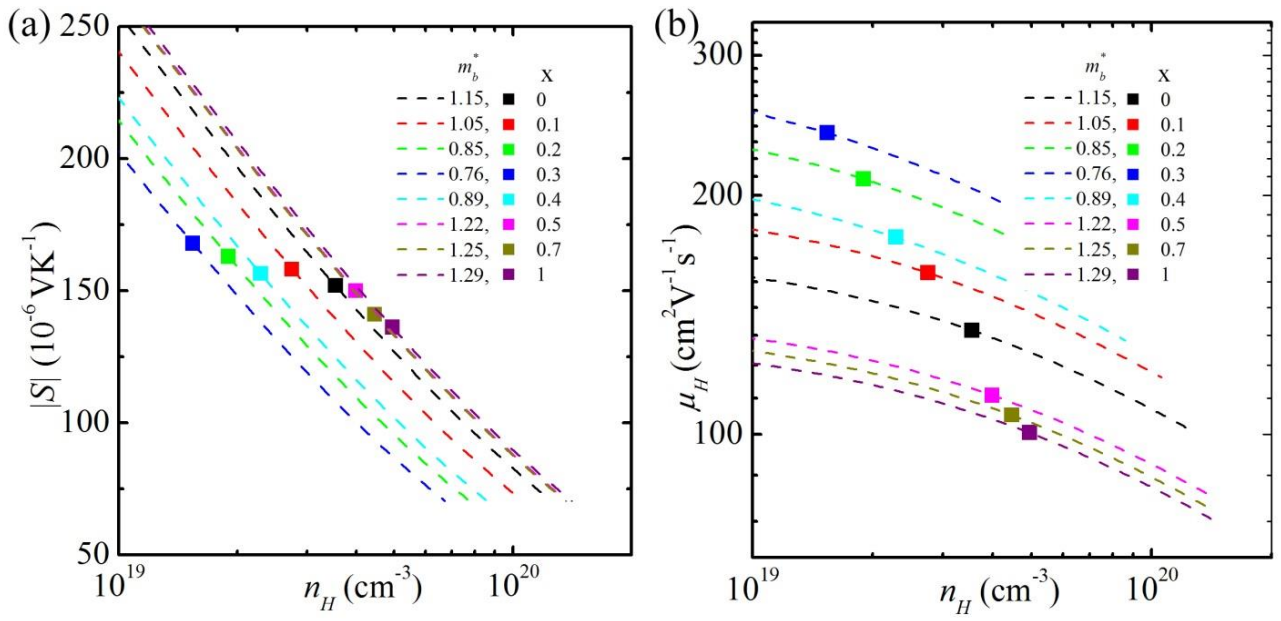

Figure S16 (a) Data points of |*S*| *versus* n_H compared with the theoratical curves of |*S*| as a function of n_H calculated with the corresponding m_b^* using single parabolic band model. (b) Data points of μ_H *versus* n_H compared with the theoretical curves of μ_H as a function of n_H calculated with the corresponding m_b^* using single parabolic band model.

12. Determination of the Carrier Scattering Mechanism and Energy Gaps

To determine the carrier scattering types and energy band gaps, we measured the optical properties of the $Bi_2Te_{3-x}Se_x$ nanoplates. Figure S17 shows the normalized absorption spectra of the $Bi_2Te_{3-x}Se_x$ nanoplates within in a small region (0.1-0.5 eV) of the phonon energy ($\hbar\omega$). For each sample, the onset of the interband absorption was found in the range of 0.2 – 0.3 eV.

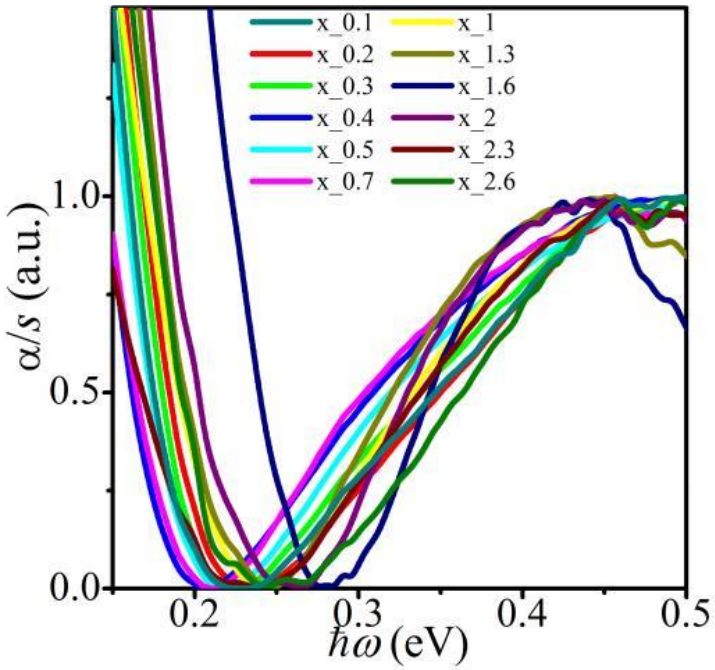

Figure S17 Normalized absorption spectra of $Bi_2Te_{3-x}Se_x$ nanoplates.

To determine the carrier scattering types, we need to examine the free carrier (FC) absorption tails. Figure S18 shows the absorption spectrum measured from the nanoplates with the composition of x = 1. As can be seen, the two different regimes: the intraband regime and the interband regime, separated by an absorption minimum at ~ 0.2 eV. It has been well documented that, for metals and crystalline semiconductors, the reduction of the FC absorption coefficient (α) with frequency (ω) (*i.e.* the curve between the FC absorption peak and the separation between intraband and interband) follows a relationship of $\alpha \propto (\omega\tau_0)^{-r}$, where τ_0 is the average FC relaxation time, and r is the scattering exponent.[21] In fact, the value of r reflects the scattering types. Applying quantum mechanics, r = 1.5 when the acoustic phonon scattering dominates, r = 2.5 when the optical phonon scattering dominates, or r = 3 (3.5) when the ionized impurity scattering dominates.[22-24] In practice , all these processes may exist.[25] Using simple power law to fit the corresponding

FC absorption tails (α_{FC}) *versus* photon energy ($\hbar\omega$) in the form of $\alpha_{FC} = \alpha_0 + C(\hbar\omega)^{-r}$ (where α_0 represents background correction term, and *C* represents the fitting coefficient), one may extract *r* values and the information about the scattering process for our nanoplates.

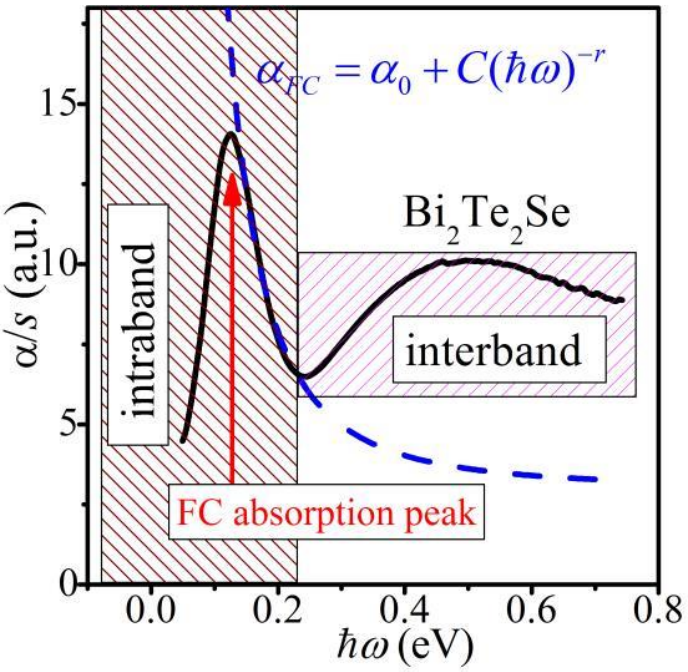

Figure S18 Raw absorption data collected from the Bi_2Te_2Se nanoplates with the dashed line showing the best fit power law to the FC absorption tail.

The optical band gaps ($E_{g,opt}$) for our $Bi_2Te_{3-x}Se_x$ nanoplates can be obtained from the absorption spectra of Figure S17. Since Bi_2Te_3 is an indirect semiconductor while Bi_2Se_3 is a direct one,[26] with the direct-indirect transition taking place at $Bi_2Te_{2.7}Se_{0.3}$,[27] we can determine $E_{g,opt}$ for different $Bi_2Te_{3-x}Se_x$ nanoplates using different models. In the case of indirect band gap ($x < 0.3$), values of $E_{g,opt}$ can be determined by extrapolating the linear part of the $\alpha^{1/2}$ against $\hbar\omega$ to zero (refer to Figure S19a as an example with x= 0.1), whereas in the case of direct band gap ($x \geq 0.3$), $E_{g,opt}$ can be obtained from fitting of the α^2 against $\hbar\omega$ (refer to Figure S19b as an example with x = 0.3).[28]

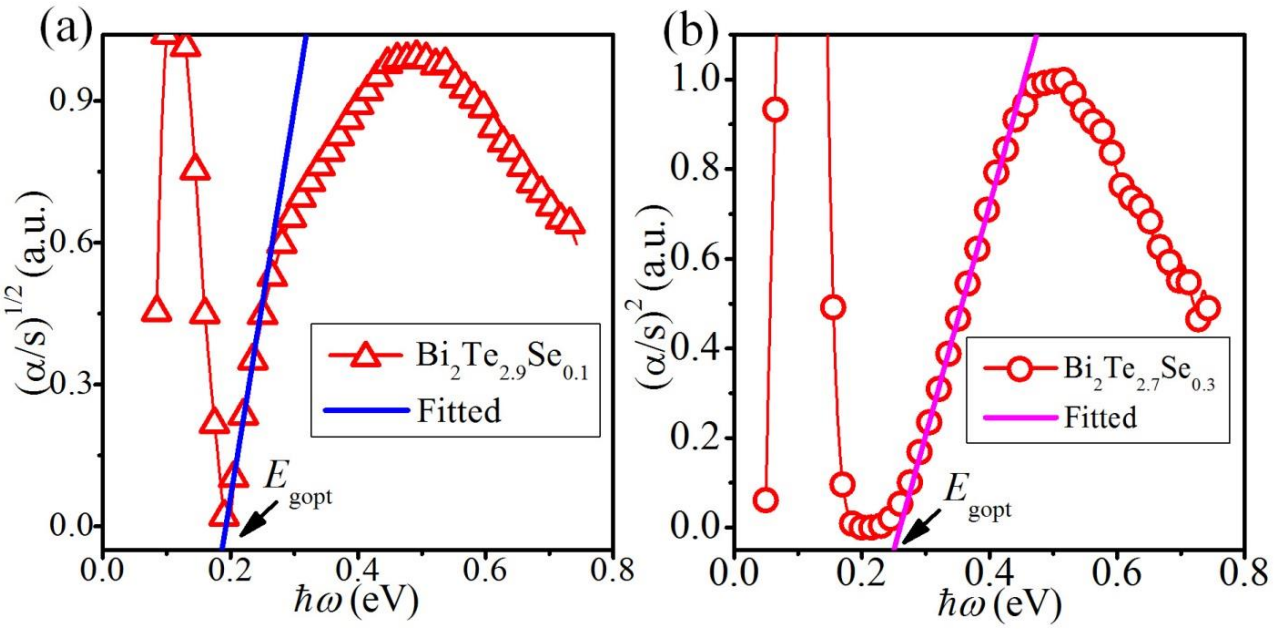

Figure S19 The absorption spectrum for (a) the $Bi_2Te_{2.7}Se_{0.1}$ nanoplates using the indirect gap model, and (b) the $Bi_2Te_{2.9}Se_{0.3}$ nanoplates using the direct gap model.

References

(1) Soni, A.; Zhao, Y. Y.; Yu, L. G.; Aik, M. K. K.; Dresselhaus, M. S.; Xiong, Q. H. Enhanced Thermoelectric Properties of Solution Grown $Bi_2Te_{3-x}Se_x$ Nanoplatelet Composites. *Nano Lett.* **2012**, 12, 1203-1209.

(2) Lotgering, F. K. Topotactical Reactions with Ferrimagnetic Oxides Having Hexagonal Crystal Structures—I. *J. Inorg. Nucl. Chem.* **1959**, 9, 113-123.

(3) Prokofieva, L. V.; Pshenay-Severin, D. A.; Konstantinov, P. P.; Shabaldin, A. A. Optimum Composition of a $Bi_2Te_{3-x}Se_x$ Alloy for the *n*-Type Leg of a Thermoelectric Generator. *Semiconductors* **2009**, 43, 973-976.

(4) Wang, S.; Tan, G.; Xie, W.; Zheng, G.; Li, H.; Yang, J.; Tang, X. Enhanced Thermoelectric Properties of $Bi_2(Te_{1-x}Se_x)_3$-Based Compounds as *n*-Type Legs for Low-Temperature Power Generation. *J. Mater. Chem.* **2012**, 22, 20943-20951.

(5) Yan, X.; Poudel, B.; Ma, Y.; Liu, W. S.; Joshi, G.; Wang, H.; Lan, Y.; Wang, D.; Chen, G.; Ren, Z. F. Experimental Studies on Anisotropic Thermoelectric Properties and Structures of *n*-Type $Bi_2Te_{2.7}Se_{0.3}$. *Nano Lett.* **2010**, 10, 3373-3378.

(6) Hu, L.; Wu, H.; Zhu, T.; Fu, C.; He, J.; Ying, P.; Zhao, X. Tuning Multiscale Microstructures to Enhance Thermoelectric Performance of *n*-Type Bismuth-Telluride-Based Solid Solutions. *Adv. Energy Mater.* **2015**, 5, 1500411.

(7) Liu, W.-S.; Zhang, Q.; Lan, Y.; Chen, S.; Yan, X.; Zhang, Q.; Wang, H.; Wang, D.; Chen, G.; Ren, Z. Thermoelectric Property Studies on Cu-Doped *n*-Type $Cu_xBi_2Te_{2.7}Se_{0.3}$ Nanocomposites. *Adv. Energy Mater.* **2011**, 1, 577-587.

(8) Zhao, L.; Lo, S. H.; He, J.; Li, H.; Biswas, K.; Androulakis, J.; Wu, C.-I.; Hogan, T. P.; Chung, D.-Y.; Dravid, V. P.; Kanatzidis, M. G. High Performance Thermoelectrics from Earth-Abundant Materials: Enhanced Figure of Merit in PbS by Second Phase Nanostructures. *J. Am. Chem. Soc.* **2011**, 133, 20476-20487.

(9) Chen, C. L.; Wang, H.; Chen, Y. Y.; Day, T.; Snyder, G. J. Thermoelectric Properties of *p*-Type Polycrystalline SnSe Doped with Ag. *J. Mater. Chem. A* **2014**, 2, 11171-11176.

(10) Hong, M.; Chen, Z.-G.; Yang, L.; Han, G.; Zou, J. Enhanced Thermoelectric Performance of Ultrathin Bi_2Se_3 Nanosheets through Thickness Control. *Adv. Electron. Mater.* **2015**, 1, 1500025.

(11) Callaway, J.; von Baeyer, H. Effect of Point Imperfections on Lattice Thermal Conductivity. *Phys. Rev.* **1960**, 120, 1149-1154.

(12) Bessas, D.; Sergueev, I.; Wille, H. C.; Perßon, J.; Ebling, D.; Hermann, R. P. Lattice Dynamics in Bi_2Te_3 and Sb_2Te_3: Te and Sb Density of Phonon States. *Phys. Rev. B* **2012**, 86, 224301.

(13) Zhu, T. J.; Fu, C. G.; Xie, H. H.; Liu, Y. T.; Feng, B.; Xie, J.; Zhao, X. B. Lattice Thermal Conductivity and Spectral Phonon Scattering in FeVSb-Based Half-Heusler Compounds. *EPL* **2013**, 104, 46003.

(14) Xie, H.; Wang, H.; Pei, Y.; Fu, C.; Liu, X.; Snyder, G. J.; Zhao, X.; Zhu, T. Beneficial Contribution of Alloy Disorder to Electron and Phonon Transport in Half-Heusler Thermoelectric Materials. *Adv. Funct. Mater.* **2013**, 23, 5123-5130.

(15) Kim, S. I.; Lee, K. H.; Mun, H. A.; Kim, H. S.; Hwang, S. W.; Roh, J. W.; Yang, D. J.; Shin, W. H.; Li, X. S.; Lee, Y. H.; Snyder, G. J.; Kim, S. W. Dense Dislocation Arrays Embedded in Grain Boundaries for High-Performance Bulk Thermoelectrics. *Science* **2015**, 348, 109-114.

(16) Jenkins, J.; Rayne, J.; Ure, R. Elastic Moduli and Phonon Properties of Bi_2Te_3. *Phys. Rev. B* **1972**, 5, 3171-3184.

(17) Clin, T.; Turenne, S.; Vasilevskiy, D.; Masut, R. A. Numerical Simulation of the Thermomechanical Behavior of Extruded Bismuth Telluride Alloy Module. *J. Electron. Mater.* **2009**, 38, 994-1001.

(18) Chen, X.; Zhou, H. D.; Kiswandhi, A.; Miotkowski, I.; Chen, Y. P.; Sharma, P. A.; Lima Sharma, A. L.; Hekmaty, M. A.; Smirnov, D.; Jiang, Z. Thermal Expansion Coefficients of Bi_2Se_3 and Sb_2Te_3 Crystals from 10 K to 270 K. *Appl. Phys. Lett.* **2011**, 99, 261912.

(19) Liu, W.; Lukas, K. C.; McEnaney, K.; Lee, S.; Zhang, Q.; Opeil, C. P.; Chen, G.; Ren, Z. Studies on the Bi_2Te_3-Bi_2Se_3-Bi_2S_3 System for Mid-Temperature Thermoelectric Energy Conversion. *Energy Environ. Sci.* **2013**, 6, 552-560.

(20) Borup, K. A.; Toberer, E. S.; Zoltan, L. D.; Nakatsukasa, G.; Errico, M.; Fleurial, J.-P.; Iversen, B. B.; Snyder, G. J. Measurement of the Electrical Resistivity and Hall Coefficient at High Temperatures. *Rev. Sci. Instrum.* **2012**, 83, 123902.

(21) Shimakawa, K.; Itoh, T. Grain Boundary Scattering of Free Electrons in Ga-Doped Microcrystalline Zinc Oxide Films. *Jpn. Appl. Phys.* **2007**, 46, L577-L579.

(22) Walukiewicz, W.; Lagowski, L.; Jastrzebski, L.; Lichtensteiger, M.; Gatos, H. C. Electron Mobility and Free Carrier Absorption in GaAs - Determination of the Compensation Ratio. *J. Appl. Phys.* **1979**, 50, 899-908.

(23) Pankove, J. I. *Optical Processes in Semiconductors*. Dover: New York, **1971**.

(24) Fan, H. Y. Infra-Red Absorption in Semiconductors. *Rep. Prog. Phys.* **1956**, 19, 107.

(25) Osamura, K.; Murakami, Y. Free Carrier Absorption in *n*-GaAs. *Jpn. J. Appl. Phys.* **1972**, 11, 365-371.

(26) Greenaway, D. L.; Harbeke, G. Band Structure of Bismuth Telluride, Bismuth Selenide and Their Respective Alloys. *J. Phys. Chem. Solids* **1965**, 26, 1585-1604.

(27) Veis, A. N.; Luk'yanova, L. N.; Kutasov, V. A. Band Gap and Type of Optical Transitions at the Interband Absorption Edge in Solid Solutions Based on Bismuth Telluride. *Phys. Solid State* **2012**, 54, 2182-2188.

(28) Scanlon, W. W. Recent Advances in the Optical and Electronic Properties of PbS, PbSe, PbTe and Their Alloys. *J. Phys. Chem. Solids* **1959**, 8, 423-428.

8

Conclusion and Future Directions

8.1 Conclusion

This PhD project focused on enhancing thermoelectric performance of Bi_2Te_3 families by nanostructuring, and understanding the parameters that determine the thermoelectric properties, as well as engineering of these parameters for further performance enhancement. We have carried out massive experiments of synthesizing nanomaterial synthesis, electronic microscopy characterization, performance evaluation, and theoretical modeling studies. On these basses, the newly proposed concepts, i.e. enlarging band gap by reducing the dimension of nanomaterials, designing the well-aligned hierarchical structures to further reduce κ, developing decoupling factor for S and σ, intensifying ionic impurity scattering for charger carriers, and broadening the phonon frequencies scattered by multi-scale sources have been successfully applied to enhance the thermoelectric performance of our as-synthesized nanomaterials, and they universally provide guidance for designing high-performance thermoelectric materials, by nanostructural, compositional and band engineering. Specifically, the conclusions of this PhD research are summarized as follows.

- A one-step microwave-assisted solvothermal method using PVP as surfactant is developed to tune the thickness of Bi_2Se_3 nanosheets. Examined by AFM and re-confirmed by Raman spectroscopy, highly-crystallized Bi_2Se_3 NSs with average thickness of 1 nm, 4 nm, 7 nm and 13 nm have been fabricated. TE property evaluations show a significantly reduced κ (0.41 W/mK), and enhanced $S^2\sigma$ (4.71×10^{-4} W/mK^2 with S = -155.32 μV/K and σ = 1.96×10^4 S/m) in the pellet composed of single-layered Bi_2Se_3 NSs. Through the nonparabolic Kane model simulation and analysis, we found that the enhanced $S^2\sigma$ in the as-prepared samples is originated from broadened E_g and optimized E_f - E_c. Moreover, the

strengthened phonon scattering, reduced κ_e and the suppressed bipolar effect lead to the significantly reduced κ.

- We successfully fabricated Te/Bi_2Te_3 hierarchical nanostructures using Te nanotubes as templates. Through systematic morphological, structural and compositional characterizations, structural quality and the epitaxial relationship between well-aligned Bi_2Te_3 nanoplates with Te nanotube stems are verified. The thermoelectric properties measured from their sintered pellets indicate an increased ZT of 1 when compared with their pure Bi_2Te_3 nanoplates ZT of 0.75. Our modeling suggests that the enhanced ZT of Te/Bi_2Te_3 hierarchical nanostructures is caused by the optimized reduced Fermi level, strengthened the phonon scatterings, and the suppressed bipolar conduction.
- We successfully fabricated $Bi_xSb_{2-x}Te_3$ nanoplates using the microwave-assisted solvothermal method. The measured thermoelectric performance depends strongly upon the Bi concentration, and a peak ZT of 1.2 was achieved from the $Bi_{0.5}Sb_{1.5}Te_3$ pellet. Based on the composition dependent $S^2\sigma$, we performed profound simulation studies using the single Kane model. We found the decoupling factor, namely λE_{def} for S and σ. On this basis, $S^2\sigma$ can be enhanced by reducing λE_{def}, when η has been sufficiently optimized. Through comparing our experimental data with the simulation results, we confirmed that through tuning Bi concentration in nanostructured $Bi_xSb_{2-x}Te_3$, η can be optimized and λE_{def} can be reduced, leading to peak $S^2\sigma$. Moreover, based on our comprehensive TEM investigations and theoretical calculations using the Callaway model, the achieved ultra-low κ is due to the high-density grain boundaries and dislocations, coupled with the inherently existed Sb-Bi lattice disorders that can remarkably strengthen the scattering of phonons with wide frequencies.
- We successfully fabricated $Bi_2Te_{3-x}Se_x$ nanoplates by a microwave-assisted solvothermal method without using surfactants. A high ZT of ~1.23 at 480 K for the n-type Bi_2Te_3-based thermoelectric material was achieved from the sintered $Bi_2Te_{2.7}Se_{0.3}$ nanoplates, which is due to the significantly reduced κ and the shifting of $S^2\sigma$ peak to high temperature compared to the conventional material. Through detailed structural investigations by SEM/TEM and theoretical modeling, the obtained ultra-low κ is understood as due to strong wide-frequency phonon scatterings by multi-scale scattering sources. The shifting of $S^2\sigma$ to higher

temperature is a result of increased $E_{g,opt}$ and the complex carrier scatterings, which respectively suppress the bipolar effect and weaken the dependence of transport properties on temperature.

8.2 Future Directions

Some of the reported results can be further optimized to achieve even higher thermoelectric performance, and the observations and the conclusions made in this PhD thesis can be extended to design other thermoelectric materials for pursuing high *ZT*. The suggestions are as follows.

- In our $Bi_2Te_{3-x}Se_x$ and $Bi_xSb_{2-x}Te_3$ nanoplates based pellets, the thermoelectric properties along in-plane and out-of-plane directions are nearly isotropic, which is different from the strong anisotropic behavior of single crystal Bi_2Te_3 systems. The isotropic feature resulting from the small texture fraction lead to low carrier mobility. Therefore, through increasing the texture fraction, by for example hot deformation; carrier mobility can be increased, which can further enhance their thermoelectric performance.
- It has been well-documented that there are multi conduction/valance subbands in Bi_2Te_3 and Sb_2Te_3 with energy offset of tens meV. The measured thermoelectric properties are contributed by these multi bands together, differentiating from the conventional scenario that the primary conduction/valance bands dominates the electronic transport properties. Therefore, understanding the contributions from each band can provide more possibilities to further enhance the thermoelectric performance.
- Nowadays, the thermoelectric research mainly focuses on the development of high performance n/p type materials. Actually, the final energy transfer efficiency of thermoelectric device is not only determined by *ZT* values, but strongly depends on the device assembly techniques. The stability of the solder materials used to connect the n/p type thermoelectric legs with the ceramic heat absorption/sink boards is critical, and the diffusion between the solder materials and the n/p type legs will also affect the final device significantly. In addition, it is necessary to ensure good heat dissipation in the code side of thermoelectric device. Therefore, to realize the application of thermoelectric device, device assembly techniques should also draw intensive efforts.